UNIVERSITY OF BIRMINGHAM

CFD MODELLING OF OSCILLATORY PERTURBED ADVECTION IN VISCOUS FLOWS

by

SHUAI TIAN

A thesis submitted to
The University of Birmingham
for the degree of
DOCTOR OF PHILOSOPHY

School of Chemical Engineering
The University of Birmingham
December 2015

Abstract

Mechanical oscillation has been proven as an effective method of affecting flow behaviour and material processing of various rheologies, including Newtonian and non-Newtonian types. Further research is required for better understanding on flow behaviour under the superimposed oscillation. In this work, Computational Fluid Dynamics (CFD) was utilised to investigate the application of mechanical oscillation from five aspects: flow and heat transfer under different modes of oscillations; further research on the heat transfer under transverse oscillation; application of transverse oscillation in continuous food sterilisation; liquid film drainage with superimposition of the oscillation; settling of particle in oscillatory fluids.

Validated CFD models were used to compare the efficacy of three modes of oscillations, namely longitudinal, transverse and rotational in enhancing the time-averaged flowrate of Newtonian, power law, Bingham plastic types in isothermal fluids with a range of oscillation parameters and rheological properties. Longitudinal oscillations were found to be generally the most effective in this respect, producing flow enhancements which exceed those generated by transverse and rotational oscillations by a considerable margin, while transverse and rotational oscillations also produce significant flow enhancements of comparable magnitudes. Results also show that transverse oscillations, unlike longitudinal or rotational oscillations, generate a vigorous swirling fluid motion and considerable radial mixing in viscous flows, thus, produce large enhancement in wall heat transfer as well as a nearly-uniform radial temperature field.

The heat transfer with forced transverse vibration was further investigated with fluid of different viscosities, vibration frequencies and amplitudes in tubes. A novel enhanced technique also has been introduced in this work which combines transverse vibration with a step rotation of oscillation orientation (**VF-SR**). This technique produces much more improved effects compared to transverse vibration alone, resulting in much shorter processing tubes. It also excels in comparison with the well-known Kenics helical static mixer which has the disadvantages of being unsuitable for hygienic fluid processing and causes large pressure drops. On the other hand, the mechanical power input associated with the vibration process is

modest. **VF-SR** was then applied to optimise the conventional continuous heat-hold-cool thermal sterilisation processing and was found to contribute fast nearly-uniform heating and cooling of the product, thus, achieving much higher levels of sterility with low loss of product quality in much shorter processing tubes, thus, obviating the need for a holding stage and overall reducing the length of the conventional heat-hold-cool sterilisation process by one or two orders of magnitude, depending on processing conditions. Vibration, therefore, appears to create processing conditions that are much more in agreement with the high temperature for short time (HTST) assumption which is often contradicted in conventional steady flow processing.

A CFD research with a validated model of multiphase flow was conducted on the drainage of a wall liquid film. The effects of rheological properties and vibration parameters were studied with Newtonian, power law and Bingham plastic models. CFD results show that flows of Newtonian rheologies are not affected. While the superimposed harmonic oscillations increases the rate of drainage in shear-thinning films by a substantial factor. Shear-thickening fluids, however, undergo retardation in drainage when subjected to vibration. The drainage of viscoplatic fluids is affected by mechanical oscillation in a similar way as shear-thinning fluids. For high values of yield stress, residual films can have a significant thickness, thus, trapping considerable amounts of material. Vibration is effective at removing most of this film and potentially all of it, if the right vibration intensity is used. In this respect, vibration could also be employed as a tool for controlling the thickness of films in surface coating applications.

Simulations were also executed to look into the settling of particle in oscillatory fluids using dynamic mesh function. Particle is assumed as density of glass. The quantity concerned in this study is the enhancement of terminal settling velocity of particle in vibrated fluid comparing to that in quiescent fluids. Results were reported that the imposition of forced vibration accelerates the settling of particle in shear-thinning fluids. While in shear-thickening fluids, the settling of particle was retarded by the vibrated motion of fluid. Such effects were greatly influenced by the vibration amplitude and frequency. These results can help to understand the particles' behaviour in multiphase flow of solid-liquid or gas-liquid mixture in industrial application, such as settling of impurity in purification and discharging of suspended bubbles in processing of molten chocolate.

ACKNOWLEDGEMENTS

I would like to express my most sincere gratitude to my supervisor **Professor Mostafa Barigou** for his excellent support, patient guidance, and continuous encouragement throughout my study. It is so lucky that I have this opportunity to conduct my research under his supervision, and learnt quite a lot from him, especially his rigorous attitude toward scientific research.

I would like to thank **Dr. Muhammad Eesa**, and **Dr. Neel Nirmalkar** for their kind help on numerical computational technique and package. Also, I appreciate the on-line technical support team at ANSYS UK, Ltd., for their great assistance and valuable suggestions on modelling in using the software package of ANSYS Workbench.

I genuinely appreciate the staff in Department of Chemical Engineering, especially **Lynn Draper** and **Ian Tidmarsh** for their excellent work in supporting my research, as well as the significant financial support offered by Department of Chemical Engineering to fund my research.

I am also grateful to my colleagues and friends, **Zainab Al-Sharify**, **Abdullah Almarshed**, **Sara Ghorbanian Farah Abadi**, **Shahad Al-Najjar**, and other group members in offices 216 and G02 for their help on my project and accompany during my postgraduate years.

Most importantly, I am deeply appreciative of the continuous encouragement and selfless love from my parents.

TABLE OF CONTENTS

LIST OF FIGURES

Chapter 2

Chapter 3

Chapter 5

Chapter 7

LIST OF TABLES

CHAPTER 1.
INTRODUCTION

Fluid is being widely investigated around the world because of its vast range of application in industry, for example, petroleum conveying, food processing, pharmaceuticals manufacturing, machine lubrication and power plant designing. Examples of fluids used in such industries include petroleum, foodstuffs such as milk, juice and molten chocolate, polymer solution, paints, suspensions and water.

Unlike water or juice, most of fluids exhibit non-Newtonian behavior which characterised by complex rheology compared to Newtonian fluids. Additionally, even Newtonian fluids may sometimes, in real industries, could be following non-Newtonian rheologies under some conditions. Therefore, attempt of studying on non-Newtonian flow becomes necessary and valuable, although such complex rheological characteristics may cause a lot of difficulties in investigations on non-Newtonian flow behavior (Chhabra and Richardson, 1999). Mechanical oscillations, which have been widely employed in industries, have shown their potential in affecting non-Newtonian flow and are receiving more and more attention from researchers. Extensive work has been conducted on investigating the effect of mechanical oscillations on non-Newtonian fluid flow over last decades. Nevertheless, further studies are still imperative and deserve large numbers of attention especially some specific applications in this research area, e.g. enhancing flow, or drainage of non-Newtonian fluids, accelerating settling of solid particle in a non-Newtonian fluid. Despite that mechanical oscillations cannot affect isothermal flow of Newtonian fluid, the chaotic advection resulted by the vibrated motion may facilitate the heat transfer, which can applied in industrial processing, such as food sterilisation.

Large volume of attempts has been devoted to study the flow behavior of non-Newtonian rheologies. Various experimental methods, such as Particle Image Velocimetry (PIV) and Laser Doppler Velocimetry (LDV), have been utilized in researches and process industries. However, the applications of those methods are usually limited where fluids studied are required to be transparent, but in fact most non-Newtonian fluids are opaque. Moreover, the Positron Emission Particle Tracking (PEPT) technique has been widely used in the study of opaque fluids by tracking a

single radioactive particle tracer in three dimensional spaces (Barigou, 2004; Doucet *et al*., 2008). However its application is also limited as its spatial requirement.

Computational Fluid Dynamics (CFD) has been proven as a reliable and effiective tool for studying flow behaviors. In recent decades, the ability and application of CFD is significantly growing as the impressive development of numerical methods and computer performance. Large number of CFD applications have been developed, for example, design of equipment, optimisation of industrial process, investigation of flow phenomenon by its lower expense and powerful capability of visualization in some important quantities, such as velocity, temperature, and pressure.

Complex fluids impose challenges which lead to difficulties in industry scale, for example, high energy is required to drive conveying flow of highly viscous fluid. It has been reported that mechanical oscillations can be used to enhance the flow of non-Newtonian fluids with shear-thinning characteristics by imposed additional shear on the flow. The effect of different modes of oscillations, including longitudinal, rotational and transverse oscillations on viscous non-Newtonian flow in tube has been exploited for many years. Indeed, some results have been given on the phenomenon of facilitating flow by oscillations, further on the effects of rheological parameters and oscillation intensities. However, comparison studies between these three types of oscillations on their efficacies in facilitating non-Newtonian flow and improving heat transfer are still missing.

Laminar tube flow characterised by wide range of velocity across the tube is always accompanied by wide temperature distributions due to its lack of radial mixing. As consequence of that vastly un-uniform thermal treatment on the product at different radial positions in the tube has been noticed. For example, in the continuous sterilisation process, the food near the hot tube wall has to be over-processed to ensure desired sterility throughout. It has been reported that forced transverse vibration superimposed on the steady laminar flow has a potential of generating a vigorous

swirling fluid motion, which contributes a substantial benefits for heat transfer including a large increase in wall heat transfer, a much more uniform radial temperature profile, a rapid development of the temperature profile along the tube, rapid heating of the core region of the flow, and relatively short processing tubes. This transverse oscillation technique excels in comparison with the well-known Kenics helical static mixer which has the disadvantages of being unsuitable for hygienic fluid processing, difficulty in cleaning for its possible intricate geometries and causes large pressure drops. However, a shortage of some possible cold vortex regions induced by this transverse oscillation technique leads to a requirement of better mixing. Also, optimisation of the conventional Heat-Hold-Cool sterilisation process remains a long-term difficulty in food industry.

Mechanical oscillation has the potential of enhancing the drainage of liquid film of non-Newtonian fluids. Free drainage is extremely slow in case of highly viscous fluids, and results in equilibrium films in case of yield-stress fluids. Additional shear resulted from shaking of adhered plate may contribute to significant reduction in viscosity of non-Newtonian fluids, thus enhancement of liquid film drainage. Some theoretical studies have been represented on the phenomenon. However, studies with wide ranges of rheological properties and oscillation parameters are still missing.

Solid particle in liquid may settle extremely slowly in case of highly viscous fluids, or suspended in case of high yield-stress fluids under gravity even if its density is greater than the fluid density. However, settling motion of particle may be greatly accelerated in oscillatory non-Newtonian fluids. A bulk of work has been reported on the settling of particle in a quiescent liquid. However, studies with oscillatory fluids are still rare, and wide ranges of rheological properties and oscillation parameters are still missing.

1.1. THE AIMS

The research reported in this thesis is conducted by commercial CFD software ANSYS-CFX. The main aim of this work is to study the flow behaviour of various types, including Newtonian, as well as non-Newtonian power law, and Bingham plastic fluids, under mechanical oscillation in following areas: flow and heat transfer in a straight tube under different modes of mechanical oscillations; liquid film drainage on vibrated substrate and solid particle settling in oscillatory fluids. The aims of this research are stated as follow:

i. To compare the efficacy of three modes of mechanical oscillations on the flow and heat transfer in a straight tube.

ii. To reveal the effect of transverse mechanical vibration on the heat transfer in the straight tube.

iii. To apply the imposed mechanical transverse oscillation technique in the food heat-hold-cool continuous sterilisation process.

iv. To investigate the potential of mechanical oscillation in affecting the fluid film drainage.

v. To study the capacity of mechanical oscillation in accelerating or retarding the motion of solid particle in non-Newtonian fluids.

1.2. LAYOUT OF THESIS

As the aims stated above, the thesis is divided into the following chapters:

Chapter 2: In this chapter, general background of rheologies, and CFD including its methodology, advantage, limitation, and procedures, is introduced.

Chapter 3: In this chapter, the effects of three modes of mechanical oscillations (i.e. longitudinal, rotational and transverse oscillations) on the flow and heat transfer in a straight tube is indicated. Rheologies used in this work are Newtonian, and non-Newtonian power law and Bingham plastic types. The effects of rheological properties including fluid consistency index, flow behaviour index and yield stress, vibration parameters including amplitude and frequency, and pressure gradient on the flow enhancement are presented.

Chapter 4: In this chapter, a further research on the effects of transverse vibration on the heat transfer in both heated and cooled tube is reported. An enhanced transverse vibration with step rotation technique is developed. Fluid used in this research is temperature-dependent Newtonian fluid. Kenics static mixer case is also included to compare with the vibrated cases. The effects of vibration frequency and amplitude, fluid viscosity, and frequency of step rotation on the temperature profiles at tube exit and temperature development along tube axis are studied.

Chapter 5: In this chapter, the enhanced technique of transverse vibration with step rotation is applied in the continuous process of food sterilisation. Three stages including heating, holding and cooling are investigated both separately and together. The effect of transverse vibration on the sterility and quality values is indicated by comparing to steady flow in a straight pipe with and without Kenics static mixer.

Chapter 6: In this chapter, the effect of mechanical vibration on the liquid drainage is reported. Fluids used are Newtonian and non-Newtonian of power law and Bingham plastic types. The effects of rheological properties including fluid consistency index, flow behaviour index and yield stress, vibration parameters including amplitude and frequency, and the inclination angle of substrate are investigated.

Chapter 7: In this chapter, mechanical vibration is applied to affect the motion of solid spherical particle in fluids. Fluids used are Newtonian and non-Newtonian of power law and Bingham plastic types. The effects of rheological properties including fluid consistency index, flow behaviour index and yield stress, vibration parameters including amplitude and frequency are investigated.

Chapter 8: In this chapter, the summary of these works is given, conclusions and recommendation for further work are made.

Journal publications list:

✧ Tian S, Barigou M., 2015. An improved vibration technique for enhancing temperature uniformity and heat transfer in viscous fluid flow. Chemical Engineering Science, 123, 609-619.

REFERENCES

Barigou, M., 2004. Particle Tracking in Opaque Mixing Systems: An Overview of the Capabilities of PET and PEPT. Chemical Engineering Research and Design, 82(9), 1258-1267.

Doucet, J., Bertrand, F., Chaouki, J., 2008. A measure of mixing from Lagrangian tracking and its application to granular and fluid flow systems. Chemical Engineering Research and Design, 86(12), 1313-1321.

CHAPTER 2.
BACKGROUND OF RHEOLOGY AND CFD

Summary

In this chapter, an introduction is given on the general background of rheologies, including Newtonian, power law, Bingham plastic and Herschel-Bulkley types. The mathematical expressions for these four rheology models are given and two popular techniques used for numerical simulation with yield stress fluids, named as bi-viscosity and exponential models, are represented. Secondly, Computational Fluid Dynamics (CFD) is introduced on the topics of its applications, advantages and limitations. The typical CFD analysis procedure is explained step by step: initial thinking, pre-processing, solving the equations and post-processing. Three most widely used discretisation methods, i.e. finite-difference, finite-element, and finite-volume methods, are presented. The most popular tools, including commercial softwares and codes, are also listed by strategies of geometry building, meshing, model setup, calculating and results analysis.

2.1. INTRODUCTION OF RHEOLOGIES

2.1.1. Fluid rheologies

The simplest mathematical model used to describe fluid is Newtonian fluid model, which is characterised by the linear relation between shear rate $\dot{\gamma}$ and shear stress τ, as $\tau = \mu\dot{\gamma}$ (Batchelor and Keith, 2000). The ratio of shear stress and shear strain rate, μ is defined as viscosity used to measure its resistance to shear stress. However, no fluid can fit Newtonian fluid model exactly, although some kinds of fluids, such as most gases and water, can be assumed as Newtonian fluid under ordinary condition. Non-Newtonian fluid, which exhibits different rheological properties from Newtonian fluid, is much more common in industry and daily life. Non-Newtonian fluid model involves time-dependent types if its viscosity relies on the duration of shearing, and time-independent types. According to the apparent viscosity derived from the General Newtonian Fluid concept, time-independent non-Newtonian fluid includes three types: shear-thinning, shear-thickening (together named as power law or Ostwald−de Waele model) and viscoplastic fluid (e.g. Bingham plastic and Herschel-Bulkley fluids). The rheological properties of Newtonian, non-Newtonian including power law (Ostwald, 1925), Bingham plastic (Bingham, 1922) and Herschel-Bulkley fluids (Herschel and Bulkley, 1926) have been depicted in Figure 2.1, and more detailed description is given as follow.

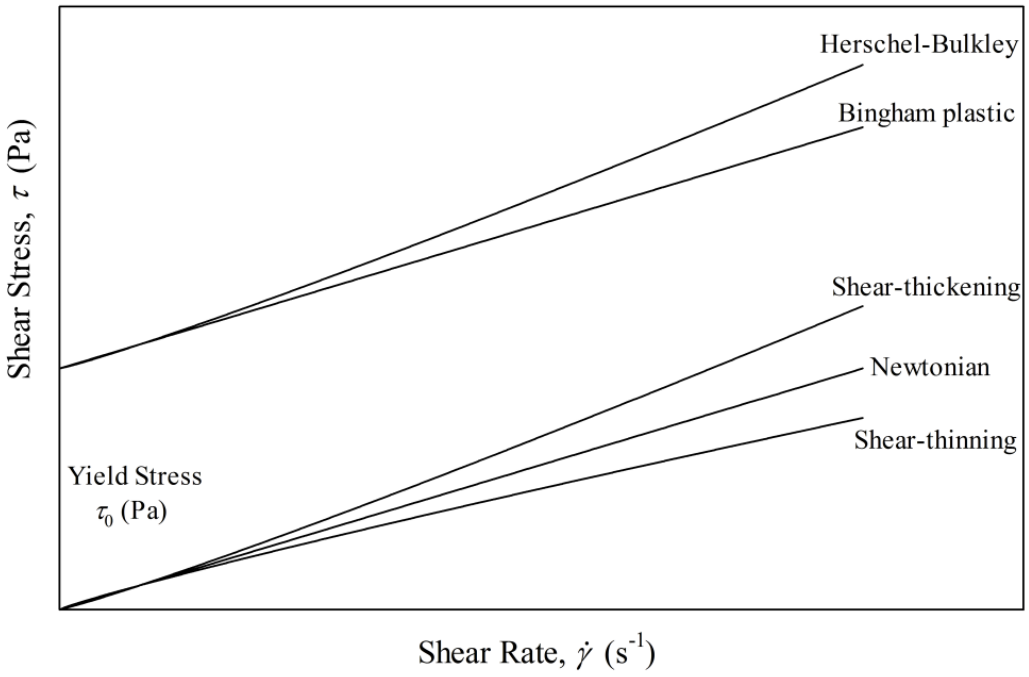

Figure 2.1. Rheological properties of Newtonian and non-Newtonian fluids.

2.1.2.1. Shear-thinning fluid

Shear-thinning fluid (i.e. Pseudoplastic fluid) can be described by the following expression (Ostwald, 1925):

$$\tau = k\dot{\gamma}^n \tag{2.1}$$

where τ is the shear stress, k is the consistency index, $\dot{\gamma}$ is shear rate, n is the flow behaviour index and for shear-thinning fluid, value of n is smaller than 1.

Shear-thinning behavior can be considered as a result of an equilibrium number of interactions or entanglements decrease when the fluid is sheared. This pseudoplastic effect happens where the suspension is initially in the state of flocculation and transited into stable state. Some examples of shear-thinning behavior can be seen in polymer

solutions, polymer melts, complex fluids and suspensions, such as ketchup, cream, and paint.

2.1.2.2. Shear-thickening fluid

Similar to shear-thinning fluid, shear-thickening fluid (i.e. Dilatant fluid) can be described by Eq. (2.1) as well. However, for shear-thickening fluid, the flow behavior index is larger than 1 ($n > 1$).

Dilatancy (i.e. Shear-thickening) effect occurs in the transition to the state of flocculation when suspension is initially stable under the condition that inter-particle forces, such as Van der Waals force are the dominate forces. This type of fluid behavior can be observed in corn starch suspensions.

2.1.2.3. Viscoplastic fluid

Viscoplastic fluid, which behave as rigid body (i.e. neither deform nor flow), exhibits fluid behavior only if a certain stress value (i.e. yield stress) is reached when shear stress is applied. Two typical models are Bingham plastic and Herschel-Bulkley types, which are described by Eqs. (2.2) and (2.3) separately.

Bingham plastic:
$$\begin{cases} \tau = \mu_B \dot{\gamma} + \tau_0, & \text{for} \quad \tau > \tau_0 \\ \dot{\gamma} = 0, & \text{for} \quad \tau \le \tau_0 \end{cases} \tag{2.2}$$

Herschel-Bulkley:
$$\begin{cases} \tau = k\dot{\gamma}^n + \tau_0 \quad (n \ne 1), & \text{for} \quad \tau > \tau_0 \\ \dot{\gamma} = 0, & \text{for} \quad \tau \le \tau_0 \end{cases} \tag{2.3}$$

where τ_0 is the yield stress, μ_B is the plastic viscosity. Common examples of viscoplastic fluids are mud, slurry and toothpaste for Bingham plastic, while minced fish paste and raisin paste for Herschel-Bulkley types. When $n = 1$, Eq. (2.3) reduces to its form for Bingham plastic fluid.

2.1.2.4. Apparent viscosity

The apparent viscosities for non-Newtonian fluids of power law, Bingham plastic and Herschel-Bulkley fluids are given by:

Shear-thinning power law: $\eta = k\dot{\gamma}^{n-1} \quad (n < 1)$ (2.4)

Shear-thickening power law: $\eta = k\dot{\gamma}^{n-1} \quad (n > 1)$ (2.5)

Bingham plastic:
$$\begin{cases} \eta = \mu_B + \tau_0/\dot{\gamma}, & \text{for} \quad \tau > \tau_0 \\ \eta \to \infty, & \text{for} \quad \tau \le \tau_0 \end{cases} \tag{2.6}$$

Herschel-Bulkley:
$$\begin{cases} \eta = k\dot{\gamma}^{n-1} + \tau_0/\dot{\gamma} \quad (n \neq 1), & \text{for} \quad \tau > \tau_0 \\ \eta \to \infty, & \text{for} \quad \tau \le \tau_0 \end{cases} \tag{2.7}$$

where η is the apparent viscosity, and especially, the shear-independent Newtonian viscosity is therefore, can be reduced from power law type where $n = 1$, thus:

$$\mu = k \tag{2.8}$$

where μ is the viscosity for Newtonian fluid. From Eqs. (2.4) and (2.5), and Figure 2.2 in which relationship between apparent viscosity and shear strain rate for both shear-thinning and shear-thickening fluids has been plotted, it can be seen that shear-thinning rheology exhibits decreased viscosity when subjected to increased shear strain rate. While for shear-thickening fluid, the increase in shear strain rate leads to an increase in viscosity.

Viscoplastic fluid is characterised by the yield stress. Due to which, both Bingham plastic and Herschel-Bulkley models used in this thesis are discontinuous. Therefore,

for general flow fields, modified numerical techniques are necessary for capturing yielded/unyielded regions (Mitsoulis, 2007; Mitsoulis and Galazoulas, 2009). For example, bi-viscosity model and exponential model were developed to help avoiding introducing the discontinuous parameters into the calculation with viscoplastic fluids.

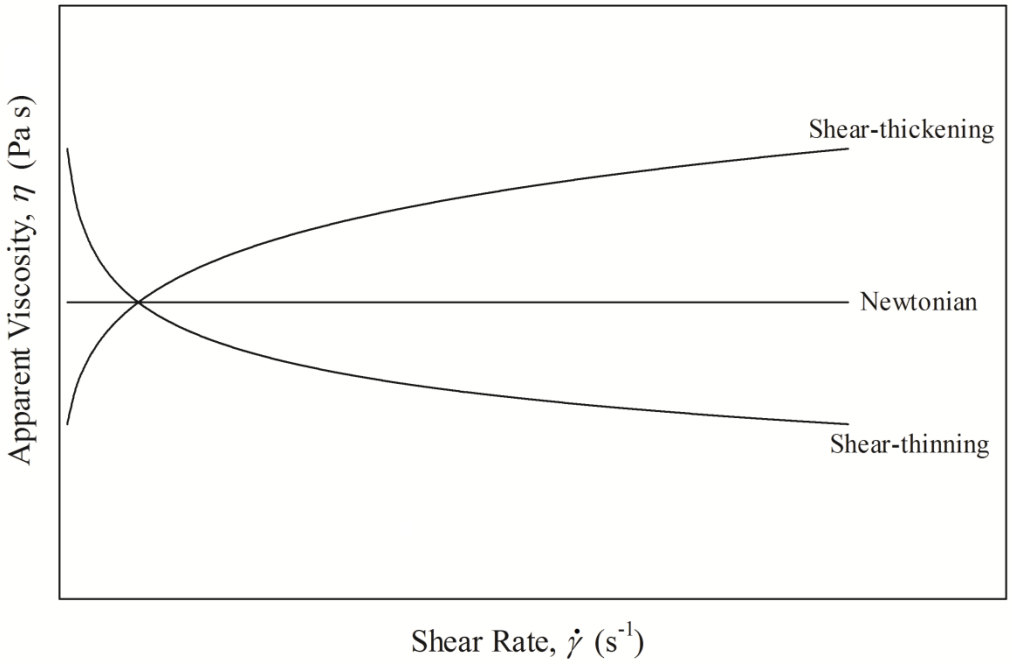

Figure 2.2. The relationship between apparent viscosity and shear rate for shear-thinning, shear-thickening and Newtonian fluids.

2.1.2. Bi-viscosity model

Bi-viscosity model is in fact a regularization of viscoplastic model with two viscosities (i.e. two Newtonian models for Bingham plastic type or one Newtonian model and one power law model for Herschel-Bulkley type), μ_1 in case of $\tau < \tau_y$, μ_2 for Bingham plastic type or η_2 for Herschel-Bulkley type in case of $\tau \geq \tau_y$ (Tanner and Milthorpe, 1983), where τ_y is a stress over than yield stress of τ_0. For a Bingham fluid, by the work of Tanner and Milthorpe (1983), the optimal relationship between μ_1 and μ_2 was found to be $\mu_1 = 1000\mu_2$. The illustration of the bi-viscosity model is shown in Figure 2.3.

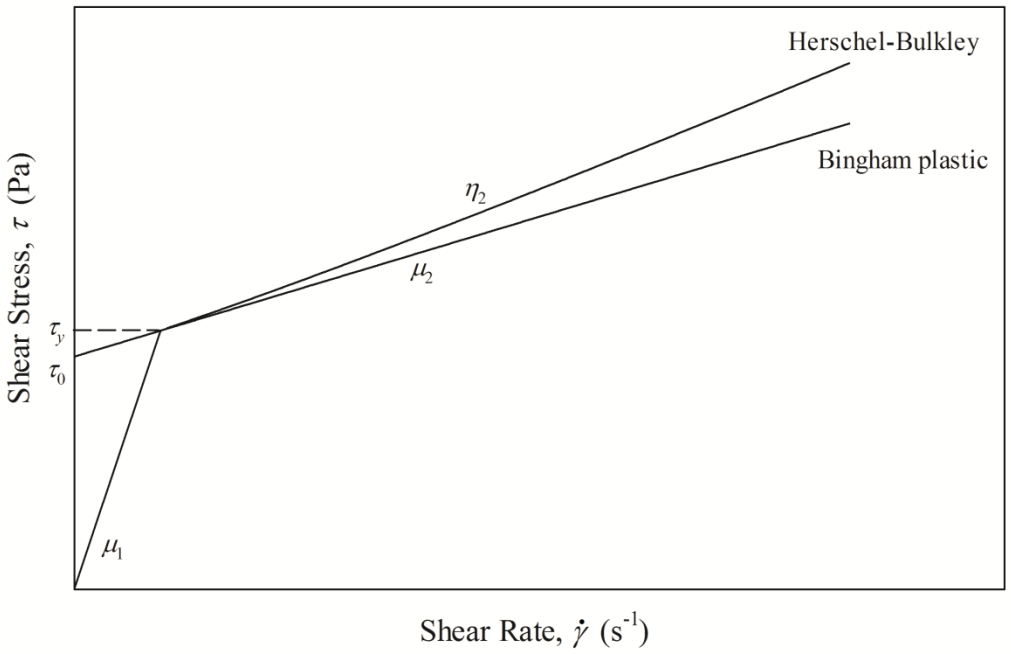

Figure 2.3. The bi-viscosity model for Bingham plastic and Herschel-Bulkley fluids (Tanner and Milthorpe, 1983).

2.1.3. Exponential model

Based on the earlier works by Shangraw (1961), Papanastasiou (1987) proposed an exponential model by introducing a regularization parameter of *m* into the expressions of Bingham plastic and Herschel-Bulkley fluids (so the exponential model is usually named as Bingham-Papanastasiou model for Bingham plastic fluid (Mitsoulis, 2007; Zhu *et al.*, 2010), or called as Herschel-Bulkley-Papanastasiou model for Herschel-Bulkley fluid (Mitsoulis, 2007; Mitsoulis and Galazoulas, 2009). The detailed expressions are given as follows:

Bingham plastic: $$\tau = \mu_B \dot{\gamma} + \tau_0 \left[1 - \exp(-m\dot{\gamma})\right] \tag{2.9}$$

Herschel-Bulkley: $$\tau = \mu_B \dot{\gamma}^n + \tau_0 \left[1 - \exp(-m\dot{\gamma})\right] \tag{2.10}$$

As Figures 2.4 and 2.5 show, with the growth of m, the exponential models (Eqs. (2.9) and (2.10)) lead to more accurate approximations of ideal Bingham plastic and Herschel-Bulkley fluids. In the limit of $m = 0$, the Newtonian or power law cases were recovered, and in the opposite limit of $m \to \infty$, Eqs. (2.4) and (2.5) were fully equal to ideal Bingham plastic and Herschel-Bulkley types separately. However, a value of over than 100 s has been sufficient for a reasonable and reliable approximation of ideal viscoplastic model (Blackery and Mitsoulis, 1997) (shown in Figure 2.4 and Figure 2.5).

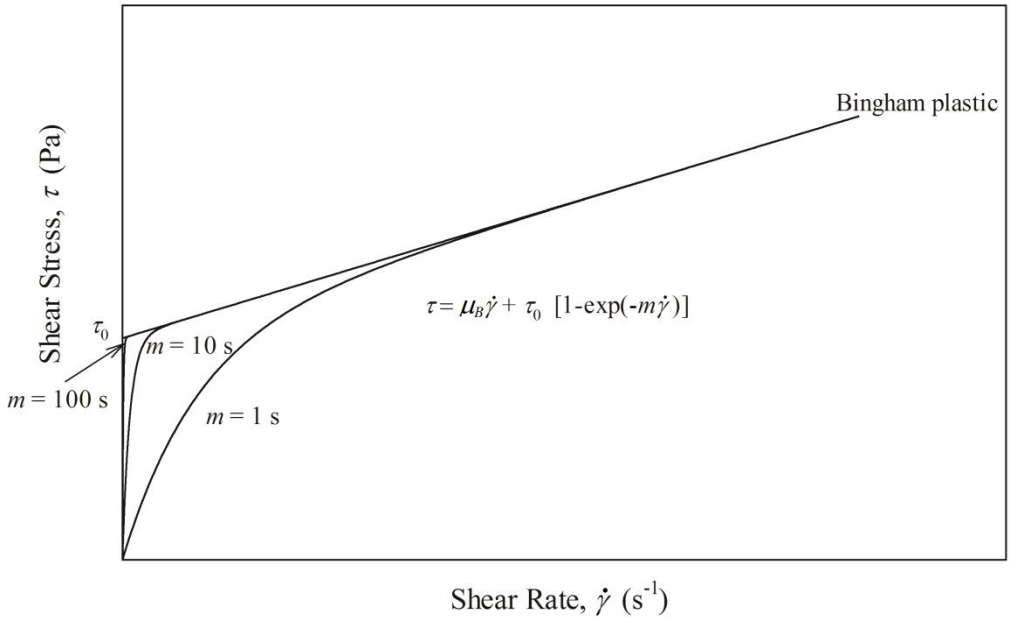

Figure 2.4. The exponential model for Bingham plastic fluid for different values of the regularization parameter m.

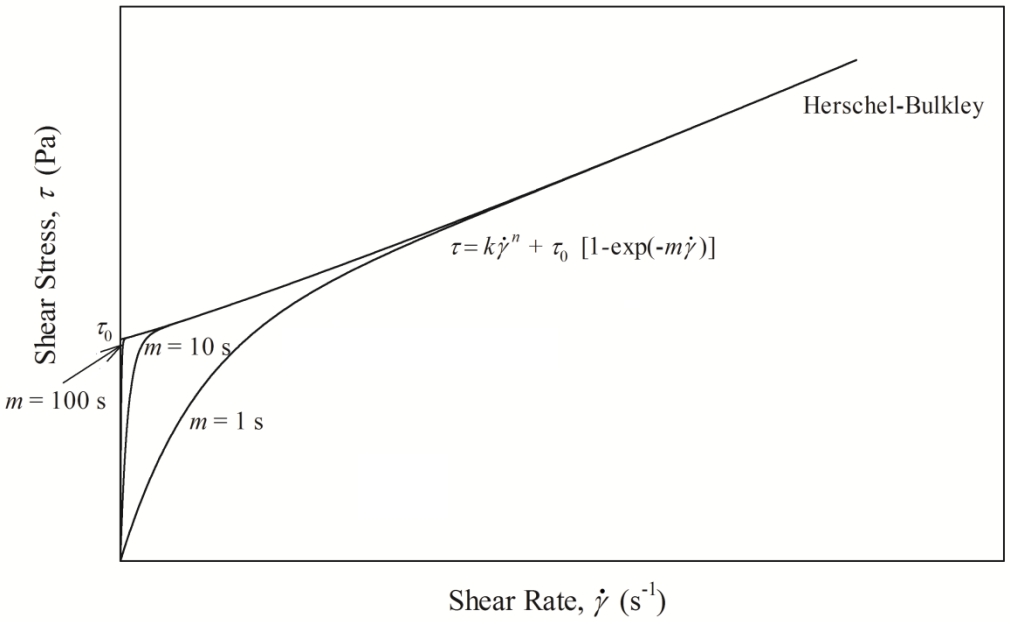

Figure 2.5. The exponential model for Herschel-Bulkley fluid for different values of the regularization parameter *m*.

2.2. INTRODUCTION OF CFD

Computational fluid dynamics which is a branch of fluid dynamics, abbreviated known as CFD, is using computer-based calculation to analyse problems involving fluid (liquid, gas or both) flow, heat transfer and associated phenomena such as chemical reactions by solving a set of governing equations (Versteeg and Malalasekera, 2007; Sayma, 2009). Computational techniques provide an alternative mean to experiment techniques and analytical methods by replacing the partial differential equations with series of algebraic equations which are much easier to solve. With the development of computer resources and packages or code, CFD become much more powerful and has been widely used in industrial and non-industrial application areas, such as:

- ✧ Aerospace engineering: tunnel test (e.g. flow around aircraft)
- ✧ Automotive engineering: shape design used to minimise the drag force and optimise the down force
- ✧ Biomedical engineering: flow of blood through vascellum
- ✧ Chemical process engineering: gasification, liquification, mixing and separation
- ✧ Food engineering: flow and heat transfer in pipes
- ✧ Meteorology: weather prediction

2.2.1. Advantages and limitations of CFD

After several decades of dramatic development, CFD has been a reliable and robust modeling technique in the design and analysis. Its powerful capability of visualisation in some important quantities, such as velocity, temperature, and pressure, provides even more detailed information than practical measure methods. Moreover, CFD offers possibility in research under ideal conditions which are impossibly or difficultly achieved. Additionally, CFD showed its significant advantage in both expense and time in engineering investigation. For example, CFD can help to do a parameter comparison without another system, and predict reliable results without a possible time-costing and/or expensive experiment.

Although CFD has become an essential alternative technique in industrial study and application, the accuracy of its solution is always dependent on the models, which are sometimes unable to fully describe the real physical problems. In addition, as a computer-based numerical method, CFD inevitably evolves numerical errors, including round-off error due to the finite size of storage unit in computer and the truncated error due to the numerical approximation which is hardly removed in practice.

2.2.2. Procedures of CFD

A typical CFD analysis should consist of the following stages:

- ✧ Build a numerical model to describe the physical problem
- ✧ Create geometry to represent the computational domain
- ✧ Generate mesh to discretise the computational domain
- ✧ Set up the simulation to describe the CFD problem
- ✧ Discretise the differential equations with particular discretisation method
- ✧ Iterate the discretisation equations to obtain the solutions to differential equations
- ✧ Analyse the results
- ✧ Representing the results by plotting or visualisation

Figure 2.6 indicates a flowchart of standard CFD analysis procedure (Shaw, 1992). And more details are given in the following sections.

2.2.2.1. Initial thinking

It is quite important to begin the numerical study with an accurate understanding on the problem that is going to be modelled. Reasonable simplification on model which is, sometimes, necessary and helpful should be considered in this stage. Other work required to do in this stage involves selection of geometry dimensions, rheologies, boundary conditions and initial conditions.

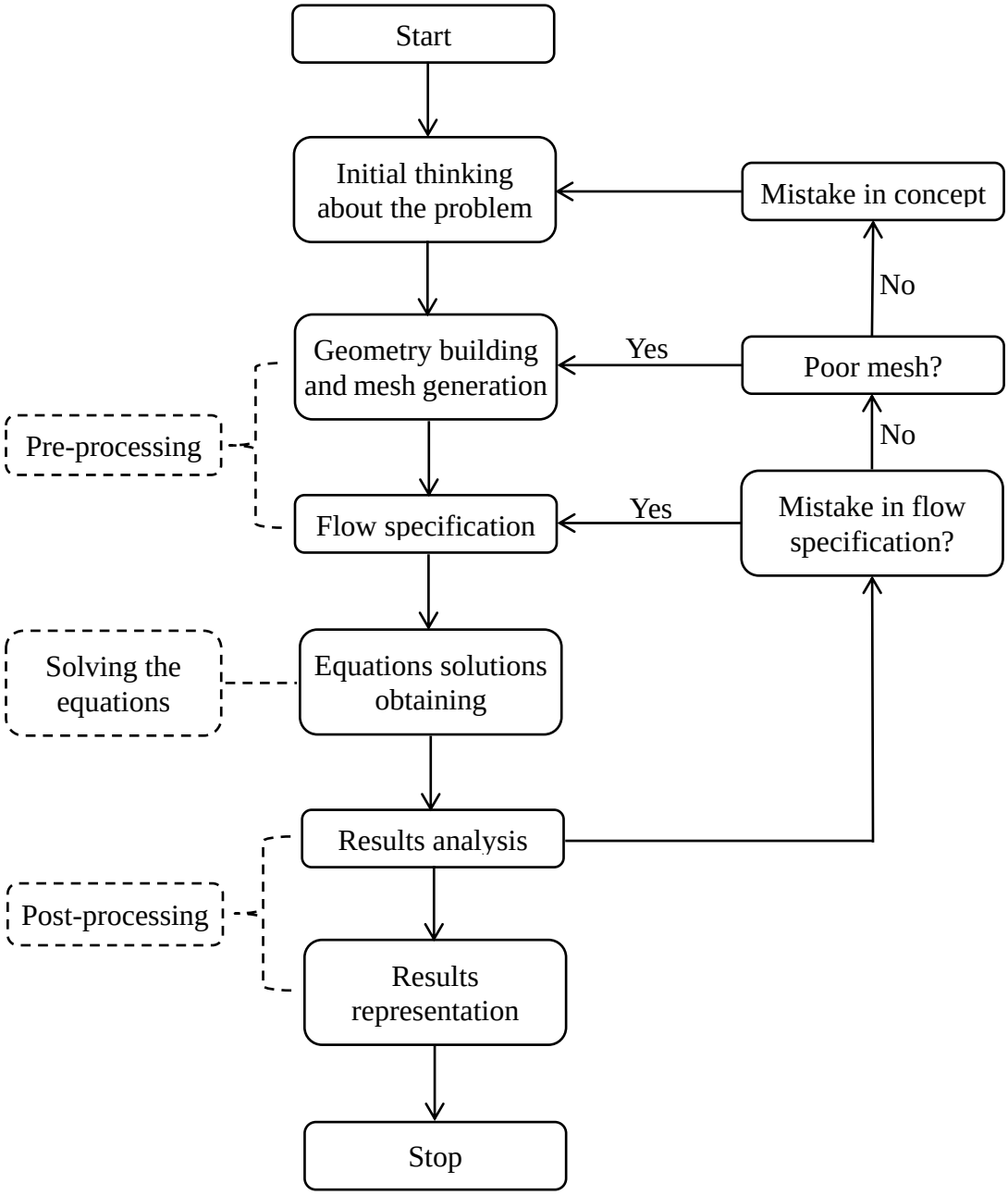

Figure 2.6. A flowchart of the CFD analysis procedure (Shaw, 1992).

2.2.2.2. Pre-processing

2.2.2.2.1. Geometry and mesh

Geometry should fully represent the computational domain in which the governing equations of fluid flow and/or heat transfer are solved, and always be created in the

sequence of points, curves, surfaces and volumes. Usually, some complex geometries are designed by the use of specialised CAD software (e.g. Pro/ENGINEER, SOLIDWORKS and CATIA) and most popular CFD packages offering the accessing interface of these CAD software.

Mesh generation is the subsequent stage of geometry building. In this stage, the continuous computational domain (line for 1-D geometry, plan for 2-D geometry and body for 3-D geometry) is discretised into small discrete cells. The nodes of cells are the positions at which the flow variables are defined and stored.

Mesh can be classified into two types namely, structured mesh and unstructured mesh. The typically possible mesh shapes are hexahedral in 3-D geometry and quadrilateral in 2-D geometry for structured mesh, while tetrahedral in 3-D geometry and triangular in 2-D geometry for unstructured mesh. Structured mesh usually behaves the following advantages: (i) higher spacing efficiency, (ii) better convergence, (iii) more reliable solution, and (iv) less computational load (George *et al.*, 1991; Castillo, 1991), but disadvantages in lower adaptability and complicated meshing work for complex geometry (Mavriplis, 1996).

In the stage of mesh generation, mesh should be particularly fine to contribute an accurate solution for the region of large variables gradients (e.g. inflation layers are quite necessary for the solving of velocity field near the wall specified as no-slip). However, fine mesh unavoidably leads to heavy computational load for which mesh independent study is always necessary and helpful. Such study can be carried out by starting with a coarse mesh and then the numerical results can said to be mesh-independent until it no longer changes with any further refinement of mesh.

2.2.2.2.2. Setup of simulation

Setup of simulation involves general specifications, such as flow model, boundary

conditions, fluid properties, simulation timestep, and typical specifications for some particular application, for example particle's travelling control for particle tracking technique and volume fractions setting up for liquid-gas flow.

2.2.2.2.3. Validation of models

All the setting up in pre-processing should be evaluated by the procedure of model validation before its application. Validation of CFD model can be carried out by comparing the numerical results to the theory, experimental or analytical data. The validation test is quite helpful in establishment of reliable and robust models because that failure in validation always contribute some modifications, such as improvement in mesh or change in the setup of simulation. However, validation is, sometimes, not possible due to the lack of theory, experimental or analytical data. Reviews of CFD validation have been summarised in literatures (e.g. Stern *et al*. (1999), Oberkampf and Trucano (2000; 2002)).

2.2.2.3. Solving the equations

2.2.2.3.1. Governing equations

CFD problems can be described in mathematical way by governing equations, including continuity, momentum and energy equations where the latest one is for the problems coupled with heat transfer. These three equations can be developed respectively on basis of conservation of mass, momentum and energy from the so-called generic transport equation. The transport equation describes the processes by which a dependent variable ϕ is transported through the fluid, and is written as the following general convection-diffusion form (Patankar, 1980; Eesa, 2009):

$$\underbrace{\frac{\partial}{\partial t}(\rho\phi)}_{\text{Transient term}} + \underbrace{\nabla\cdot(\rho\mathbf{U}\phi)}_{\text{Convection term}} - \underbrace{\nabla\cdot(\Gamma_\phi\nabla\phi)}_{\text{Diffusion term}} = \underbrace{S_\phi}_{\text{Source term}} \tag{2.11}$$

where ρ is the fluid density, t is time, ∇ is the divergent vector operator, defined as $\nabla = \frac{\partial}{\partial x}\boldsymbol{i} + \frac{\partial}{\partial y}\boldsymbol{j} + \frac{\partial}{\partial z}\boldsymbol{k}$, and $\boldsymbol{U}$ is the velocity vector consisting of u, v and w, which are velocity components separately in x, y and z direction. ϕ is a dependent variable, Γ_ϕ is a diffusion coefficient for ϕ, and S_ϕ is a source term.

In Eq. (2.11), the transient term represents the change rate of ϕ per unit volume and time. The convective term represents the flux of ϕ advected by the flow. The diffusion term represents the transport of ϕ due to random motion of molecules. The source term represents the generation and/or destruction of ϕ, and any other term which cannot be indicated by advection term or diffusion term (Patankar, 1980).

While $\phi = 1$, $\Gamma_\phi = 0$ and $S_\phi = 0$, Eq. (2.11) is rewritten to continuity equation, which states that, the fluid enters in the system is equal to that leaves the system and can be given in vectorial form as follow (Lamb, 1895):

$$\frac{\partial}{\partial t}(\rho) + \nabla(\rho \boldsymbol{U}) = 0 \tag{2.12}$$

While ϕ separately represents u, v and w, Γ_ϕ is the apparent viscosity η, and S_ϕ is the sum of forces acting on a patch of fluid, Eq. (2.11) is rewritten to momentum equations, which state that, the change in momentum is equal to the action of extraneous forces by applying Newton's second law within the system. Momentum equations are given in vectorial form as follow (Lamb, 1895):

$$\begin{cases} \dfrac{\partial}{\partial t}(\rho u) + \nabla \cdot (\rho u \boldsymbol{U}) - \nabla \cdot (\eta \nabla u) = F_x \\ \dfrac{\partial}{\partial t}(\rho v) + \nabla \cdot (\rho v \boldsymbol{U}) - \nabla \cdot (\eta \nabla v) = F_y \\ \dfrac{\partial}{\partial t}(\rho w) + \nabla \cdot (\rho w \boldsymbol{U}) - \nabla \cdot (\eta \nabla w) = F_z \end{cases} \tag{2.13}$$

Taking the first equation of Eq. (2.13) which describes the momentum conservation in x direction as an example, F_x is the extraneous force acting on the system along x, including the surface force (e.g. pressure $\dfrac{\partial p}{\partial x}$), body force (e.g. the gravity ρg_x) and viscous forces which are in addition to those described by the term of $\nabla \cdot (\eta \nabla u)$ (Patankar, 1980).

While ϕ represents specific enthalpy S_H, Γ_ϕ is the ratio of thermal conductivity λ to constant-pressure specific heat C_p which is assumed constant for ideal fluid, and S_ϕ is volumetric rate of heat generation S_h, Eq. (2.11) is rewritten to energy equation, which states that, the change of energy in the system is equal to the net change of energy that enters and leaves the system. Energy equation is given in vectorial form as follow (Patankar, 1980):

$$\frac{\partial}{\partial t}(\rho S_H) + \nabla \cdot (\rho \boldsymbol{U} S_H) - \nabla \cdot (\frac{\lambda}{C_p} \nabla S_H) = S_h \tag{2.14}$$

Substituting S_H by $C_p \times T$ (temperature) leads to:

$$\frac{\partial}{\partial t}(\rho T) + \nabla \cdot (\rho \boldsymbol{U} T) - \nabla \cdot (\frac{\lambda}{C_p} \nabla T) = \frac{S_h}{C_p} \tag{2.15}$$

2.2.2.3.2. Discretisation methods

The Eqs. (2.11) — (2.15) are partial differential equations and difficult to be solved analytically although the analytical solutions are available for some specific cases. Therefore, the first step in solving the equations is to transfer the continuous equations into discrete counterparts. This step is named as numerical discretisation, which techniques have developed various types, such as finite-difference method, finite-volume method, finite-element method, finite analytic method and so on.

2.2.2.3.2.1. Finite-difference method

Finite-difference method is based upon the use of so-called Taylor series to build a library or toolkit of equations those describe the derivatives of a variable as the differences between values of the variable at various points in space or time (Smith, 1985).

For example, consider a variable, which is function of an independent variable, position x and noted as f. If the value of this variable is known at the point of P, then the values of f at two adjacent points with a small distance of l away from P can be determined by applying finite difference method, as

$$f^{\mathrm{P}+l} = f^{\mathrm{P}} + l\frac{\mathrm{d}f}{\mathrm{d}x} + \frac{1}{2!}l^2\frac{\mathrm{d}^2 f}{\mathrm{d}x^2} + \frac{1}{3!}l^3\frac{\mathrm{d}^3 f}{\mathrm{d}x^3} + o(l^4) \tag{2.16}$$

$$f^{\mathrm{P}-l} = f^{\mathrm{P}} - l\frac{\mathrm{d}f}{\mathrm{d}x} + \frac{1}{2!}l^2\frac{\mathrm{d}^2 f}{\mathrm{d}x^2} - \frac{1}{3!}l^3\frac{\mathrm{d}^3 f}{\mathrm{d}x^3} + o(l^4) \tag{2.17}$$

where $o(l^q)$ is the truncated term, indicating the sum of all terms are of order l^q or of higher order. This term is a function of mesh spacing, indicated by the distance of l between two adjacent points. The term of $o(l^q)$ is very small and can be neglected for small l values, especially tends to zero while the mesh is very fine.

Then first and second derivatives of f can be given by the Eqs. (2.16) and (2.17) as:

$$\frac{\mathrm{d}f}{\mathrm{d}x} = \frac{1}{2l}(f^{\mathrm{P}+l} - f^{\mathrm{P}-l}) + o(l^2) \tag{2.18}$$

$$\frac{\mathrm{d}^2 f}{\mathrm{d}x^2} = \frac{1}{l^2}(f^{\mathrm{P}+l} - 2f^{\mathrm{P}} + f^{\mathrm{P}-l}) + o(l^2) \tag{2.19}$$

The order-accuracy of any discrete approximation is determined by the exponent of l in the truncated term. Eqs. (2.18) and (2.19) are second-order accurate since the truncated terms are of order l^2 or higher. Generally increasing the order-accuracy of discrete approximation leads to a rapid reduction in the error, especially with finer mesh. However, this benefit in accuracy unavoidably causes heavier computational load. And high-order accurate approximations are generally less robust than their low-order accurate counterparts because that they may result in what is known as the wiggle phenomenon (Abbott and Basco, 1989).

Eqs. (2.18) and (2.19) are called central difference formulae due to the geometrical relationship of the points used in the calculations. In other words, the derivative at a given point is calculated from the variables at points both ahead it or behind it.

Further first derivatives can also be given by

$$\frac{\mathrm{d}f}{\mathrm{d}x} = \frac{1}{l}(f^{\mathrm{P}+l} - f^{\mathrm{P}}) + o(l) \tag{2.20}$$

$$\frac{\mathrm{d}f}{\mathrm{d}x} = \frac{1}{l}(f^{\mathrm{P}} - f^{\mathrm{P}-l}) + o(l) \tag{2.21}$$

Eq. (2.20) is known as a forward difference formula and Eq. (2.21) is known as a backward difference formula. Both derivatives are calculated by the variables at the point itself and another point ahead it for forward difference formula or another point behind it for backward difference formula. Eqs. (2.20) and (2.21) are first order accurate as the truncated term is of order *l* or higher.

It should be noted that the computational domain may include the second and the third dimension in spatial direction or time direction. And applying Eqs. (2.18) — (2.21), the partial differential equations (i.e. Eqs. (2.11) — (2.15)) can be translated into a set of equations which can be sorted out by the assistance of knowledge of linear algebra.

2.2.2.3.2.2. Finite-element method

Finite-element method is a widely used method of dividing the computational domain into a collection (e.g. *M*) of elements or subdivisions which could typically be quadrangle and/or triangle for two-dimensional problems or tetrahedral and/or hexahedral for three-dimensional problems. The points used to connect the adjacent elements are called nodes (Reddy, 1993). One simple interpolation function is specified over each element. By following the interpolation function, the variable over each element is represented by the values of variable, in some cases, and the values of the derivative of the variable at the nodal points within each element in the form of equation. Then solution *h* to a differential equation can be, for example, approximated in the form, which is most used as follow (Reddy, 1993):

$$h = \sum_{j=1}^{M} h_j \psi_j + \sum_{j=1}^{m} co_j \zeta_j \tag{2.22}$$

where h_j are the values of h at nodal points, ψ_j are the interpolation functions, co_j are the nodeless coefficients, and ζ_j are the associated approximation functions. It should be noted that the interpolation equations ψ_j are independent with each other. Equations

from all elements then form matrix equations and can be solved by imposing the boundary conditions. Solution to variables from all elements can be used to describe the whole computational domain. The interaction between neighboring elements is carried out by their shared nodes. Finite-element method is superior in comparison to finite-difference method in adaptability of complicated geometries but light-duty of computational load.

2.2.2.3.2.3. Finite-volume method

Finite-volume method is a method, similar to finite-difference method and finite-element method, of solving the partial equations on meshed structures. Among all these discretisation methods, finite-volume method is known as computationally cheap, and robust, which means this method behaves reliably in treating many types of differential conversation equations (hyperbolic and elliptic for example) (Eymard *et al*., 2000; LeVeque, 2002). Probably, this method is most widely employed in numerical discretisation, and the CFD package used in current work is based on this method.

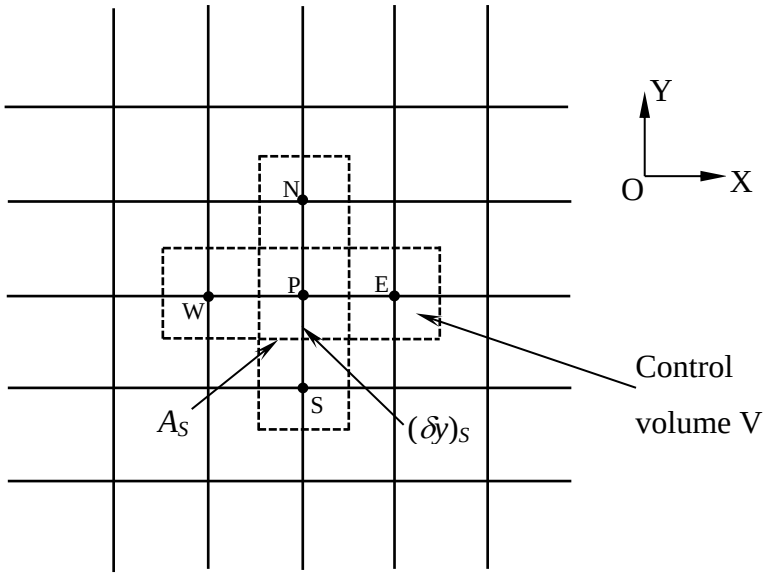

Figure 2.7. The schematic of controlled volume and its neighboring nodes.

By applying the finite-volume method, the partial differential equations are integrated over each control volume, one of which, for example, is indicated by V and represented by its centre of node P. P is surrounded by four neighboring nodes N, W, E, and S, as shown in Figure 2.7.

Integrating transport equation over a control volume in a 2-D system (for example, **X**-**Y**) leads to:

$$\int_V \frac{\partial}{\partial t}(\rho\phi)\mathrm{d}V + \int_V \nabla\cdot(\rho\boldsymbol{U}\phi)\mathrm{d}V - \int_V \nabla\cdot(\Gamma_\phi\nabla\phi)\mathrm{d}V = \int_V S_\phi \mathrm{d}V \tag{2.23}$$

By applying the Gauss Divergence Theorem, the integral form of advection and diffusion terms over volume V can be rewritten in the form of surface integrals over *S*, which indicates the control volume surface, thus,

$$\int_V \frac{\partial}{\partial t}(\rho\phi)\mathrm{d}V + \int_S \rho\boldsymbol{U}\phi\boldsymbol{n}\mathrm{d}S - \int_S \Gamma_\phi\nabla\phi\boldsymbol{n}\mathrm{d}S = \int_V S_\phi \mathrm{d}V \tag{2.24}$$

(i) Discretisation of transient term

For incompressible fluid, the integral form of transient term at time level of *ts* can be approximately given by

$$\int_V \frac{\partial}{\partial t}(\rho\phi)\mathrm{d}V \approx V\rho\frac{\phi^{ts+\frac{1}{2}} - \phi^{ts-\frac{1}{2}}}{\Delta t} \tag{2.25}$$

Where $ts-\frac{1}{2}$ and $ts+\frac{1}{2}$ respectively indicate the start and end time of the timestep

ts, Δt is the size of the timestep. With First Order Backward Euler Scheme, $\phi^{ts+\frac{1}{2}}$ and $\phi^{ts-\frac{1}{2}}$ are approximated by ϕ^{ts} and ϕ^{ts-1} respectively. With Second Order Backward Euler Scheme, $\phi^{ts+\frac{1}{2}}$ and $\phi^{ts-\frac{1}{2}}$ are obtained by values at three time level of *ts* - 2, *ts* - 1 and *ts*, thus,

$$\phi^{ts-\frac{1}{2}} \approx \phi^{ts-1} + \frac{1}{2}\left(\phi^{ts-1} - \phi^{ts-2}\right) \tag{2.26}$$

$$\phi^{ts+\frac{1}{2}} \approx \phi^{ts} + \frac{1}{2}\left(\phi^{ts} - \phi^{ts-1}\right) \tag{2.27}$$

Second Order Backward Euler Scheme is superior in accuracy, but more computationally expensive in comparison to First Order Backward Euler Scheme.

(ii) Discretisation of convection term

The integral form of convection term are usually approximated as

$$\int_S \rho \mathbf{U}\phi \mathbf{n} \mathrm{d}S \approx \rho u_{\mathrm{E}} A_{\mathrm{E}} \phi_{\mathrm{E}} - \rho u_{\mathrm{W}} A_{\mathrm{W}} \phi_{\mathrm{W}} + \rho u_{\mathrm{N}} A_{\mathrm{N}} \phi_{\mathrm{N}} - \rho u_{\mathrm{S}} A_{\mathrm{S}} \phi_{\mathrm{S}} \tag{2.28}$$

where *A* indicate the interface area between P and its neighboring points, represented by E, W, N and S.

As can be seen, the integration of convection term is now expressed by the values at adjacent nodes, E, W, N and S. The rule, following which the face value is represented by the values at adjacent nodes is known as ‘advection scheme’ (CFX manual, ANSYS,

Inc). The face value of variable ϕ at an integration point, then can be given by the values at the upwind node, ϕ_{up} and the variable gradient, $\nabla\phi$, thus,

$$\phi_{ip} = \phi_{up} + \beta\nabla\phi\Delta\mathbf{r} \tag{2.29}$$

where β is a blend factor and $\Delta\mathbf{r}$ is the vector from the upwind node to the integration point. According to the choices of β and $\nabla\phi$, the advection scheme can be classified into three types, as,

First order Upwind Differencing Scheme

This scheme can be achieved by specifying β equals to 0 and thus, $\phi_{ip} = \phi_{up}$. This scheme is very robust because of its superiority in avoiding the non-physical values. But this scheme is only first-order accurate due to the numerical diffusion.

Numerical Advection Correction Scheme (Specify Blend)

This scheme can be obtained by specifying β a value between 0 and 1. And, $\nabla\phi$ is given by averaging the gradients at adjacent nodes. This scheme is of first-order accurate while β = 1, but of second-order accurate while β = 1, which means that the scheme of Specify Blend contributes a higher accuracy than the Upwind Differencing Scheme. However, with β = 1, some non-physical values may be produced in case of the large gradient of variables.

High Resolution Scheme

The blend factor β is computed locally in this scheme. In order to satisfy both accuracy and boundedness requirements, the value of β should be as close to 1 as possible without resulting in non-physical values, and meanwhile the gradient ∇ is set

equal to the control volume gradient at the upwind node. The recipe for β adopted in CFX is based on the boundedness principles used by Barth and Jesperson (1989).

(iii) Discretisation of diffusion term

The integral form of diffusion terms are usually approximated as

$$\int_S \Gamma_\phi \nabla\phi \boldsymbol{n} \mathrm{d}S = \int_S \Gamma_\phi \left(\frac{\partial\phi}{\partial x}\boldsymbol{i} + \frac{\partial\phi}{\partial y}\boldsymbol{j}\right)\boldsymbol{n}\mathrm{d}S$$

$$\approx \frac{\Gamma_\phi A_{\mathrm{E}}}{(\delta x)_{\mathrm{E}}}\left(\phi_{\mathrm{E}} - \phi_{\mathrm{P}}\right) - \frac{\Gamma_\phi A_{\mathrm{W}}}{(\delta x)_{\mathrm{W}}}\left(\phi_{\mathrm{P}} - \phi_{\mathrm{W}}\right) + \frac{\Gamma_\phi A_{\mathrm{N}}}{(\delta y)_{\mathrm{N}}}\left(\phi_{\mathrm{N}} - \phi_{\mathrm{P}}\right) - \frac{\Gamma_\phi A_{\mathrm{S}}}{(\delta y)_{\mathrm{S}}}\left(\phi_{\mathrm{P}} - \phi_{\mathrm{S}}\right) \tag{2.30}$$

where δx or δy indicates distance between P and its neighboring points, represented by E, W, N and S.

(iv) Discretisation of source term

The integral form of source terms are approximated as (Patankar, 1980)

$$\int_V S_\phi \mathrm{d}V \approx \overline{S}_\phi V = \left(S_C + S_{\mathrm{P}}\phi_{\mathrm{P}}\right)V \tag{2.31}$$

where $\overline{S}_\phi$ is the averaged value of S_ϕ and formally considered to be consisting of two parts: constant part of S_c and linear part of $S_{\mathrm{P}}\phi_{\mathrm{P}}$.

By discretising the integral terms over the whole meshed domain, the governing equations are translated to a set of discretized equations which can be solved as matrix equations (Versteeg and Malalasekera, 2007).

2.2.2.3.3. Iteration for solutions

Based on the discretized equation, the numerical solutions can be obtained by iterating process, which is in fact, a repetition procedure of updating the numerical solutions until the normalized residual error (or the residual root mean square error for the whole calculation domain) reaches the convergent target. During this process, the values of variables should always start from initial solutions and be satisfying the governing equations. Normally, final solutions are dependent on the initial solutions in transient simulations (i.e. time-dependent simulations). While in steady state simulations (i.e. time-independent simulations), the final solutions cannot be affected by the initial solutions, although a good guess on the initial solutions contributes a quick convergence to the final solutions.

In order to obtain the convergent solution, the iterative procedure must be regulated in some way to prevent the residual errors becoming larger from iteration to iteration. To control the iteration process, there are two commonly used methods, named as under-relaxation or the use of a time-dependent scheme (Shaw, 1992). In steady-state simulations, under-relaxation parameter scheme can be used to prevent divergence. The method can help the solution from the following iteration to be not too different form the solution at the beginning of the current iteration by scaling solution from current iteration. The calculation process can be given by

$$\Phi_{new} = \varphi\Phi_{cal} + (1 - \varphi)\Phi_{old} \tag{2.32}$$

Here, φ is under-relaxation and should be between zero and unity. Φ_{old} is the value of a variable at the start of the current iteration and Φ_{cal} is the value of the same variable calculated from the current iteration. Then Φ_{new} values between Φ_{old} and Φ_{cal}, and becomes the new Φ_{old} for the next iteration. If $\varphi = 0$, the solution will be kept unchanged, while no under-relaxation is applied if $\varphi = 1$. Another approach used to control the iteration process is time-dependent scheme. Even in a steady-state

simulation, this mean can also be used by mimicking the changes of flow with time, like a fictitious transient-state simulation. For transient flows, the most import method of controlling the iteration process is the utilization of time step, which is calculated by dividing a period of time into a modest number of parts, also can be regarded as discretization on the scale of time. Such period of time should be specified to reasonably represent the time scale of the phenomenon investigated in the simulation. The solution should satisfy the governing equations at each time step and then be used for next time step. A sufficient small time step is always helpful in contributing accurate solutions and quick convergence. However, small size of time step must result in a large number of time steps, therefore a heavy computational load. Similar to choice of mesh size, the final solution also should not be affected by the size of time step.

2.2.2.4. Post-processing

Data can be plotted and visualised after the solution obtained by solving the discretised equations. This work can be done in various forms, including contour, scatter or line plot, volume representation, streamline indication, path line tracking with the help of some advanced scientific statistical and graphing software, such as SigmaPlot and Origin, and data processing with further calculation by the assistance of programming packages, such as MATLAB, and excel.

2.2.3. Computer-based CFD analysis softwares

After several decades of progress, large amount of public codes and commercial software packages has been developed. The popular software packages used in CFD involves Gambit, ICEM CFD, DesignModeler, Hypermesh and PointWise for geometries and mesh generation; CFX-Pre and CFX-Solver, FLUENT, and OpenFOAM for simulation setup and numerical solving of equations; CFD-Post, Tecplot, and Ensight for representing of numerical results.

ICEM CFD 14.5, CFX 14.5 consisting of CFX-Pre and CFX-Solver, and CFD-Post are employed in current work. Both packages are developed by ANSYS Inc.

NOTATION

A	Surface area
C_p	Constant-pressure specific heat, J kg^{-1} K^{-1}
$o(l^q)$	Truncated term
k	Fluid consistency index, Pa s^n
l	Distance between two adjacent points in finite-difference method, m
m	The growth exponent in exponential model, s
n	Flow behaviour index, -
p	Pressure, Pa
S	Surface of control volume
S_H	Specific enthalpy, J kg^{-1}
S_h	Volumetric rate of heat generation, J m^{-3}
S_ϕ	Source term
t	Time, s
Δt	Size of timestep, s
$\boldsymbol{U}$	Velocity vector, m s^{-1}
u	Velocity component along X
V	Volume of control volume
v	Velocity component along Y
w	Velocity component along Z
x	Cartesian coordinate along X
y	Cartesian coordinate along Y
z	Cartesian coordinate along Z

Greek symbols

β Blend factor

Γ_ϕ Diffusion coefficient for ϕ

η Fluid viscosity, Pa s

ρ Fluid density, kg m^{-3}

ϕ Dependent variable

$\dot{\gamma}$ Shear rate, s^{-1}

τ Shear stress, Pa

τ_0 Yield stress, Pa

λ Thermal conductivity, W m^{-1} K^{-1}

μ Viscosity for Newtonian fluid, Pa s

μ_1 Newtonian viscosity in bi-viscosity model, Pa s

μ_B Plastic viscosity, Pa s

η Apparent viscosity, Pa s

φ Under-relaxation factor

δx Distance between adjacent cell nodes along X in finite-volume method

δy Distance between adjacent cell nodes along Y in finite-volume method

REFERENCES

Abbott, M. B., Basco, D. R., 1989. Computational fluid dynamics-An introduction for engineers. NASA STI/Recon Technical Report A, 90, 51377.

Barth, T. J., Jesperson, D. C., 1989. The design and application of upwind schemes on unstructured meshes, AIAA Paper 89-0366.

Batchelor, G. K., 2000. *An introduction to fluid dynamics*. Cambridge University Press, Cambridge.

Bingham, E.C., 1922. *Fluidity and Plasticity*. McGraw-Hill, New York.

Blackery, J., Mitsoulis, E., 1997. Creeping motion of a sphere in tubes filled with a Bingham plastic material. Journal of Non-Newtonian Fluid Mechanics, 70(1), 59-77.

Castillo, J. E., 1991. *Mathematical aspects of numerical grid generation* (Vol. 8). Cambridge University Press, Cambridge.

CFX user manual, release 15.0, 2013. ANSYS Inc.

Eymard, R., Gallouët, T., Herbin, R. 2000. Finite volume methods. Handbook of numerical analysis, 7, 713-1018.

Gavrus, A., Ragneau, E., Caestecker, P., 2001. Rheological behaviour formulation of solid metallic materials for dynamic forming processes simulation. In 4th International ESAFORM Conference on Material Forming (pp. 403-406).

George, P. L., Hecht, F., Saltel, E., 1991. Automatic mesh generator with specified boundary. Computer Methods in Applied Mechanics and Engineering, 92(3), 269-288.

Herschel, W. H., Bulkley, R., 1926. Konsistenzmessungen von gummi-benzollösungen. Kolloid-Zeitschrift, 39(4), 291-300.

Lamb, H., 1895. *Hydrodynamics*. Cambridge University Press, Cambridge.

LeVeque, R. J., 2002. Finite volume methods for hyperbolic problems (Vol. 31).

Cambridge University Press, Cambridge.

Mavriplis, D. J., 1996. Mesh generation and adaptivity for complex geometries and flows. Handbook of Computational Fluid Mechanics, 417-459.

Mitsoulis, E., 2007. Flows of viscoplastic materials: models and computations. Rheology reviews, 135-178.

Mitsoulis, E., Galazoulas, S., 2009. Simulation of viscoplastic flow past cylinders in tubes. Journal of Non-Newtonian Fluid Mechanics, 158(1), 132-141.

Oberkampf, W. L., Trucano, T. G., 2000. Validation methodology in computational fluid dynamics. AIAA paper, 2549, 19-22.

Oberkampf, W. L., Trucano, T. G., 2002. Verification and validation in computational fluid dynamics. Progress in Aerospace Sciences, 38(3), 209-272.

Ostwald, W., 1925. Ueber die geschwindigkeitsfunktion der viskosität disperser systeme. I. Colloid & Polymer Science, 36(2), 99-117.

Papanastasiou, T. C., 1987. Flows of materials with yield. Journal of Rheology, 31(5), 385-404.

Patankar, S. V., 1980. *Numerical heat transfer and fluid flow*. McGraw-Hill, New York.

Reddy, J. N., 1993. *An introduction to the finite element method*. McGraw-Hill, New York.

Sayma, A., 2009. *Computational fluid dynamics*. Abdulnaser Sayma & Ventus Publishing ApS, London.

Shangraw, R., Grim, W., Mattocks, A. M., 1961. An equation for non-Newtonian flow. Transactions of The Society of Rheology, 5(1), 247-260.

Shaw, C. T., 1992. *Using computational fluid dynamics.* Hemel Hempstead, England: Prentice Hall.

Smith, G. D., 1985. *Numerical solution of partial differential equations: finite difference methods.* Oxford University Press, Oxford.

Stern, F., Wilson, R. V., Coleman, H. W., Paterson, E. G., 1999. Verification and validation of CFD simulation. Iowa Institute of Hydraulic Research, University of Iowa. Iowa, US.

Tanner, R. I., Milthorpe, J. F., 1983. Numerical simulation of the flow of fluids with yield stress. Numer Methods Lami Turb Flow, Seattle, 680-690.

Versteeg, H. K., Malalasekera, W., 2007. *An introduction to computational fluid dynamics: the finite volume method.* Pearson Education, Boston.

Zhu, H., Martys, N. S., Ferraris, C., De Kee, D., 2010. A numerical study of the flow of Bingham-like fluids in two-dimensional vane and cylinder rheometers using a smoothed particle hydrodynamics (SPH) based method. Journal of Non-Newtonian Fluid Mechanics, 165(7), 362-375.

CHAPTER 3.

COMPARISON OF DIFFERENT MODES OF OSCILLATIONS FOR AFFECTING FLOW AND HEAT TRANSFER IN PIPE

Summary

The superimposition of a mechanical oscillation under a constant pressure gradient can lead to a large change in the flow of viscous non-Newtonian fluids. As a consequence the fluids of a shear-thinning rheology move faster whilst shear-thickening fluids are retarded. A validated Computational Fluid Dynamics (CFD) model created by ANSYS-CFX was employed to compare the efficacy of three types of oscillation namely, longitudinal, transverse and rotational. It was found that longitudinal oscillation is, however, by far the most effective, with transverse and rotational oscillations show a significant enhancement effect upon the flow under large vibration intensity. In comparison to longitudinal and rotational oscillations, transverse oscillations uniquely generate a chaotic fluid motion which causes considerable radial mixing in viscous flows, and always responds much more quickly to the change of fluid consistency index, flow behaviour index and yield stress than either longitudinal or rotational vibration. Additionally, in Newtonian non-isothermal flow, CFD results show that transverse oscillations generate a large enhancement in uniformity of radial temperature profile. However, neither longitudinal nor rotational oscillation is able to result in obvious enhancement in radial heat transfer.

3.1. INTRODUCTION

Complex fluids of non-Newtonian rheology are widely encountered in the process industries. Examples include most multi-phase mixtures, (e.g. emulsions, foams, suspensions, dispersions), high-molecular weight fluids (e.g. polymers, proteins, gums), foods, pharmaceuticals, consumer and household products, agricultural chemicals, and slurry fuels. The flow of such fluids through pipes and processing equipment usually requires much pumping energy. The usually high viscosity and complex rheology of these fluids can give rise to challenging problems, for example, in operations of moulding and coating of chocolate bars and shells in the confectionery industry (Gonçalves, 2010). The entrapment of unwanted air bubbles is also a huge problem in many industrial applications including consumer products, confectionery, metal and polymer melts, and concrete. These and other problems have motivated the search for various ways of facilitating the flow and processing of these fluids over the years.

Mechanical vibration has been shown to enhance the fluidity of viscous non-Newtonian fluids (Mena *et al*., 1979; Isayev *et al*., 1990; Deshpande and Barigou, 2001; Piau and Piau, 2002; Wu *et al*, 2003; Shin *et al*., 2003; Eesa and Barigou, 2008). Mena *et al*. (1979) showed that the superimposition of longitudinal oscillation on a viscoelastic flow in a pipe gives rise to an increase in the time-averaged flowrate. By means of flow visualisation, the effect of oscillation on the velocity profile was qualitatively analysed. It was concluded that the dominating factor in the oscillating flow of viscoelastic liquids in tubes is the shear-dependent viscosity.

Deshpande and Barigou (2001) investigated, experimentally and numerically, the effects of longitudinal oscillation on the time-averaged flowrate of Newtonian and inelastic time-independent non-Newtonian fluids of the power law, Bingham plastic and Herschel-Bulkley types. Their numerical results, obtained using a Computational Fluid Dynamics (CFD) model validated by experiment, showed that: (i) vibration does not alter the flowrate of Newtonian fluids; (ii) shear-thinning (pseudoplastic) fluids exhibit flow enhancement under vibration; (iii) shear-thickening (dilatant) fluids exhibit flow

retardation; (iv) vibration can reduce plug region in flow of yield stress fluids, including Bingham plastic and Herschel-Bulkley types; (v) in power law and Herschel-Bulkley type fluids, flow enhancement is most sensitive to the flow behavior index comparing with the other rheological properties. The observed effects of vibration were attributed to the shear-dependent viscosity of the fluid, which, in turn, affects the time-averaged flowrate. The study showed that substantial enhancements in flow were potentially possible, depending on the vibration frequency and amplitude used and the fluid rheological properties.

Shin *et al*. (2003) investigated the effects of transverse acoustic vibration on the flow resistance of both Newtonian fluids and human blood in a capillary tube. While the superimposed vibration did not alter the flowrate of Newtonian fluids, a reduction in the flow resistance of blood was observed which was attributed to the breakdown of aggregated red blood cells. The extent of reduction was strongly dependent on both the vibration frequency and amplitude, but more detailed numerical and experimental work was deemed necessary to explain the effects.

In recent work, Eesa and Barigou (2008) used a validated CFD model to study the effects of rotational pipe oscillations on the flow of Newtonian, power law, Bingham plastic and Herschel-Bulkley fluids. The results showed that shear-thinning fluids as well as viscoplastic fluids exhibited an increase in flowrate, while the flowrate of shear-thickening fluids was reduced below the steady-state value. The degree of flow enhancement was dependent on the vibration parameters and the fluid rheological properties. Oscillations of ultrasonic frequencies generated orders of magnitude enhancement in highly viscous flows.

Mechanical vibration can also bring benefits to the thermal processing of viscous Newtonian and non-Newtonian fluids. For example, in continuous food sterilisation, the velocity profile in the heating or holding tube translates into a non-uniform temperature distribution, thus, resulting in a wide variation of product sterility and

nutritional quality across the pipe. The challenge is to be able to sterilise the fastest parts in the core region of the pipe without over-processing the slowest parts near the wall. When the fluids involved are relatively viscous, processing them under turbulent conditions can be impractical and/or uneconomical. On the other hand, the use of static in-line mixers to promote radial mixing may be prohibited in hygienic processes because they are difficult to keep clean.

A number of studies have demonstrated the effects of mechanical vibration on the heat flux and Nusselt number in pipe flows (Klaczak, 1997; Gündoğdu and Çarpinlioğlu, 1999; Lee and Chang, 2003). However, such studies did not investigate the effects on the radial temperature distribution and the development of the thermal boundary layer along the pipe. In non-isothermal pipe flows, recent work has shown that transverse oscillations can lead to a large enhancement in the wall heat transfer coefficient as well as a nearly-uniform radial temperature distribution and a substantial reduction in the thermal entrance length compared to steady-state flow (Eesa and Barigou, 2010).

In this chapter, a validated CFD model is used to (i) compare the efficacy of three modes of oscillation, i.e. longitudinal, transverse and rotational in enhancing the time-averaged flowrate in isothermal fluids with different vibration parameters and rheological properties, (ii) indicate that transverse vibration has the capability to accelerate radial heat transfer whilst longitudinal and rotational vibration cannot lead to an obvious enhancement in radial temperature profile.

3.2. THEORY

3.2.1. Fluid rheologies, volume flowrate and axial velocity profiles

The fluids considered are inelastic, time-independent, viscous Newtonian and non-Newtonian of power law and Bingham plastic types. These three rheologies have been described separately in Chapter 2 by the general expressions Eqs. (2.1) — (2.3).

The apparent viscosities are given by Eqs. (2.4) — (2.6) separately for shear-thinning, shear-thickening and Bingham plastic fluids.

It is assumed that the flow is driven by a constant pressure gradient $\Delta p/L$, where Δp is the pressure drop over the pipe, and L is the length of pipe. Thus, the steady volumetric flowrate, Q, of power law and Bingham plastic fluids in laminar pipe flow, can be predicted from the following exact relationship (Steffe, 1996):

Newtonian: $$Q = \frac{\pi \Delta p R^4}{8 \mu L} \tag{3.1}$$

power law: $$Q = \pi \left(\frac{\Delta p}{2kL} \right)^{1/n} \left(\frac{n}{3n+1} \right) R^{\frac{3n+1}{n}} \tag{3.2}$$

Bingham plastic: $$Q = \frac{\pi \Delta p R^4}{8 \mu_B L} \left[1 - \frac{8}{3} \frac{\tau_0 L}{R \Delta p} + \frac{1}{3} \left(\frac{2 \tau_0 L}{R \Delta p} \right)^4 \right] \tag{3.3}$$

where R is the pipe radius. The fully developed axial laminar velocity profile is given by the expressions (Chhabra and Richardson, 1999):

Newtonian:

$$w = \frac{\pi \Delta p R^4}{16 \mu L} \left(R^2 - r^2 \right) \tag{3.4}$$

power law:

$$w = \frac{\pi \Delta p R^4}{8kL}\left(\frac{n}{n+1}\right)\left[(R)^{\frac{n+1}{n}} - (r)^{\frac{n+1}{n}}\right] \tag{3.5}$$

Bingham plastic:

$$\begin{cases} w = \dfrac{L}{\mu_B \Delta p}\left[\left(\dfrac{R\Delta p}{2L} - \tau_0\right)^2 - \left(\dfrac{r\Delta p}{2L} - \tau_0\right)^2\right], & \text{for} \quad \dfrac{2L\tau_0}{\Delta p} \le r \le R \\ w = \dfrac{L}{\mu_B \Delta p}\left(\dfrac{R\Delta p}{2L} - \tau_0\right)^2, & \text{for} \quad 0 \le r < \dfrac{2L\tau_0}{\Delta p} \end{cases} \tag{3.6}$$

where r is radial position, and w is the axial velocity of flow. When n = 1, Eqs. (3.2) and (3.5) reduce to their forms for a Newtonian fluid of constant shear-independent viscosity (i.e. Eqs. (3.1) and (3.5)). When τ_0 = 0 Pa, Eqs. (3.3) and (3.6) reduce to their forms for a Newtonian fluid as well ($\mu_B = \mu$).

3.2.2. Influence of temperature on viscosity

For non-isothermal flows, the temperature dependence of the fluid physical properties needs to be taken into account. Here, account was taken of the temperature dependence of the viscosity only. Fluids considered in the study of heat transfer in this chapter is Newtonian type, reported by Steffe (1996), known as Arrhenius model:

$$\mu = k_0 \exp\left(\frac{E_\alpha}{R_g T}\right) \tag{3.7}$$

where T is temperature, k_0 is a pre-exponential factor, E_a is the activation energy for viscosity, and R_g is the ideal gas constant.

3.2.3. Forced vibration

Three modes of vibration (longitudinal, transverse and rotational) are studied and for each mode the sinusoidal oscillatory movement superimposed at the pipe wall are described mathematically as follows:

3.2.3.1. Longitudinal vibration

In this case, the sinusoidal displacement of the pipe wall is applied in the direction of flow which coincides with the Cartesian Z axis, as shown in Figure 3.1(*a*), and is given by:

$$z = A\sin(\omega t) \tag{3.8}$$

where A is the vibration amplitude and $\omega = 2\pi f$, where f is the vibration frequency. The vibrational velocity of the pipe wall in the flow direction, u_z, can then be obtained by differentiating Eq. (3.8) with respect to time, thus

$$u_z = \frac{\mathrm{d}z}{\mathrm{d}t} = A\omega\cos(\omega t) \tag{3.9}$$

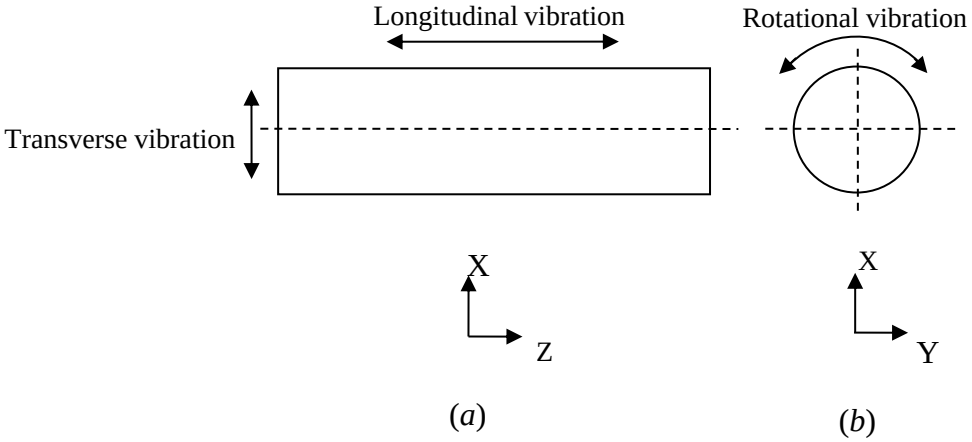

Figure 3.1. Geometry of vibrated pipe: (*a*) longitudinal view; (*b*) pipe cross-section.

3.2.3.2. Transverse vibration

For vibration in a direction perpendicular to the direction of flow, the linear sinusoidal displacement of the pipe wall along the X axis (see Figure 3.1(*a*)) is given by:

$$x = A\sin(\omega t) \tag{3.10}$$

and the linear velocity u_x of the wall can then be derived, thus:

$$u_x = \frac{\mathrm{d}x}{\mathrm{d}t} = A\omega\cos(\omega t) \tag{3.11}$$

3.2.3.3. Rotational vibration

For a pipe oscillating about its axis (see Figure 3.1(*b*)), the angle of rotation θ is given by the function:

$$az = R\theta = R\Theta\sin(\omega t) \tag{3.12}$$

where az is the displacement in the azimuthal direction at $r = R$, θ is the angular displacement and Θ is the angular amplitude of the rotational vibration. The angular velocity u_θ is therefore:

$$u_\theta = \frac{\mathrm{d}\theta}{\mathrm{d}t} = \Theta\omega\cos(\omega t) \tag{3.13}$$

3.2.4. CFD models

3.2.4.1. Model of pipe flow without heat transfer

The flow considered here is laminar, incompressible, isothermal and fully developed. The geometry consisted of a horizontal pipe 4 mm in diameter and 10 mm in length. The pipe Reynolds number Re is expressed as:

$$\mathrm{Re} = \frac{\rho \overline{w} D}{\eta} \tag{3.14}$$

where ρ is the fluid density, D is the diameter of the pipe, and η is the effective viscosity for a non-Newtonian fluid, which is the viscosity of a hypothetical Newtonian fluid that would give the same relationship between flowrate and pressure drop. The flow was laminar for all cases of steady flow as Re < 10. For vibrational flow, an additional Reynolds number, the vibration Reynolds number, can be calculated from:

$$\mathrm{Re}_v = \frac{\rho A \omega D}{\eta} \qquad \text{Longitudinal and transverse vibration} \tag{3.15}$$

$$\mathrm{Re}_v = \frac{\rho \Theta \omega D}{\eta} \qquad \text{Rotational vibration} \tag{3.16}$$

Re_v was always less than 100, satisfying condition of laminar flow.

In the CFD model adopted here, a pressure boundary condition was used at the inlet. Using such a pressure boundary condition allows the CFD code to calculate the fully developed velocity profile at the tube inlet based on the static pressure value prescribed there, thus, allowing the use of a small L and reducing the computational cost.

The governing transport equations considered in this model are developed from Eqs. (2.13) and (2.14) in Chapter 2, rewritten as

Continuity: $$\nabla(\boldsymbol{U}) = 0 \tag{3.17}$$

Momentum: $$\rho \frac{\mathrm{D}\boldsymbol{U}}{\mathrm{D}t} = -\nabla p + \nabla \cdot \eta\dot{\gamma} \tag{3.18}$$

where $\frac{\mathrm{D}\boldsymbol{U}}{\mathrm{D}t}$ is the fully differential form of $\boldsymbol{U}$ with respect to t, thus,

$$\frac{\mathrm{D}\boldsymbol{U}}{\mathrm{D}t} = \frac{\partial \boldsymbol{U}}{\partial t} + u\frac{\partial \boldsymbol{U}}{\partial x} + v\frac{\partial \boldsymbol{U}}{\partial y} + w\frac{\partial \boldsymbol{U}}{\partial z} \tag{3.19}$$

3.2.4.2. Model of pipe flow with heat transfer

The flow considered in this model is laminar, incompressible and fully developed. The pipe geometry was 30 mm in diameter and 400 mm in length. This pipe length was sufficient to obtain a fully developed velocity profile and to demonstrate the effects of vibration on radial temperature uniformity. For all of the steady-state flow cases investigated, the Reynolds number at the pipe inlet was always less than 500. The flow also remained laminar at the outlet with Re < 900. In all the unsteady-state cases studied, Re_v was always less than 1500, so flow remained laminar throughout as well.

In addition to the equations of continuity and momentum (Eqs. (3.17) and (3.18)), the equation of energy (Eq. (2.15)) has to be taken into account (Bird *et al*., 1987) and rewritten as:

$$\frac{\mathrm{D}}{\mathrm{D}t}(C_p \rho T) - \nabla \cdot (\lambda \nabla T) = 0 \tag{3.20}$$

The term on the left hand side represents the rate of increase of enthalpy per unit volume, while the terms on the right hand side is the rate of addition of energy by heat conduction per unit volume.

3.3. CFD SIMULATIONS

3.3.1. Simulations of pipe flow without heat transfer

The 3-D geometry consisted of a straight pipe with three surfaces: inlet, outlet, and wall. As a pressure boundary condition was used at the inlet, the flow was fully developed throughout the whole tube, thus requiring only a small tube length for the CFD computations.

The geometry was meshed with hexahedral cells. The mesh size was optimised by conducting a mesh-independence study wherein an initially coarse mesh was refined until results were no longer sensitive to the mesh size. Newtonian fluid with constant viscosity of 1 Pa s was used in mesh-independent study.

Ratio of CFD-predicted non-vibrated and vibrated flowrates to the theory (i.e. Eq. (3.1)) with different node number was summarised in Tables 3.1 and 3.2. The extent of approaching to value of 1 reveals the reliability of model.

Table 3.1. Mesh-independent study in axial direction: Newtonian fluid: μ = 1 Pa s

Node number	Ratio of flowrate			
	40	60	80	100
Steady	0.99	0.99	0.99	0.99
Longitudinal	0.95	0.98	0.99	0.99
Rotational	1.00	1.00	1.00	1.00
Transverse	0.98	0.99	0.99	0.99

Table 3.2. Mesh-independent study in radial direction: Newtonian fluid: μ = 1 Pa s.

Node number	Ratio of flowrate			
	12	16	20	24
Steady	0.99	0.99	0.99	0.99
Longitudinal	0.97	0.97	0.97	0.99
Rotational	1.00	1.00	1.00	1.00
Transverse	0.98	0.98	0.98	0.99

The mesh size parameters were set to give 100 cells across the pipe length and 24 cells across the pipe radius with a relatively fine mesh near the wall in order to accurately capture the flow variables enhance where large velocity gradients exist, as that the CFD-results is not affected by the mesh refinement beyond this node number.

The range of parameter values used in the study of pipe flow without heat transfer is summarised in Table 3.3.

Table 3.3. Range of parameters used in simulations of pipe flow without heat transfer.

D (mm)	L (mm)	f (Hz)	A (mm)	k (Pa s^n)	n (-)	τ_0 (Pa)	Δp (Pa)	ρ (kg m^{-3})
4	10	0 - 200	2	1 - 12	0.6 - 1.4	1 - 9	200	1000

Simulations were conducted in two steps: (i) steady-state flow and (ii) unsteady vibrational flow. In the steady-state flow simulations, constant static gauge pressure

(200 Pa) was set at the tube inlet, while the outlet of the tube was specified with a zero gauge pressure boundary condition. A no-slip condition was assumed at the tube wall. The velocity field and the total volumetric flowrate through the tube were, hence, obtained.

The ratio of the time-averaged volumetric flowrate under vibration, Q_v was used to calculate the flow enhancement ratio E defined as:

$$E = \frac{Q_v}{Q} \tag{3.21}$$

Unsteady simulations were executed to investigate the vibrational flow. The inlet and outlet boundary conditions were the same as those used in the steady-state simulations. However, in addition to the no-slip boundary condition at the wall, a wall velocity was imposed using the appropriate expression amongst Eqs. (3.09), (3.11), and (3.13) corresponding to the mode of vibration being studied. The simulation was carried out over a number of vibration periods until time-averaged flowrate over one whole vibration period no long changes with additional vibration periods. A considerable amount of computational experimentation was required to obtain the optimal number of time steps for one whole vibration cycle. Also, the specification of the maximum iterations for one time step had to be sufficient for convergent solution. While a small size of time step contributed a better accuracy and a quick convergence at each time step, however, it prolongs the simulation considerably. The optimum number of time steps per cycle which gave an acceptable level of accuracy whilst keeping simulation time reasonable was 12. Convergence was assumed when the root mean square (RMS) residuals of all the equations reached 10^{-4} at each time step, and achieved with 10 — 12 iterations. Such a level of convergence is good, given the complex unsteady nature of the flow.

In steady-state simulations, second order accurate advection scheme was used (i.e. with a

constant blend factor $\beta = 1$), while the vibrational flow simulations were run under the 'High Resolution' Advection Scheme to avoid boundedness problems. The temporal terms in the governing transport Eq. (3.17) were discretised using the 'Second Order Backward Euler Scheme'.

3.3.2. Simulations of pipe flow with heat transfer

The 3-D pipe geometry was meshed into approximately 4000 hexahedral cells per centimetre of pipe length and 24 cells along the pipe radius. Relatively finer meshes were created near the wall: the first layer which is closest to the wall had a thickness of 0.1 mm expanding by a factor of 1.2 in successive layers.

A Newtonian fluid with temperature-dependent viscosity, as described in Eq. (3.7) was used in the simulation. Table 3.4 presents the parameter values used in the simulations. All other physical properties were assumed to be independent of temperature.

In both steady and unsteady flow simulations, the mean velocity was specified at the inlet at 0.04 m s^{-1}. The fluid entering the pipe was at a constant and uniform temperature T_{in} = 20 ℃. At the outlet, a zero gauge pressure was specified. A no-slip condition and a constant and uniform temperature T_w = 140 ℃ were assigned at the pipe wall. In the unsteady flow simulations, the wall was subjected to a vibrational velocity given by the relevant expression from Eqs. (3.09), (3.11) and (3.13), as appropriate.

The total simulation time was chosen to cover the full residence time of the fluid in the pipe. Numerical experimentation resulted in an optimised number of time steps per vibration cycle equal to 12. The convergent target was set at an RMS residual of 10^{-4} for all of the equations solved. Most of the equations, however, generally reached RMS residual values well below the specified target. In steady flow simulations, the RMS residuals reached 10^{-4} for all of the equations in about 100 iterations. Governing equations of (3.17), (3.18) and (3.20) were discretised by 'High Resolution' Advection

Scheme for advection terms and by ‘Second Order Backward Euler Scheme’ for transient terms.

Table 3.4. Range of parameters used in simulations of pipe flow with heat transfer.

D (mm)	f (Hz)	A (mm)	L (mm)	k_0 (Pa s^n)	E_a (kJ g^{-1} mol^{-1})	n (-)	$\overline{w}$ (m s^{-1})	ρ (kg m^{-3})	C_p (J kg^{-1} K^{-1})	λ (W m^{-1} K^{-1})
30	50	2	400	5×10^{-7}	35.0	1.0	0.04	998	4180	0.668

3.4. VALIDATION OF CFD MODEL

3.4.1. Validation of model of pipe flow without heat transfer

The CFD model used was validated in two steps: (i) steady-state flow, and (ii) unsteady vibrational flow. CFD simulations of the steady-state flow were validated by comparing the CFD-predicted flowrate and velocity profile with theoretical solutions. The comparison showed excellent agreement, usually within ±1% (Eesa and Barigou, 2008). On the other hand, vibrational flow simulations were successfully validated to within approximately ±10% using the experimental results of Deshpande and Barigou (2001) for the isothermal flow of a shear-thinning fluid in a longitudinally vibrated tube.

3.4.2. Validation of model of pipe flow with heat transfer

The CFD model of steady non-isothermal flow in a pipe with an isothermal wall was validated by comparing the CFD predictions of temperature with theoretical (temperature-independent Newtonian fluid) and experimental data (temperature-dependent Newtonian fluid and power law fluid) gleaned from the literature. The full validation will be represented in Chapter 4. The mean deviation of the CFD predictions was within approximately ±2%, showing an excellent degree of accuracy (Eesa and Barigou, 2010). Although there is no experimental data available that can be used directly to validate the simulations of the non-isothermal flow when subjected to vibration, the excellent agreement achieved between CFD and theory or experimental results in all the above stages of the validation process shows that the present CFD model is sufficiently robust and reliable.

3.5. RESULTS AND DISCUSSION

3.5.1. Effect of vibration on the pipe flow without heat transfer

3.5.1.1. The efficacy of vibrations with different values of vibration amplitude

The first group of simulations were taken with non-Newtonian shear-thinning power law fluid: k = 1 Pa $s^{0.6}$ and n = 0.6. CFD results showed that flow enhancement is very sensitive to the amplitude of vibration.

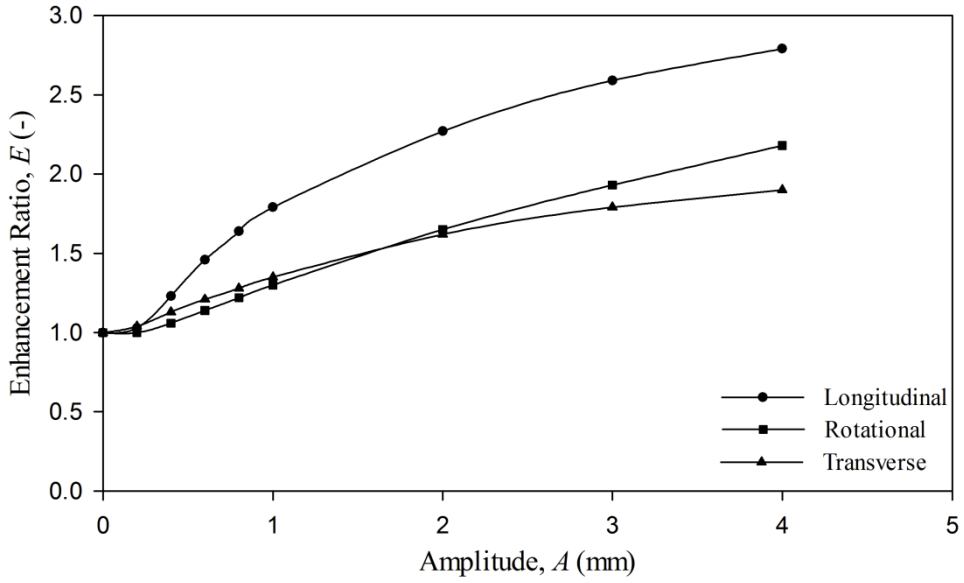

Figure 3.2. Comparison of efficacy of longitudinal, transverse and rotational oscillations in enhancing flow with different values of oscillation amplitude for a power law fluid:
k = 1 Pa $s^{0.6}$; n = 0.6; $\Delta p/L = 2 \times 10^4$ Pa m^{-1}; f = 50 Hz; D = 4 mm; L = 10 mm.

Figure 3.2 depicted the variation of E with the amplitude A for the three vibration modes. Increase in the vibration amplitude at a constant frequency results in higher enhancement ratios. Longitudinal oscillation yields significantly higher enhancement ratios than rotational or transverse oscillations under the same conditions. The results shown in Figure 3.2 also suggest that rotational and transverse vibrations lead to similar effects on flow within the range of amplitudes studied in this work. These effects can also be demonstrated by plotting the velocity profiles of a shear-thinning fluid at different

amplitudes, as shown in Figure 3.3.

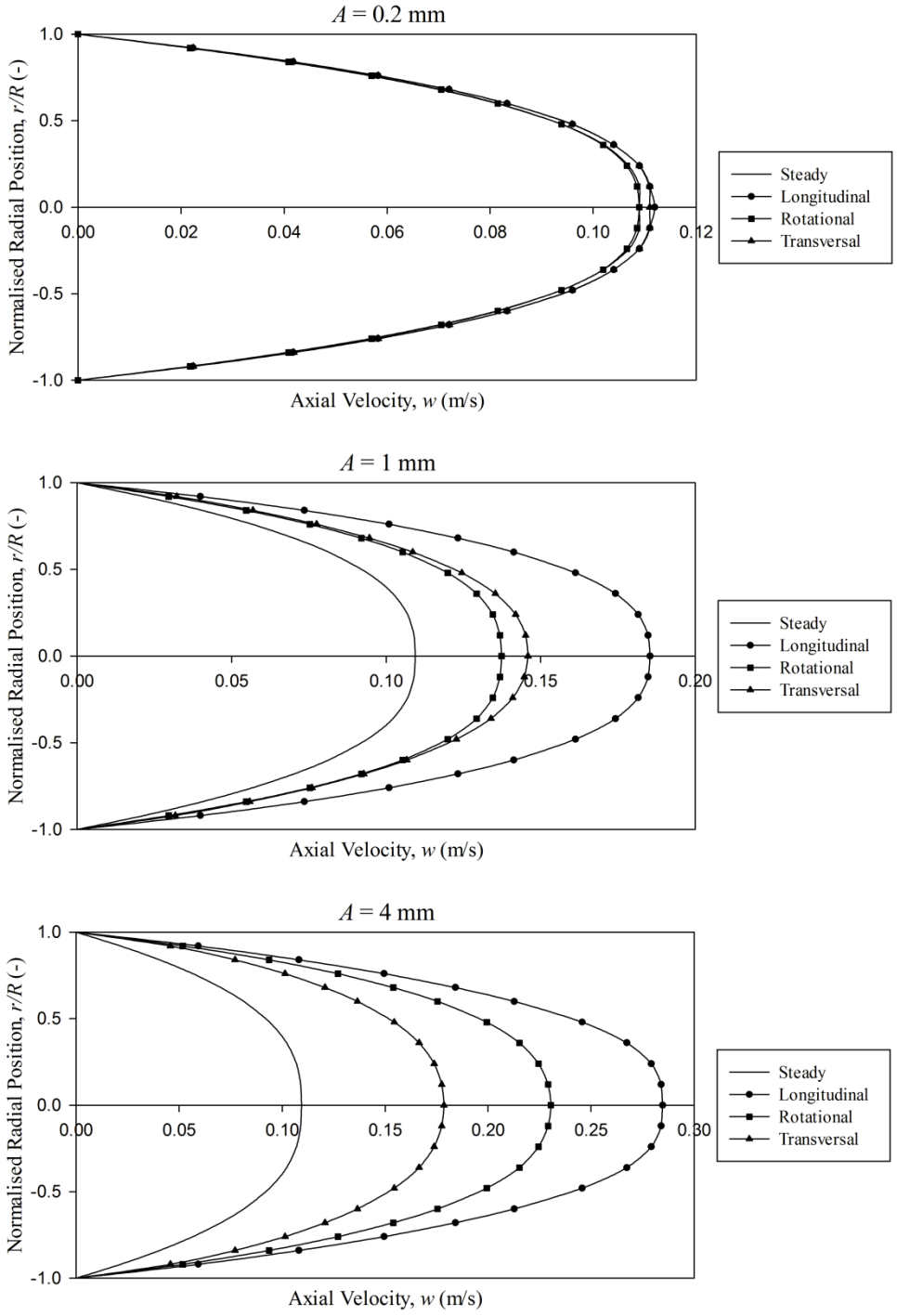

Figure 3.3. Comparison of efficacy of longitudinal, transverse and rotational oscillations in affecting velocity profile with different values of oscillation amplitude for a power law fluid:

k = 1 Pa s$^{0.6}$; n = 0.6; $\Delta p/L = 2 \times 10^4$ Pa m^{-1}; f = 50 Hz; D = 4 mm; L = 10 mm.

On the account of effect of vibration amplitude on flow enhancement, following simulations were carried out with two different amplitudes, 2 mm and 0.2 mm, providing more comprehensive investigation on the comparison of these three modes of vibration.

3.5.1.2. The efficacy of vibrations with different values of vibration frequencies

This group of simulations is also based on the power law fluid: k = 1 Pa $s^{0.6}$ and n = 0.6. There is a marked rise in flow enhancement with vibration frequency for all the three vibration modes which was shown in both Figures 3.4 and 3.5. The figures also show that longitudinal vibration is the most effective mode under the flow conditions used as it yields the highest enhancement ratio. Rotational and transverse oscillations, on the other hand, result in lower, albeit still significant, enhancement ratios, with transverse vibration being generally more effective at low frequencies whilst rotational vibration being more effective at higher frequencies. The margin between the flow enhancement generated by longitudinal vibration and the other two modes of vibration widens as f increases.

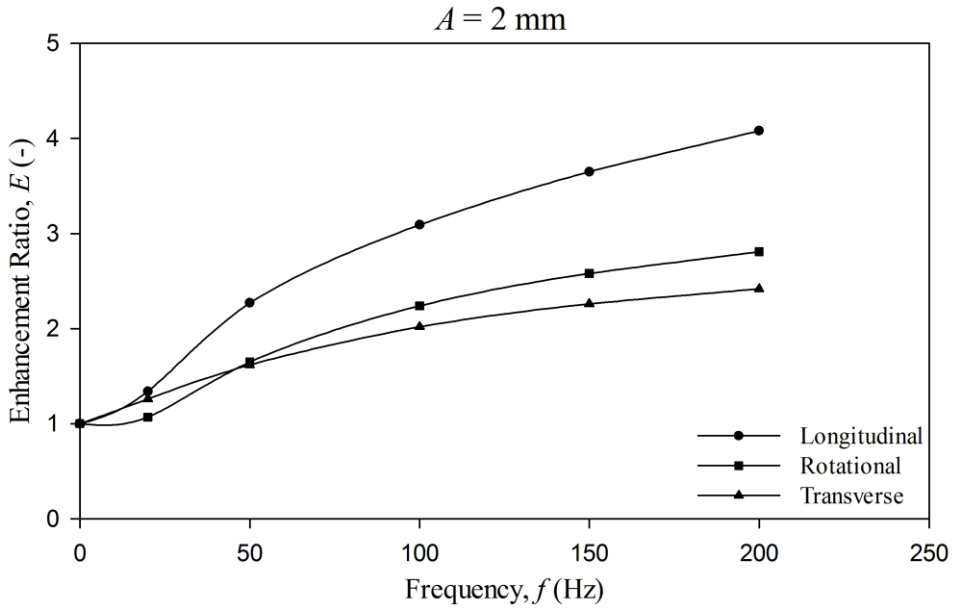

Figure 3.4. Comparison of efficacy of longitudinal, transverse and rotational oscillations in enhancing flow with different values of oscillation frequency for a power law fluid:

k = 1 Pa $s^{0.6}$; n = 0.6; $\Delta p/L = 2 \times 10^4$ Pa m^{-1}; A = 2.0 mm; D = 4 mm; L = 10 mm.

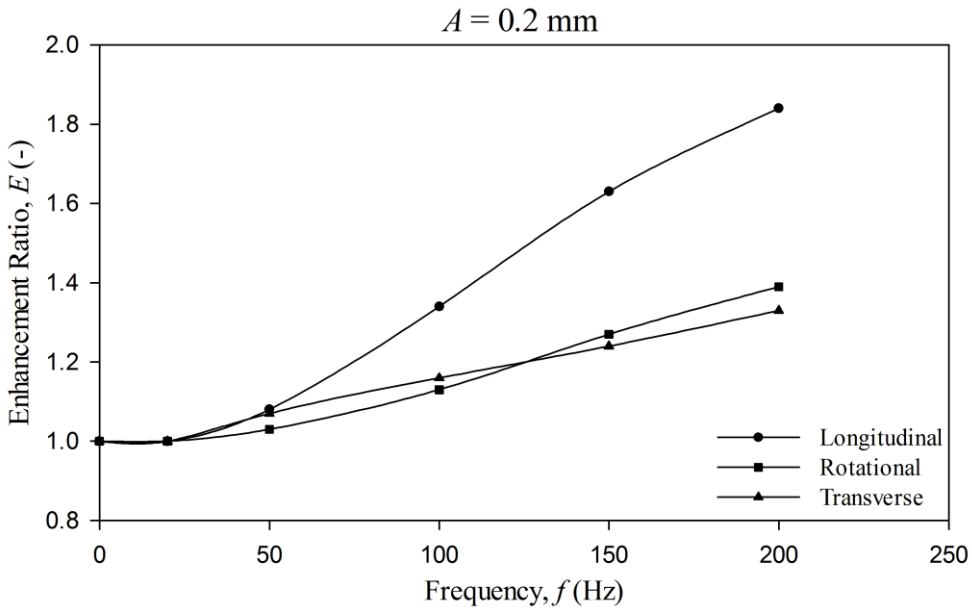

Figure 3.5. Comparison of efficacy of longitudinal, transverse and rotational oscillations in enhancing flow with different values of oscillation frequency for a power law fluid:

k = 1 Pa s$^{0.6}$; n = 0.6; $\Delta p/L = 2 \times 10^4$ Pa m^{-1}; A = 0.2 mm; D = 4 mm; L = 10 mm.

In a shear-thinning fluid, the added shear due to the superimposed vibration leads to a considerable reduction in the shear-dependent apparent viscosity, giving rise to an elongated or sharpened velocity profile in the axial direction compared with the steady-state profile, hence the observed flow enhancement. The axial velocity profile of the same fluid is shown in Figures 3.6 and 3.7 for these three modes of vibration at three different frequencies. The strongest elongation or sharpening effect on the velocity profile is observed under longitudinal vibration.

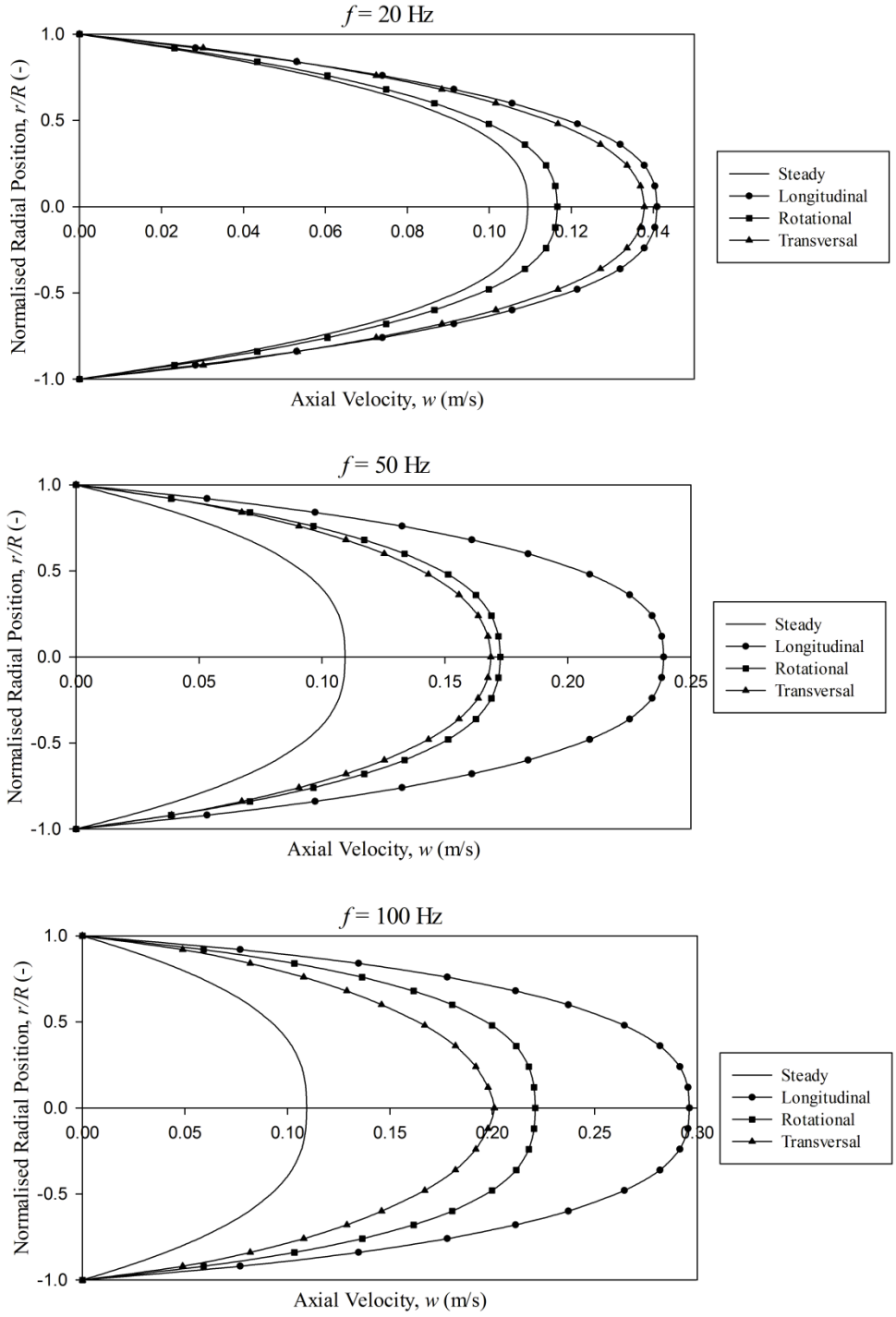

Figure 3.6. Comparison of efficacy of longitudinal, transverse and rotational oscillations in affecting velocity profile with different values of oscillation frequency for a power law fluid:

k = 1 Pa $s^{0.6}$; n = 0.6; $\Delta p/L = 2 \times 10^4$ Pa m^{-1}; A = 2.0 mm; D = 4 mm; L = 10 mm.

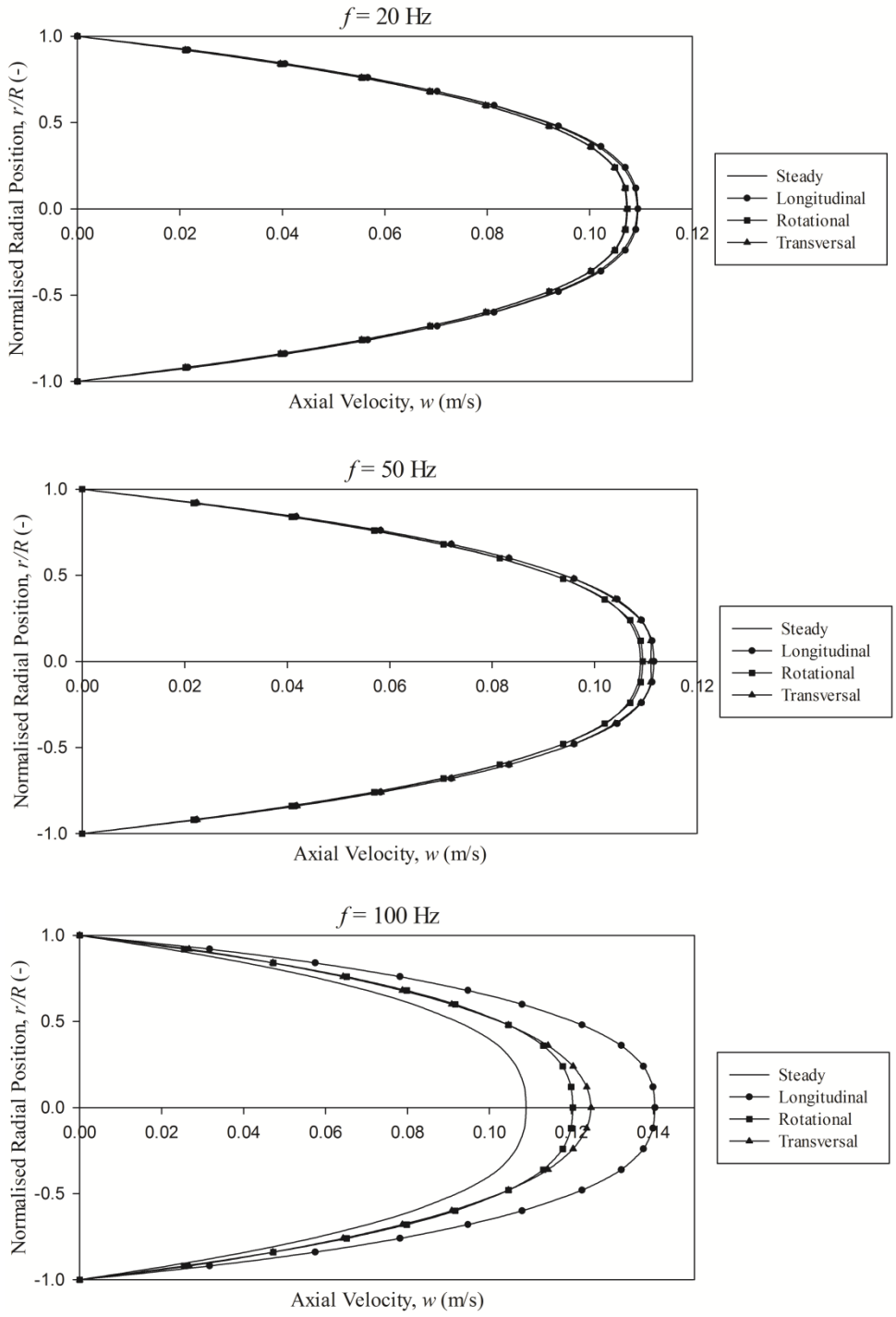

Figure 3.7. Comparison of efficacy of longitudinal, transverse and rotational oscillations in affecting velocity profile with different values of oscillation frequency for a power law fluid:

k = 1 Pa s$^{0.6}$; n = 0.6; $\Delta p/L = 2 \times 10^4$ Pa m^{-1}; A = 0.2 mm; D = 4 mm; L = 10 mm.

3.5.1.3. The efficacy of vibrations with different values of flow behaviour index

The flow behaviour index n is a measure of the degree of non-Newtonian behaviour; the greater the departure from unity the more pronounced are the non-Newtonian properties of the fluid. When $n = 1$, the fluid is Newtonian.

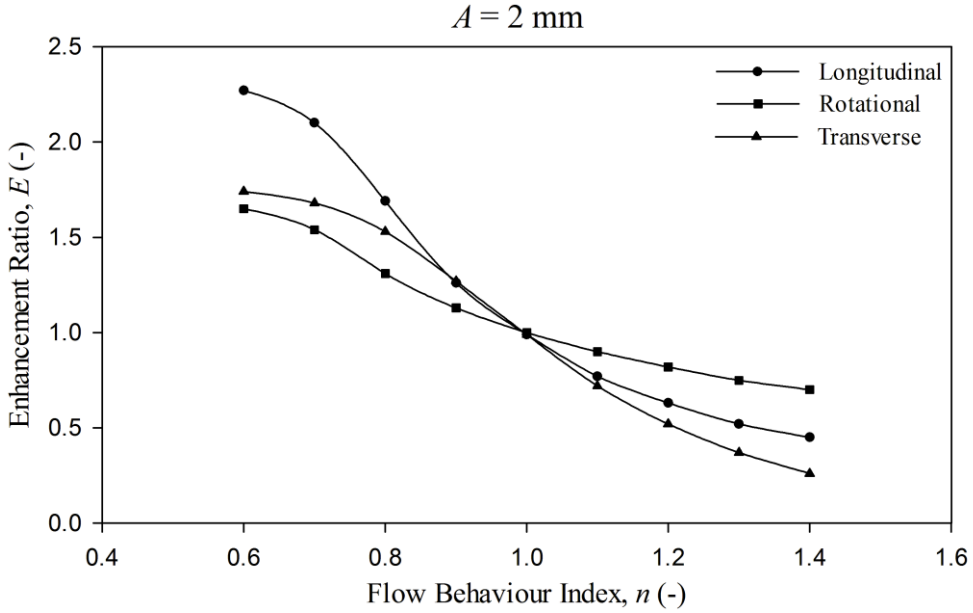

Figure 3.8. Comparison of efficacy of longitudinal, transverse and rotational oscillations in enhancing flow with different values of flow behaviour index for a power law fluid:

$k = 1$ Pa s^n; $\Delta p/L = 2 \times 10^4$ Pa m^{-1}; $A = 2.0$ mm; $f = 50$ Hz; $D = 4$ mm; $L = 10$ mm.

As discussed above, the observed effects of vibration on the flowrate of a power law fluid are due to the shear-dependence of its viscosity. The larger the dependence of viscosity on shear is, the greater the influence of vibration on the flow is. Figures 3.8 and 3.9 show that for shear-thinning fluids, E increases as n decreased, i.e. as the shear-thinning behaviour becomes more pronounced. For shear-thickening fluids, vibration results in flow retardation, with E falling below unity as n increased above one. Based on present work, it can be concluded that (i) transverse vibration yields the strongest retardation effects throughout $n > 1$; (ii) rotational vibration has the weakest influence on E

throughout the whole range of n in this study; (iii) for $n < 1$, the strongest effect on flow enhancement is yielded by longitudinal vibration at high vibration amplitude of 2 mm, while by transverse vibration, at low vibration amplitude of 0.2 mm.

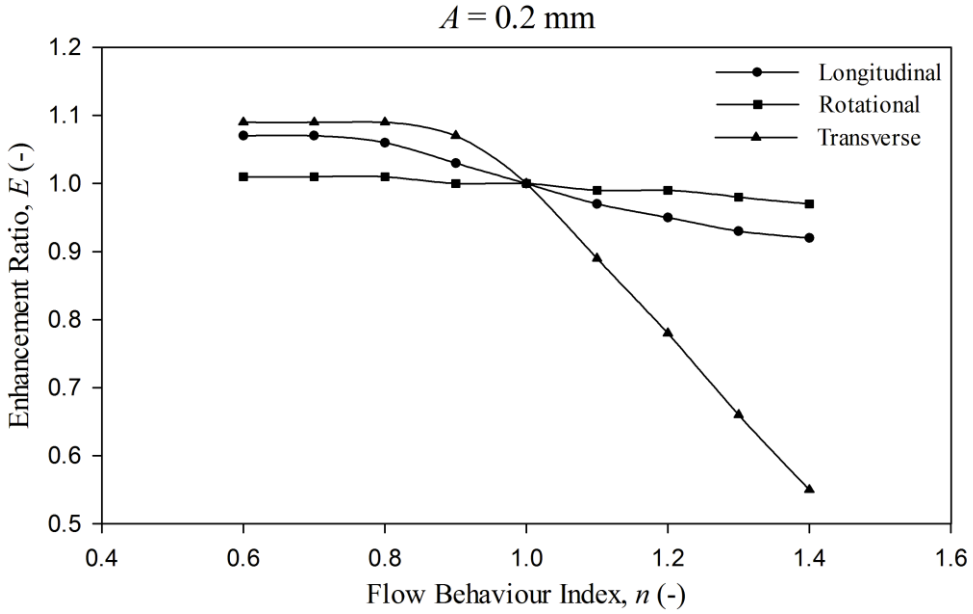

Figure 3.9. Comparison of efficacy of longitudinal, transverse and rotational oscillations in enhancing flow with different values of flow behaviour index for a power law fluid:

k = 1 Pa s^n; $\Delta p/L = 2 \times 10^4$ Pa m^{-1}; A = 0.2 mm; f = 50 Hz; D = 4 mm; L = 10 mm.

Sample velocity profiles for different n values are given in Figures 3.10 and 3.11 separately with vibration amplitudes of 2 mm and 0.2 mm. Note that while vibration results in a sharpened velocity profile in shear-thinning fluids compared to steady state, it leads to an increase in the apparent viscosity due to its imposed shear, and thus, gives rise to a flatter velocity profile in shear-thickening fluids.

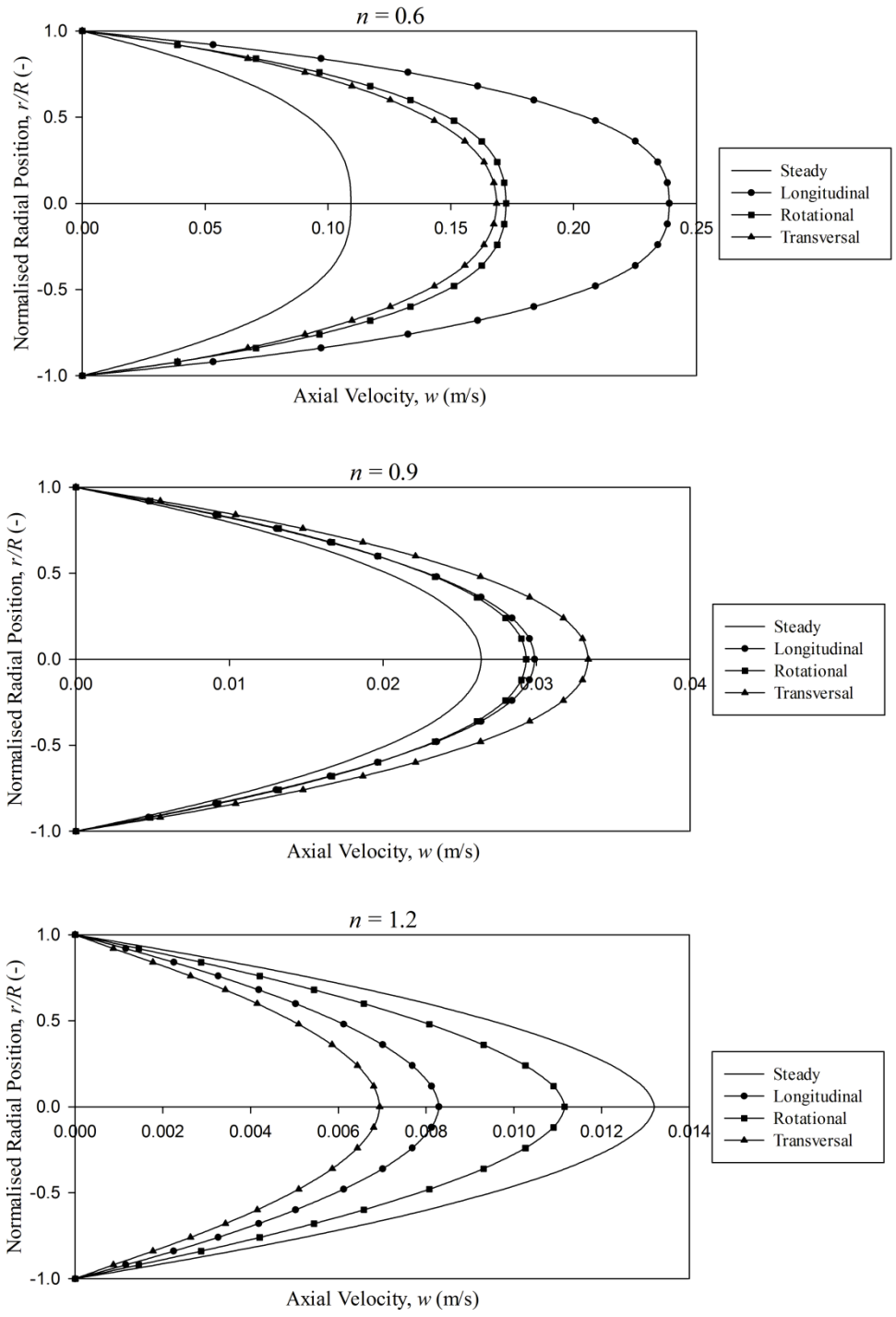

Figure 3.10. Comparison of efficacy of longitudinal, transverse and rotational oscillations in affecting velocity profile with different values of flow behaviour index for a power law fluid:

k = 1 Pa s^n; $\Delta p/L = 2 \times 10^4$ Pa m^{-1}; A = 2.0 mm; f = 50 Hz; D = 4 mm; L = 10 mm.

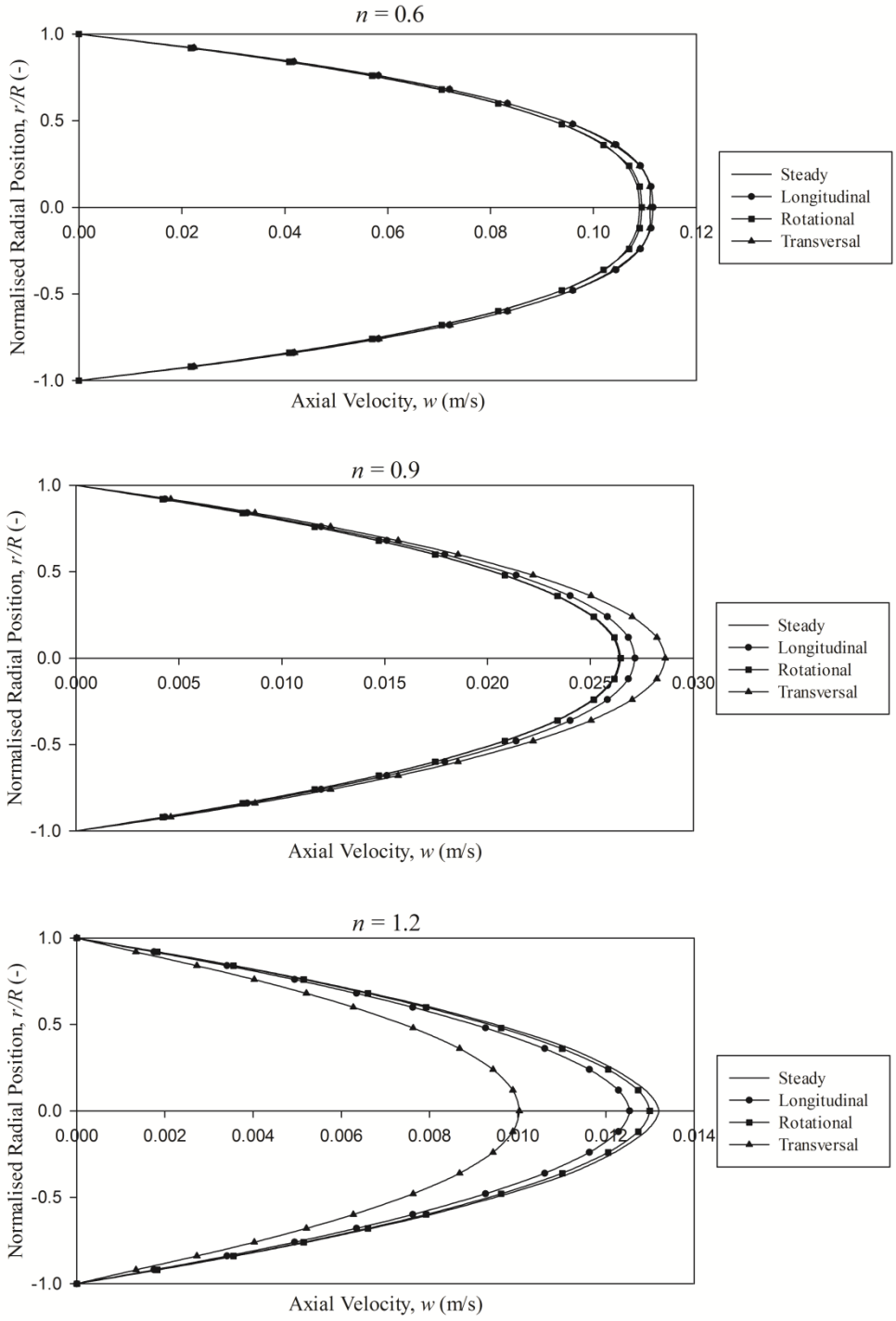

Figure 3.11. Comparison of efficacy of longitudinal, transverse and rotational oscillations in affecting velocity profile with different values of flow behaviour index for a power law fluid:

k = 1 Pa s^n; $\Delta p/L = 2 \times 10^4$ Pa m^{-1}; A = 0.2 mm; f = 50 Hz; D = 4 mm; L = 10 mm.

3.5.1.4. The efficacy of vibrations with different values of fluid consistency index

Despite of the conclusion that vibration cannot alter flow of Newtonian fluid, with a shear-dependent apparent viscosity fluid, e.g. power law rheology, variation of fluid consistency index also results in change of flow as demonstrated in Figures 3.12 and 3.13. It can also be concluded from Figures 3.12 and 3.13 that transverse vibration is most sensitive to the fluid consistency index *f*. Contractively, flow enhancements generated by longitudinal and rotational vibrations keep nearly unchanged as the fluid consistency *f* increases at both vibration amplitudes of 2 mm and 0.2 mm. It should be noted that, longitudinal vibration excels rotational vibration throughout the range of fluid consistency index *k* investigated in this study, while the margin between the flow enhancements generated by them broadens as *f* increases from 0.2mm to 2 mm.

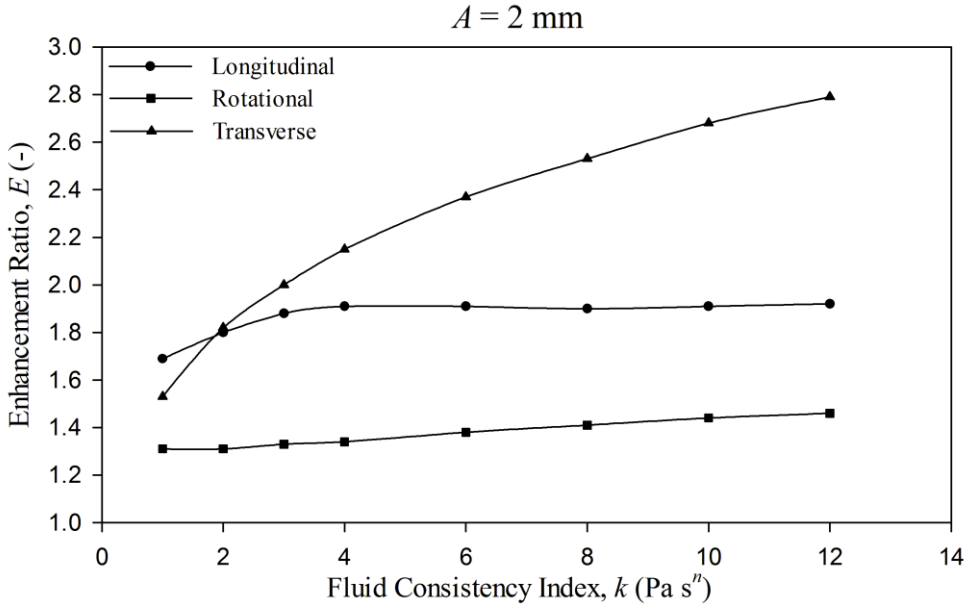

Figure 3.12. Comparison of efficacy of longitudinal, transverse and rotational oscillations in enhancing flow with different values of fluid consistency index for a power law fluid:

n = 0.8; $\Delta p/L = 2 \times 10^4$ Pa m^{-1}; A = 2.0 mm; f = 50 Hz; D = 4 mm; L = 10 mm.

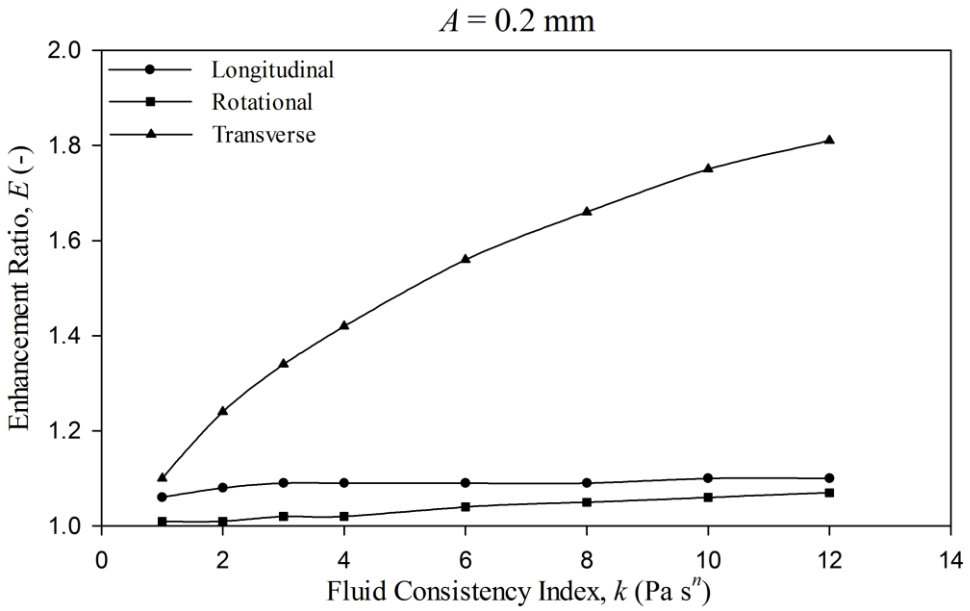

Figure 3.13. Comparison of efficacy of longitudinal, transverse and rotational oscillations in enhancing flow with different values of fluid consistency index for a power law fluid:

n = 0.8; $\Delta p/L = 2 \times 10^4$ Pa m^{-1}; A = 0.2 mm; f = 50 Hz; D = 4 mm; L = 10 mm.

Velocity profiles plotted in Figure 3.14 and 3.15 also confirm the similar tendency which is observed in flowrate enhancement comparisons. The effects of elongation or sharpening on the velocity profiles under transverse vibrations are most sensitive to the fluid consistency index k. The margin between the velocity profiles generated by transverse vibration and the other two kinds of vibrations (i.e. longitudinal and rotational) widens with the increase of the fluid consistency index k. While at the vibration amplitude of 0.2 mm, both longitudinal and rotational vibrations show a very weak influence on the velocity profiles.

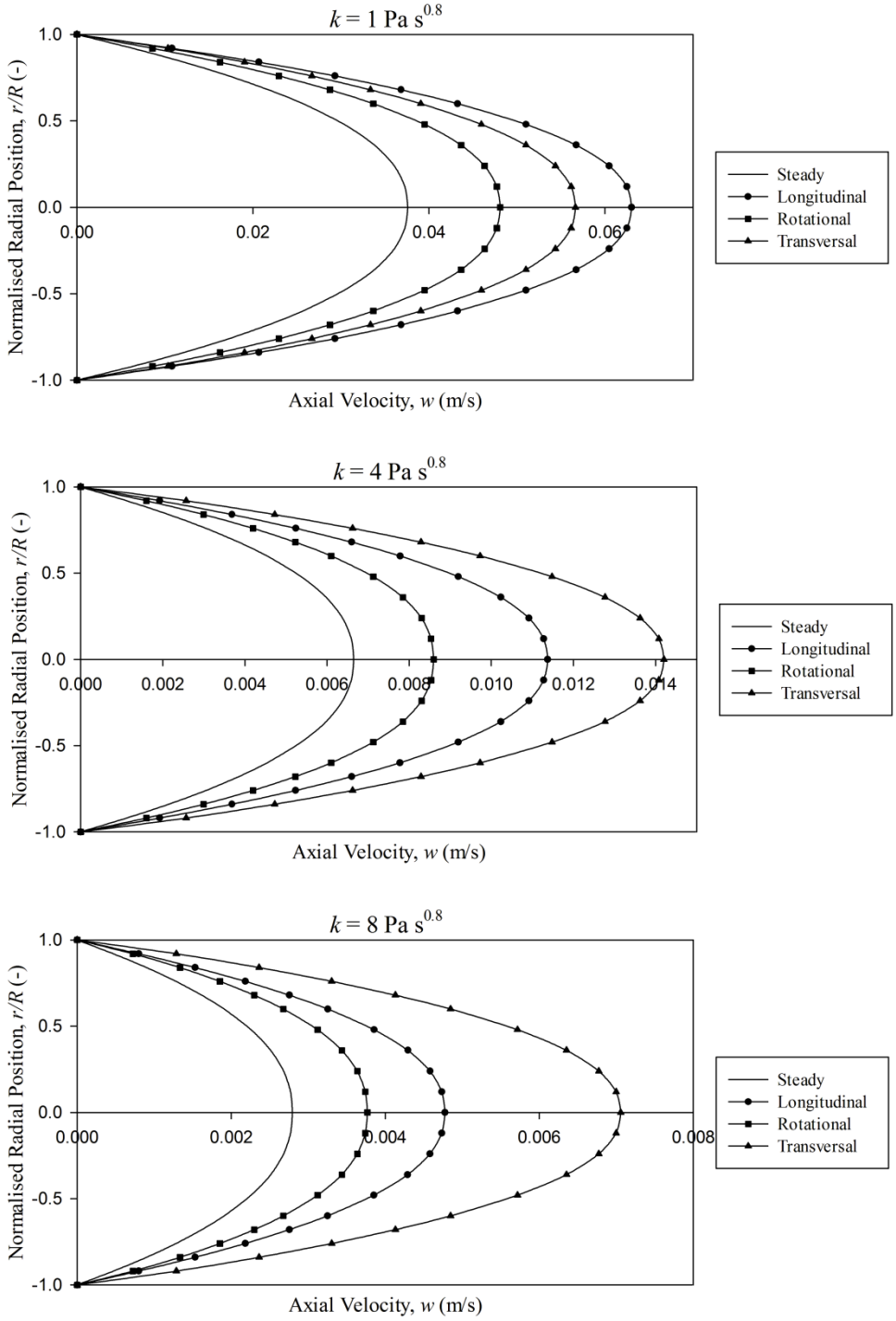

Figure 3.14. Comparison of efficacy of longitudinal, transverse and rotational oscillations in affecting velocity profile with different values of fluid consistency index for a power law fluid:

$n = 0.8$; $\Delta p/L = 2 \times 10^4$ Pa m^{-1}; $A = 2.0$ mm; $f = 50$ Hz; $D = 4$ mm; $L = 10$ mm.

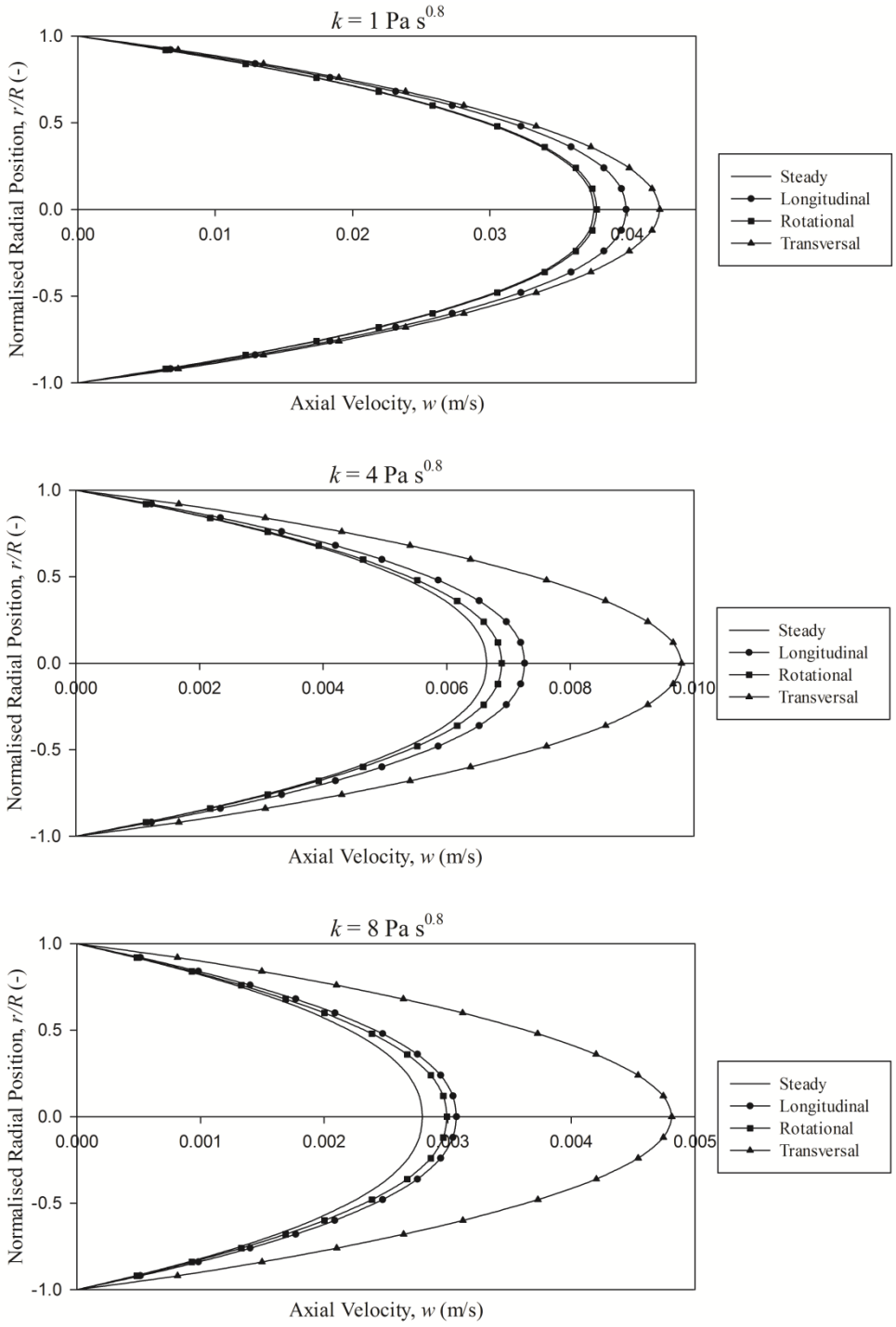

Figure 3.15. Comparison of efficacy of longitudinal, transverse and rotational oscillations in affecting velocity profile with different values of fluid consistency index for a power law fluid:

n = 0.8; $\Delta p/L = 2 \times 10^4$ Pa m^{-1}; A = 0.2 mm; f = 50 Hz; D = 4 mm; L = 10 mm.

3.5.1.5. The efficacy of vibrations with different values of yield stress

In the steady state flow of yield stress fluids, fluid can be sheared when the shear stress overcome the yield stress. Contractively fluid cannot be sheared if the yield stress is beyond the shear stress. Thus, flow should be divided into yielded and unyielded regions, and a so-called plug region, where fluid flows in a constant velocity, is formed in the core region of the pipe (i.e. unyielded region). Superimposition of vibration leads to increase of shear stress, broadens the yielded region, decreases the apparent viscosity in the pipe, and successively contributes to an enhancement in flowrate. As what can be observed in Figures 3.16 and 3.17, transverse vibration is always the most, whilst rotational vibration the least effective among these three types of vibration. Longitudinal vibration, which is nearly the same effective as transverse vibration at high vibration amplitude of 2 mm, exhibited more significant influence on the flow enhancement over either transverse or rotational vibration at low vibration amplitude of 0.2 mm.

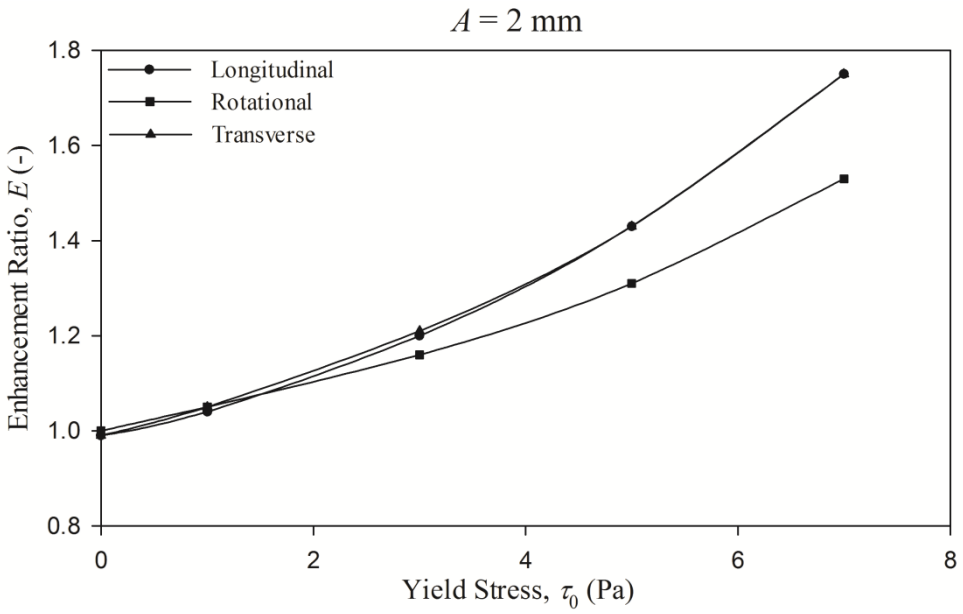

Figure 3.16. Comparison of efficacy of longitudinal, transverse and rotational oscillations in enhancing flow with different values of yield stress for a Bingham plastic fluid:

μ_B = 1 Pa s; $\Delta p/L = 2 \times 10^4$ Pa m^{-1}; A = 2.0 mm; f = 50 Hz; D = 4 mm; L = 10 mm.

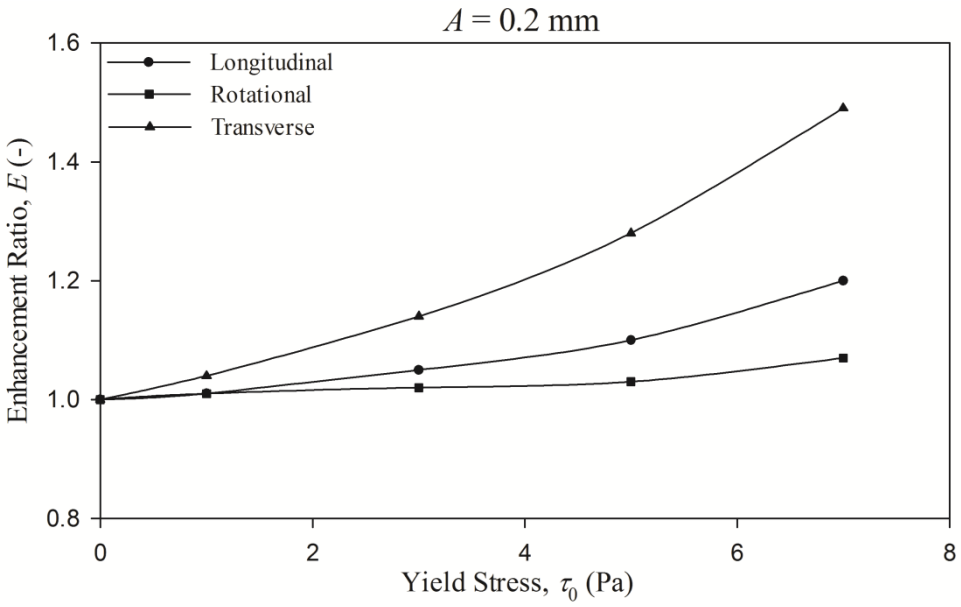

Figure 3.17. Comparison of efficacy of longitudinal, transverse and rotational oscillations in enhancing flow with different values of yield stress for a Bingham plastic fluid:

μ_B = 1 Pa s; $\Delta p/L = 2 \times 10^4$ Pa m^{-1}; A = 0.2 mm; f = 50 Hz; D = 4 mm; L = 10 mm.

The flat regions (i.e. plug regions), where the fluids are unyielded in the steady-state flow are clearly depicted in Figures 3.18 and 3.19. However, by the superimposition of vibrations, such plug regions are yielded in varying degree, even reduced to negligible level at some cases as the additional shear. Moreover, Bingham plastic fluids exhibit shear-dependent apparent viscosity which decreases with increasing shear rate. Therefore, elongation effect on the velocity profiles comparing with steady-state flow can also be observed in Figures 3.18 and 3.19.

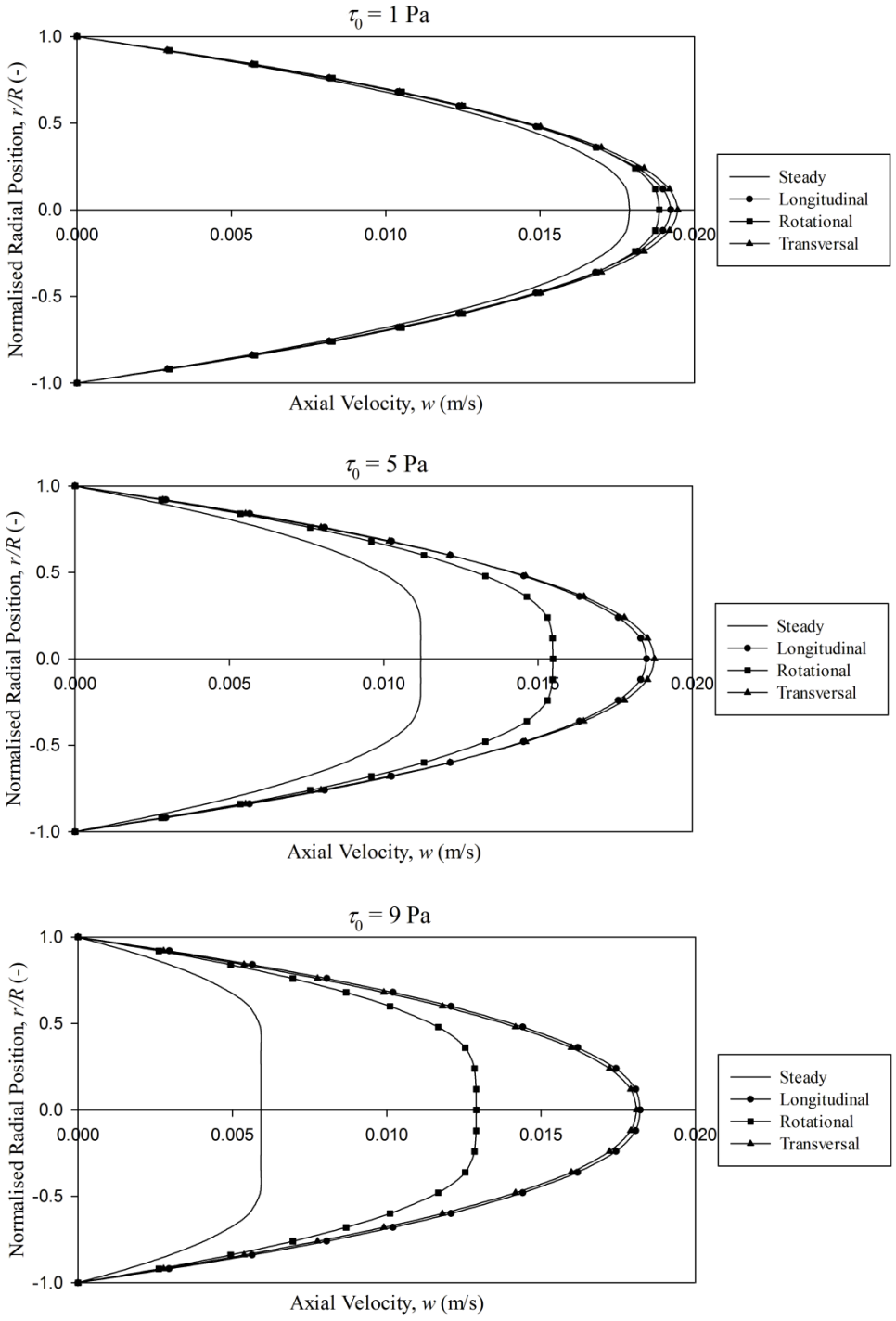

Figure 3.18. Comparison of efficacy of longitudinal, transverse and rotational oscillations in affecting velocity profile with different values of yield stress for a Bingham plastic fluid:

μ_B = 1 Pa s; $\Delta p/L = 2 \times 10^4$ Pa m^{-1}; A = 2.0 mm; f = 50 Hz; D = 4 mm; L = 10 mm.

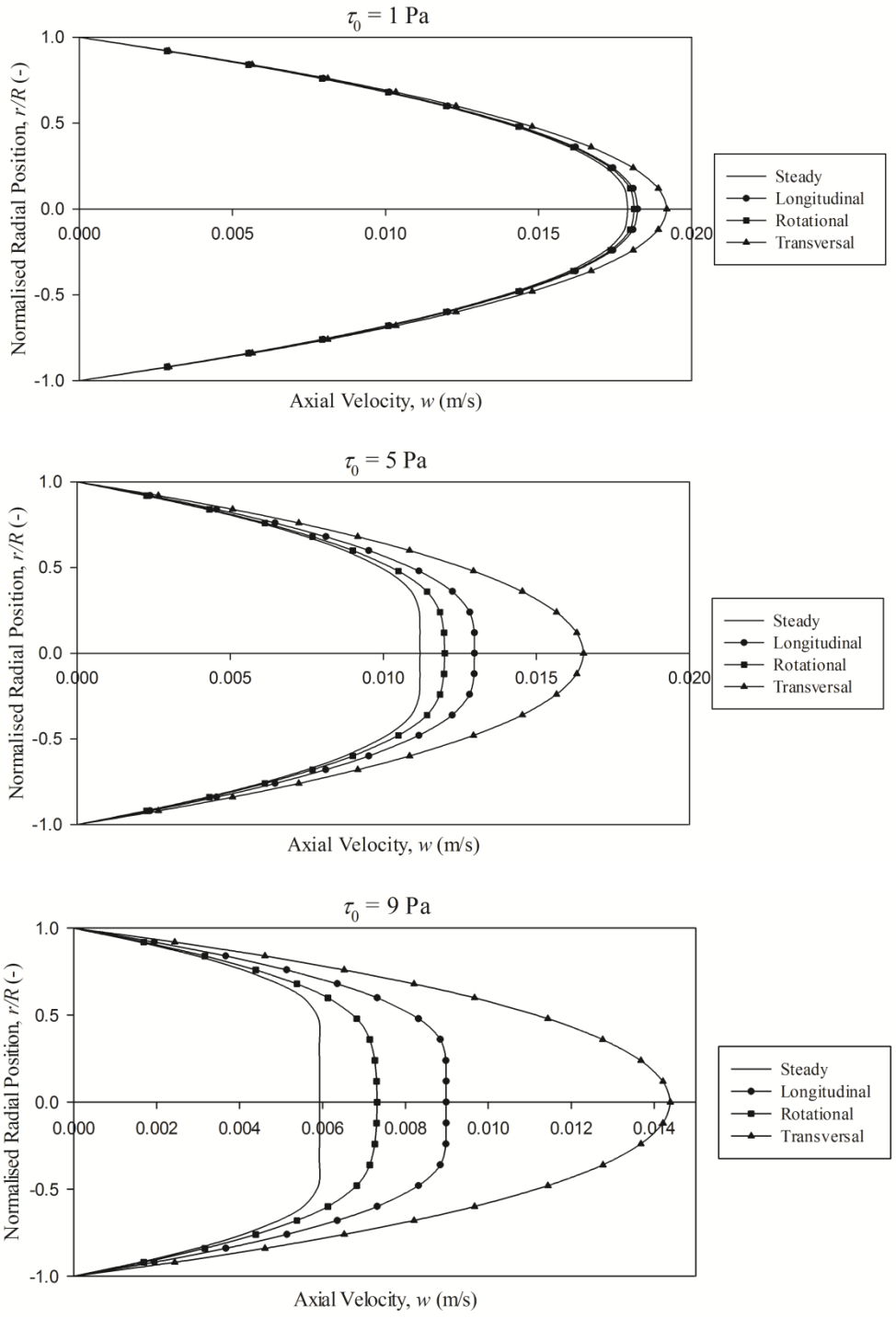

Figure 3.19. Comparison of efficacy of longitudinal, transverse and rotational oscillations in affecting velocity profile with different values of yield stress for a Bingham plastic fluid:

μ_B = 1 Pa s; $\Delta p/L = 2 \times 10^4$ Pa m^{-1}; A = 0.2 mm; f = 50 Hz; D = 4 mm; L = 10 mm.

3.5.2. Effect of vibration on the pipe flow with heat transfer

Simulations of the flow of a Newtonian fluid in a vibrated tube with a constant wall temperature showed that only transverse vibration can have substantial effects on the radial temperature profile, longitudinal and rotational vibrations have no significant effect under the same conditions as transverse vibration.

Figure 3.20 indicated the temperature distribution at pipe exit of, separately steady-state, under longitudinal, rotational and transverse vibration. This can be explained by the observation that longitudinal and rotational oscillations do not result in any radial mixing, but transverse oscillations induce a significant degree of radial mixing and chaotic motion in the fluid (see Figure 3.21) that leads to better temperature uniformity. Full description of heat transfer under transverse vibration will be presented in Chapter 4.

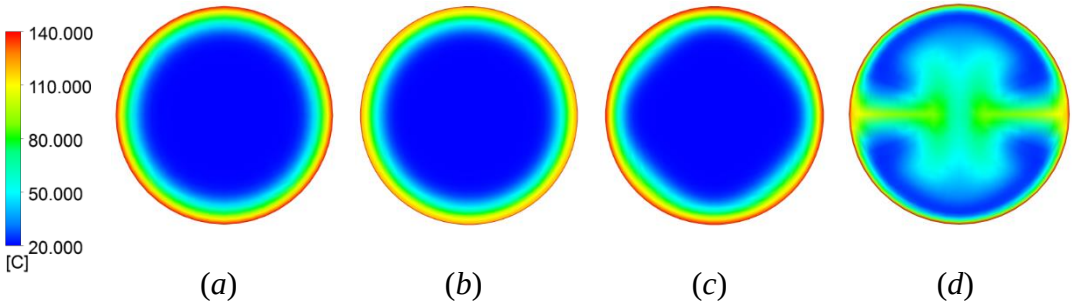

Figure 3.20. Temperature distribution at pipe exit: z = 0.4 m; T_{in} = 20 ℃; T_w = 140 ℃; $\overline{w}$ = 0.04 m s^{-1}; fluid properties: $\mu = k_0 \exp(E_\alpha / R_g T)$; ρ = 998 kg m^{-3}; C_p = 4180 J kg^{-1} K^{-1}; λ = 0.668 W m^{-1} K^{-1}.

(*a*) Steady state; (*b*) Longitudinal vibration;

(*c*) Rotational vibration; (*d*) Transverse vibration.

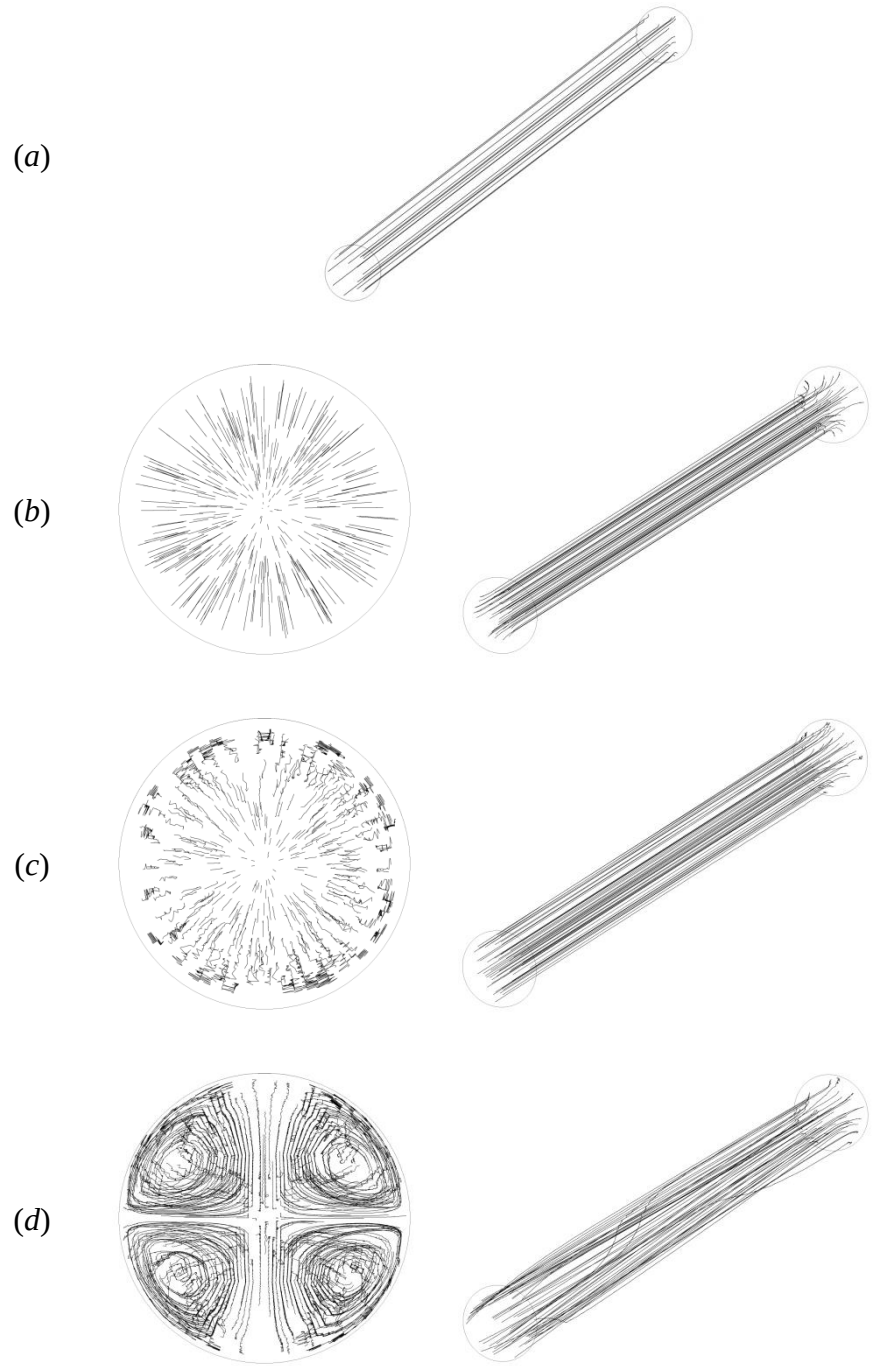

Figure 3.21. Fluid trajectories of flow in pipe: z = 0.4 m; T_{in} = 20 ℃; T_w = 140 ℃; $\overline{w}$ = 0.04 m s^{-1}; fluid properties: $\mu = k_0 \exp(E_\alpha / R_g T)$; ρ = 998 kg m^{-3}; C_p = 4180 J kg^{-1} K^{-1}; λ = 0.668 W m^{-1} K^{-1}.

(*a*) Steady state; (*b*) Longitudinal vibration;

(*c*) Rotational vibration; (*d*) Transverse vibration.

3.6. CONCLUSIONS

The oscillation of pipes conveying viscous fluids has a good potential for the processing of these materials. Whilst the flow of Newtonian fluids is unaffected by any type of vibration, the flow of shear-thinning and shear-thickening fluids can be, respectively, substantially enhanced or retarded by the superimposition of longitudinal, transverse or rotational oscillations. Longitudinal oscillations are generally the most effective in this respect, producing flow enhancements which exceed those generated by transverse and rotational vibration by a considerable margin, while transverse and rotational oscillations also produce significant flow enhancements of comparable magnitudes, especially under large vibration intensity. However, transverse oscillations are always more sensitive to the change of fluid consistency index, flow behaviour index and yield stress than either longitudinal or rotational vibrations. For all these three types of vibration, the extent of the flow enhancement produced is a function of the amplitude and frequency of vibration and fluid rheology. Vibration results in a sharpened velocity profile in shear-thinning fluids and a blunted velocity profile in shear-thickening fluids comparing to steady state.

Unlike longitudinal and rotational oscillations, transverse oscillations generate a vigorous swirling fluid motion and considerable radial mixing in viscous flows. Thus, transverse vibration produces a large enhancement in wall heat transfer as well as a nearly-uniform radial temperature field accompanied by a substantial heating of the inner region of the flow. These findings open up new opportunities for the application of mechanical vibration as a non-intrusive technique in processes where reducing non-uniformity in heat transfer represents a challenge. Whilst the implementation of vibrational motion in practice may not always be feasible, in processes and operations where this is possible, however, the effects can be very significant. The strong spiralling fluid motion generated by transverse oscillations could have further practical benefits in reducing pipe fouling because of the cleaning action that the fluid motion would create at the wall.

NOTATION

A	Vibration amplitude, m
az	The displacement in the azimuthal direction, m
C_p	Specific heat capacity, J Kg^{-1} K^{-1}
D	Diameter of pipe, m
E	Flow enhancement ratio, -
E_α	Activation energy for viscosity, J mol^{-1}
f	Vibration frequency, Hz
$\boldsymbol{g}$	Gravitational acceleration, m s^{-2}
k	Fluid consistency index, Pa s^n
k_0	Pre-exponential factor, Pa s
L	Length of pipe, m
n	Flow behaviour index, -
Q	Volumetric flowrate, m^3 s^{-1}
Q_v	Time-averaged volumetric flowrate under vibration, m^3 s^{-1}
Δp	Pressure drop, Pa
p	Pressure, Pa
r	Radial position, m
R	Radius of pipe, m
R_g	Gas constant, J mol^{-1} K^{-1}
Re	Reynolds number, -
Re_v	Reynolds number for vibrated flow, -
t	Time, s
T	Temperature, ℃ or K

T_{in} Inlet temperature, ℃ or K

T_w Wall temperature, ℃ or K

u_x Pipe velocity in radial direction, m s^{-1}

$\boldsymbol{U}$ The velocity vector, m s^{-1}

u_θ The angular velocity of pipe, m s^{-1}

u_z Pipe velocity in axial direction, m s^{-1}

w Fluid velocity in axial direction, m^3 s^{-1}

$\overline{w}$ Mean fluid velocity in axial direction, m^3 s^{-1}

x Wall position for transverse vibration, m

z Axial position, m

Greek symbols

$\dot{\gamma}$ Shear rate, s^{-1}

$\ddot{\boldsymbol{\gamma}}$ Second invariant of tensor shear rate, s^{-1}

θ Displacement in azimuthal direction, rad

Θ The angular amplitude of the rotational vibration, rad

ω Function of vibration frequency: $\omega = 2\pi f$, rad s^{-1}

τ Shear stress, Pa

τ_0 Yield stress, Pa

η Apparent viscosity, Pa s

λ Thermal conductivity, W m^{-1} K^{-1}

ρ Density, Kg m^{-3}

μ Viscosity for Newtonian fluid, Pa s

μ_B Plastic viscosity, Pa s

REFERENCES

Barth, T. J., Jesperson, D. C., 1989. The design and application of upwind schemes on unstructured meshes. AIAA Paper 89-0366.

Bird, R. B., Armstrong, R. C., Hassager, O., 1987. Dynamics of Polymeric Liquids: Fluid mechanics, 2nd Edition: Wiley, New York.

Cengel, Y. A., 2003. *Heat Transfer: A Practical Approach.* McGraw-Hill, New York.

Chhabra, R. P., Richardson, J. F., 1999. *Non-Newtonian flow in the process industries: fundamentals and engineering applications.* Butterworth-Heinemann, Oxford.

Christiansen, E. B., Craig, S. E., 1962. Heat transfer to pseudoplastic fluids in laminar flow. AIChE Journal, 8(2), 154-160.

Deshpande, N. S., Barigou, M., 2001. Vibrational flow of non-Newtonian fluids. Chemical Engineering Science, 56(12), 3845-3853.

Eesa, M., Barigou, M., 2008. CFD analysis of viscous non-Newtonian flow under the influence of a superimposed rotational vibration. Computers & Fluids, 37(1), 24-34.

Eesa, M., Barigou, M., 2010. Enhancing radial temperature uniformity and boundary layer development in viscous Newtonian and non-Newtonian flow by transverse oscillations: A CFD study. Chemical Engineering Science, 65(6), 2199-2212.

Gonçalves, E. V., Lannes, S. C. D. S., 2010. Chocolate rheology. Food Science and Technology (Campinas), 30(4), 845-851.

Gündoğdu, M.Y., Çarpinlioğlu, M.Ö., 1999. Present State of Art on Pulsatile Flow Theory. Part 1. Laminar and Transitional Flow Regimes. JSME International Journal Series B Fluids and Thermal Engineering, 42(3), 384-397.

Isayev, A. I., Wong, C. M., Zeng, X., 1990. Flow of thermoplastics in an annular die under orthogonal oscillations. Journal of Non-Newtonian Fluid Mechanics, 34(3), 375-397.

Jung, A., Fryer, P. J., 1999. Optimising the quality of safe food: Computational modelling of a continuous sterilisation process. Chemical Engineering Science, 54(6), 717-730.

Klaczak, A., 1997. Report from experiments on heat transfer by forced vibrations of exchangers. Heat and Mass Transfer, 32(6), 477-480.

Kwant, P. B., Zwaneveld, A., & Dijkstra, F. C., 1973. Non-isothermal laminar pipe flow - I. Theoretical. Chemical Engineering Science, 28(6), 1303-1316.

Kwant, P. B., Fierens, R. H. E., Van Der Lee, A., 1973. Non-isothermal laminar pipe flow － II. Experimental. Chemical Engineering Science, 28(6), 1317-1330.

Lee, Y. H., Chang, S. H., 2003. The effect of vibration on critical heat flux in a vertical round tube. Journal of Nuclear Science and Technology, 40(10), 734-743.

Mena, B., Manero, O., Binding, D. M., 1979. Complex flow of viscoelastic fluids through oscillating pipes. Interesting effects and applications. Journal of Non-Newtonian Fluid Mechanics, 5, 427-448.

Piau, J. M., Piau, M., 2002. Easier flow of viscoplastic materials with ultrasonic longitudinal wall motion. Journal of Non-Newtonian Fluid Mechanics, 104(2), 185-226.

Shin, S., Ku, Y., Suh, J. S., Moon, S. Y., Jang, J. Y., 2003. Characteristics of blood flow resistance under transverse vibration: red blood cell suspension in dextran-40. Annals of Biomedical Engineering, 31(9), 1077-1083.

Steffe, J. F., 1996. Rheological Methods in Food Process Engineering, 2nd Edition: Freeman Press, East Lansing, Michigan.

Wu, H., Guo, S. Y., Chen, G. S., Lin, J., Chen, W., Wang, H. T., 2003. Ultrasonic oscillations effect on rheological and processing properties of metallocene-catalyzed linear low density polyethylene. Journal of Applied Polymer Science, 90(7), 1873-1878.

CHAPTER 4.
VIBRATION TECHNIQUE FOR ENHANCING TEMPERATURE UNIFORMITY AND HEAT TRANSFER IN VISCOUS FLUID FLOW

Summary

Radial heat transfer in viscous pipe flow is controlled by thermal conduction which leads to a wide radial temperature distribution and slow heating of the core region of the flow. This is highly undesirable in many industrial processes as it results in a grossly uneven distribution of fluid heat treatment. The use of static in-line mixers to promote radial mixing and, thus, heat transfer and temperature uniformity, engenders large pressure drops and the devices are generally prohibited in processes where hygiene is paramount as they are difficult to keep clean. Computational Fluid Dynamics (CFD) study has showed that the superimposing of transverse mechanical oscillations on the steady flow of a viscous fluid in a pipe with an isothermal wall, results in a large enhancement in wall heat transfer, as well as a considerably more uniform radial temperature distribution accompanied by rapid heating of the inner region of the flow. Such a transverse vibration also causes the thermal boundary layer to grow more rapidly and, thus, the temperature profile to develop very rapidly in the axial direction. In this study, a validated CFD model was used to develop an enhanced vibration technique which combines transverse oscillations with a step rotation of oscillation orientation. The technique produces much more improved effects compared to transverse vibration alone, and it also excels in comparison with the well-known Kenics helical static mixer.

4.1. INTRODUCTION

When laminar fluid flow in a tube is accompanied by radial heat transfer, the associated parabolic radial velocity profile leads to a wide radial temperature distribution as heat transfer is controlled by slow conduction. Such conditions pose a considerable challenge in a number of industrial processes, such as the processing of food products, polymer melts and pharmaceutical formulations, where the fluid to be heated is often viscous and temperature dependent. This problem has been recognized for a long time but effective technological solutions are still missing.

In the heating stage of continuous food sterilisation, for example, heat is transferred from the hot tube wall to the fluid such that the core region of the flow is the coldest, thus, resulting in an undesirable wide variation of product sterility and nutritional quality across the tube which leads to poor product quality (Jung and Fryer, 1999). The challenge is, therefore, to be able to sterilise the fastest parts in the core region of the tube without over-processing the slowest parts near the wall so that, ideally, all parts of the fluid should receive equal heat treatment. The optimisation of such thermal processes poses a challenging manufacturing problem. The overriding importance of safety often results in the food being exposed to a more severe process than is desirable from a quality aspect, resulting in poor sensory and nutritional attributes, especially with sensitive products. In the cooling stage of the process the problem is reversed and instead of rapid uniform cooling of the product, the central parts of the flow incur the slowest cooling rates, again leading to significant losses in product quality. These problems become even more complicated when more than one phase is present such as in solid-liquid flows.

To improve the uniformity of the temperature distribution, methods are needed to promote radial mixing in viscous fluid flow. Radial mixing can be enhanced by operating under turbulent flow conditions, but the high fluid viscosities encountered in practice make this proposition impractical and/or uneconomical. Various ways have been proposed to improve heat convection by adding internal screw-thread structures on the wall to disrupt the boundary layer (Shrirao *et al*., 2013), but such technological

solutions are limited by their manufacturing complexity, cost, their high proneness to fouling and clogging, and the difficulty to keep them clean. Similarly, inserts or inline static mixers are used to promote radial fluid mixing and a number of designs exist (Hobbs and Muzzio, 1997; Saatdjian *et al*., 2012). In viscous flow, such devices can achieve a high degree of fluid mixing but usually at the expense of a high pressure drop. These inserts too are generally prohibited in hygienic processes because of the risk of contamination as their complex geometries also promote fouling and make them difficult to clean.

A number of studies have also demonstrated the effects of pulsating flow on the heat flux and Nusselt number in tube flows (Gundogdu and Carpinlioglu, 1999). However, the effects on the radial temperature distribution in viscous fluids do not seem to have been reported.

Eesa recently reported a Computational Fluid Dynamics (CFD) study which showed that superimposing transverse mechanical oscillations on the steady flow of a viscous fluid in a tube with an isothermal wall, results in a large enhancement in wall heat transfer, as well as a considerably more uniform radial temperature distribution accompanied by a substantial heating of the inner region of the flow (Eesa and Barigou, 2010; 2011). Transverse vibration also causes the thermal boundary layer to grow more rapidly and, thus, the temperature profile to develop very rapidly in the axial direction. It should be noted that this type of flow is different from the pulsatile (oscillatory) flow mentioned above.

This study confirmed that combination of transverse oscillations and a stepwise angular motion was an effective technique to achieve a high degree of radial fluid mixing, temperature uniformity and heat transfer. A validated CFD model was used to assess and compare the performance of this new method to previous results using simple transverse vibration, as well as to the performance of the well-known Kenics helical static mixer, one of the best in this category of mixers.

4.2. CFD MODEL

4.2.1. Fluid viscosity

The fluid used is an incompressible, temperature-dependent Newtonian fluid whose viscosity is assumed constant at a given temperature and is described by the well-known Arrhenius relationship:

$$\mu = k_0 \exp\left(\frac{E_\alpha}{R_g T}\right) \tag{4.1}$$

The constants k_0 and E_a are determined experimentally and their values for various fluids have been reported in the literature (e.g. Steffe, 1996). These parameters, as well as other physical properties (density ρ, specific heat capacity C_p, and thermal conductivity λ) were assumed constant and their values are given in Table 4.1 (Eesa and Barigou, 2010; Jung and Fryer, 1999).

Table 4.1. Rheological parameters used.

E_a	R_g	ρ	C_p	λ	k_0	$\mu = k_0 \exp(E_a/R_gT)$ (Pa s)	
(J mol^{-1})	(J mol^{-1} K^{-1})	(kg m^{-3})	(J kg^{-1} K^{-1})	(W m^{-1} K^{-1})	(Pa s)	20 °C	140 °C
					5.0×10^{-7}	0.868	0.0134
35000	8.314	998	4180	0.668	1.2×10^{-6}	2.083	0.0322
					5.8×10^{-6}	9.980	0.1541

4.2.2. Transverse oscillation

Transverse oscillations are imposed on the tube wall in a direction perpendicular to the tube axis, as illustrated in Figure 4.1(*c*),

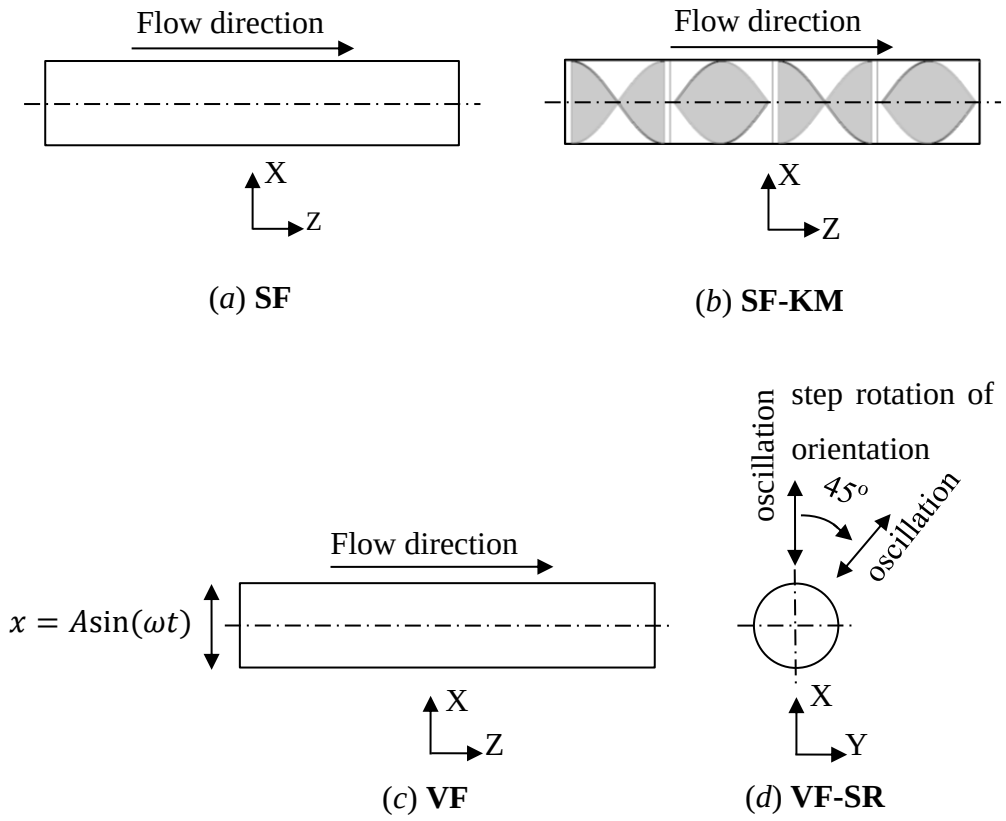

Figure 4.1. (*a*) steady flow through a straight tube (**SF**); (*b*) steady flow through a straight tube fitted with a Kenics static mixer (**SF-KM**), showing 4 elements out of 48; (*c*) flow through a straight tube subjected to transverse oscillations (**VF**); (*d*) flow through a straight tube subjected to transverse oscillations with step rotation of vibration orientation (**VF-SR**).

and the wall displacement x is described by the function:

$$x = A\sin(\omega t) \tag{4.2}$$

where A is the amplitude of vibration, t is time, and ω is the angular function of the frequency of vibration, f, such that $\omega=2\pi f$. The linear transversal velocity of the tube wall is then:

$$u_x = \frac{\mathrm{d}x}{\mathrm{d}t} = A\omega\cos(\omega t) \tag{4.3}$$

In the named transverse vibration with step rotation of orientation, the tube is continuously oscillated transversally but the orientation of oscillation is rotated instantly in a stepwise manner by an angle of 45 degrees about the tube axis, as depicted in Figure 4.1(*d*). The time interval, Δt, between changes of orientation steps, needs to be optimised for a given set of flow conditions. For the conditions investigated in this work, a value of ~ 10 s was determined via numerical experimentation, thus, the frequency of the step rotation, Ω, is (and is expected to always be) very low compared with the frequency of lateral oscillations; for example, in this case Ω is ~ 0.1 Hz compared to f = 50 Hz.

In all the numerical experiments conducted, under steady state, the flow regime was always laminar with a Reynolds number ($\mathrm{Re} = \rho\overline{w}D/\mu$) less than 100, where D is tube diameter and $\overline{w}$ is mean axial velocity. When the tube was vibrated, the vibration Reynolds number:

$$\mathrm{Re}_v = \frac{\rho A\omega D}{\mu} \tag{4.4}$$

was always less than 1500, so flow remained laminar throughout, in all the unsteady-state cases studied.

4.2.3. Governing equations

The governing transport equations involve the mass, momentum and energy balance equations:

Continuity: $$\nabla(\boldsymbol{U}) = 0 \tag{4.5}$$

Momentum: $$\rho \frac{\mathrm{D}\boldsymbol{U}}{\mathrm{D}t} = -\nabla p + \left[\nabla \cdot \eta\dot{\gamma}\right] \tag{4.6}$$

Energy: $$\frac{\mathrm{D}}{\mathrm{D}t}(C_p \rho T) - \nabla \cdot (\lambda \nabla T) = 0 \tag{4.7}$$

4.2.4. Mean temperature and pressure

The coefficient of variation is used as a measure of temperature uniformity across the tube:

$$C_{v-T} = \frac{\sigma_T}{\left|\overline{T} - T_{in}\right|} \tag{4.8}$$

where σ_T is the standard deviation of T. The volume-flowrate weighted mean temperature across the tube, $\overline{T}$, is obtained by dividing the tube cross-section into a large number of cells (N = 1860), as shown in Figure 4.2, which can be identified by their polar coordinates r and θ. The analysis was conducted using this regular grid implemented in MATLAB to avoid the difficulties associated with the complex and varied cell shapes of the computational CFD grid.

The temperature and axial velocity in a given cell are denoted by $T(r,\theta)$ and $w(r,\theta)$, respectively, and are considered at their nearly constant time-average values reached after a vibration time equivalent to the fluid residence time in the tube. Thus, $\sum_{i=1}^{N} w(r,\theta)S(r,\theta) = Q$ represents the volumetric flowrate through a cell, where $S(r,\theta)$ is the cross-sectional area of the cell. The volume-flowrate weighted mean temperature over the tube cross-section is, therefore, given by:

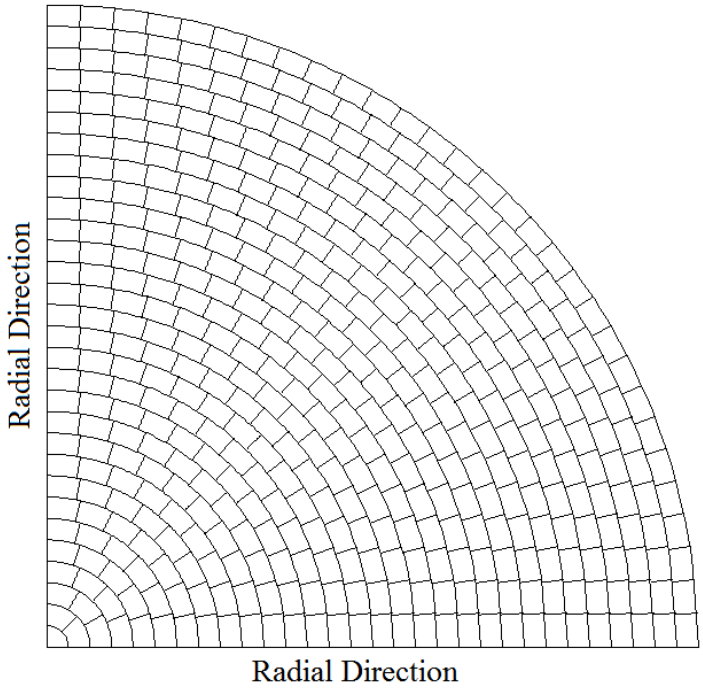

Figure 4.2. Illustration of grid used for evaluation of volume-flowrate weighted mean temperature and area-weighted pressure over tube section (total number of cells, N = 1860 cells).

$$\bar{T} = \frac{1}{Q}\sum_{i=1}^{N} T(r,\theta)w(r,\theta)S(r,\theta) \tag{4.9}$$

In the limit as $S(r,\theta) \to 0$, i.e. for large N, the uniformity of the temperature distribution over the tube cross-section can be well described by the standard deviation:

$$\sigma_T = \sqrt{\frac{1}{Q^2}\sum_{i=1}^{N}\left[T(r,\theta)w(r,\theta)S(r,\theta) - \bar{T}w(r,\theta)S(r,\theta)\right]^2} \tag{4.10}$$

and the coefficient of variation $C_{v\text{-}T}$ (Eq. (4.8)).

Similarly, to compute the total pressure drop, Δp, along the tube, the area-weighted mean pressure across the tube is needed and is computed, thus:

$$\bar{p} = \frac{4}{\pi D^2} \sum_{i=1}^{N} p(r,\theta) S(r,\theta) \tag{4.11}$$

4.2.5. Mean wall heat transfer coefficient

Heat transfer coefficient is defined as the ratio of the heat flux to the temperature difference, which is typically resulted by convection. The mean wall heat transfer coefficient was calculated using the heat balance equation:

$$\dot{m} C_p \left(\bar{T}_{out} - T_{in} \right) = hA\Delta T_m \tag{4.12}$$

where $\dot{m}$ is the mass flowrate, A is the tube wall surface area, $\bar{T}_{out}$ is the volume-flowrate averaged temperature at the tube exit, T_{in} is the uniform temperature at inlet, T_w is the temperature of the isothermal wall, and the log mean temperature difference is defined as $\Delta T_m = \frac{\left(T_w - \bar{T}_{out}\right) - \left(T_w - T_{in}\right)}{\ln\left[\left(T_w - \bar{T}_{out}\right) / \left(T_w - T_{in}\right)\right]}$ (Sinnott, 2005).

4.3. CFD SIMULATIONS

Three-dimensional simulations were set up and executed using the commercial software package ANSYS Workbench 14.5. The flow geometries were created and meshed using the software ICEM, while flow specification, solving and post-processing were all performed using CFX 14.5.

4.3.1. Geometry

One geometry consisted of a straight tube 30 mm in diameter and 2400 mm in length with three surface boundaries: inlet, outlet, and wall. Other simulations were conducted using the same setup with 48 segments of the helical Kenics static mixer, shown in Figure 4.3, inserted to fill the whole inside of the tube.

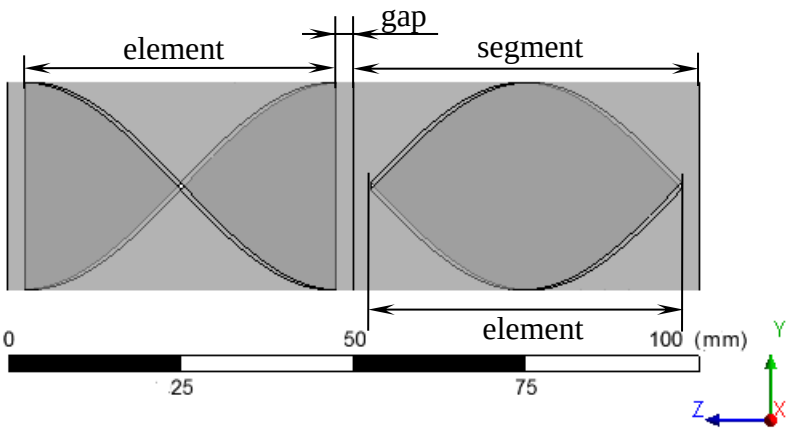

Figure 4.3. Geometry of helical Kenics static mixer showing two adjacent mixer segments.

The mixer consists of left and right twisting helical elements with a standard length to diameter ratio of 1.5; detailed dimensions are given in Table 4.2.

Table 4.2. Dimensions of Kenics static mixer (Figure 4.3).

Segment length (mm)	Gap width (mm)	Element length (mm)	Mixer diameter (mm)	Element thickness (mm)	Twist angle (rad)
50	2.5	45	30	1	π

4.3.2. Mesh

The geometry of straight tube was meshed with hexahedral cells. To optimise the mesh size it was necessary to carry out a mesh-independence study; this was done by performing a number of simulations with different mesh sizes, starting from a coarse mesh and refining it until results were no longer dependent on the mesh size. The mesh thus achieved contained approximately 4000 hexahedral cells per centimetre of tube length and around 1000 cells across the tube section, giving a mesh size in the core region of about 1 mm. The mesh size near the wall was progressively reduced down to 0.1 mm, as indicated in Figure 4.4(*a*), to enhance mesh resolution in this region where high velocity and temperature gradients exist. The quality of the mesh measured by its orthogonality and warpage was over 0.75, well above the generally accepted minimum value of 0.4 for a good mesh.

Other simulations were conducted using the same setup with 48 segments of the helical Kenics static mixer inserted to fill the whole tube, as illustrated in Figure 4.1(*b*). The mixer consists of left and right twisting helical elements with a standard length to diameter ratio of 1.5; detailed dimensions are given in Table 4.2. It should be noted that a mesh-independence study was conducted for each one of the flow geometries used. Very fine inflation layers of hexahedral cells were generated around the helical surfaces, so that the mesh was progressively reduced down to 0.15 mm at these surfaces and at the pipe wall to accurately capture the velocity and temperature gradients in these regions as shown in Figure 4.4(*b*)

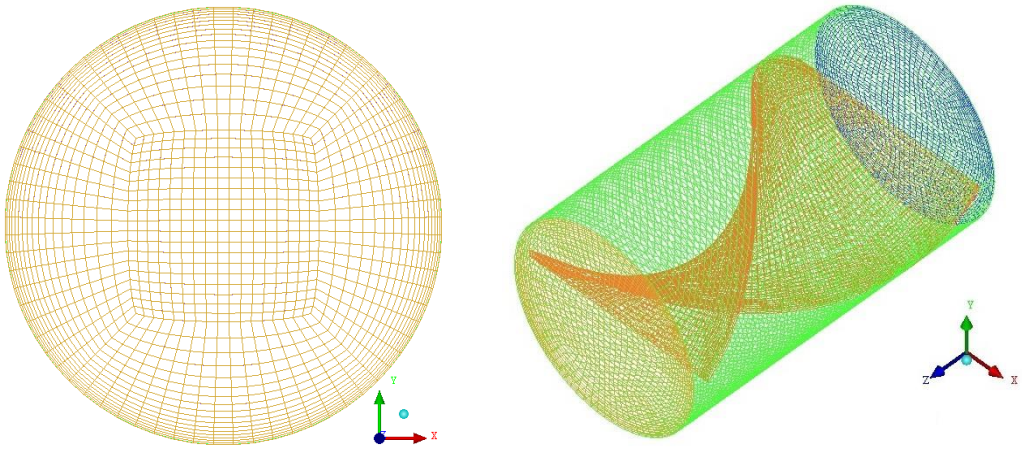

(*a*) (*b*)

Figure 4.4. Schematic mesh of straight tube (*a*) and straight tube fitted with Kenics static mixer (*b*).

4.3.3. Simulation setting

The numerical simulations were executed separately in a heating tube and cooling tube. A uniform temperature and a mass flowrate $\dot{m}$ = 0.0281 kg s^{-1} were specified at the tube inlet, and a zero gauge pressure was set at the tube outlet. The mass flowrate was chosen to give a mean flow velocity $\overline{w}$ = 4.0 cm s^{-1}, which is typical of values used in the processing of viscous food materials (Jung and Fryer, 1999; Steffe, 1996). A constant uniform wall temperature and a no-slip condition were assigned at the wall. In the heating stage of a continuous food sterilisation processing, wall temperatures lower than 180 ℃ are usually used in practice; therefore, here, in the heating tube, the bulk of the work was done with T_w = 140 °C, but simulations were also run for T_w = 180 C to investigate the effects, a value of 20 °C was specified as the inlet temperature in the heating tube. In the cooling stage, fluid was assumed at uniform temperature of 140 °C at the tube inlet. A room temperature of 20 °C was used as the wall temperature. As well, simulations have been done with typical temperature of chilled water of 5 °C as wall temperature to study the effect of wall temperature in the cooling tube. Where a static mixer was used, the helical surface was assumed adiabatic. Other simulation parameters are summarised in Table 4.3.

Table 4.3. Simulation parameters used.

Flow regime	Simulation time t (s)	Vibration frequency f (Hz)	Vibration amplitude A (mm)	Heating tube			Cooling tube		
				Inlet temperature T_{in} (°C)	Temperature of isothermal wall T_w (°C)	Frequency of step rotation of vibration orientation Ω (Hz)	Inlet temperature T_{in} (°C)	Temperature of isothermal wall T_w (°C)	Frequency of step rotation of vibration orientation Ω (Hz)
SF	-	-	-	20	140, 180	-	140	5, 20	-
SF-KM	-	-	-	20	140, 180	-	140	5, 20	-
VF	60	25, 50	1, 2	20	140, 180	-	140	5, 20	-
VF-SR	60	25, 50	1, 2	20	140, 180	0.2, 0.1, 0.067	140	5, 20	0.5, 0.2, 0.1

Simulations involving steady flow were conducted in the steady-state mode, whereas simulations of vibrational flow were conducted in the transient mode. For a transversely moving boundary, the mesh deformation option in CFX was used which allows the specification of the motion of nodes on boundary regions of the mesh. The motion of all remaining nodes is determined by the so-called displacement diffusion model which is designed to preserve the relative mesh distribution of the initial mesh. The mesh displacement was specified using Eq. (4.2), and an oscillatory velocity function defined by Eq. (4.3) was applied at the wall.

The advection scheme used in this investigation is 'High Resolution' Advection Scheme, which is helpful to satisfy the requirements of both accuracy and boundedness (see Chapter 2).

The transient scheme used for the solution to march in time was the 'Second Order Backward Euler Scheme'. The simulation was solved over the entire mean residence time of the fluid which is determined by the tube length and mean flow velocity. For example, for a tube length of 2400 mm and flow velocity of 4.0 cm s^{-1}, as used here, the fluid residence time in the tube is 60 s. This time duration was divided into equal time steps, the size of which (1.6667×10^{-3} s for frequency of 50 Hz and 3.3333×10^{-3} s for frequency of 25 Hz) was determined by dividing the vibration cycle into an optimised number of 12 equal time steps. Using a larger number of time steps per vibration cycle did not change the simulation results but prolonged the simulations considerably.

Convergence of the numerical solution was assumed when the root mean square (RMS) of mass, momentum and energy residuals all reached 10^{-4} at each time step which is a good level of accuracy given the complexity of the problem. Achieving this level of convergence typically required 8 — 12 iterations per time step for vibrational flow and about 50 iterations for steady flow. In practice, however, most of the equations generally reached RMS residual values well below the specified target.

4.4. VALIDATIONS OF CFD MODEL

Though CFX is a generally well validated code as it is widely used, the computational work reported here was further validated where possible either by comparing results with theoretical solutions or experimental data from the literature. The intention here was to try and validate the CFD model as much as possible so as to maximise confidence in the numerical results. The various stages of the validation process are described below.

4.4.1. Adiabatic isothermal steady flow through a straight tube

CFD simulation of the adiabatic isothermal steady flow of inelastic non-Newtonian fluids has been extensively validated in recent studies in previous research for a variety of rheological behaviours, namely power law, Herschel-Bulkley and Bingham plastic, showing excellent agreement with exact analytical solutions within approximately ±1% (Eesa and Barigou, 2008).

4.4.2. Steady flow through a straight tube with heat transfer

Three different cases were considered, as follows:

(i) Laminar flow of an isoviscous (i.e. temperature-independent viscosity) Newtonian fluid through the straight tube described above, was simulated using an isothermal wall at 140 ℃ and a uniform inlet temperature set at 60 ℃. This is a classic problem which was analytically described and solved by Jakob (1949), as follows:

$$2\overline{w}\left[1-\left(\frac{r}{R}\right)^2\right]\frac{\partial\theta_T}{\partial z}=\frac{\lambda}{\rho C_p}\left(\frac{\partial^2\theta_T}{\partial r^2}+\frac{1}{r}\frac{\partial\theta_T}{\partial r}\right) \tag{4.13}$$

Subject to boundary conditions:

$\theta_T = 0$ at $r = R$

$$\frac{\partial \theta_T}{\partial r} = 0 \quad \text{at } r = 0$$

where r is radial position, R is tube radius, z is axial position, and the dimensionless temperature θ_T is defined as $\theta_T = (T - T_W)/(T_{in} - T_W)$.

The axial temperature variations obtained from the solution of the above differential equation was compared to CFD predictions at three different radial positions: centre, mid-radius and near the wall. The agreement between CFD and theory was excellent, as shown in Figure 4.5.

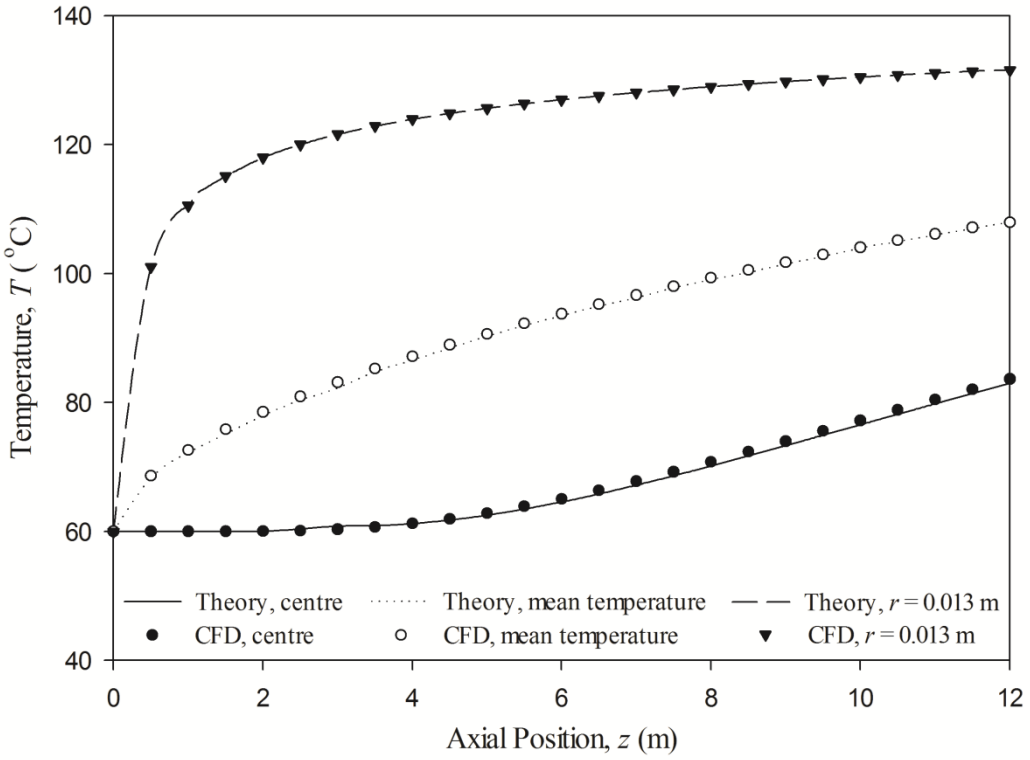

Figure 4.5. Comparison of CFD-predicted and theoretical (Eq. (4.13)) axial temperature profiles at three different radial positions for isoviscous Newtonian fluid in steady laminar tube flow.

T_{in} = 60 °C; T_w = 140 °C; D = 30 mm; $\overline{w}$ = 4.0 cm s^{-1}; μ = 0.001 Pa s; ρ = 998 kg m^{-3}; C_p = 4180 J kg^{-1} K^{-1}; λ = 0.6 W m^{-1} K^{-1}.

(ii) The numerical solution of Eq. (4.13) for the case of laminar flow of an isoviscous non-Newtonian power law fluid was first obtained and tabulated by Lyche and Bird (1956) (see also, for example, Chhabra and Richardson (1999) for graphical representation of the data). Comparison of this solution in Figure 4.6 with the CFD-predicted axial temperature profile for a considerably shear-thinning power law fluid (k = 1 Pa s$^{0.5}$, n = 0.5), shows an excellent agreement.

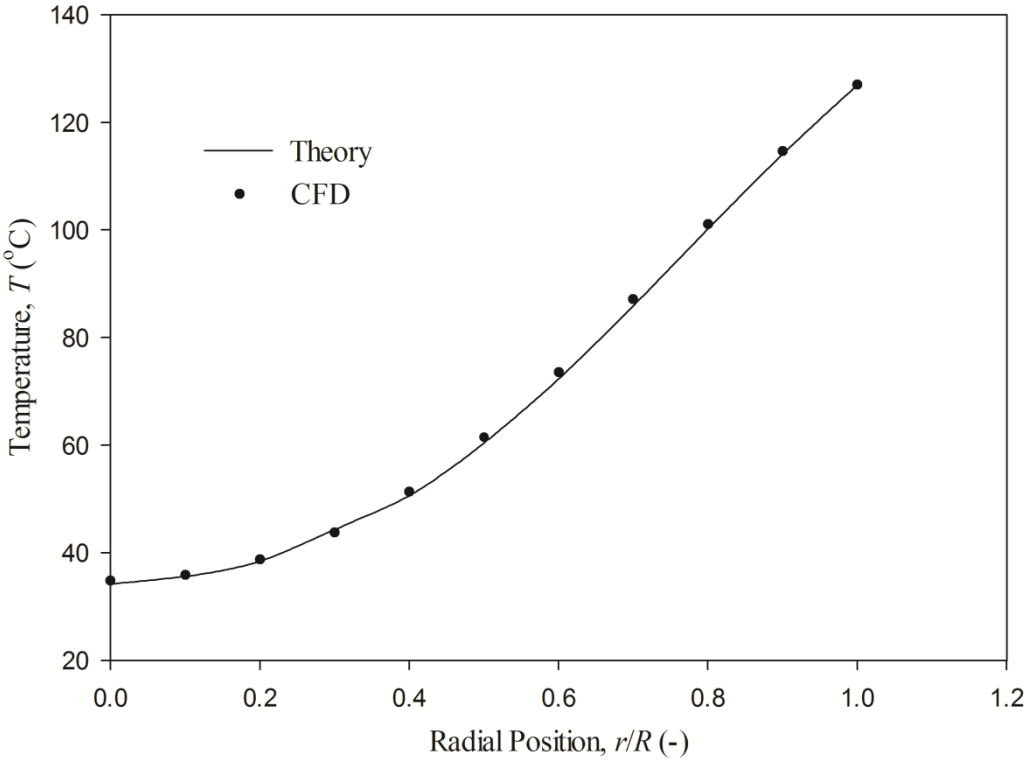

Figure 4.6. Comparison of CFD-predicted and theoretical (Eq. (4.13)) axial temperature profiles for isoviscous non-Newtonian power law fluid in steady laminar tube flow. T_{in} = 27 °C; T_w = 127 °C; D = 30 mm; $\overline{w}$ = 1.0 cm s^{-1}; ρ = 998 kg m^{-3}; k = 1 Pa s$^{0.5}$; n = 0.5; C_p = 4180 J kg^{-1} K^{-1}; λ = 0.6 W m^{-1} K^{-1}.

(iii) Since the variation of viscosity with temperature alters the flow field of the fluid considerably, the velocity profile in the tube computed by CFD under the conditions of a temperature-dependent viscosity was also validated against experimental results from Kwant *et al*. (1973), as shown in Figure 4.7. Comparison shows a close agreement

between CFD and experiment with a mean difference well within ±3.0%. It should also be noted that in all simulations undertaken in this study, including steady flow and vibrated flow, the energy balance was verified to a very high degree of accuracy (±1.0%).

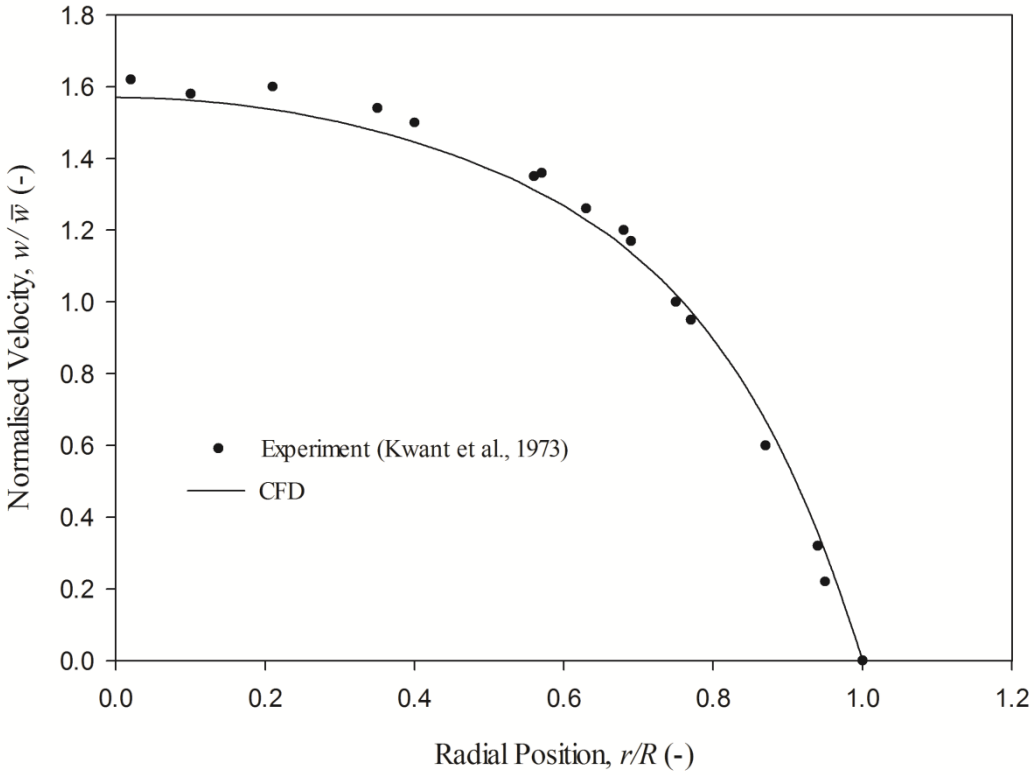

Figure 4.7. Comparison of CFD-predicted and experimental velocity profiles for a temperature-dependent Newtonian fluid in steady tube flow with heat transfer. T_{in} = 27 °C; T_w = 127 °C; D = 30 mm; $\overline{w}$ = 2.0 cm s^{-1}; μ = 1.3exp[(T – 25 °C)/(T_w – T_{in})] Pa s; ρ = 998 kg m^{-3}; C_p = 4180 J kg^{-1} K^{-1}; λ = 0.6 W m^{-1} K^{-1}.

4.4.3. Adiabatic isothermal flow in a straight tube with superimposed vibration

The modelling by CFD of adiabatic isothermal non-Newtonian flow under forced vibration was reported and experimentally validated in the previous studies (Deshpande and Barigou, 2001; Eesa and Barigou, 2008; Eesa, 2009). Comparison with experiment showed that CFD is able to predict such complex flows with a very good accuracy, within approximately ±10%, under a wide range of vibration conditions and for a variety of

rheological behaviours, namely power law, Herschel-Bulkley and Bingham plastic. There are, however, no experimental data available on the temperature profile in non-isothermal flows when subjected to vibration. Nonetheless, given the excellent agreement achieved between CFD and theory or experimental results in all the above stages of the validation process, it can be seen that the present CFD model is sufficiently robust and reliable for the purposes of studying the effects of vibration on the heat transfer characteristics of the flows considered here.

4.5. RESULTS AND DISCUSSION

Simulation results for the laminar flow with heat transfer of a Newtonian fluid with temperature-dependent viscosity through both heating and cooling tubes with an isothermal wall are discussed in the following sections for four cases: (*a*) steady flow through a straight tube (**SF**); (*b*) steady flow through a straight tube fitted with a Kenics static mixer (**SF-KM**); (*c*) flow through a straight tube subjected to transverse oscillations (**VF**); and (*d*) flow through a straight tube subjected to transverse oscillations with step rotation of vibration orientation (**VF-SR**). Additionally, the effects of time interval, vibration amplitude and frequency on heat transfer are studied as well in this chapter.

4.5.1. The effect of transverse vibration on heat transfer in a heating tube

4.5.1.1. Steady flow through a straight pipe

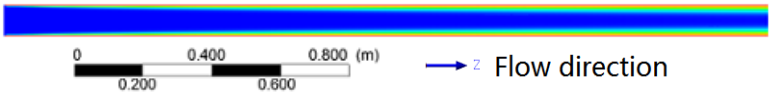

(*a*)

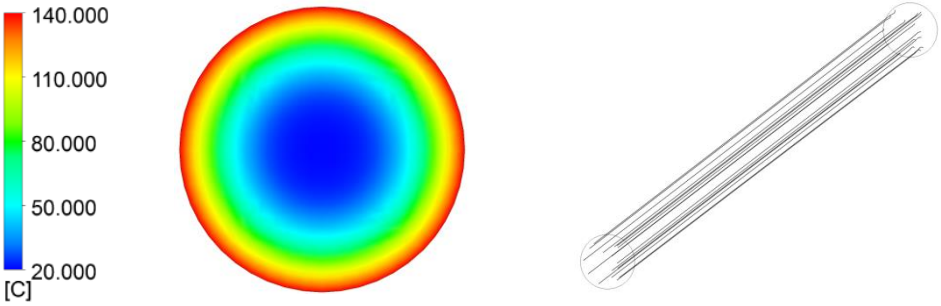

(*b*) (*c*)

Figure 4.8. **SF** in the heating tube: (*a*) temperature distribution along the tube; (*b*) temperature distribution at tube exit; (*c*) fluid streamlines.
T_{in} = 20 °C; T_w = 140 °C; $\mu = k_0 \exp(E_a / R_g T)$; $k_0 = 5.0 \times 10^{-7}$ Pa s.

Simulations of the steady tube flow of a Newtonian fluid with a temperature-dependent

viscosity confirmed the usual features of viscous flow, i.e. straight streamlines and a highly non-uniform radial temperature distribution, as shown in Figure 4.8. At the tube exit, there is a substantial cold fluid core which is at temperatures close to the inlet temperature surrounded by outer layers of hot fluid within a sharp temperature gradient. There is little improvement in temperature uniformity along the tube because of the lack of radial mixing and the reliance on slow thermal conduction for radial heat transfer. The coefficient of radial temperature variation at the tube exit cross-section defined in Eq. (4.8) is $C_{v\text{-}T} \sim 0.5$.

4.5.1.2. Steady flow through a straight pipe fitted with a Kenics static mixer

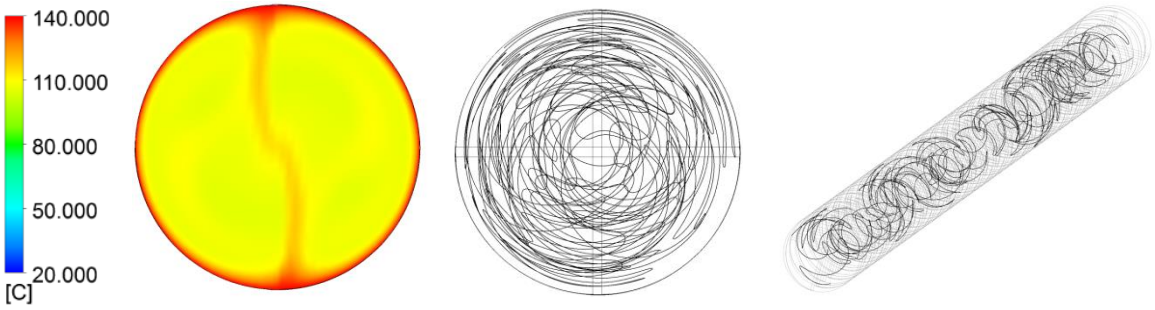

(*a*) (*b*)

Figure 4.9. **SF-KM** in the heating tube: (*a*) temperature distribution at tube exit; (*b*) fluid trajectories.

T_{in} = 20 °C; T_w = 140 °C; $\mu = k_0 \exp(E_a / R_g T)$; $k_0 = 5.0 \times 10^{-7}$ Pa s.

The Kenics static mixer is widely used in industry to promote radial fluid mixing in tubes, especially where flow is viscous, to improve heat transfer or chemical reactions (Hobbs and Muzzio, 1997; Rahmani *et al*., 2006). This popular static mixer was selected here as a reference for high quality mixing of viscous flow in a tube. As described in Section 4.3 above, simulations were conducted of the steady flow through the same straight tube fitted with 48 segments of the Kenics mixer (Figure 4.3). The flow pattern generated by this configuration is characterised by complex winding fluid streamlines, as shown in Figure 4.9, and the resulting temperature contour is fairly uniform across the tube exit section. The static mixer achieves a coefficient of radial temperature variation at the tube exit of ~

0.0483 which is a vast improvement on **SF** ($C_{v\text{-}T}$ ~ 0.73). The mean fluid temperature increases from 20 °C at the tube inlet to ~ 61 °C at the exit in **SF**, but it increases to ~ 108 °C in **SF-KM**. This substantial improvement in the heating of the fluid was caused by a large enhancement in the mean wall heat transfer coefficient, *h*, a factor of 3 approximately. However, this enhancement in heat transfer comes at the expense of a large pressure drop, an increase of approximately 8 folds.

4.5.1.3. Flow through a straight pipe subjected to transverse oscillations

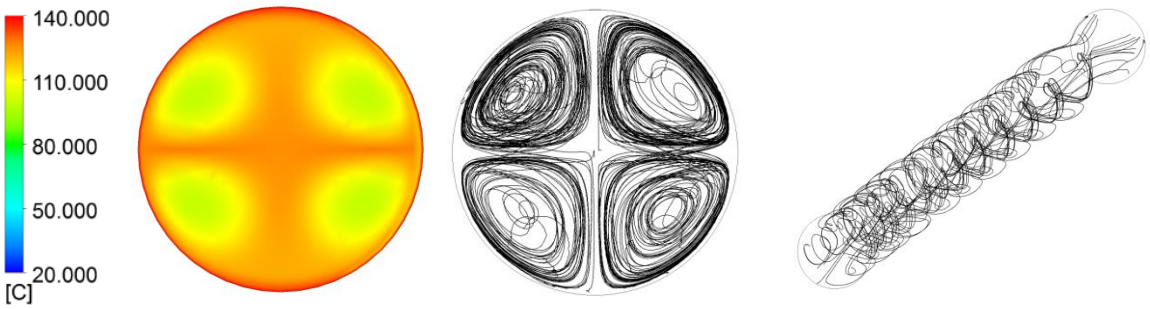

(*a*) (*b*)

Figure 4.10. **VF** in the heating tube: (*a*) temperature distribution at tube exit; (*b*) fluid trajectories.

T_{in} = 20 °C; T_w = 140 °C; $\mu = k_0 \exp(E_a / R_g T)$; $k_0 = 5.0 \times 10^{-7}$ Pa s; A = 2 mm; f = 50 Hz.

Simulations of flow in the same straight tube but with superimposed oscillations in the transverse direction revealed a very different flow pattern. Vibration induces a swirling or spiralling motion in the fluid as clearly represented by the complex fluid trajectories depicted in Figure 4.10(*b*). Such a flow pattern is characterised by significant vortical structures which cause considerable radial mixing, thus, leading to a much more uniform temperature distribution, as shown in Figure 4.10(*a*). Thus, the coefficient of radial temperature variation, improved from $C_{v\text{-}T}$ ~ 0.73 for **SF** to ~ 0.083 for **VF**. The mean fluid temperature increased from 20 °C at the inlet of the straight tube to ~ 61 °C at the exit when flow was steady, but it increased to ~ 117 °C when flow was vibrated. This

considerable improvement in the heating of the fluid was caused by a large enhancement in the mean wall heat transfer coefficient, a factor of 4 approximately.

4.5.1.3.1. Effect of vibration frequency and amplitude

Simulations with different vibration amplitude of 1 mm and frequency of 25 Hz were executed as well. Radial temperature profiles for three vibration configurations (i.e. (*a*) A = 1 mm & f = 50 Hz; (*b*) A = 2 mm & f = 25 Hz; (*c*) A = 2 mm & f = 50 Hz) are depicted in Figure 4.11. The mean fluid temperature at the tube exit decreases to ~ 110 °C as the vibration frequency reduces to 25 Hz from 50 Hz, whilst drops to ~ 104 °C as the vibration amplitude decreases to 1 mm from 2 mm. In other words, these vibrational effects depend on both the vibration amplitude and frequency but are more sensitive to the amplitude than the frequency of wall oscillations, at least within the range of vibration amplitudes and frequencies used in this study. The comparison between these three vibration configurations is summarised in Table 4.4.

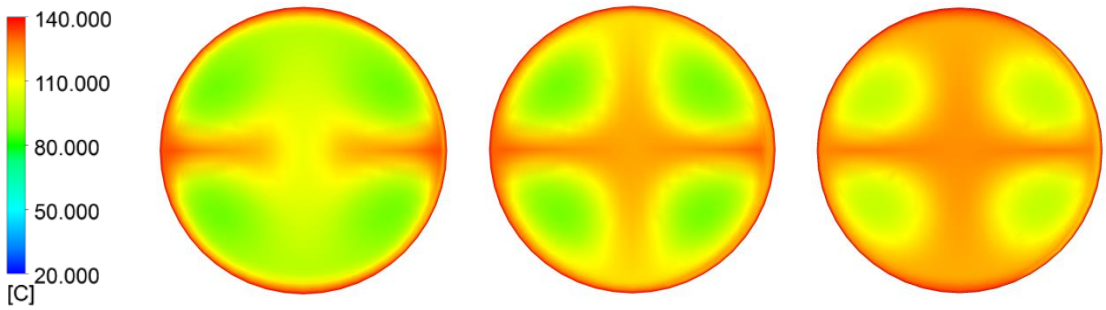

Figure 4.11. Effects of vibration amplitude and frequency on temperature distribution in oscillated heating tube:
(*a*) A = 1 mm & f = 50 Hz; (*b*) A = 2 mm & f = 25 Hz; (*c*) A = 2 mm & f = 50 Hz.
T_{in} = 20 °C; T_w = 140 °C; $\mu = k_0 \exp(E_a / R_g T)$; $k_0 = 5.0 \times 10^{-7}$ Pa s.

Table 4.4. Effects of vibration amplitude and frequency in the heating tube (T_w =140 °C).

Vibration amplitude A (mm)	1	2	2
Vibration frequency f (Hz)	50	25	50
Mean temperature at tube exit $\bar{T}_{out}$ (°C)	103.7	109.9	116.8
Coefficient of radial temperature variation at tube exit $C_{v\text{-}T}$ (-)	0.124	0.132	0.0833
Mean wall heat transfer coefficient h (W m^{-2} K^{-1})	623.5	721.2	856.9
Pressure drop Δp (Pa)	270.0	268.0	267.5

Whilst the imposition of transverse oscillations gives a substantial improvement in heat transfer compared with **SF**, and despite the considerable improvement in radial mixing, the degree of mixing averaged across the tube section ($C_{v\text{-}T}$ ~ 0.083 for A = 2 mm & f = 50 Hz) is still short of the level achieved by the **SF-KM** ($C_{v\text{-}T}$ ~ 0.048), albeit the pressure drop caused by the latter system is a factor of ~ 5.6 higher.

The vibrated flow is characterised by four salient symmetrical regions of relatively colder fluid being trapped in swirling flow inside clearly delineated vortices located in the four quadrants of the tube cross-section, as shown in Figure 4.12, which hamper fluid mixing. The local temperature in the centre of these vortex regions is ~ 99 °C compared to ~ 128 °C

in the centre of the tube. Whilst the results reported in our previous study on heat transfer enhancement through vibration are in agreement with present findings, it should be noted that these relatively cold vortex regions were not clearly apparent in previous analysis (Eesa and Barigou, 2010; 2011). However, it has been possible to identify them here because of the superior quality of the hexahedral mesh used in the present simulations compared with the tetrahedral mesh used previously. Hexahedral meshes are known to achieve a higher solution accuracy than tetrahedral meshes for the same cell amount, and provide the best resolution of the boundary layer close to walls with significantly fewer cells. Hexahedral elements also reduce numerical diffusion, aid convergence, and have important computing cost and stability advantages over tetrahedral elements (see for example, Biswas and Strawn, 1998; Tadepalli *et al*., 2011).

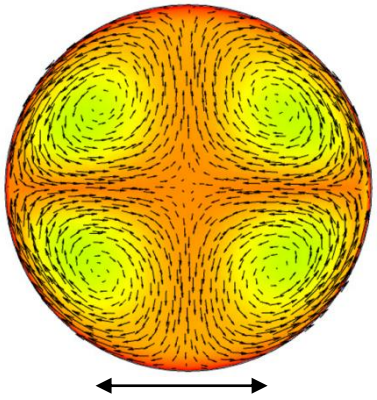

Figure 4.12. Velocity vector plot superimposed on temperature distribution across the oscillated heating tube.

T_{in} = 20 °C; T_w = 140 °C; $\mu = k_0 \exp(E_a / R_g T)$; $k_0 = 5.0 \times 10^{-7}$ Pa s; A = 2 mm; f = 50 Hz.

The velocity field in a plane normal to the direction of flow is depicted in Figure 4.12. The velocity vector plot shows how hot fluid is forced by the transverse oscillations to flow inwards from the wall and recirculate around the vortex regions before returning to the wall. Therefore, better fluid mixing is needed in these regions for optimal heat transfer and temperature uniformity. To improve on this situation, a fresh technique was presented to rotate the orientation of transverse oscillation in a stepwise manner by an angle of

45-degrees (**VF-SR**), as described in Section 4.2.2 and illustrated in Figure 4.1(*d*), in order to force the centres of the four cold regions to move around and, hence, enable the relatively cold fluid in these regions to better mix with hotter fluid flowing inwards from the wall.

4.5.1.4. Flow through a straight pipe subjected to transverse oscillations with a superimposed step rotation of vibration orientation

This regime of flow creates much more intense radial fluid mixing, as demonstrated by the fluid trajectories shown in Figure 4.13(*b*). As a result, the cold vortex regions have disappeared from the temperature contour plot and a much improved temperature distribution is obtained, as depicted in Figure 4.13(*a*).

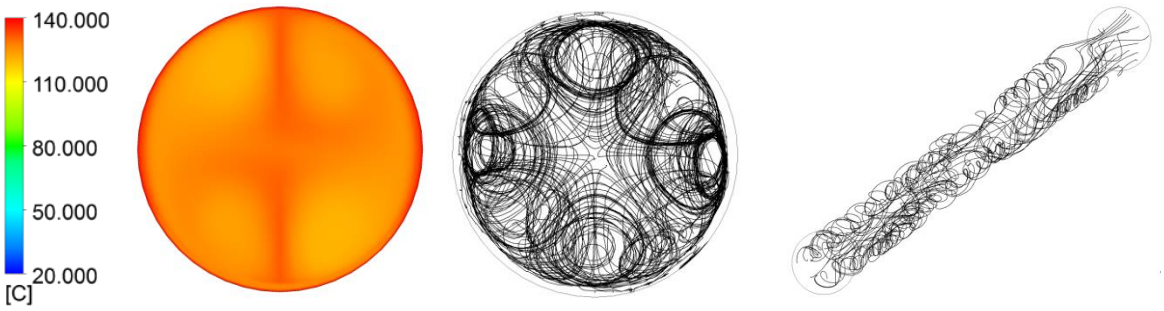

(*a*) (*b*)

Figure 4.13. **VF-SR** in the heating tube: (*a*) temperature distribution at tube exit; (*b*) fluid trajectories.

T_{in} = 20 °C; T_w = 140 °C; $\mu = k_0 \exp(E_a / R_g T)$; $k_0 = 5.0 \times 10^{-7}$ Pa s; A = 2 mm; f = 50 Hz; Ω = 0.1 Hz.

This radial flow also can be indicated from the comparison of the mean resultant velocity in the radial plane in the heating tube, as shown in Figure 4.14, $\bar{u}_{xy}$, is ~ 0 for **SF**, ~ 2.1 cm s^{-1} for **SF-KM**, and ~ 1.0 cm s^{-1} for **VF** and 1.1 cm s^{-1} **VF-SR**. Even though $\bar{u}_{xy}$ is larger for the Kenics mixer, the secondary flow is dominated by fluid body rotation which is not as effective for radial mixing as the flow generated by the wall oscillations, which

can be clearly illustrated by the temperature comparison at tube exit (Figure 4.14).

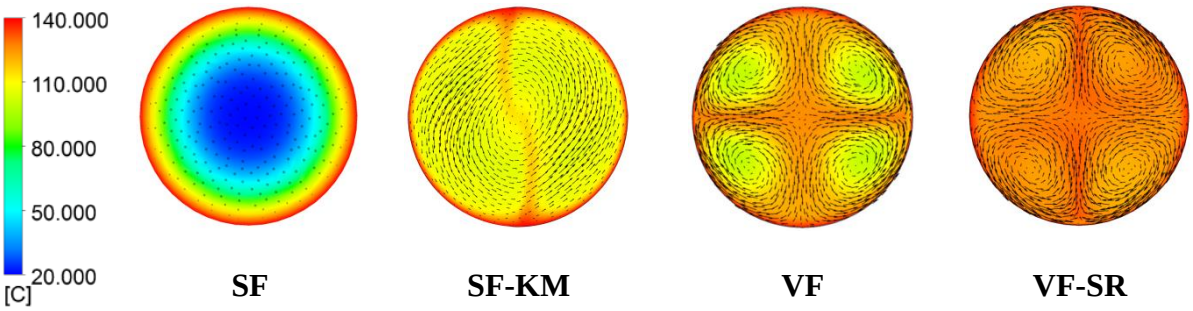

($\bar{u}_{xy}$ = ~ 0 mm s^{-1}) ($\bar{u}_{xy}$ = ~ 20 mm s^{-1}) ($\bar{u}_{xy}$ = ~ 10 mm s^{-1}) ($\bar{u}_{xy}$ = ~ 11 mm s^{-1})

Figure 4.14. Radial temperature and velocity vector distributions at the exit sections of heating tube.

T_{in} = 20 °C; T_w = 140 °C; $\mu = k_0 \exp(E_a / R_g T)$; $k_0 = 5.0 \times 10^{-7}$ Pa s; A = 2 mm; f = 50 Hz; Ω = 0.1 Hz.

A comparison is drawn in Table 4.5 between the four regimes of flow studied, i.e. simple steady tube flow (**SF**), steady flow with a Kenics static mixer (**SF-KM**), vibrated flow (**VF**), and vibrated flow with a superimposed step rotation of orientation (**VF-SR**). **VF** exhibits huge improvements in heat transfer characteristics compared with **SF**. For example, the uniformity of the temperature distribution is vastly improved and the heat transfer coefficient h is enhanced by ~ 5 folds. With respect to **VF**, **VF-SR** brings about considerable improvements in these parameters; for example, $C_{v\text{-}T}$ reduces from ~ 0.08 down to ~ 0.02. Even when compared with **SF-KM** $C_{v\text{-}T}$ shows a significant improvement from ~ 0.048 to ~ 0.02, whilst the pressure drop incurred in the tube fitted with the static mixer is much greater, ~ 6.2 times. It is worth noting that when using static mixers, $C_{v\text{-}T}$ ~ 0.05 is generally accepted in the literature as a target level for good fluid mixing (Reed *et al*., 2002). This corroborates the conclusion that transverse vibration with step changes in orientation provides an elegant non-invasive technique for enhancing radial fluid mixing and heat transfer.

Table 4.5. Comparison of the four different flow regimes studied in the heating tubes (T_w =140 °C).

	SF	**SF-KM**	**VF**	**VF-SR**
Mean temperature at exit $\bar{T}_{out}$ (°C)	61.3	108.1	116.8	126.5
Coefficient of radial temperature variation $C_{v\text{-}T}$ (-)	0.727	0.0483	0.0833	0.0234
Mean wall heat transfer coefficient h (W m^{-2} K^{-1})	219.9	690.9	856.9	1139.3
Pressure drop Δp (Pa)	195.0	1500.7	267.5	244.0

The effects of vibration on the development of the thermal boundary layer are depicted in Figure 4.15. In steady flow, the azimuthally-averaged axial temperature profile shows little change over the whole tube length as the thermal boundary layer develops extremely slowly. With the Kenics mixer fitted, the situation improves considerably. Under **VF-SR**, however, the thermal entrance length (< ~ 0.9 m) is dramatically reduced by an order of magnitude compared to the steady state (> ~ 11 m), with **VF-SR** being clearly superior to **VF**. This shows that the full effects of the oscillations are felt in the early stages of the flow and, consequently, the tube length required for a given thermal process could be greatly reduced.

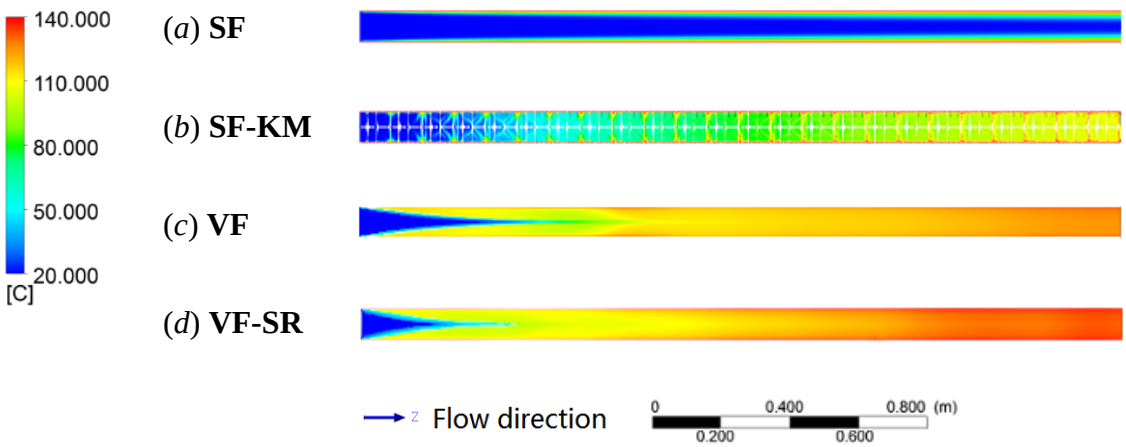

Figure 4.15. Development of azimuthally-averaged temperature profile along the axis in the heating tube.

T_{in} = 20 °C; T_w = 140 °C; $\mu = k_0 \exp(E_a / R_g T)$; $k_0 = 5.0 \times 10^{-7}$ Pa s; A = 2 mm; f = 50 Hz; Ω = 0.1 Hz.

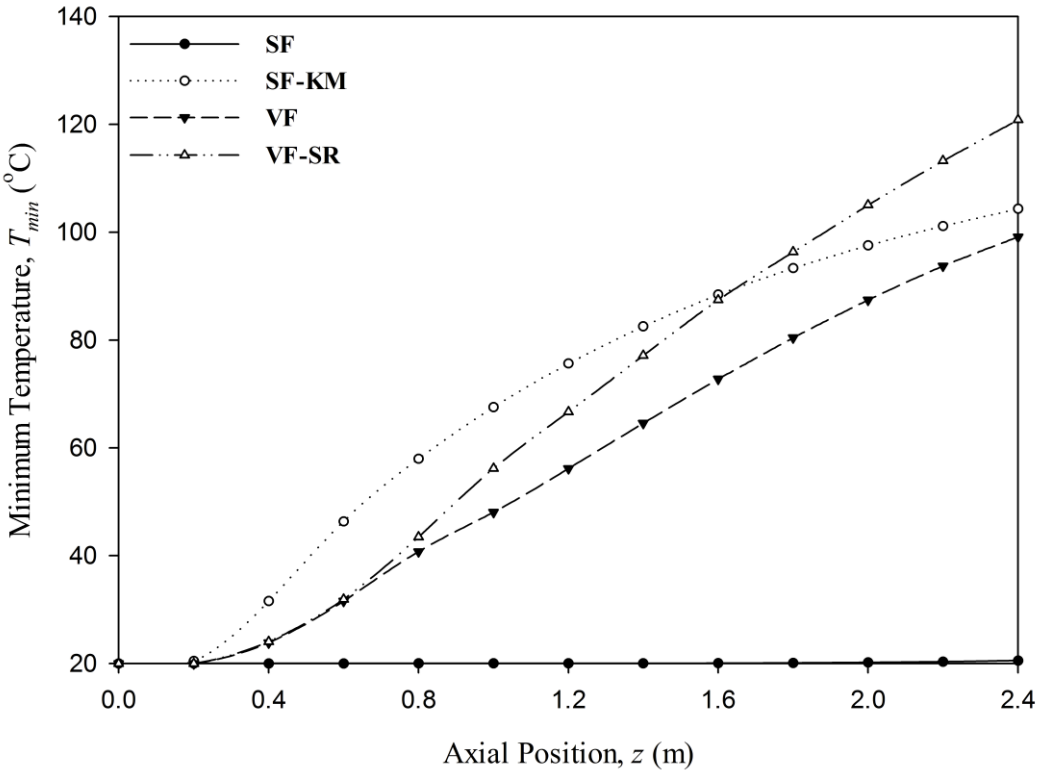

Figure 4.16. Minimum temperature development along the axis in the heating tube.

T_{in} = 20 °C; T_w = 140 °C; $\mu = k_0 \exp(E_a / R_g T)$; $k_0 = 5.0 \times 10^{-7}$ Pa s; A = 2 mm; f = 50 Hz; Ω = 0.1 Hz.

The vibrational effect on the heat transfer can also be graphically illustrated in the form of minimum temperature and mean temperature variations as a function of axial position in Figure 4.16 and Figure 4.17 separately. Although at the beginning, **SF-KM** leads the fastest development of minimum temperature among these four flow configurations, **VF-SR** surpasses the other flow regimes by a wide margin at the tube exit in the respects of both minimum temperature and volume-flow weighted mean temperature.

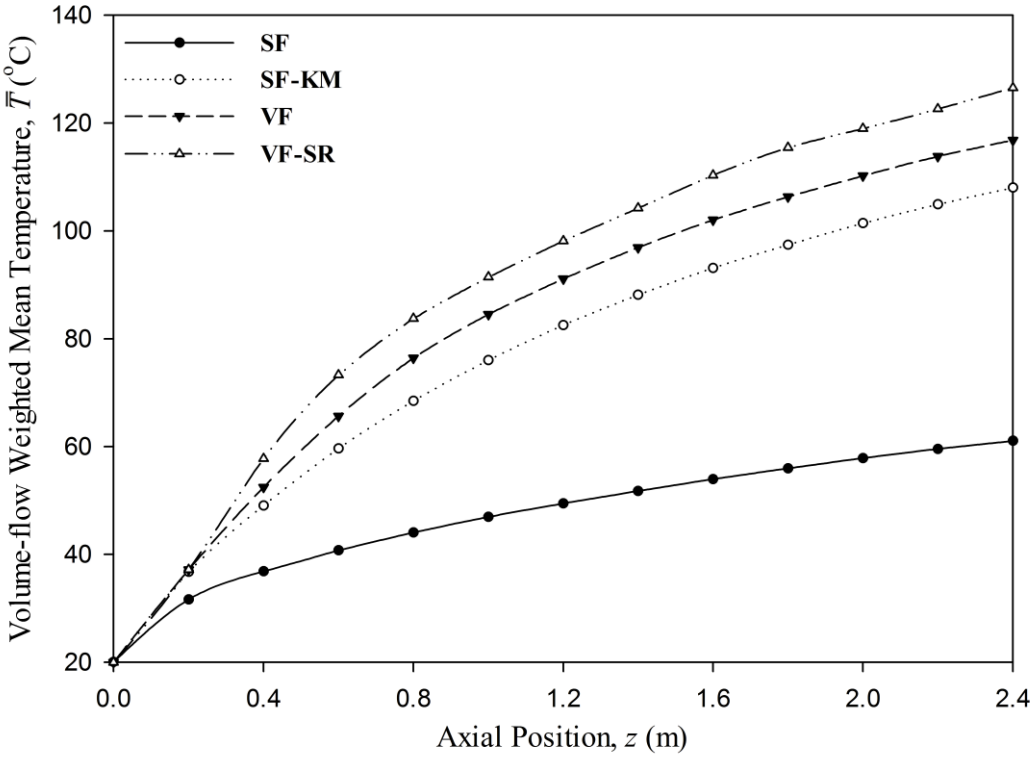

Figure 4.17. Mean temperature development along the axis in the heating tube. T_{in} = 20 °C; T_w = 140 °C; $\mu = k_0 \exp(E_a / R_g T)$; $k_0 = 5.0 \times 10^{-7}$ Pa s; A = 2 mm; f = 50 Hz; Ω = 0.1 Hz.

To put the above results in context, in order to obtain the same mean temperature achieved by **VF-SR** at the exit of the 2.4 m tube used here, the length of tubes would have to be, approximately, 26 m in **SF**, 3.2 m compared with **VF**, and 4 m with **SF-KM**.

4.5.1.4.1. Effect of frequency of step rotation of vibration orientation

The effect of varying the frequency, Ω, of **VF-SR** was investigated and radial temperature profile results are displayed in Figure 4.18. It turns out that the value of this frequency is quite significant in achieving the highest mean temperature at the tube exit, the best temperature uniformity across radius, and the best wall heat transfer coefficient whilst Δp is more or less unchanged (Table 4.6). As discussed above, efficient radial fluid mixing is achieved through transverse vibration by forcing the hot liquid to continuously flow from the wall to the centre of the tube, mix with fluid in the cold regions, before returning to the wall. Out of the frequency values which were tested for the flow conditions investigated, the best temperature uniformity (and correspondingly the best temperature development along the tube) corresponded to $\Omega = 0.1$ Hz (i.e. a time interval between rotation steps of $\Delta t = 10$ s). The value of this optimum step rotation frequency is expected to depend on process conditions, however.

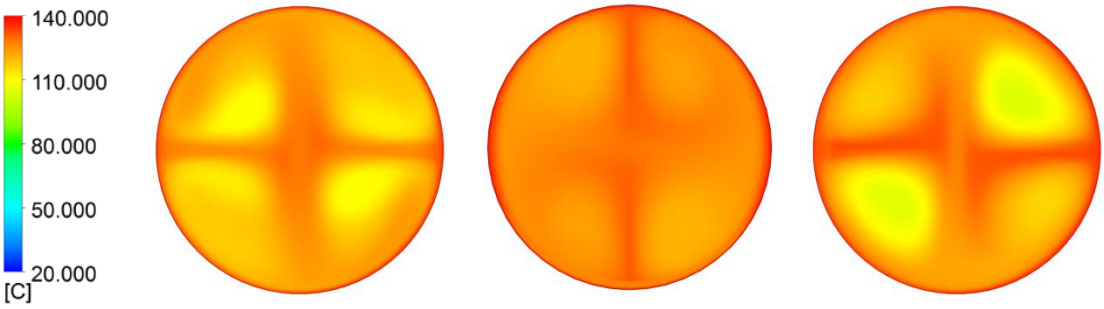

Figure 4.18. Effect of frequency of step rotation of vibration orientation on temperature distribution at tube exit of **VF-SR** in the heating tube: (*a*) Ω = 0.2 Hz; (*b*) Ω = 0.1 Hz; (*c*) Ω = 0.067 Hz.

T_{in} = 20 °C; T_w = 140 °C; $\mu = k_0 \exp(E_a / R_g T)$; $k_0 = 5.0 \times 10^{-7}$ Pa s; A = 2 mm; f = 50 Hz.

As shown in Figure 4.19, with higher frequencies (e.g. Ω = 0.2 Hz; Δt = 5 s; distance travelled z = 0.2 m) the hot fluid does not get to reach the tube centre, thus, there is insufficient mixing of the hot fluid flowing inwards from the wall with cold fluid conveyed

in the cold vortex regions before recirculating back; whilst with lower frequencies (e.g. Ω = 0.067 Hz; Δt = 15 s; distance travelled z = 0.6 m) the cold vortex regions are moved around too slowly for optimum heat transfer to take place from the hot fluid flowing inwards from the wall; thus, the temperature gradient between cold and hot fluid is not as high as it could be for efficient heat transfer. In this case, a rotation frequency of 0.1 Hz (i.e. Δt = 10 s; distance travelled z = 0.4 m) gives the best condition for radial mixing and heat transfer.

Table 4.6. Effect of step rotation frequency of vibration orientation in the heating tube (T_w = 140 °C).

Step rotation frequency Ω (Hz)	0.2	0.1	0.067
Mean temperature at tube exit $\bar{T}_{out}$ (°C)	121.1	126.5	121.3
Coefficient of radial temperature variation at tube exit $C_{v\text{-}T}$ (-)	0.054	0.0234	0.074
Mean wall heat transfer coefficient h (W m^{-2} K^{-1})	963.82	1139.3	969.37
Pressure drop Δp (Pa)	241.2	244.0	228.5

Simulations for a higher wall temperature of 180 °C gave similar results under all conditions of flow investigated, respectively; however, because of the large temperature gradient across the tube radius, to achieve a degree of temperature uniformity similar to that attained in the 140 °C case required a slightly longer tube (~ 2.6 m).

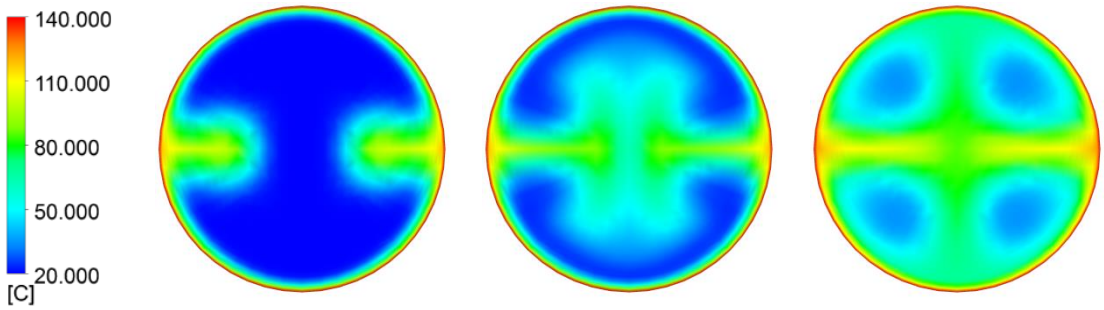

(*a*) (*b*) (*c*)

Figure 4.19. Effect of step rotation frequency of vibration orientation on radial flow and temperature distribution in the heating tube: (*a*) Ω = 0.2 Hz (Δ*t* = 5 s; *z* = 0.2 m); (*b*) Ω = 0.1 Hz (Δ*t* = 10 s; *z* = 0.4 m); (*c*) Ω = 0.067 Hz (Δ*t* = 15 s; *z* = 0.6 m).
T_{in} = 20 °C; T_w = 140 °C; $\mu = k_0 \exp(E_a / R_g T)$; $k_0 = 5.0 \times 10^{-7}$ Pa s; *A* = 2 mm; *f* = 50 Hz.

4.5.1.5. Effect of viscosity

However, whilst the value of inlet fluid viscosity used throughout the study (0.868 Pa s) is high enough to be representative of a wide range of food materials, the effects of fluid viscosity were studied using an-order-of magnitude higher value at inlet (10 Pa s). Radial temperature and velocity vector distributions at the exit sections corresponding to this higher viscosity are presented in Figure 4.20. The heat treatment in the **SF** and **SF-KM** flows is not affected by viscosity as the same degree of radial uniformity and the same mean exit temperature are achieved in each case. As viscosity is increased from 0.868 to 10 Pa s, the mean exit temperature in the **VF** technique reduces slightly by 1.3 °C, but temperature uniformity improves significantly ($C_{v\text{-}T}$ reduces from 0.083 to 0.050) as viscosity increases. At the same time, the mean exit temperature achieved with **VF-SR** drops significantly from 126.5 to 118.3 °C, and radial temperature uniformity deteriorates as $C_{v\text{-}T}$ increases from 0.0234 to 0.0471. However, even at 10 Pa s, **VF-SR** still outperforms the other three flow configurations, especially **SF** and **SF-KM** where the differential improvement is substantial. For this high viscosity, Ω was reduced from 0.1 to 0.08 Hz. As viscosity increases, the radial flow slows down and to achieve better results, Ω has to be reduced down to an optimum value which would enable maximum mixing of the cold vortex regions and give the best exit temperature and temperature uniformity.

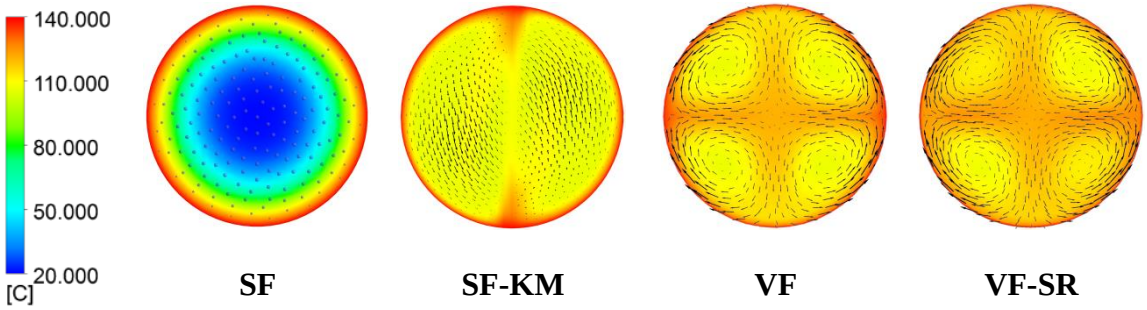

Figure 4.20. Radial temperautre and velocity vector distributions at the exit sections of heating tube.

T_{in} = 20 °C; T_w = 140 °C; $\mu = k_0 \exp(E_a / R_g T)$; $k_0 = 5.75 \times 10^{-6}$ Pa s; A = 2 mm; f = 50 Hz; Ω = 0.08 Hz.

Table 4.7. Comparison of the four different flow regimes studies in the heating tubes (T_w = 140 °C).

	SF	SF-KM	VF	VF-SR
Mean temperature at exit $\bar{T}_{out}$ (°C)	61.20	108.46	115.51	118.32
Coefficient of radial temperature variation $C_{v\text{-}T}$ (-)	0.729	0.04811	0.05005	0.04715
Mean wall heat transfer coefficient h (W m^{-2} K^{-1})	219.2467	696.7865	828.7103	887.00
Pressure drop Δp (Pa)	2156.67	16867.9	2779.81	2659.04

However, reducing Ω beyond this optimum value (e.g. in this case around 0.08 Hz for 10 Pa s) would reduce the quality of heat treatment as the benefits of the superimposed step rotation are gradually lost and **VF-SR** tends to **VF**. In this case, Ω = 0.05 Hz yielded the same results for **VF-SR** as for **VF**. The comparison between these four configurations has been summarised in Table 4.7.

4.5.2. The effect of transverse vibration on heat transfer in a cooling tube

4.5.2.1. Steady flow through a straight pipe

Steady viscous flow in a cooling tube showed opposite radial temperature profile comparing to the viscous flow in the heating tube, i.e. hot core region in the tube centre which temperature is close to the inlet condition, and cold outer layers near the tube wall, as indicated in Figure 4.21(*b*). As shown in Figure 4.21(*c*), the streamlines are straight, which is the same as that in the heating tube, indicating the poor radial mixing in this simple steady flow. The coefficient of radial temperature variation at the tube exit cross-section is $C_{v\text{-}T} \sim 1.2$.

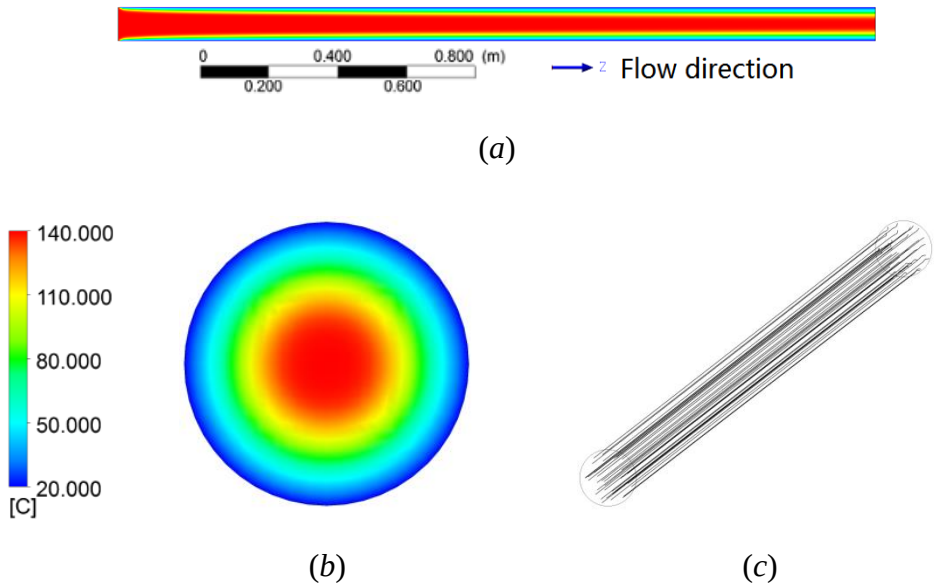

Figure 4.21. **SF** in the cooling tube: (*a*) temperature distribution along the tube; (*b*) temperature distribution at tube exit; (*c*) fluid streamlines.
T_{in} = 140 °C; T_w = 20 °C; $\mu = k_0 \exp(E_a / R_g T)$; $k_0 = 5.0 \times 10^{-7}$ Pa s.

4.5.2.2. Steady flow through a straight pipe fitted with a Kenics static mixer

Similarly as it is in heating stage, Kenics static mixer agitates complex winding fluid motion, as shown in Figure 4.22(*b*), and leads to temperature distribution which is fairly uniform across the tube exit section, as indicated in Figure 4.22(*a*). The static mixer achieves a coefficient of radial temperature variation at the tube exit of ~ 0.10, which is vastly improved from **SF** ($C_{v\text{-}T}$ ~ 1.2). The mean fluid temperature decreases from 140 ℃ at the tube inlet to ~ 119 ℃ at the exit in **SF**, however decreases to ~ 86 ℃ in **SF-KM**. The wall heat transfer coefficient, *h*, improves by a factor of over 3, but with a larger energy expense, indicated in terms of pressure drop, as approximate 3 folds.

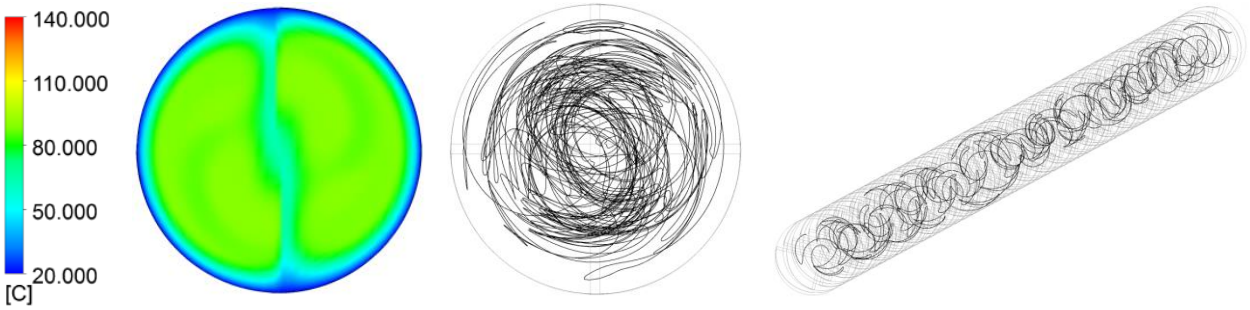

(*a*) (*b*)

Figure 4.22. **SF-KM** in the cooling tube: (*a*) temperature distribution at tube exit; (*b*) fluid trajectories.

T_{in} = 140 °C; T_w = 20 °C; $\mu = k_0 \exp(E_a / R_g T)$; $k_0 = 5.0 \times 10^{-7}$ Pa s.

4.5.2.3. Flow through a straight pipe subjected to transverse oscillations

Simulations of flow showed that vibration, in cooling tube as it in heating tube, induces a swirling motion in the fluid which is indicated by the fluid trajectories in Figure 4.23(*b*). Such intense radial mixing contributes to a much more uniform temperature distribution across the tube exit section, as depicted in Figure 4.23(*a*). Thus, the coefficient of radial temperature variation, improved from $C_{v\text{-}T}$ ~ 1.2 for **SF** to ~ 0.027 for **VF**. The mean fluid temperature decreased from 140 °C at the inlet of the straight tube to ~ 119.4 °C at the exit when flow was steady, but it decreased to ~ 38.9 °C when flow was vibrated. This

considerable improvement in the cooling of the fluid was resulted by a large enhancement in the mean wall heat transfer coefficient, a factor of 10 approximately.

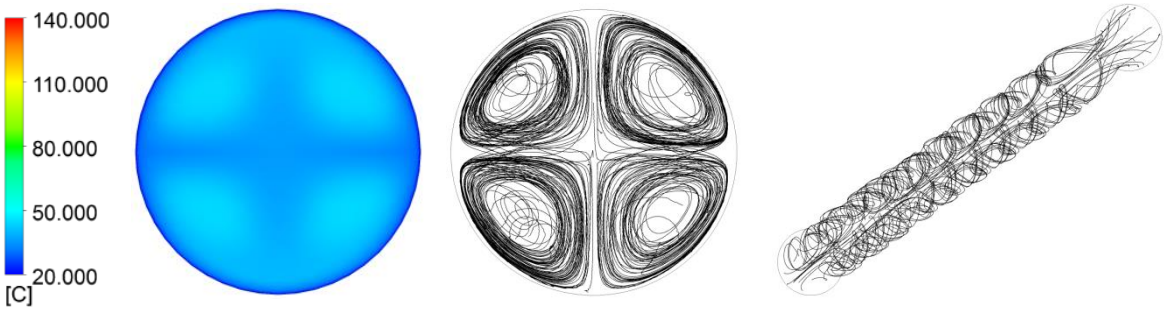

(*a*) (*b*)

Figure 4.23. **VF** in the cooling tube: (*a*) temperature distribution at tube exit; (*b*) fluid trajectories.

T_{in} = 140 °C; T_w = 20 °C; $\mu = k_0 \exp(E_a / R_g T)$; $k_0 = 5.0 \times 10^{-7}$ Pa s; A = 2 mm; f = 50 Hz.

4.5.2.3.1. Effect of vibration frequency and amplitude

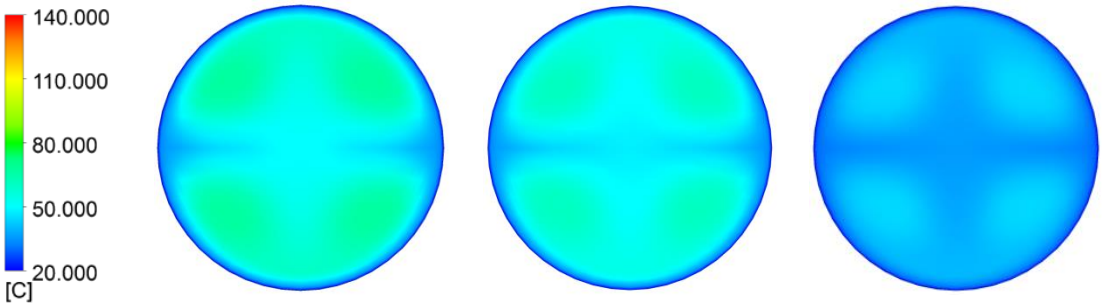

(*a*) (*b*) (*c*)

Figure 4.24. Effects of vibration amplitude and frequency on temperature distribution in oscillated cooling tube:

(*a*) A = 1 mm & f = 50 Hz; (*b*) A = 2 mm & f = 25 Hz; (*c*) A = 2 mm & f = 50 Hz.

T_{in} = 140 °C; T_w = 20 °C; $\mu = k_0 \exp(E_a / R_g T)$; $k_0 = 5.0 \times 10^{-7}$ Pa s.

Simulations with different vibration amplitude of 1 mm and frequency of 25 Hz were executed as well. Radial temperature profiles for three vibration configurations (i.e. (*a*) A = 1 mm & f = 50 Hz; (*b*) A = 2 mm & f = 25 Hz; (*c*) A = 2 mm & f = 50 Hz) were depicted in Figure 4.24. Numerical results show that the mean temperature at tube exit is 53.02 °C for f = 25 Hz & A = 2 mm, and 56.62 °C for A = 1 mm & f = 50 Hz, comparing to 38.94 °C for f = 50 Hz & A = 2 mm. Decrease in either vibration frequency or amplitude lead to a reduction in the effectiveness of vibration. It also can be concluded that these vibrational effects depend on both the vibration amplitude and frequency but are more sensitive to the amplitude than the frequency of wall oscillations in the cooling tube, which is accordance as the conclusion in the heating tube. The comparison between these three vibration configurations is summarized in Table 4.8.

Table 4.8. Effects of vibration amplitude and frequency in the cooling tube (T_w = 20 °C).

Vibration amplitude A (mm)	1	2	2
Vibration frequency f (Hz)	50	25	50
Mean temperature at tube exit $\overline{T}_{out}$ (°C)	56.62	53.02	38.94
Coefficient of radial temperature variation at tube exit $C_{v\text{-}T}$ (-)	0.081	0.063	0.027
Mean wall heat transfer coefficient h (W m^{-2} K^{-1})	618.91	672.87	962.72
Pressure drop Δp (Pa)	327.17	367.14	577.42

4.5.2.4. Flow through a straight pipe subjected to transverse oscillations with a superimposed step rotation of vibration orientation

Albeit, in the cooling tube, the temperature variation in **VF** is not as significant as that in the heating tube, **VF-SR** still gives improvement as its intense radial fluid mixing, as depicted in Figure 4.25.

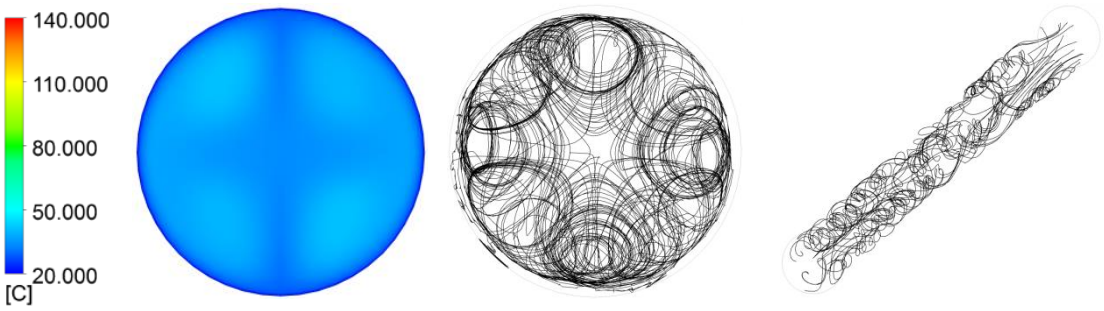

(*a*) (*b*)

Figure 4.25. **VF-SR** in the cooling tube: (*a*) temperature distribution at tube exit; (*b*) fluid trajectories.

T_{in} = 140 °C; T_w = 20 °C; $\mu = k_0 \exp(E_a / R_g T)$; $k_0 = 5.0 \times 10^{-7}$ Pa s; A = 2 mm; f = 50 Hz; Ω = 0.1 Hz.

Again, as in the heating tube, the comparison of the mean resultant velocity in the radial plan in the cooling tube was graphically shown in Figure 4.26, $\bar{u}_{xy}$, is ~ 0 mm s^{-1} for **SF**, ~ 17 mm s^{-1} for **SF-KM**, and ~ 8 mm s^{-1} for **VF** and **VF-SR**. Even though $\bar{u}_{xy}$ is larger for the Kenics mixer, the secondary flow is dominated by fluid body rotation which is not as effective for radial mixing as the flow generated by the wall oscillations, which can be clearly illustrated by the temperature comparison at the tube exit (Figure 4.26). This effect can also be indicated by the comparison in these parameters: for example, h increases by a factor of 10, respect with **SF**. Even when compared with **SF-KM**, **VF-SR** shows a large improvement, ~3 times. All the comparisons between these four regimes have been given in Table 4.9.

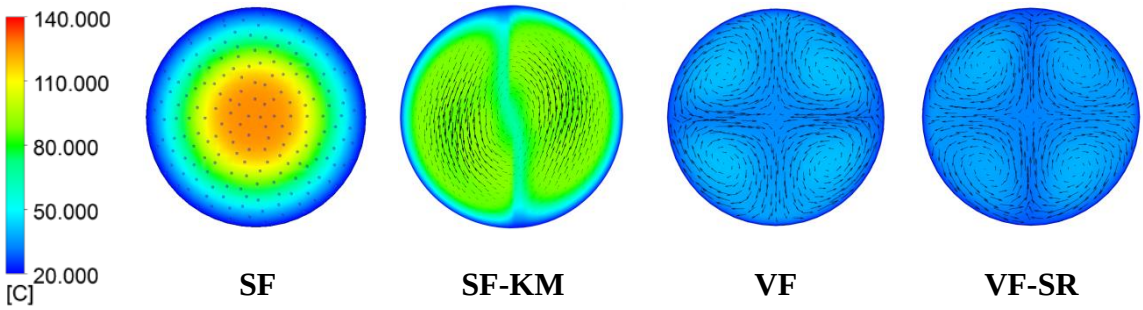

Figure 4.26. Radial temperature and velocity vector distributions at the exit sections of cooling tube.

T_{in} = 140 °C; T_w = 20 °C; $\mu = k_0 \exp(E_a / R_g T)$; $k_0 = 5.0 \times 10^{-7}$ Pa s; A = 2 mm; f = 50 Hz; Ω = 0.1 Hz.

Table 4.9. Comparison of the four different flow regimes studied in the cooling tubes (T_w = 20 °C).

	SF	**SF-KM**	**VF**	**VF-SR**
Mean temperature at exit $\bar{T}_{out}$ (°C)	119.40	86.18	38.94	36.15
Coefficient of radial temperature variation $C_{v\text{-}T}$ (-)	1.20	0.10	0.027	0.021
Mean wall heat transfer coefficient h (W m^{-2} K^{-1})	98.21	310.32	963.72	1045.82
Pressure drop Δp (Pa)	264.62	786.58	577.65	656.52

The vibrational effects in the axial direction are depicted in Figure 4.27. In steady flow, the azimuthally-averaged axial temperature profile shows little change over the whole tube length as the lack of radial mixing. With the Kenics mixer fitted, the situation improves considerably. However under transverse vibration, it can be observed that for both **VF** and **VF-SR**, after ~ 0.5 m, the azimuthally-averaged temperature dropped below 80 °C, which is superior to the mean temperature achieved at the exit of 2.4 m tube by **SF-KM** ($\overline{T}_{out}$ = ~ 86 °C). Consequently, the tube length required for a given cooling target could be greatly reduced by the implementation of transverse vibration.

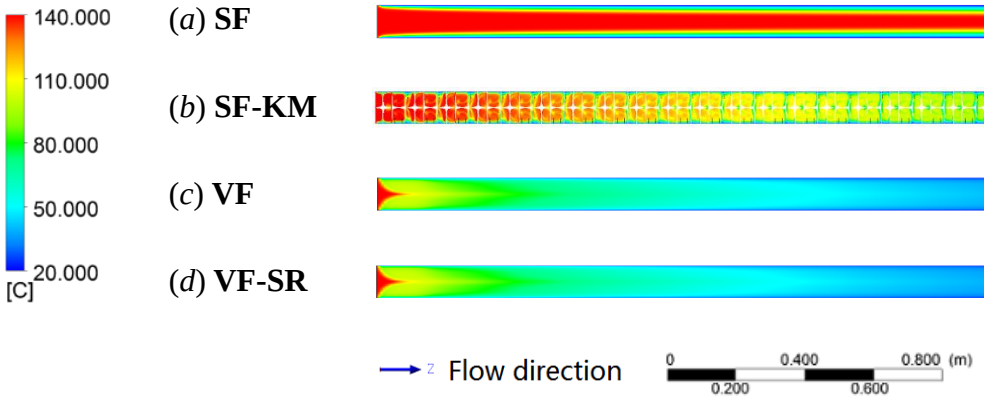

Figure 4.27. Development of azimuthally-averaged temperature profile along the axis in the cooling tube.

T_{in} = 140 °C; T_w = 20 °C; $\mu = k_0 \exp(E_a / R_g T)$; $k_0 = 5.0 \times 10^{-7}$ Pa s; A = 2 mm; f = 50 Hz; Ω = 0.1 Hz.

Mean temperature variations as a function of axial position are graphically indicated in Figure 4.28. Throughout the whole tube, transverse vibration contributes the fastest cooling, and both **VF** and **VF-SR** surpass the other two flow regimes (i.e. **SF** and **SF-KM**) by a wide margin at the tube exit in the respect of volume-flow weighted mean temperature.

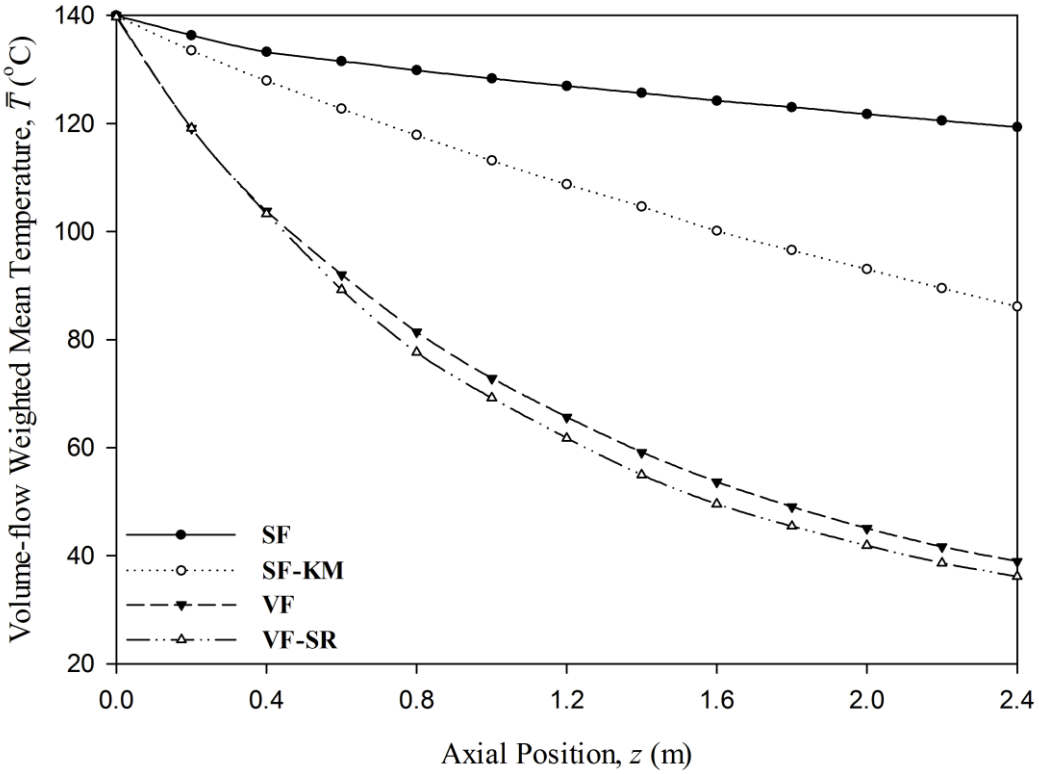

Figure 4.28. Mean temperature development along the axis in the cooling tube. T_{in} = 140 °C; T_w = 20 °C; $\mu = k_0 \exp(E_a / R_g T)$; $k_0 = 5.0 \times 10^{-7}$ Pa s; A = 2 mm; f = 50 Hz; Ω = 0.1 Hz.

It is worth to note that, by the comparison in the cooling tube, **VF-SR** did not show the same significant advantage over **VF** as it did in the heating tube. It can be explained from two aspects: (i) the utilization of step rotation leads to lower temperature of flow, which results in additional viscosity comparing to **VF**, therefore weakening on the efficacy of rotation. This is a completely opposite of process in the heating tube. (ii) the result above is based on a step rotation frequency of 0.1 Hz, which is selected for the consistency with that in the heating tube. However, as stated in Section 4.5.1.4.1, the vibrational effects are function of the step rotational frequency which is expected to depend on the process conditions. In other words, frequency of 0.1 Hz contributes best performance in mixing, amongst the values (i.e. 0.05 Hz, 0.1 Hz and 0.2 Hz) investigated in the study in the heating tube. But in cooling tube, Ω is required to be re-optimised as the change of process conditions, which necessitates the study on the frequency of step

rotation, Ω.

4.5.2.4.1. Effect of frequency of step rotation of vibration orientation

The effect of frequency of step rotation of oscillation orientation of **VF-SR**, Ω, was investigated and radial temperature profile results are displayed in Figure 4.29. It turns out that the value of this frequency is quite significant in achieving the best temperature uniformity across radius, but, mean temperature, or mean wall heat transfer coefficient, whilst Δp is more or less unchanged (Table 4.10). Out of the frequency values which were tested for the flow conditions investigated, the best temperature uniformity (and correspondingly the best temperature decay along the tube) corresponded to $\Omega = 0.2$ Hz (i.e. a time interval between rotation steps of $\Delta t = 5$ s). The value of this optimum step rotation frequency is expected to depend on process conditions, however, and should be worked out by a small amount of trial and error, as stated in Section 4.5.1.4.1.

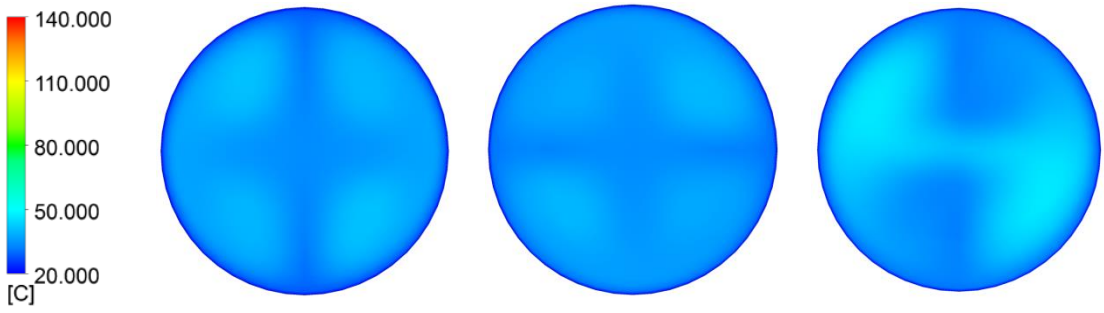

Figure 4.29. Effects of frequency of step rotation of vibration orientation on temperature distribution at tube exit of **VF-SR** in the cooling tube:

(*a*) Ω = 0.1 Hz; (*b*) Ω = 0.2 Hz; (*c*) Ω = 0.5 Hz.

T_{in} = 140 °C; T_w = 20 °C; $\mu = k_0 \exp(E_a / R_g T)$; $k_0 = 5.0 \times 10^{-7}$ Pa s; A = 2 mm; f = 50 Hz.

Simulations for a lower wall temperature of 5 °C gave similar results under all conditions of flow investigated, respectively; however, because of the large temperature gradient

across the tube radius, to achieve a degree of temperature uniformity similar to that attained in the 20 °C case required a slightly longer tube (~ 2.5 m).

Table 4.10. Effect of frequency of step rotation of vibration orientation in the cooling tube (T_w = 20 °C).

Step rotation frequency Ω (Hz)	0.1	0.2	0.5
Mean temperature at tube exit $\bar{T}_{out}$ (°C)	36.15	35.59	38.21
Coefficient of radial temperature variation at tube exit $C_{v\text{-}T}$ (-)	0.021	0.018	0.040
Mean wall heat transfer coefficient h (W m^{-2} K^{-1})	1045.82	1064.22	983.21
Pressure drop Δp (Pa)	656.52	686.05	619.25

4.5.2.5. Effect of viscosity

Viscosity of ~ 2 Pa s at temperature of 20 °C was employed to investigate the effect of viscosity in the cooling tube. Figure 4.30 indicates temperature fields at tube exit for these four flow configurations. It can be observed that the superiority of **VF-SR** and **VF** is still significant with the increased viscosity, including fastest cooling on the mean temperature, good uniformity in the temperature distribution, and modest pressure cost. However, the efficacy of **VF** and **VF-SR** in cooling is weakening as viscosity increases, whilst **SF** is unaffected. Comparisons between these four configurations (i.e. **SF**, **SF-KM**, **VF** and **VF-SR**) with a more viscous fluid have been summarised in Table 4.11.

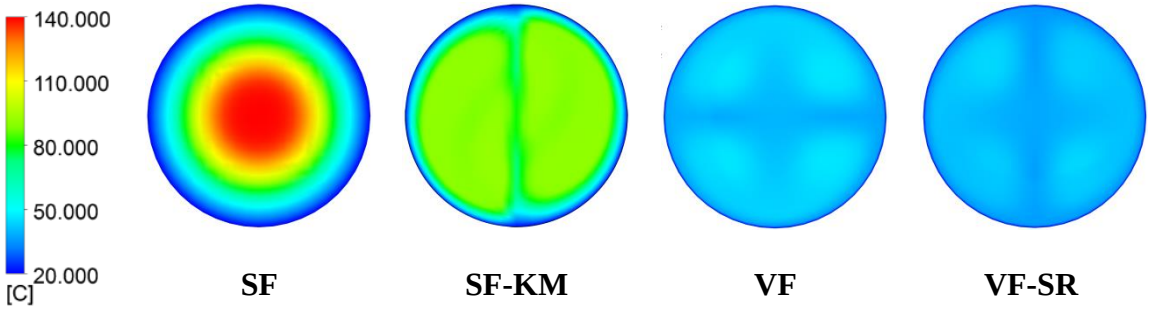

Figure 4.30. Radial temperature distributions at the exit sections of cooling tube. T_{in} = 140 °C; T_w = 20 °C; $\mu = k_0 \exp(E_a / R_g T)$; $k_0 = 1.2 \times 10^{-6}$ Pa s; A = 2 mm; f = 50 Hz; Ω = 0.1 Hz.

Table 4.11. Comparison of the four different flow regimes studied in the cooling tubes (T_w = 20 °C).

	SF	**SF-KM**	**VF**	**VF-SR**
Mean temperature at exit $\bar{T}_{out}$ (°C)	119.41	88.30	42.17	39.95
Coefficient of radial temperature variation $C_{v\text{-}T}$ (-)	1.20	0.112	0.025	0.0214
Mean wall heat transfer coefficient h (W m^{-2} K^{-1})	33.26	293.88	880.61	935.63
Pressure drop Δp (Pa)	625.779	1646.41	1259.03	1385.15

4.6. MECHANICAL ENERGY CONSUMPTION THROUGH VIBRATION

The mechanism of superimposing a step rotation of oscillation orientation on the vibrated flow should be easy to implement in practice and should provide an elegant technological solution for enhancing heat transfer operations in viscous flows, as discussed above. The technique excels in comparison with the Kenics helical mixer which suffers from its unsuitability for hygienic processes, as well as the relatively high energy losses caused by the large pressure drops it engenders.

To complete the evaluation of the vibration process, we estimate the mechanical energy involved in implementing the mechanical oscillations. The mathematical derivation is given in Appendix 4.A. The estimation for the flow case discussed above indicates that the power required to run the vibration process is rather modest (~ 130 W), and the benefits in terms of temperature uniformity and enhanced heat transfer should far outweigh this additional cost.

4.7. CONCLUSIONS

Forced transverse vibration superimposed on the steady laminar flow of a fluid in a tube with an isothermal wall generates a vigorous swirling fluid motion represented by a strong vorticity field and complex spiralling fluid streamlines and trajectories. The method has been shown to have substantial benefits for heat transfer including a large (several folds) increase in wall heat transfer, a much more uniform radial temperature profile, a rapid development of the temperature profile along the tube, rapid heating of the core region of the flow, and relatively short processing tubes.

A new enhanced technique has been introduced in this work which combines transverse vibration with a step rotation of oscillation orientation. This technique produces much more improved effects compared to transverse vibration alone, resulting in much shorter processing tubes. It also excels in comparison with the well-known Kenics helical static mixer which has the disadvantages of being unsuitable for hygienic fluid processing and causes large pressure drops. On the other hand, the mechanical power input associated with the vibration process is modest.

APPENDIX 4.A – MECHANICAL ENERGY CONSUMPTION THROUGH VIBRATION

From Eq. (4.2) which describes the tube wall displacement, the acceleration can be obtained as:

$$\dot{u}_x = \frac{\mathrm{d}u_x}{\mathrm{d}t} = \frac{\mathrm{d}^2 x}{\mathrm{d}t^2} = -A\omega^2 \sin(\omega t) \tag{4.A.1}$$

The vibration force is given by Newton's second law of motion, thus:

$$F = m \times \dot{u}_x = -m \times A\omega^2 \sin(\omega t) \tag{4.A.2}$$

where m is the mass of the tube full of fluid. The elemental work developed across the infinitesimal displacement dx is given by:

$$\mathrm{d}W = F \times \mathrm{d}x$$

$$\mathrm{d}W = -m \times A\omega^2 \sin(\omega t) \times A\omega \cos(\omega t) \times \mathrm{d}t \tag{4.A.3}$$

So through a whole oscillation cycle, ignoring any energy losses due to friction or imperfect transmission, the total work is obtained from:

$$W = \int_0^{\frac{1}{f}} -mA^2\omega^3 \sin(\omega t)\cos(\omega t)\mathrm{d}t \tag{4.A.4}$$

$$W = \int_0^{\frac{1}{4f}} -mA^2\omega^3 \sin(\omega t)\cos(\omega t)\mathrm{d}t + \int_{\frac{1}{4f}}^{\frac{2}{4f}} -mA^2\omega^3 \sin(\omega t)\cos(\omega t)\mathrm{d}t$$
$$\int_{\frac{2}{4f}}^{\frac{3}{4f}} -mA^2\omega^3 \sin(\omega t)\cos(\omega t)\mathrm{d}t + \int_{\frac{3}{4f}}^{\frac{1}{f}} -mA^2\omega^3 \sin(\omega t)\cos(\omega t)\mathrm{d}t$$

The total algebraic work given by the above expression through a complete vibration cycle amounts to zero as the 2nd integral negates the 1st integral, and the 4th integral negates the 3rd integral. Note that the 2nd and 4th integrals represent work dissipated during the deceleration parts of the cycle. Therefore, the net work input in one cycle is given by the sum of the 1st and 3rd integrals, thus:

$$W = -mA^2\omega^3 \tag{4.A.5}$$

Assuming, for example, a tube wall thickness of 2.5 mm, a stainless steel density of 8000 kg m^{-3}, and using the values of the various other parameters introduced for the flow case set out above, the power consumption turns out to be rather modest:

$$\mathcal{P} = f \times mA^2\omega^3 \approx 130\,\mathrm{W} \tag{4.A.6}$$

NOTATION

A	Vibration amplitude, m
C_p	Specific heat capacity, J kg^{-1} K^{-1}
E_a	Activation energy for viscosity, J mol^{-1}
f	Vibration frequency, Hz
h	mean wall heat transfer coefficient, W m^{-2} K^{-1}
k_0	Pre-exponential factor, Pa s
p	Pressure, Pa
Δp	Pressure drop, Pa
r	Radial position, m
R	Radius of pipe, m
R_g	Gas constant, J mol^{-1} K^{-1}
t	Time, s
Δt	Time interval, s
T	Temperature, °C
$\overline{T}$	Volume-flowrate weighted mean temperature, °C
T_{in}	Inlet temperature, °C
$\overline{T}_{out}$	Volume-flowrate averaged temperature at the pipe exit, °C
T_w	Wall temperature, °C
u_x	Pipe velocity in radial direction, m s^{-1}
w	Fluid velocity in axial direction, m s^{-1}
$\overline{w}$	Mean fluid axial velocity at inlet, m s^{-1}
x	Wall displacement, m
z	Axial position, m

Greek symbols

μ Temperature-dependent viscosity of Newtonian fluid, Pa s

ρ Density, kg m^{-3}

λ Thermal conductivity, W m^{-1} K^{-1}

θ_T Dimensionless temperature, -

θ Azimuthal position, rad or deg

ω Angular function of frequency of vibration, rad s^{-1}

Ω Frequency of step rotation of vibration orientation, Hz

REFERENCES

Biswas, R., Strawn, R. C., 1998. Tetrahedral and hexahedral mesh adaptation for CFD problems. Applied Numerical Mathematics, 26(1), 135-151.

Chhabra, R. P., Richardson, J. F., 1999. *Non-Newtonian flow in the process industries: Fundamentals and engineering applications*. Butterworth Heinemann, Oxford.

Deshpande, N. S., Barigou, M., 2001. Vibrational flow of non-Newtonian fluids. Chemical Engineering Science, 56(12), 3845-3853.

Eesa, M., Barigou, M., 2008. CFD analysis of viscous non-Newtonian flow under the influence of a superimposed rotational vibration. Computers & Fluids, 37(1), 24-34.

Eesa, M., 2009. CFD studies of complex fluid flows in pipes. Ph.D. thesis. University of Birmingham, Birmingham, UK.

Eesa, M., Barigou, M., 2010. Enhancing radial temperature uniformity and boundary layer development in viscous Newtonian and non-Newtonian flow by transverse oscillations: A CFD study. Chemical Engineering Science, 65(6), 2199-2212.

Eesa, M., Barigou, M., 2011. CFD simulation of transverse vibration effects on radial temperature profile and thermal entrance length in laminar flow. AIChE Journal, 57(1), 51-56.

Gundogdu, M. Y., & Carpinlioglu, M. O., 1999. Present state of art on pulsatile flow theory - (Part 1: Laminar and transitional flow regimes). JSME International Journal Series B-Fluids and Thermal Engineering, 42(3), 384-397.

Hobbs, D. M., Muzzio, F. J., 1997. The Kenics static mixer: a three-dimensional chaotic flow. Chemical Engineering Journal, 67(3), 153-166.

Jakob, M., 1949. *Heat transfer*. Wiley, New York.

Jung, A., & Fryer, P. J., 1999. Optimising the quality of safe food: Computational modelling of a continuous sterilisation process. Chemical Engineering Science, 54(6),

717-730.

Kwant, P. B., Fierens, R. H. E., Vanderle. A., 1973. Non-isothermal laminar pipe flow - II. Experimental. Chemical Engineering Science, 28(6), 1317-1330.

Lyche, B. C., Bird, R. B., 1956. The Graetz-Nusselt problem for a power law non-Newtonian fluid. Chemical Engineering Science, 6(1), 35-41.

Rahmani, R. K., Keith, T. G., Ayasoufi, A., 2006. Numerical study of the heat transfer rate in a helical static mixer. Journal of Heat Transfer, 128(8), 769.

Reed, G. F., Lynn, F., Meade, B. D., 2002. Use of coefficient of variation in assessing variability of quantitative assays. Clinical and Diagnostic Laboratory Immunology, 9(6), 1235-1239.

Saatdjian, E., Rodrigo, A. J. S., Mota, J. P. B., 2012. On Chaotic Advection in a Static Mixer. Chemical Engineering Journal, 187, 289- 298.

Shrirao, P. N., Sambhe, R. U., Bodade, P. R., 2013. Convective Heat Transfer Analysis in a Circular Tube with Different Types of Internal Threads of Constant Pitch. International Journal of Engineering and Advanced Technology, 2(3), 335-340.

Sinnott, R. K., 2005. *Chemical Engineering Design: Chemical Engineering*. Elsevier Science, Oxford.

Steffe, J. F., 1996. *Rheological methods in food process engineering*. 2nd Edition. Freeman Press, East Lansing, Michigan.

Tadepalli, S. C., Erdemir, A., Cavanagh, P. R., 2011. Comparison of hexahedral and tetrahedral elements in finite element analysis of the foot and footwear. Journal of Biomechanics, 44(12), 2337-2343.

CHAPTER 5.
OPTIMISING THE CONTINUOUS HEAT-HOLD-COOL STERILISATION PROCESS THROUGH CHAOTIC ADVECTION

Summary

Continuous food sterilisation is required to achieve the desired level of sterility with minimum loss of quality. In a conventional process, the food product flows steadily through a heat-hold-cool system, but the processing of fluids in viscous flow poses a serious challenge as radial heat transfer is controlled by thermal conduction which leads to a wide radial temperature distribution and slow heating of the core region of the flow. This results in a wide variation of product sterility and nutritional quality across the tube, with much of the product having to be over-processed to ensure sterility throughout, thus, often violating the high temperature for short time (HTST) processing assumption. Inline static mixers, inserts or vortex generators can be used to promote radial fluid mixing, heat transfer and temperature uniformity, but they tend to generate large pressure drops and are generally prohibited in hygienic processes. Chaotic advection has been proved potential in promoting fluid mixing and enhancing radial heat transfer. In this chapter, with the help of massless particle tracking function in CFX, the technique of mechanical transverse vibration was applied in continuous food sterilisation process. Results show that the vibrated process leads to fast nearly-uniform heating and cooling, thus, achieving much higher levels of sterility and product quality in much shorter processing tubes, and obviating the need for a holding stage.

5.1. INTRODUCTION

Cooking is a critical step in most food manufacturing processes. Thermal processing brings about irreversible changes in food textural and sensory properties, whilst at the same time achieving the desired level of microbial sterility. It is not possible nor is it necessary to eliminate all viable organisms from the material. Organoleptic and nutritive properties of foods are adversely affected by heat, and the process must only be as severe as necessary to ensure commercial sterility. Spore reduction and nutrient loss are governed by different kinetics, the rates of which are dictated by the processing conditions. A food that is optimally cooked would be safe but would also have sensory and nutritious properties that are most acceptable to the consumer. The optimisation of such thermal treatments poses a challenging manufacturing problem (Barigou *et al.*, 1998). The overriding importance of food safety often results in the food being exposed to a more severe process than is desirable from a quality aspect, resulting in lower sensory and nutritional attributes, especially with sensitive products, than is actually possible.

In continuous aseptic processing, a food mixture passes continuously through a heat-hold-cool system, and is then packaged in pre-sterilized containers (Holdsworth, 1992; David *et al*., 2012). The food is heated to the required temperature in the heating stage, is then held at such a temperature in an insulated tube for long enough to ensure that the required level of sterility has been attained, and is then cooled to typically ambient temperature. Most foodstuffs tend to be viscous (e.g., soups, sauces) and in general flow occurs in the laminar regime. In a tubular heat exchanger, radial laminar heat transfer is governed essentially by slow thermal conduction which leads to a wide radial temperature distribution that poses a serious challenge in such manufacturing processes. In continuous food sterilisation, the non-uniform velocity profile which characterises viscous flow coupled with a non-uniform temperature distribution means that the coldest parts of the fluid at the centre of the tube travel the fastest, thus, resulting in a wide variation of product sterility and nutritional quality across the tube. The output conditions will be a mixture of fluid at different radial positions. The challenge is to be able to sterilise the fastest parts in the core region of the tube without over-processing too

much the slowest parts near the wall. Increasing the temperature of the inner regions of the fluid is highly desirable so that ideally all parts of the fluid receive equal thermal treatment. Furthermore, better uniformity in the temperature profile helps reduce local variations in the fluid rheological properties which cause distortions in the velocity profile, thus making the flow behaviour of the fluid more predictable. Another aspect that should be considered in the design of such processes is the contribution of the cooling stage to product sterilisation. The product leaving the holding tube will cool at a finite rate and some reaction leading to microbial lethality must occur. Conservative approaches tend to ignore this contribution. An optimal process design should take into account all contributions to lethality from the heating, holding and cooling stages (Barigou *et al.*, 1998).

To evaluate sterility level, analysis of Baetson (1971) is followed in this chapter. If an initial number of organisms is assumed as N_0, and N is the number at time of t, then, $N = N_0 e^{-kt}$, where k is the reaction rate. The reduction time can be calculated as:

$$t = \frac{\ln 10}{k} \log_{10}(N_0/N) = \frac{2.3026}{k} \log_{10}(N_0/N) \tag{5.1}$$

If the number of organisms is reduced by a factor of 10 (i.e. $N_0 = 10N$), manipulation of Eq. (5.1) gives:

$$t = \frac{2.3026}{k} = D_T \tag{5.2}$$

where D_T is the decimal reduction time at temperature T. Besides temperature, D_T depends on the micro-organism and pH value (Fryer, 1997). The variations of D_T at different temperature can be incorporated via a variable of z, whose value is equal to the slope of the logarithm of the ratio of decimal reduction times at different temperatures,

verse the difference of the temperature, and in mathematical form, as:

$$D_{T1} = D_{T2} 10^{(T_1 - T_2)/z} \tag{5.3}$$

where T_1 and T_2 are different temperatures. In practice, for convenience and efficiency, decimal reduction times at varying temperatures are always compared to a process at some given reference temperatures, i.e. T_{Fref}. The heating time at reference temperature, which is required for a given thermal treatment (i.e. reduction in the micro-organism) is defined as the sterility value, F (or F-value). For example, for a treatment at constant temperature of T, a relation between F and t can be developed from Eqs. (5.1) and (5.3):

$$F = \frac{D_{TFref}}{D_T} t = t 10^{(T_{Fref} - T)/z_F} \tag{5.4}$$

It should be noted that Eq. (5.4) for the F-value, was originally derived for a static batch system and applies to materials where all the food has the same temperature-time profile (Ball and Olson, 1957; Jung and Fryer, 1999; Hui, 2006). In a continuous flow, different fluid elements have different thermal histories and are subjected to different levels of microbial lethality. Therefore, the equation which is for a process with varying temperature, $T(t)$ can be developed by using concept of integrating :

$$F = \int_0^t 10^{\left(T - T_{Fref}\right)/z_F} \mathrm{d}t \tag{5.5}$$

Eq. (5.5) is the most often used mathematical model for accessing sterility level (Holdsworth, 1985) and was originally developed by Ball and Olson (1957).

Product quality loss is estimated using the cook value, *C*, also known as the C-value, a parameter defined in a similar way to the F-value, which gives a measure of the extent of nutrient loss in units of time (Holdsworth, 1992):

$$C = \int_0^t 10^{\left(T - T_{Cref}\right)/z_C} \mathrm{d}t \tag{5.6}$$

where T_{Cref} is a reference temperature dependent on the nutrient under consideration, and z_C is the temperature change which produces a 10-fold change in reaction rate from the rate at the reference temperature.

The microbiological lethality delivered to the product and the extent to which product quality is preserved is a function of the residence time of the product in the sterilisation process as well as the temperatures to which it is exposed. This must be taken into account when designing a continuous heat preservation process. To calculate the length of the process, conservative design rules usually assume that all of the fluid flows at twice the mean velocity (i.e. the maximum centreline velocity in Newtonian flow) to ensure complete product sterility. Whilst, this ensures sterility, such an assumption results in poor sensory and nutritional attributes, especially with sensitive products. A good process design should aim at achieving a narrow residence time distribution and coupling safety assurance with quality optimisation, so that the process delivers the necessary microbial lethality to the slowest heating zones of the flow whilst not over-processing any significant amounts of the product.

To improve the uniformity of the temperature distribution, methods of increasing radial mixing are required. This problem has been recognised for a long time but effective technological solutions are still missing. Radial mixing can be achieved by turbulent flow conditions but the usually high fluid viscosities encountered in practice make this proposition often impractical and/or uneconomical. Various ways have been proposed in the engineering literature to improve heat convection by using Dean vortex generators

(Chagny *et al.*, 2000) or adding internal screw-thread structures on the wall to disrupt the boundary layer (Shrirao *et al*., 2013), but such technological solutions are limited by their manufacturing complexity, cost, their high proneness to fouling and clogging, and the difficulty to keep them clean. Similarly, inserts or inline static mixers are used to promote radial fluid mixing and a number of designs exist (Hobbs and Muzzio, 1997; Saatdjian *et al.*, 2012). In viscous flow, such devices can achieve a high degree of fluid mixing but usually at the expense of a high pressure drop. However, these inserts too are generally prohibited in hygienic processes because of the risk of contamination as their complex geometries also promote fouling and make them difficult to clean. A number of studies have also demonstrated the effects of pulsating flow on the heat flux and Nusselt number in tubes (Gundogdu and Carpinlioglu, 1999). However, its efficacy in achieving a uniform radial temperature distribution in viscous fluids has not been reported.

In Chapter 4, it has been reported that a novel technique of combining transverse mechanical oscillations with a stepwise angular change of oscillation orientation was developed to generate a strong oscillatory-perturbed or chaotic flow in the heating and cooling tubes, which achieves a high degree of radial fluid mixing, thermal boundary layer development, temperature uniformity and heat transfer in viscous tube flow (Tian and Barigou, 2015). In this chapter, a validated Computational Fluid Dynamics (CFD) model is employed to demonstrate the large positive effects that such a technique can have on the thermal processing of a viscous fluid in a continuous sterilisation process. The performance of the technique is compared to traditional heat-hold-cool processing with and without the use of an inline Kenics static mixer, one of the best in this category of mixers.

5.2. CFD MODEL

5.2.1. Fluid viscosity model and transverse oscillation

The detailed study on the fluid viscosity has been presented in Section 4.5.1.5 and Section 4.5.2.5, from which it can be concluded that the technique of **VF-SR** still works well with more viscous fluid. Therefore, one viscosity model is sufficient for demonstrating the application of transverse vibration in continuous heat-hold-cool food processing. The fluid model used here is given in Eq. (4.1) (i.e. $\mu = k_0 \exp(E_\alpha / R_g T)$) and all the fluid parameters used in this chapter are summarised in Table 5.1.

Table 5.1. Rheological parameters used in simulations.

k_0	E_a	R_g	ρ	C_p	λ	$\mu = k_0 \exp(E_\alpha / R_g T)$ (Pa s)	
(Pa s)	(J mol^{-1})	(J mol^{-1} K^{-1})	(kg m^{-3})	(J kg^{-1} K^{-1})	(W m^{-1} K^{-1})	20 °C	140 °C
5.0×10^{-7}	35000	8.314	998	4180	0.668	0.868	0.0134

The transverse oscillation technique used in this chapter, including the basic form (**VF**) and the novel enhanced form (**VF-SR**), has been introduced in Section 4.2.2.

5.2.2. Governing equations

The governing transport equations involve the mass, momentum and energy balance equations (Eqs. (4.5) — (4.7)).

5.2.3. In-flow sterility and quality

In a continuous flow such as the one considered here, food sterility and quality levels are calculated by respectively integrating Eqs. (5.5) and (5.6) along a given fluid trajectory whose thermal history is described by $T(t)$ profile to give the local value of in-flow sterility at any given point in the flow within the computational grid, as introduced in

Section 5.1. In order to ensure the safety of product, one of the most heat-resistant pathogenic spores, *C. botulinum* is used in this work. Here, the reference temperatures used for both sterility and quality values are 121.1 °C. z_F = 10 °C for *C. botulinum* (Jung and Fryer, 1999; Stumbo *et al.*, 1950) and z_C = 48 °C for thiamine denaturation (Mulley *et al.*, 1975).

5.2.4. Uniformity of radial distribution of in-flow sterility and quality

The coefficient of variation, C_v, is used as a measure of sterility and quality uniformity across the tube and is usually defined as the ratio of the standard deviation, σ_F or σ_C, to the volume-flowrate weighted mean value, $\overline{F}$ or $\overline{C}$. However, it should be noted that when the mean value is small, such a definition can lead to artificially high values of C_v. To avoid such erroneous values, we use a modified coefficient of variation, such that for F:

$$C_{v-F} = \frac{\sigma_F}{\left|\overline{F} - \overline{F}_{ideal}\right|} \tag{5.7}$$

where $\overline{F}_{ideal}$ is the volume-flowrate weighted mean value achieved at a given axial position z of an ideal plug flow having the same inlet conditions of mean velocity and temperature as the actual laminar flow.

The volume-flowrate weighted mean sterility across the tube, $\overline{F}$, is obtained in a similar way to the mean temperature $\overline{T}$ which is defined in Section 4.2.4. The volume-flowrate weighted mean sterility is, therefore, given by:

$$\overline{F} = \frac{1}{Q}\sum_{i=1}^{N} F(r,\theta)w(r,\theta)S(r,\theta) \tag{5.8}$$

In the limit as $S(r,\theta) \to 0$, i.e. for large N, the uniformity of the sterility distribution over the tube cross-section can be well described by the standard deviation:

$$\sigma_F = \sqrt{\frac{1}{Q^2}\sum_{i=1}^{N}\left[F(r,\theta)w(r,\theta)S(r,\theta) - \overline{F}w(r,\theta)S(r,\theta)\right]^2} \tag{5.9}$$

and the coefficient of variation $C_{v\text{-}F}$ (Eq. (5.7)).

Similarly, the above relationships can be used to evaluate the standard deviation, σ_C, and coefficient of variation, $C_{v\text{-}C}$, for the quality, C.

5.3. CFD SIMULATIONS

Three-dimensional simulations were set up and executed using the commercial software package ANSYS Workbench 14.5. The flow geometries were created and meshed using the software ICEM, while flow specification, solving and post-processing were all performed using CFX 14.5.

5.3.1. Geometry and mesh

Two geometries are considered in this chapter. One geometry consisted of a straight tube 30 mm in diameter, 2400 mm in length for heating, holding and cooling tube separately. The other one is additionally filled with helical Kenics static mixer whose dimension is stated in Table 4.2.

Both geometries were meshed with hexahedral cells and the detailed description has been given in Section 4.3.2.

5.3.2. Simulation setting

The numerical simulations were executed separately in a heating tube, holding tube and cooling tube. A uniform temperature and a mass flowrate $\dot{m}$ = 0.0281 kg s^{-1} were specified at the tube inlet, and a zero gauge pressure was set at the tube outlet. The mass flowrate was chosen to give a mean flow velocity $\overline{w}$ = 4.0 cm s^{-1}, which is typical of values used in the processing of viscous food materials (Jung and Fryer, 1999; Steffe, 1996). A constant uniform wall temperature and a no-slip condition were assigned at the wall in the heating and cooling tubes. For holding tube, an adiabatic and no-slip condition was specified at the wall. In the heating stage of a continuous food sterilisation processing, wall temperatures lower than 180 ℃ are usually used in practice; therefore, here, in the heating tube, the bulk of the work was done with T_w = 140 °C, but simulations were also run for T_w = 180 C to investigate the effects, a value of 20 °C was specified as the inlet temperature in the heating tube. In the cooling tube, fluid was assumed at uniform temperature of 126.53 °C at the tube inlet. A room

temperature of 20 °C was used as the wall temperature. As well, simulations have been done with typical temperature of chilled water of 5 °C as wall temperature to study the effect of wall temperature in the cooling tube. Other simulation parameters are summarised in Table 5.2.

Simulations involving steady flow were conducted in the steady-state mode, whereas simulations of vibrational flow were conducted in the transient mode. For a transversely moving boundary, the mesh deformation option in CFX was used which allows the specification of the motion of nodes on boundary regions of the mesh. The motion of all remaining nodes is determined by the so-called displacement diffusion model which is designed to preserve the relative mesh distribution of the initial mesh. The mesh displacement was specified using Eq. (4.2), and an oscillatory velocity function defined by Eq. (4.3) was applied at the wall.

The advection scheme used in this investigation is 'High Resolution' Advection Scheme, which is helpful to satisfy the requirements of both accuracy and boundedness (see Chapter 2). The transient scheme used for the solution to march in time was the 'Second Order Backward Euler Scheme'. The simulation was solved over the entire mean residence time of the fluid which is determined by the tube length and mean flow velocity. For example, for a tube length of 2400 mm and flow velocity of 4.0 cm s^{-1}, as used here, the fluid residence time in the tube is 60 s. This time duration was divided into equal time steps, the size of which (1.6667×10^{-3} s) was determined by dividing the vibration cycle into an optimised number of 12 equal time steps. Using a larger number of time steps per vibration cycle did not change the simulation results but prolonged the simulations considerably.

Convergence of the numerical solution was assumed when the root mean square (RMS) of mass, momentum and energy residuals all reached 10^{-4} at each time step which is a good level of accuracy given the complexity of the problem. Achieving this level of convergence typically required 8 — 12 iterations per time step for vibrational flow and

about 50 iterations for steady flow. In practice, however, most of the equations generally reached RMS residual values well below the specified target.

Table 5.2. Simulation parameters used.

Flow regime	Axial velocity $\overline{w}$ (m s^{-1})	Simulation time t (s)	Vibration frequency f (Hz)	Vibration amplitude A (mm)	Heating tube			Cooling tube		
					Inlet temperature T_{in} (°C)	Wall temperature T_w (°C)	Frequency of step rotation of vibration orientation Ω (Hz)	Inlet temperature T_{in} (°C)	Wall temperature T_w (°C)	Frequency of step rotation of vibration orientation Ω (Hz)
SF	0.04	-	-	-	20	140, 180	-	126.53	5, 20	-
SF-KM	0.04	-	-	-	20	140, 180	-	126.53	5, 20	-
VF	0.04	60	50	2	20	140, 180	-	126.53	5, 20	-
VF-SR	0.04	60	50	2	20	140, 180	0.2, 0.1, 0.067	126.53	5, 20	0.5, 0.2, 0.1

5.3.3. Sterility and quality profiles: Lagrangian particle tracking

In a continuous flow process, different fluid elements will have different thermal histories and will be subjected to different levels of microbial lethality. To calculate local values of sterility at the exit, a Lagragian particle tracking method was used. Thus, the function of one-way coupled particle tracking was implemented in the CFD code to predict fluid trajectories along the tube. Unlike two-way coupling (i.e. full coupling) which takes into account not only the effect of particles on continuous phase flow but also the influence of continuous phase flow on particles, one-way coupling simply predicts the particles' path lines as a post-process based on the computed flow field (Mostofa *et al.*, 2010). One-way coupling does not allow particles to affect continuous phase flow and therefore gives a much more accurate tracking of fluid flow than full coupling. Thus, massless microscopic fluid particles (1 μm) were introduced at the tube inlet and their trajectories and, hence, their temperature and velocity histories, were recorded. Thus, these massless particles are assumed to faithfully track the motion of the microorganisms and their temperature history. In the case of vibrated flow, because of the harmonic motion of the tube wall, some of these fluid particles near the wall may move outside the numerical domain and are, therefore, ignored by the solver. In addition, some fluid particles become trapped in the slow moving fluid in the boundary layer and, thus, acquire extremely low velocities and do not reach the exit by the end of the simulation. Some numerical leaking of particles is unavoidable despite using a small time-step. In order to ensure that in vibrated flow a sufficient number of fluid particles were successfully tracked so that the flow field could be completely mapped, a large number (10^4) of such particles were introduced. The temperature and velocity histories of such particles were then used to calculate the sterility and quality profiles along the tube using a MATLAB code.

5.4. VALIDATION OF CFD MODEL

Though CFX is a generally well validated code as it is widely used, the computational work reported in Chapter 4 was further validated where possible either by comparing results with theoretical solutions or experimental data where possible. The intention here was to involve the holding and cooling stages to validate the CFD model by extending the validation in Section 4.4.2.

Table 5.3. Process parameters (Jung and Fryer, 1999).

Flowrate ($m^3\ h^{-1}$)	Density ($kg\ m^{-3}$)	Viscosity (Pa s)	Specific heat ($J\ kg^{-1}\ K^{-1}$)	Thermal conductivity ($W\ m^{-1}\ K^{-1}$)	Heating temperature (°C)	Cooling temperature (°C)	Heating length (m)	Holding length (m)	Cooling length (m)
0.1	998	0.001	4180	0.6	140	20	12	12	12

Validation was done by predicting the temperature against the classic analytical solution (Jakob, 1949) for the laminar flow of an isoviscous (i.e. temperature-independent viscosity) Newtonian fluid through a straight heating tube, and compare them to simulation results from Jung and Fryer (1999) executed with a different code (FIDAP), for the process conditions shown in Table 5.3. Both sets of simulations show excellent agreement with theory in Figure 5.1. Then, validation with predictions of sterility and quality in the same continuous

heat-hold-cool tube against simulation results from Jung and Fryer (1999) is carried out, and the sterility and quality profiles along the tube are compared in Figure 5.2, showing excellent agreement between the two simulations.

There are, however, no experimental data available on the temperature profile in flows with heat transfer when subjected to vibration. Nonetheless, given the excellent agreement of our CFD predictions of flow and heat transfer characteristics with theory and experimental results in all the above stages of the validation process, in addition tosimulations of food sterility and quality from Jung and Fryer (1999), it is worth to believe that the present CFD model is sufficiently robust and reliable for the purposes of studying the effects of vibration on the thermal processing of viscous fluids.

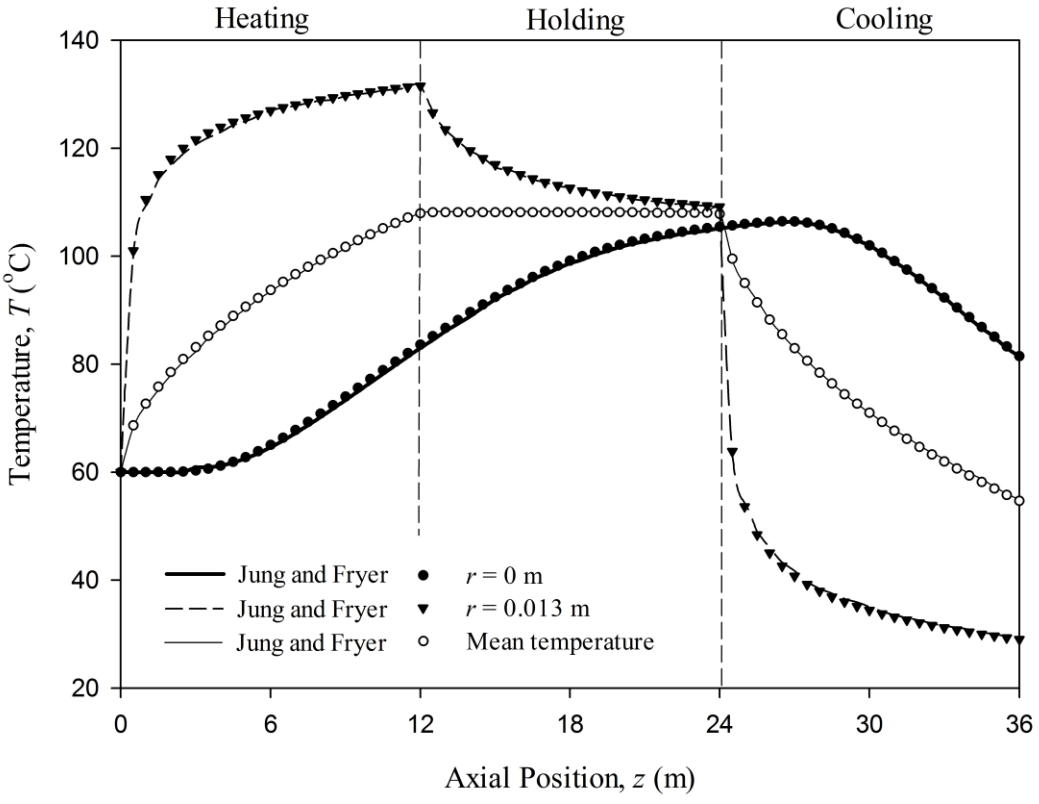

Figure 5.1. Validation of CFD-predicted temperature profiles in a heat-hold-cool process against simulation results from Jung and Fryer (1999) for the processing conditions of Table 5.3.

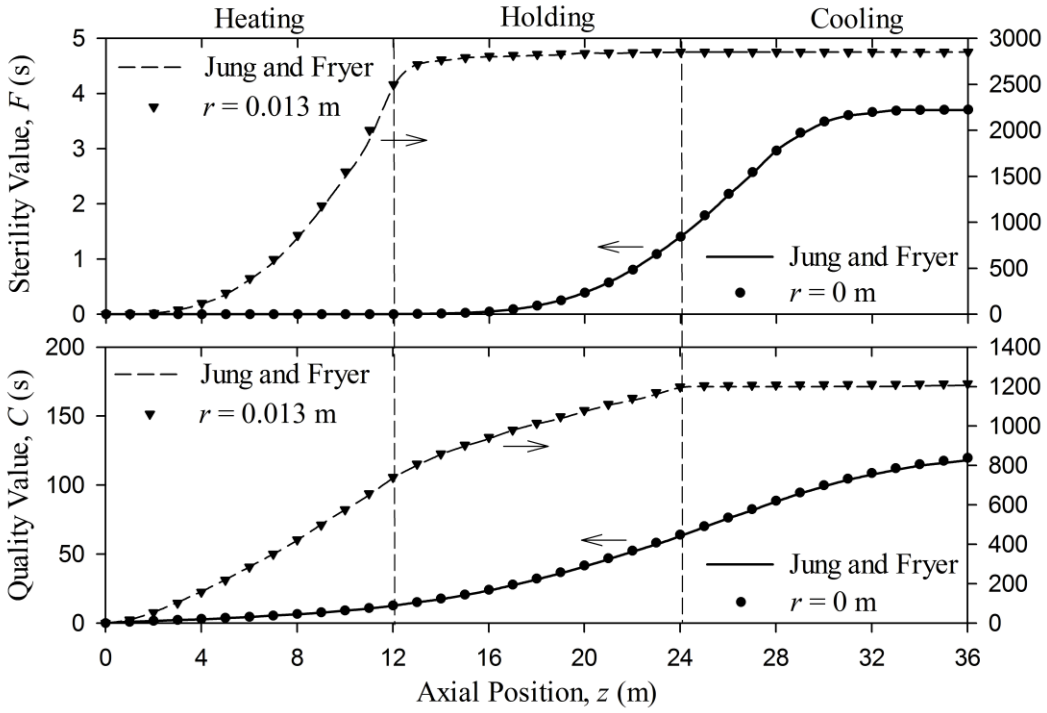

Figure 5.2. Validation of CFD-predicted sterility and quality profiles in a heat-hold-cool process against simulation results from Jung and Fryer (1999) for the processing conditions of Table 5.3.

5.5. RESULTS AND DISCUSSION

In this chapter, as what has been done in Chapter 4, four tube flow configurations are considered: (i) steady flow through a straight tube as used in a conventional sterilisation process (**SF**); (ii) steady flow through a straight tube fitted along its whole length with a Kenics static mixer (**SF-KM**); (iii) steady flow through a straight tube with superimposed transverse oscillations (**VF**); and (iv) steady flow through a straight tube subjected to transverse oscillations with step rotation of vibration orientation (**VF-SR**).

5.5.1. Effects of vibration on food sterility

As discussed above, in a safe sterilisation process, all of the fluid must receive the required minimum level of lethality. In normal steady-state flow, the fluid flowing along the centerline, being the fastest, is the slowest to reach such a level of sterility. This situation is much worse for viscous fluids flowing in the laminar regime. The challenge facing any continuous process of this kind, therefore, is to ensure that the fluid at the centre is safe without overcooking too much the slow moving fluid near the hot tube wall.

5.5.1.1. Heating stage

Low acid foods with a sterility value greater than 2.52 min are usually considered safe. Such a value is based on the lethality of the organism *Clostridium botulinum*, but in practice many pathogens are more heat resistant and F-values of 5 – 12 min are typically used (Steffe and Daubert, 2006). Such F-values usually require extremely long processing tubes which can run into hundreds of metres (Jung and Fryer, 1999).

Using the massless particle tracking algorithm described above, the temperature history profiles obtained by CFD in a heating tube were used to compute the radial sterility distribution at different axial positions. As pointed out above, in these calculations the thin boundary layer region (1 mm) adjacent to the hot wall was ignored, as it contains extremely large F-values (in this region $F \to \infty$). Radial contour plots of sterility at the

exit section of the heating tube are shown in Figure 5.3. The **VF-SR** technique produces the highest local F-values. Results for steady flow show that $F << 10^{-2}$ s over about 80% of the tube radius, and increases exponentially towards the wall reaching extremely high values, many orders of magnitude greater than the value at the centre (hence the use of a log scale). In contrast, due to better radial mixing, steep variations in F are confined within a much narrower (~ 1 mm) annular wall region for the other three flow regimes, thus reducing the impact of the wall region on the heat treatment of the fluid. The tube cross-section was divided into 15 shells of equal width and an azimuthally averaged F-value was calculated to represent each shell. Thus, azimuthally-averaged radial sterility profiles were obtained at the tube exit and are compared in Figure 5.4.

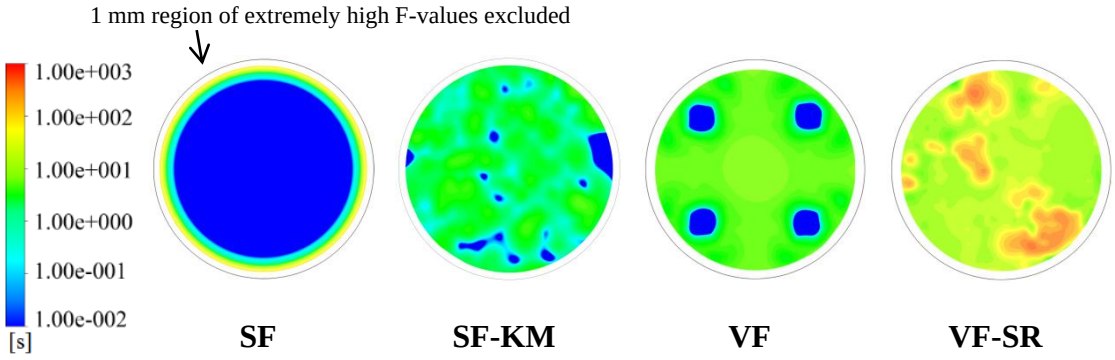

Figure 5.3. Radial contour plot of F-value at the exit section of the heating tubes: T_{in} = 20 °C; T_w = 140 °C; L = 2400 mm.

The **VF-SR** technique produces the highest local F values; as shown in Table 5.4, the mean sterility $\bar{F}_{\mathbf{VF-SR}}$ is much greater than for the other flow regimes ($117.5 \times \bar{F}_{\mathbf{SF}}$; $21.7 \times \bar{F}_{\mathbf{SF-KM}}$; $5.3 \times \bar{F}_{\mathbf{VF}}$). The uniformity of the radial F distribution across the tube section is also the best ($C_{v\text{-}F}$ ~ 1.09), significantly better than for **VF** ($C_{v\text{-}F}$ ~ 1.33) and substantially better than for **SF-KM** ($C_{v\text{-}F}$ ~ 1.58) and **SF** ($C_{v\text{-}F}$ ~ 3.75). As a result of the remarkable radial uniformity of sterility achieved by **VF-SR**, the mean value $\overline{F}$ across the tube, is close to the local F values; in particular, the ratio of $\overline{F}$ to F_c, the value at the centre, which is conventionally regarded as the coldest point, is ~ 1.0 (note in vibrated

flow the coldest point is not located at the centre); in steady flow, however, $\overline{F} \sim 8\times10^{7} \times F_c$. The static mixer shows segregation areas of very low F-values and the four cold vortex regions are also apparent in the **VF** contours as regions of low sterility (Figure 5.3), but this regime still outperforms the **SF-KM** configuration, yielding a mean F-value which is several times greater (Table 5.4).

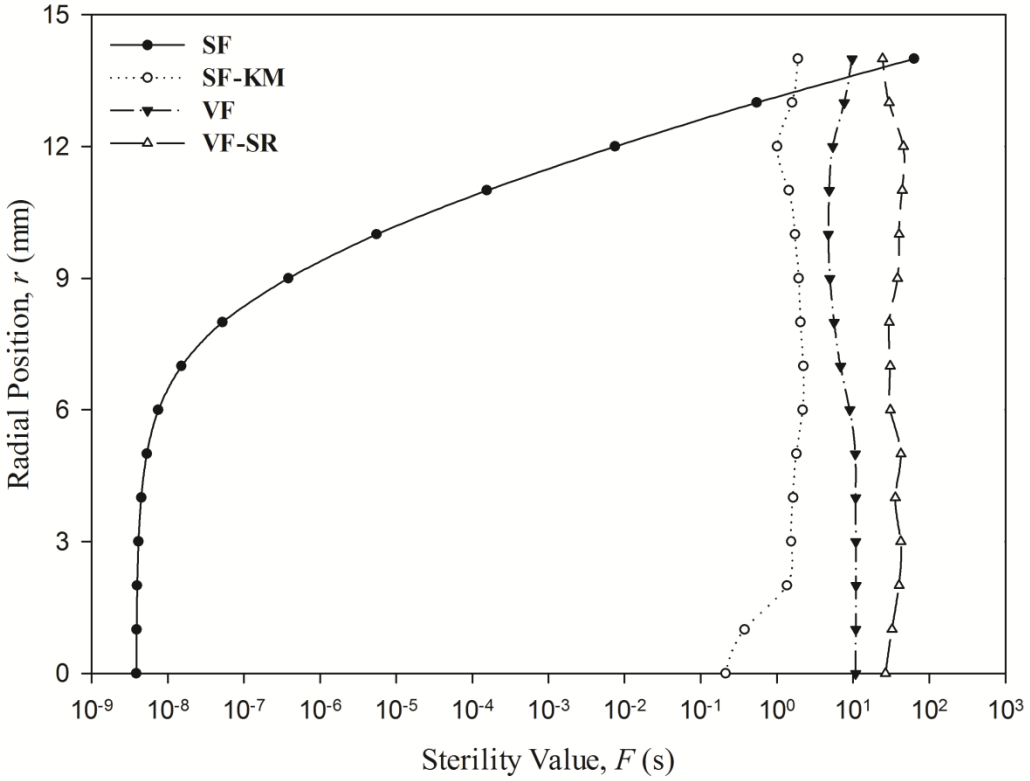

Figure 5.4. Radial profile of azimuthally-averaged F-value at the exit section of the heating tubes:

T_{in} = 20 °C; T_w = 140 °C; L = 2400 mm.

The values of the minimum sterility achieved, F_{min}, are also shown in Table 5.4. These values are in the main much smaller than $\overline{F}$, and the relative superiority of **VF-SR** over the other configurations (**SF**, **SF-KM**, **VF**) based on minimum sterility is even more staggering (respectively, ~ 3.2 $\times 10^{9}$, ~ 146 and ~ 94 folds).

Table 5.4. Mean sterility and quality in heating and cooling stages.

	Heating stage				Cooling stage			
	SF	**SF-KM**	**VF**	**VF-SR**	**SF**	**SF-KM**	**VF**	**VF-SR**
$\overline{F}$ (s)	0.32	1.73	7.15	37.59	49.53	10.87	7.70	7.35
F_{min} (s)	3.9×10^{-9}	0.086	0.13	12.5	-	-	-	-
$C_{v\text{-}F}$ (-)	3.75	1.58	1.33	1.09	0.091	0.022	0.022	0.020
$\overline{C}$ (s)	4.71	10.77	15.02	25.98	31.56	17.07	9.15	8.77
$C_{v\text{-}C}$ (-)	1.69	0.28	0.27	0.14	0.099	0.050	0.032	0.029

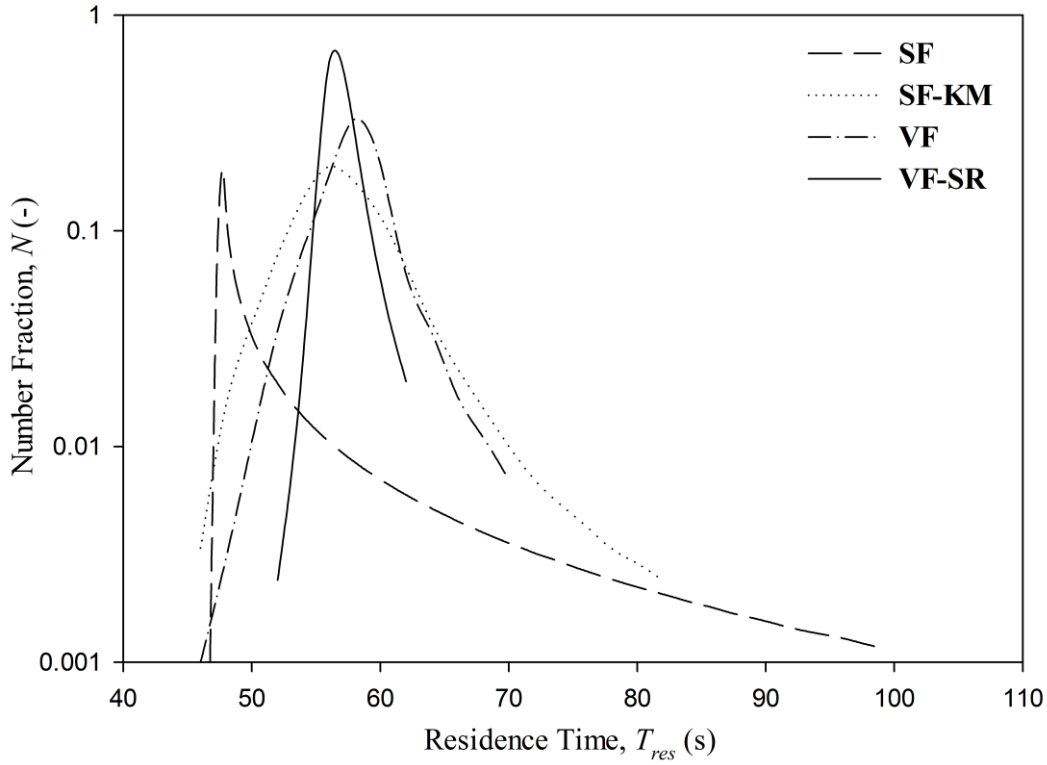

Figure 5.5. Fluid residence time distribution in the heating tube:

T_{in} = 20 °C; T_w = 140 °C; L = 2400 mm.

The above results also serve to show the potential danger of using $\overline{T}$ and $\overline{F}$ to assess the thermal processing of the fluid. As the fluid flows in parallel layers with little/no radial mixing, $\overline{F}$ is clearly not a reliable measure of sterility in steady flow, so that high mean values do not necessarily imply a safe level of sterility because of the lack of uniformity. Even with the Kenics mixer the temperature history along the tube results in many scattered pockets where the local F-value is ~ 20 times smaller than $\overline{F}$. The use of an average F-value is, however, much more justifiable in a radially well-mixed flow such as the vibrated flow (**VF-SR**) considered here, where chaotic advection ensures that fluid elements continuously exchange radial position along the tube, thus, narrowing the residence time distribution substantially, as shown in Figure 5.5, and consequently the radial temperature distribution. Consequently, a more rational evaluation of these different thermal processing regimes should be based on the minimum local sterility value, F_{min}, achieved at exit.

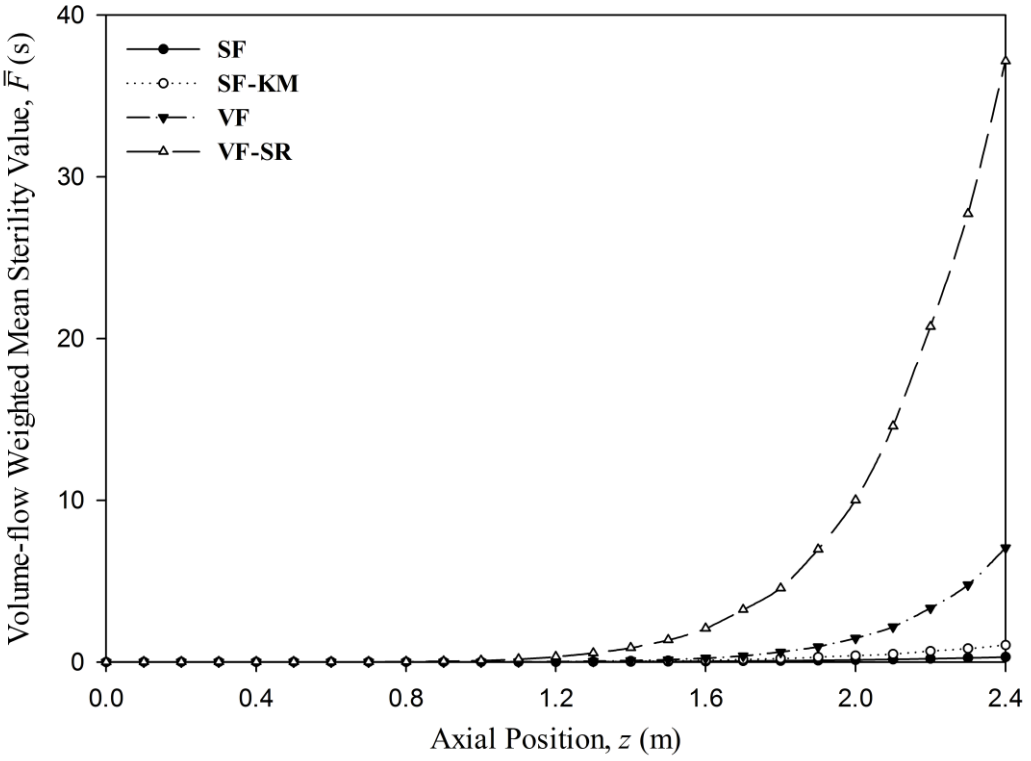

Figure 5.6. Development of mean F-value along heating tubes of the same length: T_{in} = 20 °C; T_w = 140 °C; L = 2400 mm.

There is also a huge difference in the axial growth of the mean F-value between the four regimes of flow, as shown in Figure 5.6. In steady flow and in steady flow with Kenics mixer, *F* rises relatively very slowly along the tube. Under vibration, however, radial mixing ensures that the fluid at the tube centre is heated much more rapidly, thus causing *F* to grow exponentially rapidly with *z*; the effect is much more pronounced for **VF-SR** than for **VF**, however. Thus, it follows that a given level of mean sterility can be achieved in much shorter tubes when flow is vibrated; for example, for the process conditions considered here, achieving the mean sterility value of 37.6 s obtained with **VF-SR** in the 2.4 m long tube, as shown in Figure 5.7, would require a heater which has a length of ~ 7.7 m with **SF**, ~ 3.8m with **SF-KM** and ~ 2.9 m with **VF**.

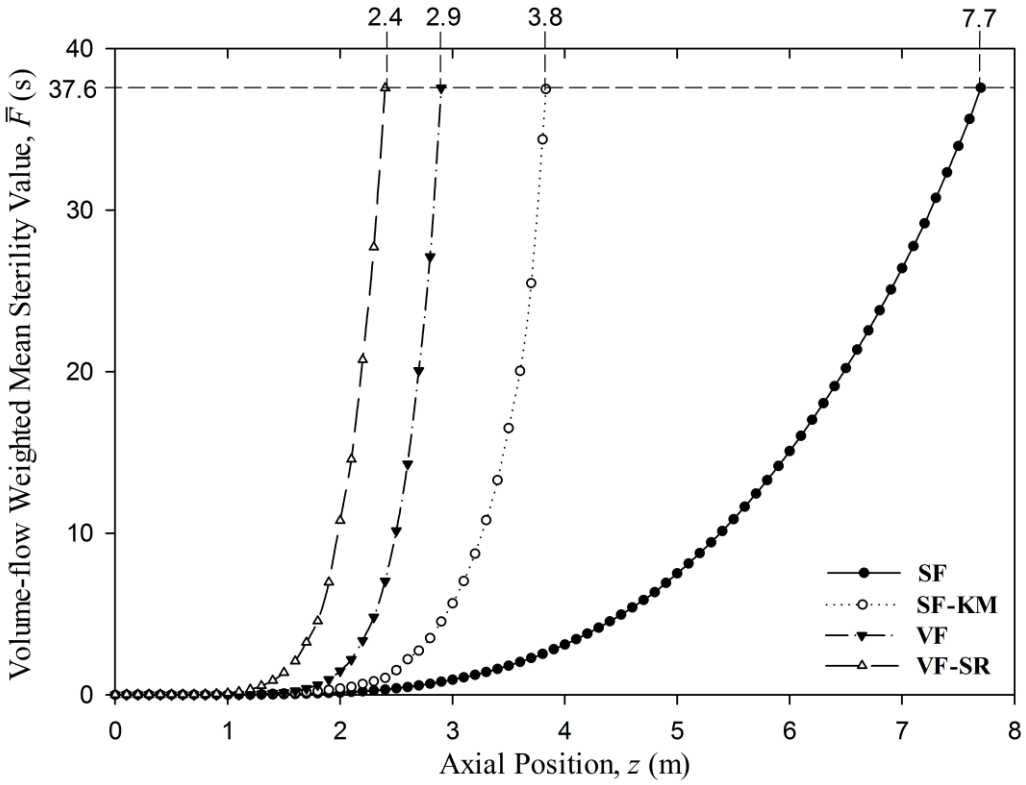

Figure 5.7. Development of mean F-value along heating tubes of different lengths with different flow regimes achieving the same value ($\bar{F}$ = 37.6 s) at the exit section: T_{in} = 20 °C; T_w = 140 °C.

However, as pointed out above, it is important to note that the use of mean temperature and mean sterility can be seriously misleading. Indeed, any assessment or comparison should be made on the basis of the minimum sterility value attained in the flow. There is also a huge difference in the axial growth of F_{min} between the four regimes of flow, as shown in Figure 5.8. In steady flow and in steady flow with Kenics mixer, F_{min} rises relatively very slowly along the tube. On the other hand, under vibration, radial mixing ensures that the fluid at the tube centre is heated much more rapidly, thus causing F_{min} to grow exponentially rapidly with z; the effect is much more pronounced for **VF-SR** than for **VF**, however. Thus, it follows that a given level of minimum sterility can be achieved in much shorter tubes when flow is vibrated; for example, for the process conditions considered here, achieving the minimum sterility value of 12.5 s obtained with **VF-SR** in the 2.4 m long tube, as shown in Figure 5.9, would require a heater which has a length of ~ 26.0 m for **SF**, 4.0 m for **SF-KM** and 3.2 m for **VF**.

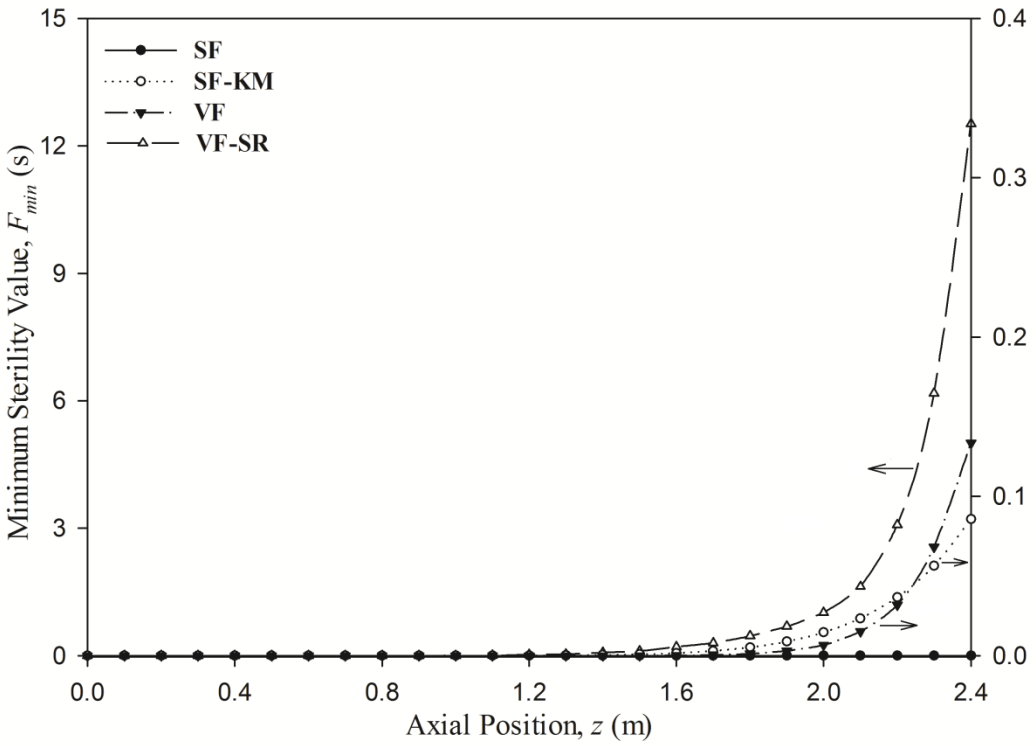

Figure 5.8. Development of minimum F-value along heating tubes of the same length: T_{in} = 20 °C; T_w = 140 °C; L = 2400 mm.

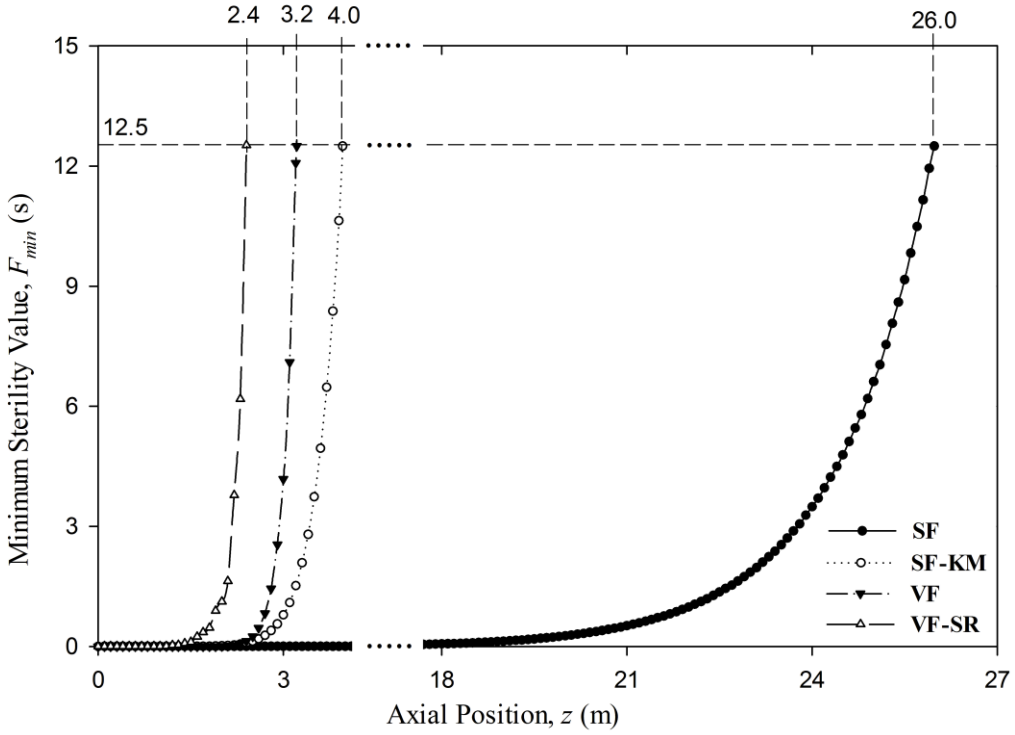

Figure 5.9. Development of minimum F-value along heating tubes of different lengths with different flow regimes achieving the same value (F_{min} = 12.5 s) at the exit section: T_{in} = 20 °C; T_w = 140 °C.

5.5.1.2. Cooling stage

In the cooling stage of a heat-hold-cool process, to preserve as much of the product quality as possible, ideally the cooking process should not proceed any further. Thus, further build-up of sterility along the tube is undesirable. The mean values of sterility reached at the end of a cooling tube operating under the four different flow regimes are given in Table 5.4, whilst the variations of $\overline{F}$ along the tube are plotted in Figure 5.10 alongside radial contour plots and azimuthally-averaged profiles of sterility. For discussion purposes and to enable easy comparison of the performance of the four different flow configurations, in this case the same uniform temperature of 126.5°C was used at the inlet of each cooling tube. This, in fact, is the temperature reached at the exit of the **VF-SR** heating tube. Note that the sterility values obtained in the cooling tubes of **SF**, **SF-KM** and **VF** are higher than those obtained in their corresponding heating tubes,

but only because the high inlet temperature (126.5 °C) assumed for these three flow regimes would in practice require much longer (>> 2.4 m) heating tubes to achieve it, in which case the sterility accumulated in the heater would also be correspondingly much higher than in the cooler.

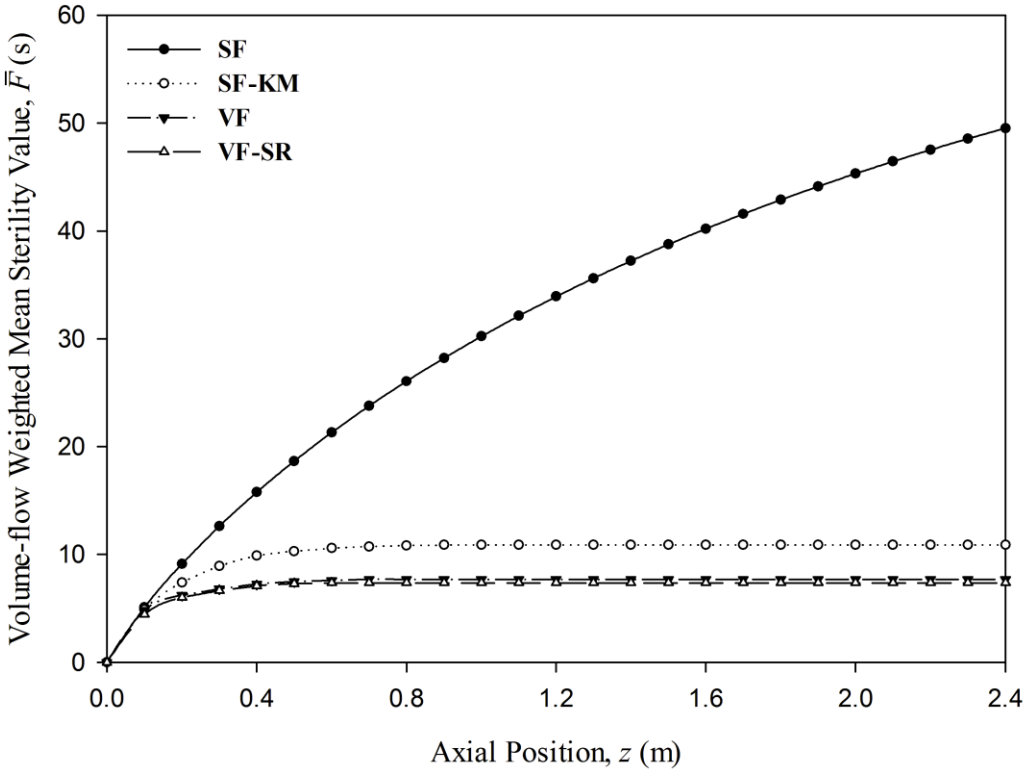

Figure 5.10. Development of mean F-value along cooling tubes of the same length: T_{in} = 126.5 °C; T_w = 20 °C; L = 2400 mm.

Under **SF**, there is a substantial monotonic growth in $\overline{F}$ with z. The **SF-KM** configuration causes initially a considerable rise in $\overline{F}$, reaching a plateau after ~ 1.0 m. With vibration superimposed on the flow, for both **VF** and **VF-SR** there is an initial rise in the F-value over a short length of tube, levelling off at a ~ 0.6 m and reaching about 60% of the $\overline{F}$ value attained with **SF-KM**. Thus, vibrated flow is by far the closest to the ideal situation of zero cooking in a cooling tube. Furthermore, similar to the heating tube, vibration has the added advantage of producing nearly uniform distributions of F across the cooling tube cross-section, as shown in Figure 5.11; the corresponding $C_{v\text{-}F}$

values are given in Table 5.4.

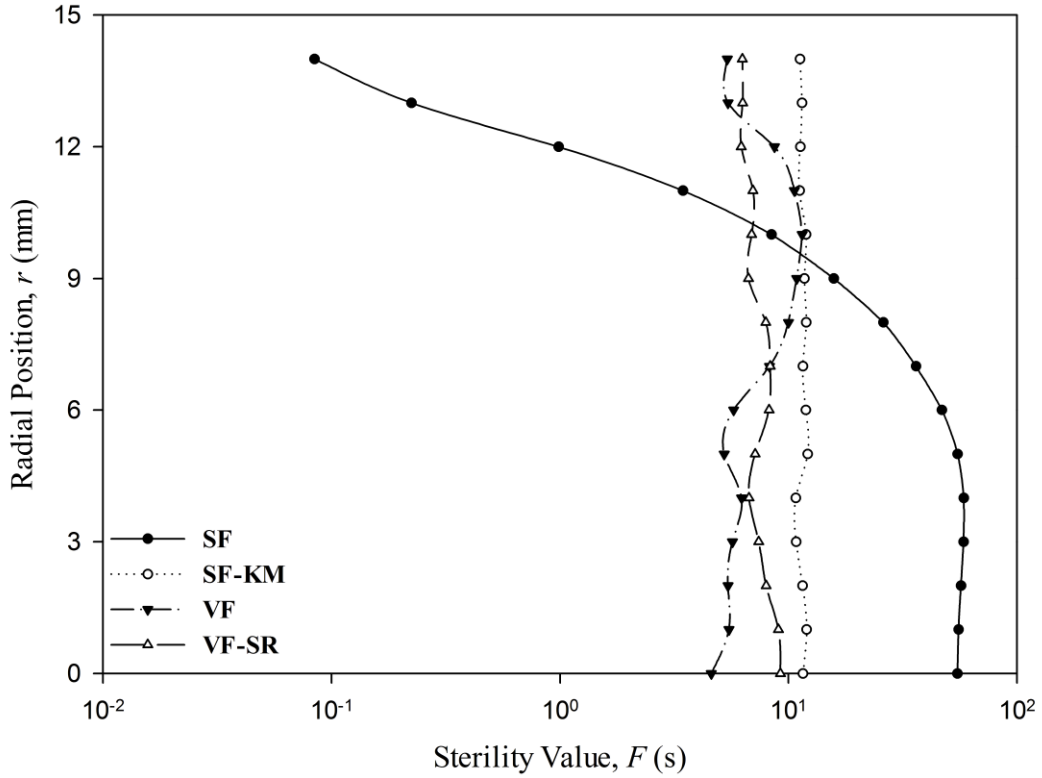

Figure 5.11. Radial profile of azimuthally-averaged F-value at the exit section of the cooling tubes:

T_{in} = 126.5 °C; T_w = 20 °C; L = 2400 mm.

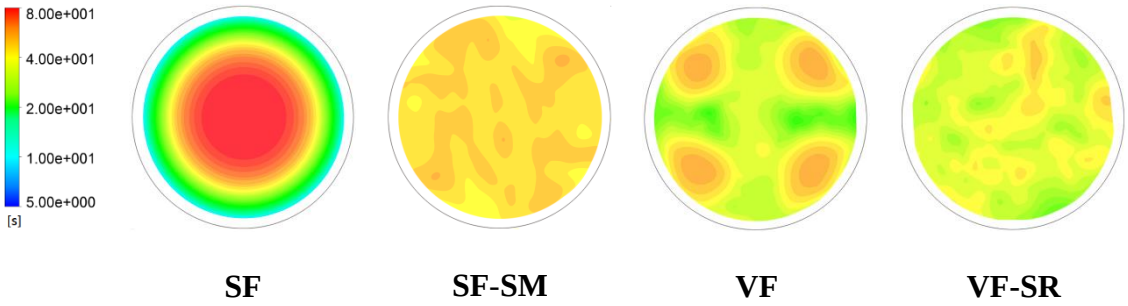

Figure 5.12. Radial contour plot of F-value at the exit section of the cooling tubes:

T_{in} = 126.5 °C; T_w = 20 °C; L = 2400 mm.

The four salient vortex regions observed in the **VF** heating tube (see Figure 5.7) are still apparent in Figure 5.12; these are detrimental to mixing and prevent effective fluid cooling. As a result, these vortex regions are now regions of relatively high sterility contrary to the situation in the heating tube.

5.5.2. Effects of vibration on food quality

5.5.2.1. Heating stage

For a given level of sterility, the aim is to minimise food quality loss, i.e. the C-value defined above in Eq. (5.2) to preserve nutritional value. Thus, comparison of quality loss is only meaningful when based on equal sterility. Initially, we make such a comparison on the basis of equal $\overline{F}$ and then on the basis of equal F_{min}.

Contours of the radial distribution of quality for the four flow regimes studied are compared in Figure 5.13, for a given mean sterility $\overline{F}$ = 37.6 s, which is the value achieved by **VF-SR** at the exit of a 2.4 m tube.

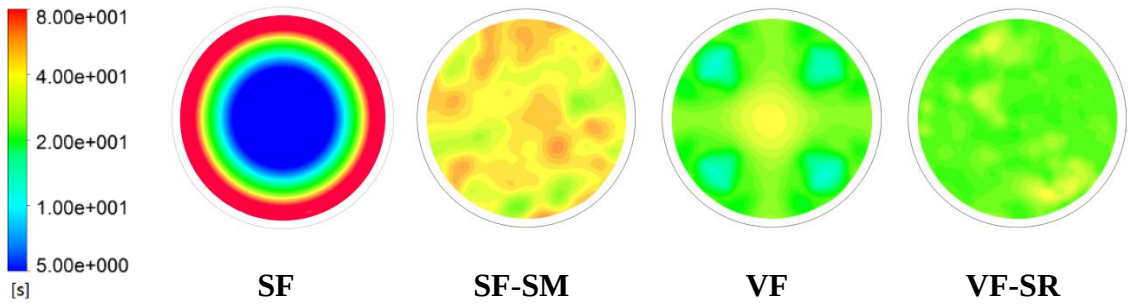

Figure 5.13. Radial contour plot of C-value at the exit section of heating tubes with different flow regimes achieving the same mean sterility ($\overline{F}$ = 37.6 s) at the exit section: T_{in} = 126.5 °C; T_w = 140 °C (note that the red colour in the **SF** plot is ~ 4-fold greater than the top end of the scale).

As discussed above, and as shown in Figure 5.7, to achieve this same mean sterility value, **SF** requires ~ 7.7 m of heating tube, **SF-KM** requires ~ 3.8 m and **VF** requires ~ 2.9 m. The corresponding radial profiles of azimuthally-averaged C-value are also plotted in Figure 5.14. Clearly, **VF-SR** produces by far the lowest C-values and the most uniform profile ($C_{v\text{-}C}$ values are given in Table 5.5), outperforming by far the traditional steady flow process as well as the Kenics mixer. The axial profiles of the mean C-value depicted in Figure 5.15 show that the **VF-SR** technique produces a much lower quality loss compared to **SF** and **SF-KM**.

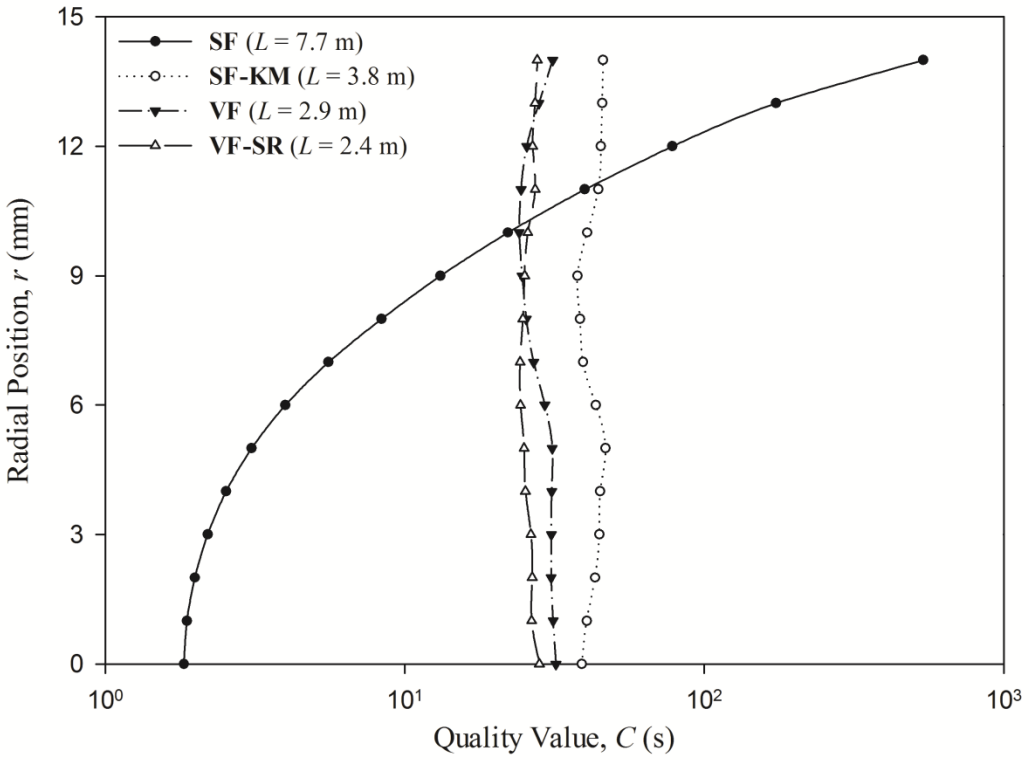

Figure 5.14. Radial profile of azimuthally-averaged C-value at the exit section of heating tubes with different flow regimes achieving the same mean sterility ($\overline{F}$ = 37.6 s) at the exit section: T_{in} = 126.5 °C; T_w = 140 °C.

Table 5.5. Mean quality corresponding to the same mean sterility at exit ($\overline{F}$ = 37.6 s).

	SF	**SF-KM**	**VF**	**VF-SR**
$\overline{C}$ (s)	47.8	39.2	29.1	26.0
$C_{v\text{-}C}$ (-)	1.45	0.27	0.23	0.14
L (m)	7.7	3.8	2.9	2.4

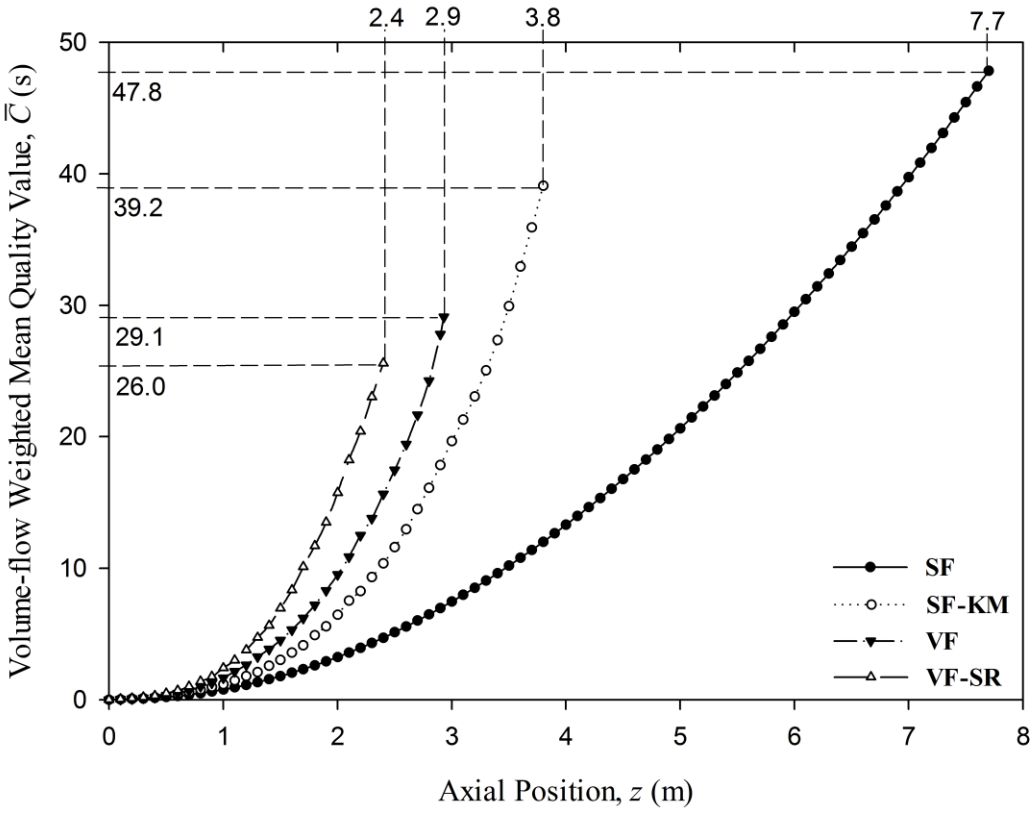

Figure 5.15. Development of mean C-value in heating tubes with different flow regimes achieving the same mean sterility ($\overline{F}$ = 37.6 s) at the exit section: T_{in} = 20 °C; T_w = 140 °C.

Again, contours of the radial distribution of quality (Figure 5.16) as well as the azimuthally-averaged radial profiles (Figure 5.17) for the four flow regimes studied are

compared on the basis of the minimum sterility value F_{min} = 12.5 s, which is the value achieved at the exit of the 2.4m **VF-SR** tube.

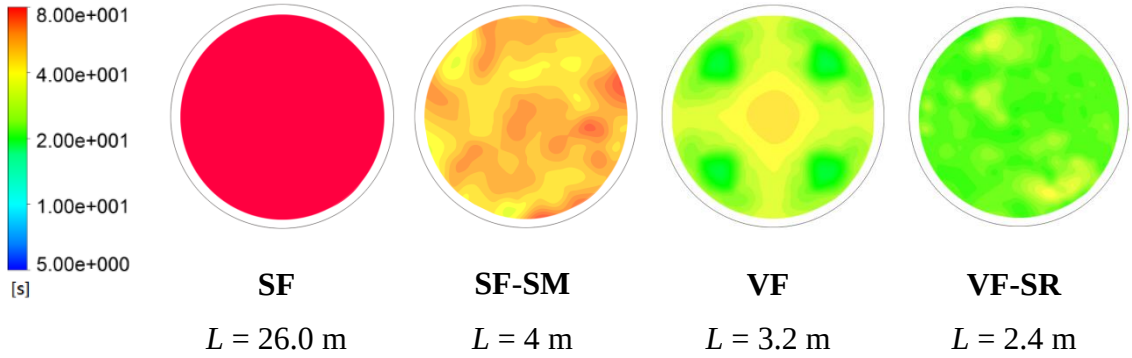

Figure 5.16. Radial contour plots of C-value at the exit section of heating tubes with different flow regimes achieving the same minimum sterility (F_{min} = 12.5 s) at the exit section: T_{in} = 20 °C; T_w = 140 °C (note the red colour in the **SF** contour exceeds the top of the scale by 2 orders of magnitude).

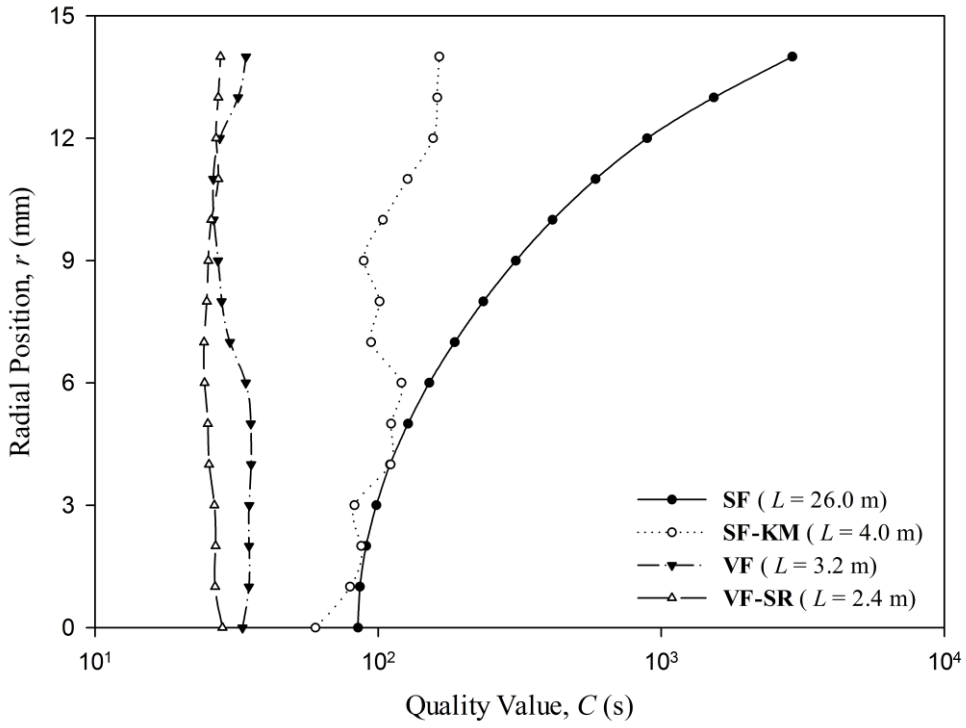

Figure 5.17. Radial profile of azimuthally-averaged C-value at the exit section of heating tubes with different flow regimes achieving the same minimum sterility (F_{min} = 12.5 s) at the exit section: T_{in} = 20 °C; T_w = 140 °C.

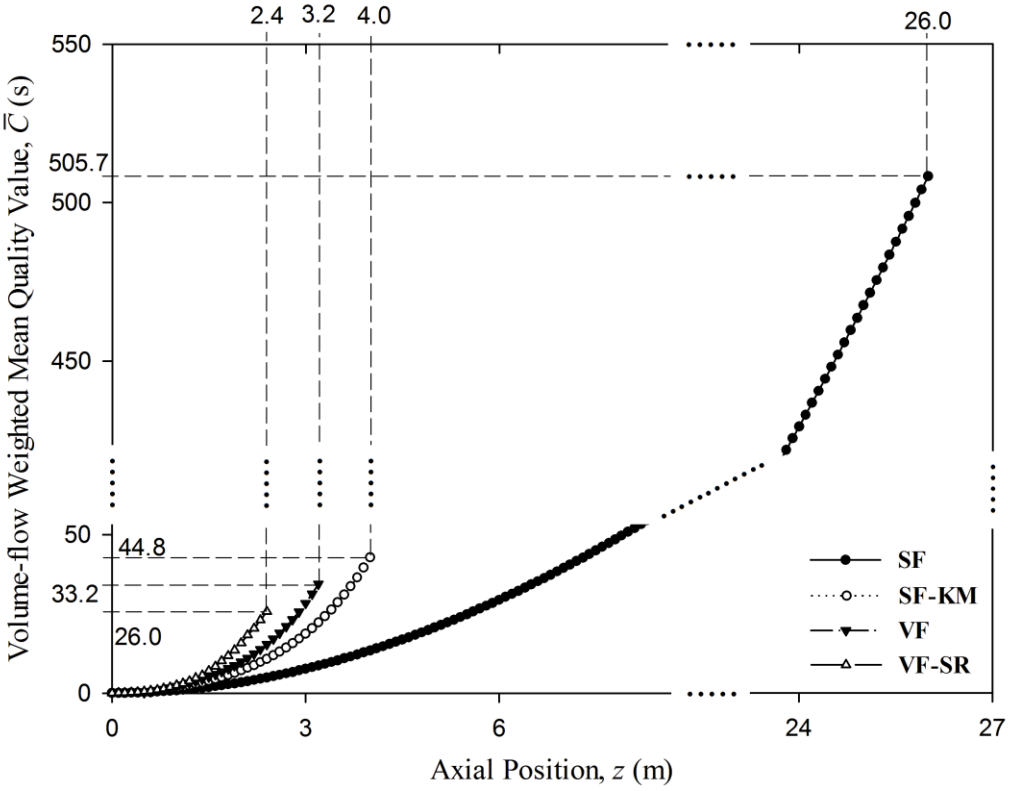

Figure 5.18. Development of mean C-value in heating tubes with different flow regimes achieving the same minimum sterility (F_{min} = 12.5 s) at the exit section: T_{in} = 20 °C; T_w = 140 °C.

Table 5.6. Mean quality corresponding to the same minimum sterility at exit (F_{min} = 12.5 s).

	SF	**SF-KM**	**VF**	**VF-SR**
$\overline{C}$ (s)	505.74	44.83	33.21	25.98
$C_{v\text{-}C}$ (-)	0.96	0.32	0.16	0.14
L (m)	26.0	4.0	3.2	2.4

As discussed above, and as shown in Figure 5.9, to achieve this same minimum sterility

value, **SF** requires ~ 26.0 m of heating tube, **SF-KM** requires ~ 4.0 m and **VF** requires ~ 3.2 m, even much larger losses of food quality: $\overline{C}$ = 505.7 s for **SF**, 44.8 s for **SF-KM** and 33.2 s for **VF (**Figure 5.18**)**. Clearly, **VF-SR** produces the lowest and most uniform C-values ($C_{v\text{-}C}$ values are given in Table 5.6), outperforming by far the traditional steady flow process as well as the Kenics mixer.

5.5.2.2. Cooling stage

As discussed above, vibrating the flow in the heating tube led to a fast rise in fluid temperature along the tube. Similarly, vibration causes a fast drop in fluid temperature in the cooling tube which helps to minimize the loss of product quality. The variations of $\overline{C}$ along the tube, depicted in Figure 5.19, show how vibration quickly limits the rise in quality value. Both **VF** and **VF-SR** achieve a low plateau after a short length of tubing, whilst **SF-KM** shows a substantial rise in C-value about twice as high.

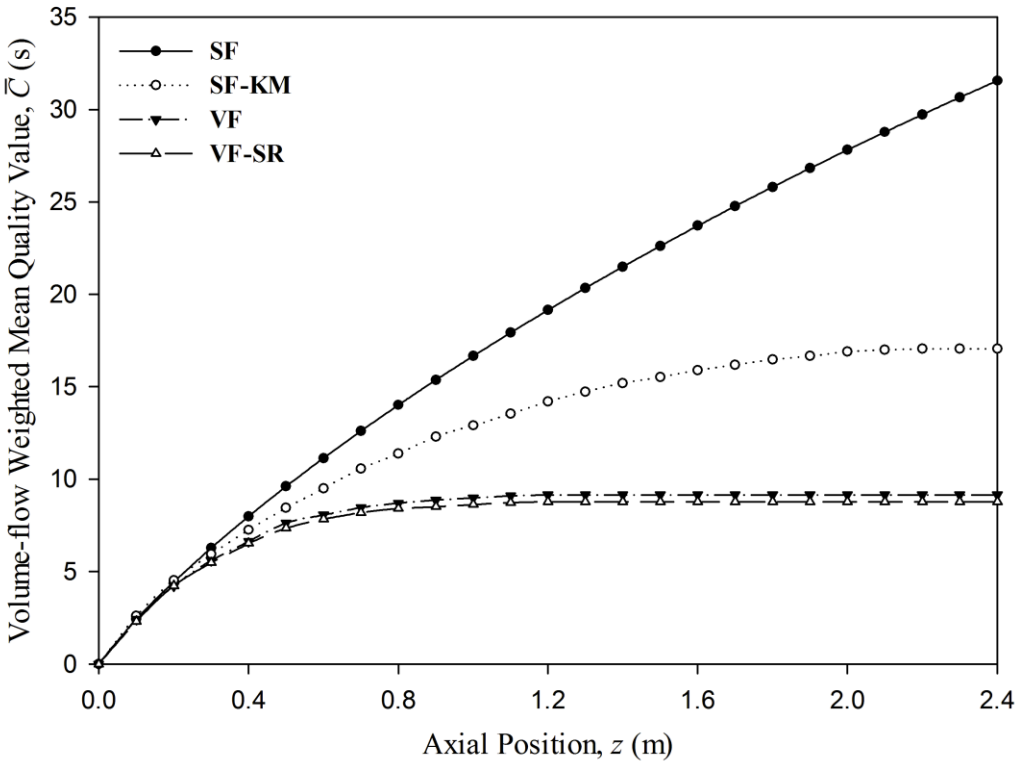

Figure 5.19. Development of mean C-value along cooling tubes of the same length: T_w = 20 °C; L = 2400 mm.

In contrast, **SF** exhibits a large monotonic increase in $\overline{C}$ as a function of *z*. The radial quality contours at the exit are also shown in Figure 5.20, whilst the corresponding $C_{v\text{-}C}$ values are given in Table 5.4. Again, the **VF-SR** regime gives the best uniformity in quality distribution across the cooling tube. The Kenics mixer (**SF-KM**) performs considerably better than **SF** both in terms of mean quality and uniformity achieved, but it is much inferior to **VF** and **VF-SR**.

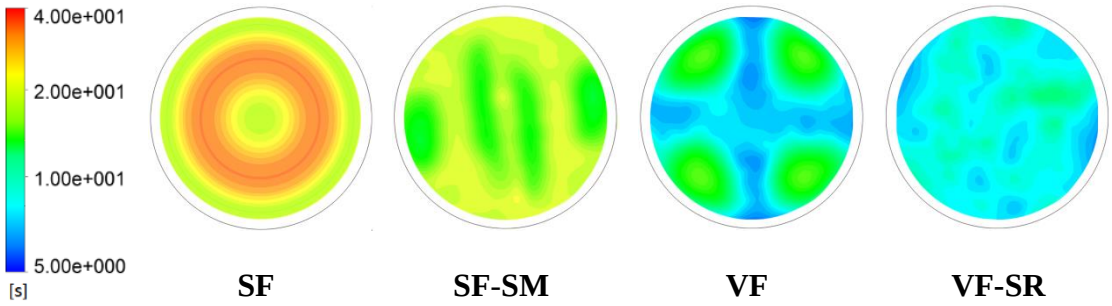

Figure 5.20. Radial contour plots of C-value at the exit section in the cooling tubes: T_{in} = 126.5 °C; T_w = 20 °C; L = 2400 mm.

5.5.3. Vibration in the context of a heat-hold-cool system

Industrial processes do not aim to achieve the required level of food sterility in the heating tube. In continuous aseptic processing, a heat-hold-cool system is normally used. There is a clear quality advantage in in-flow sterilisation at higher temperatures and for shorter times i.e. HTST, because the activation energy for the reactions which cause microbial destruction, i.e. sterility, are higher than those which result in quality loss (Holdsworth, 1992). Sterilisation reactions proceed ~100 times faster than loss of quality reactions. Therefore, compared to in-can processing the time needed for sterilisation is reduced and the amount of quality loss is also reduced (Hallstrom *et al.*, 1988).

HTST processes involve heating to the required sterilisation temperature, holding the

product at such a temperature for long enough to ensure sufficient pathogen spore destruction, and then cooling to packaging temperature. In practice, to ensure product safety, the length of the holding tube is usually calculated based on the assumption of Newtonian laminar flow with all of the fluid flowing at the centreline maximum velocity, i.e. twice the mean velocity. Inevitably, such a conservative approach leads to very long holding tubes on the order of hundreds of metres, and very long residence times, thus, contradicting the HTST assumption and producing food of poor quality.

In this section, the complete heat-hold-cool process is assessed under the four different flow regimes studied using the simulation parameters shown in Table 5.7.

Table 5.7. Simulation parameters for complete heat-hold-cool process.

Mean velocity ($m\ s^{-1}$)	Heating wall temperature (°C)	Cooling wall temperature (°C)	Heating length (m)	Holding length (m)	Cooling length (m)
0.04	140	20	2.4	2.4	2.4

The mean temperature history curves for these four processes are compared in Figure 5.21. The **VF-SR** process comes on top achieving fast heating and fast cooling, outperforming by a substantial margin the conventional steady-state process both with and without the Kenics static mixer. In terms of temperature profile, simple transverse vibration (**VF**) compares reasonably well with **VF-SR**, but, as pointed out earlier, the seemingly modest differences in temperature in fact translate into large differences in F-value. The results discussed above have shown that **VF-SR** can achieve much higher sterility values in a relatively short tube compared with **SF** (~ 117 times in a 2.4 m tube, see Table 5.4). It should be noted that in a conventional steady-state process, relatively little lethality is accumulated in the heater, and most of the sterility is achieved in the holding tube. However, given the fast rise in temperature accompanied by the fast rise in

F achieved by the **VF-SR** technique in the heater, a holding stage may not be necessary. This represents an additional significant improvement in the sterilisation process. In cases where higher $\overline{F}$ values are required at the exit of the heating stage, a longer vibrated heating tube could be used. The exponential variation of $\overline{F}$ with *z*, shown in Figure 5.6, indicates that a large increase in $\overline{F}$ could be achieved through only a relatively small increase in tube length. However, we need to assess whether an increase in $\overline{F}$ is better achieved by using a longer vibrated heater or by using a holding tube instead.

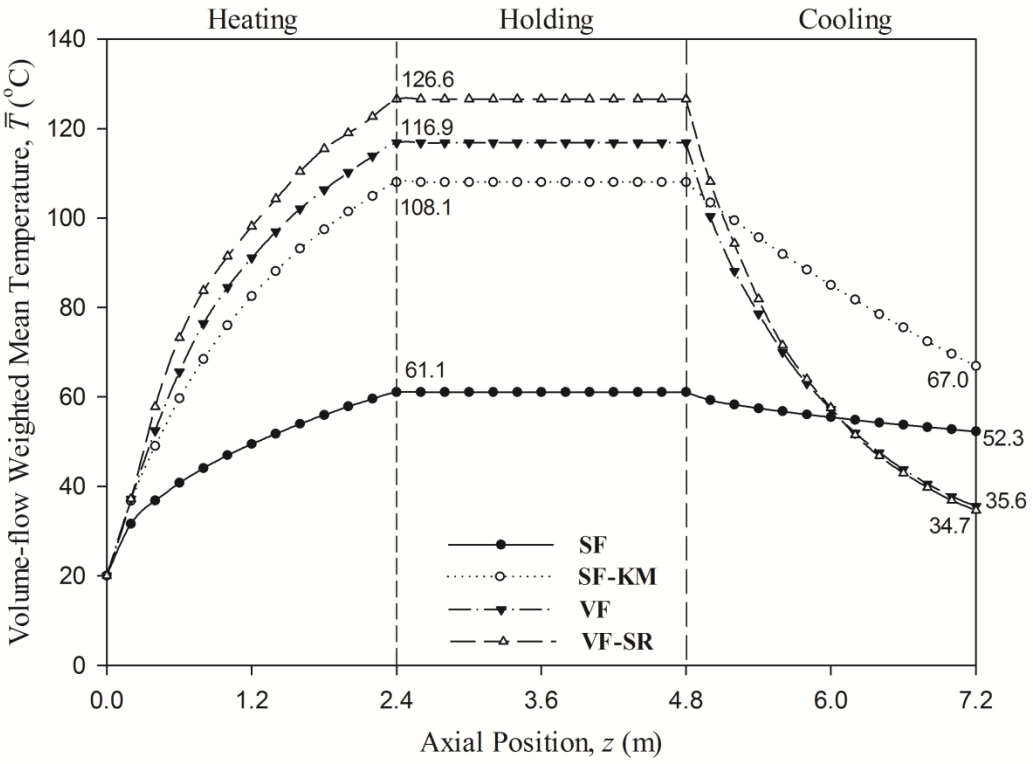

Figure 5.21. Development of mean temperature along heat-hold-cool process: T_w = 140 °C (heating); T_w = 20 °C (cooling).

The axial profiles of mean sterility in the heating tube and holding tube are shown in Figure 5.22. An average sterility value of 37.6 s is reached at the end of the heating stage.

Adding a holding tube of 2.4 m length yields a total average sterility of ~ 250 s. The same value could be achieved by extending the **VF-SR** heating tube by only an extra ~ 0.6 m. At the same time, the associated increase in the mean C-value would be ~ 78 s for the holding tube and ~ 32 s for the extended heater as shown in Figure 5.23; i.e. a relatively short extension of the heater achieves the same mean sterility with a much reduced loss of quality.

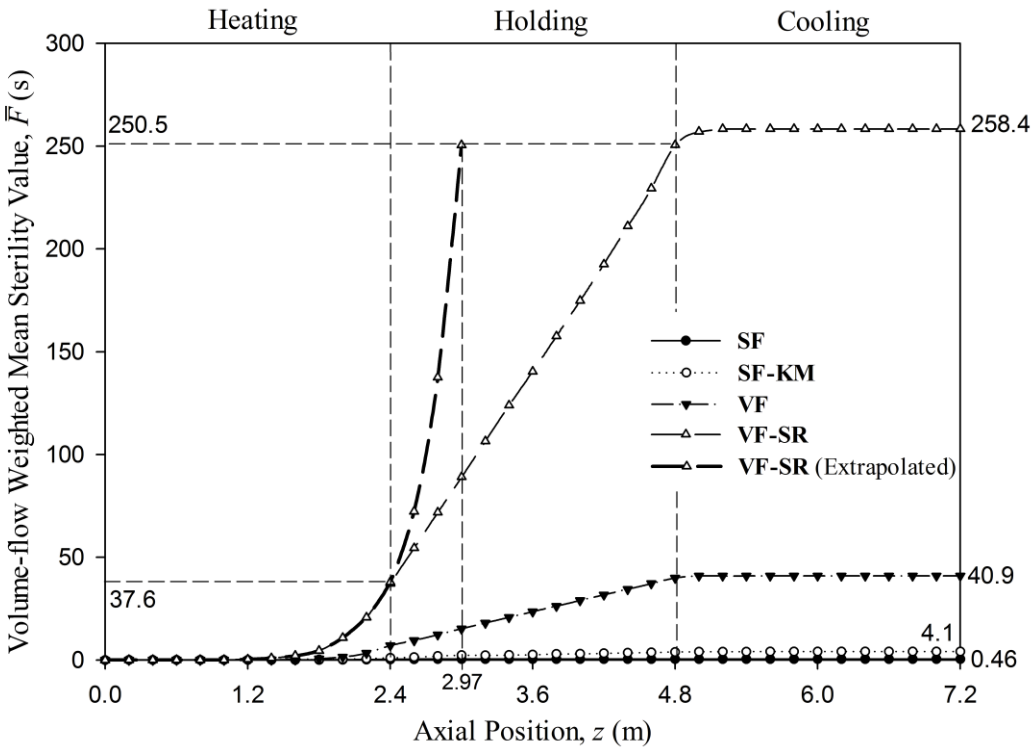

Figure 5.22. Development of mean F-value along heat-hold-cool process: T_w = 140 °C (heating); T_w = 20 °C (cooling) – process axial temperature profile shown in Figure 5.21.

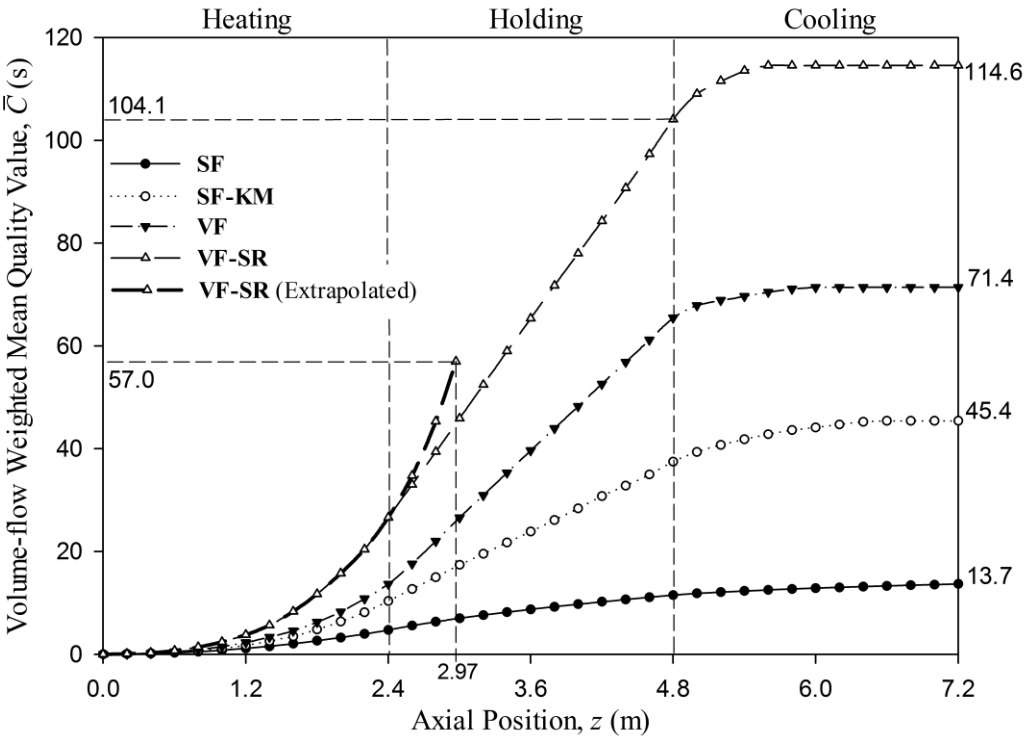

Figure 5.23. Development of mean C-value along heat-hold-cool process: T_w = 140 °C (heating); T_w = 20 °C (cooling) – process axial temperature profile shown in Figure 5.21.

Again a comparison on the basis of the minimum sterility value shows that adding a holding tube of 2.4 m length will increase F_{min} from 12.5 s to 190.9 s as shown in Figure 5.24, with the exit mean C-value rising from 26.5 s to 104.9 s as shown in Figure 5.25. In contrast, to achieve this same minimum sterility could be achieved by extending the heating tube by only ~ 0.43 m, with an average quality at exit of 48.5 s. Therefore, it can be clearly seen that a heating tube extension of 0.43 m would increase the minimum level of sterility by 178.4 s , the same as a holding tube of 2.4 m length, but with much less loss of quality (22 s compared with 78.4 s).

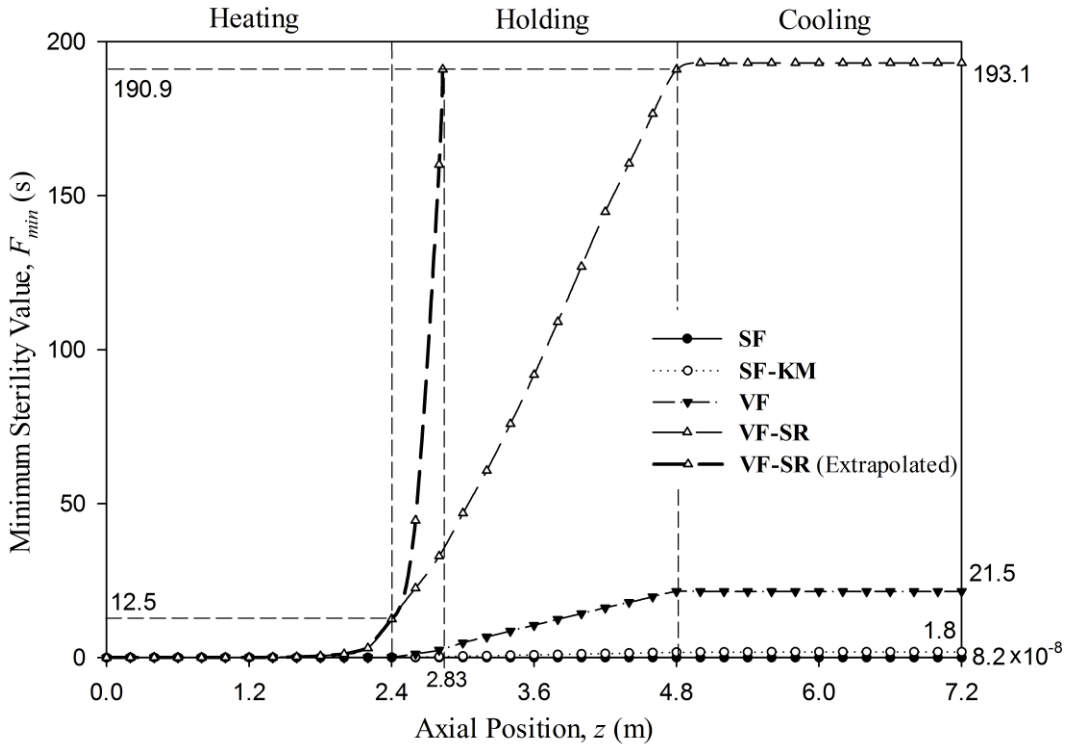

Figure 5.24. Development of minimum F-value along heat-hold-cool process: T_w = 140 °C (heating); T_w = 20 °C (cooling) – process axial temperature profile shown in Figure 5.21.

The axial profiles of mean quality along the whole process depicted in Figure 5.25 considered together with the sterility profiles in Figure 5.24 show that for an-order-of-magnitude larger minimum sterility, **VF-SR** incurs an average quality loss comparable to that of **VF** in a process of the same length. Similarly, for about 2 to 10 orders of magnitude difference in minimum sterility between **VF-SR**, **SF-KM and SF**, the **VF-SR** process incurs an average quality loss only about an order of magnitude greater. Results in Figures 5.10 — 5.12 and 5.19 — 5.20 have also shown how **VF-SR** severely limits the rise in *F* and *C* in the cooling stage. Combined together, these results indicate that **SF**, **SF-KM** and **VF** processes which would produce equivalent sterility to the **VF-SR** process would have to be extremely long by comparison and would generate orders of magnitude more quality loss. These results demonstrate that there are considerable benefits in using an extended heater and that for most applications a holding stage may not be necessary if a **VF-SR** heater is used. Hence, the whole sterilisation

process can be performed using only two relatively short heat-cool processing tubes.

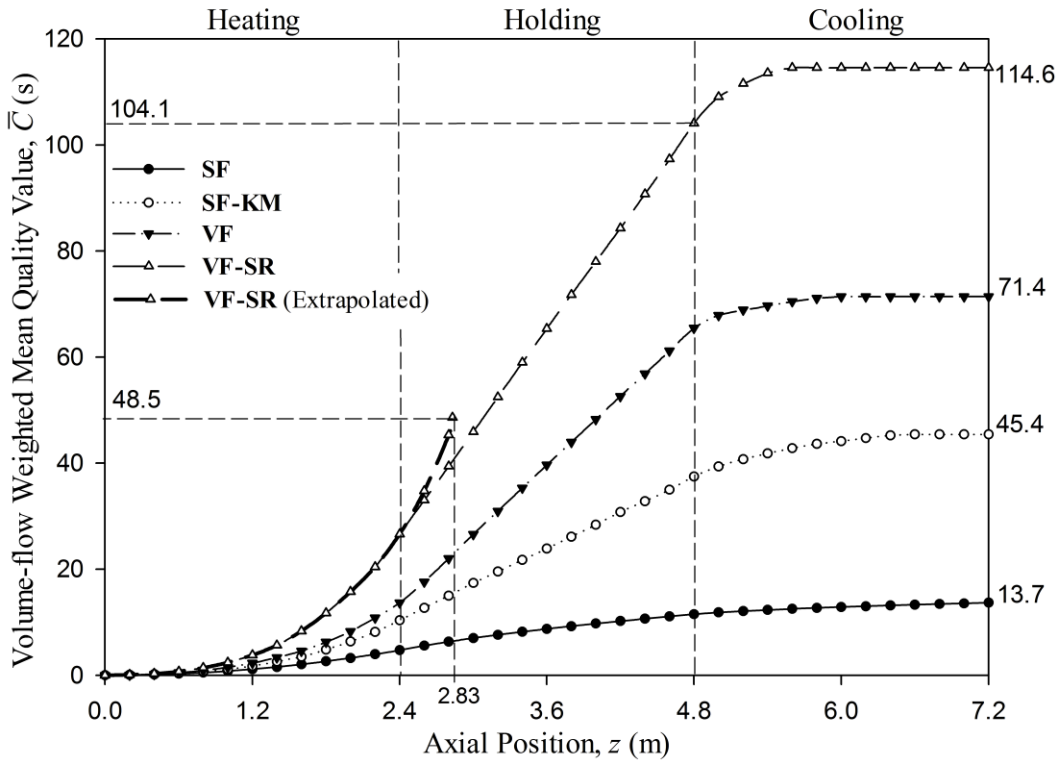

Figure 5.25. Development of mean C-value along heat-hold-cool process: T_w = 140 °C (heating); T_w = 20 °C (cooling) – process axial temperature profile shown in Figure 5.21.

To achieve a given level of sterility, the question then arises as to whether it would be better to use a vibrated holding tube, or instead use an extended vibrated heating tube and conduct all the sterilisation within the heating stage? The overall performance of an extended **VF-SR** heater is compared with that of a **VF-SR** holding tube in Figure 5.26, where the increase ΔF_{min} and the associated increase $\Delta\overline{C}$ for both tubes are plotted as a function of z. The results demonstrate that there are considerable benefits in using an extended heater and, perhaps for most applications, a holding stage may not be necessary if a **VF-SR** heating stage is used. The use of a vibrated heater would then seem to obviate the need for a holding tube which represents an additional significant advantage. However, if a holding stage is used, even though the radial temperature profile at the exit

of the vibrated heater would usually be virtually uniform, it appears that there would still be some significant advantage in vibrating the holding tube. Results in this case showed that, whilst the mean sterility achieved would be the same, vibrating the holding tube (2.4 m) would yield a minimum sterility which is ~ 65% greater (equivalent to using a 4.0 m non-vibrated holding tube).

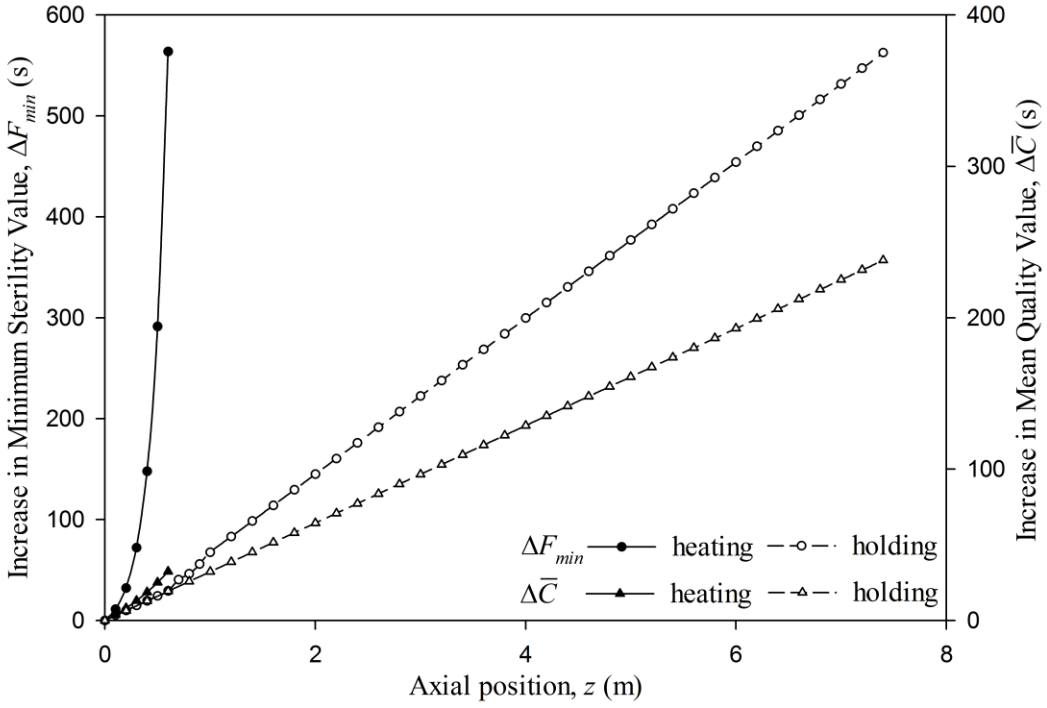

Figure 5.26. Increase in minimum sterility and mean quality arising from extending the **VF-SR** heating tube compared with using a **VF-SR** holding tube.

5.6. CONCLUSIONS

The superimposition of transverse vibratory motion with step change in oscillation orientation on the steady laminar flow of a viscous single-phase fluid, introduces chaotic fluid motion which leads to vast improvements in wall heat transfer and radial temperature uniformity. When applied to a continuous heat-hold-cool sterilisation process, these effects translate into large improvements in thermal processing uniformity and efficiency compared with a conventional process with or without an inline static mixer fitted. Simple oscillations without a change in orientation also give good improvements but they are not nearly as effective.

The novel (**VF-SR**) technique leads to fast nearly-uniform heating and cooling of the product, thus, achieving much higher levels of sterility with low loss of product quality in much shorter processing tubes, thus, obviating the need for a holding stage and overall reducing the length of the conventional heat-hold-cool sterilisation process by one or two orders of magnitude, depending on processing conditions. Vibration, therefore, appears to create processing conditions that are much more in agreement with the high temperature for short time (HTST) assumption which is often contradicted in conventional steady flow processing. This shows that the **VF-SR** technique has considerable potential in optimising the continuous sterilisation process by creating conditions for achieving HTST processing, a long-standing problem in food sterilisation.

Whilst this numerical analysis has been fairly well validated, a full experimental validation, as is usual practice, would be needed to fully confirm the benefits of oscillatory perturbations on the sterilisation process. It should also be noted that the above conclusions are only valid for single-phase flows as considered in this analysis. Heat transfer in two-phase solid-liquid flows where particle properties such as size and density are such that the mixture cannot be treated as a homogenous fluid, is much more complex and the applicability of the oscillatory perturbation technique to such flows warrants a more detailed study.

Furthermore, it can be argued that the chaotic flow would have added practical benefits: first, for the reduction of fouling because of the cleaning action that the fluid motion would create at the wall, and second in two-phase solid-liquid flow, assuming that the applicability of the oscillatory technique is proven, it would be expected to help keep solid particles in suspension and may also potentially enhance liquid-particle heat transfer. The implementation of mechanical vibration in practice should not be difficult. To avoid mechanical fatigue, the vibrated pipe should be connected to other pipework via flexible piping or flexible couplings. Whilst the use of vibration industrially may not always be feasible, in processes where this is possible, however, results indicate that benefits can be very significant.

NOTATION

A Vibration amplitude, m

C Quality value, s

$\overline{C}$ Volume-flowrate weighted mean quality value, s

C_p Specific heat capacity, J kg^{-1} K^{-1}

$C_{v\text{-}C}$ Coefficient of variation for quality value, -

$C_{v\text{-}F}$ Coefficient of variation for sterility value, -

$C_{v\text{-}T}$ Coefficient of variation for temperature, -

E_a Activation energy for viscosity, J mol^{-1}

F Sterility value, s

F_{min} Minimum sterility value at given cross–section, s

$\overline{F}$ Volume-flowrate weighted mean sterility value, s

f Vibration frequency, Hz

k_0 Pre-exponential factor, Pa s

L Tube length, m

r Radial position, m

R Radius of tube, m

R_g Gas constant, J mol^{-1} K^{-1}

t Time, s

Δt Time interval, s

T Temperature, °C

$\overline{T}$ Volume-flowrate weighted mean temperature, °C

T_{in} Inlet temperature, °C

$\overline{T}_{out}$ Volume-flowrate averaged temperature at the tube exit, °C

T_w Wall temperature, °C

u_x Pipe velocity in radial direction, m s^{-1}

$\overline{u}_{xy}$ Mean resultant velocity in radial plane, m s^{-1}

$\overline{w}$ Mean fluid inlet velocity, m s^{-1}

w Fluid velocity in axial direction, m s^{-1}

x Wall displacement, m

z Axial position, m

Greek symbols

μ Viscosity for Newtonian fluid, Pa s

ρ Density, kg m^{-3}

λ Thermal conductivity, W m^{-1} K^{-1}

ω Angular function of frequency of vibration, rad s^{-1}

Ω Frequency of step rotation of oscillation orientation, Hz

REFERENCES

Ball, C. O., Olson, F. C., 1957. *Sterilization in food technology: Theory, practice, and calculations*. McGraw-Hill, New York.

Barth, T. J., Jespersen, D. C., 1989. The design and application of upwind schemes on unstructured meshes, in 27th AIAA Aerospace Sciences Meeting, Reno, NV, Paper AIAA 89-0366.

Bateson, R. N., 1971. The effect of age distribution on aseptic processing. Chemical Engineering Progress Symposium Series, 108(67), 44-52.

Bird, R. B., Armstrong, R. C., Hassager, O., Curtiss, C. F., 1987. *Dynamics of polymeric liquids*, Vol. 1: Fluid Mechanics. 2nd Edition, John Wiley, NewYork.

Biswas, R., Strawn, R. C., 1998. Tetrahedral and hexahedral mesh adaptation for CFD problems. Applied Numerical Mathematics, 26(1), 135-151.

Chhabra, R. P., Richardson, J. F., 1999. *Non-Newtonian flow in the process industries: Fundamentals and engineering applications*. Butterworth Heinemann, Oxford.

Deshpande, N. S., Barigou, M., 2001. Vibrational flow of non-Newtonian fluids. Chemical Engineering Science, 56(12), 3845-3853.

Eesa, M., Barigou, M., 2008. CFD analysis of viscous non-Newtonian flow under the influence of a superimposed rotational vibration. Computers & Fluids, 37(1), 24-34.

Eesa, M., 2009. CFD studies of complex fluid flows in pipes. Ph.D. thesis. University of Birmingham, Birmingham, UK.

Eesa, M., Barigou, M., 2010. Enhancing radial temperature uniformity and boundary layer development in viscous Newtonian and non-Newtonian flow by transverse oscillations: A CFD study. Chemical Engineering Science, 65(6), 2199-2212.

Eesa, M., Barigou, M., 2011. CFD simulation of transverse vibration effects on radial temperature profile and thermal entrance length in laminar flow. AIChE Journal, 57(1), 51-56.

Fryer, P.J., 1997. Thermal treatment of foods, in: Fryer, P. J., Pyle, D. L., Rielly, C. D., *Chemical engineering for the food industry*. Springer, Boston, MA, pp. 331-382.

Gundogdu, M. Y., Carpinlioglu, M. O., 1999. Present state of art on pulsatile flow theory - (Part 1: Laminar and transitional flow regimes). JSME International Journal Series B-Fluids and Thermal Engineering, 42(4), 384-397.

Hobbs, D. M., Muzzio, F. J., 1997. The Kenics static mixer: a three-dimensional chaotic flow. Chemical Engineering Journal, 67(4), 153-166.

Holdsworth, S. D., 1985. Optimisation of thermal processing - a review. 4(2), 89-116.

Holdsworth, S. D., 1992. *Aseptic processing and packaging of food products*. Elsevier

Applied Science, London.

Hui, Y. H., 2006. *Handbook of Food Science, Technology, and Engineering*, vol. 3. CRC Press, Florida, US.

Jakob, M., 1949. *Heat transfer*. Wiley, New York.

Jung, A., Fryer, P. J., 1999. Optimising the quality of safe food: Computational modelling of a continuous sterilisation process. Chemical Engineering Science, 54(6), 717-730.

Kwant, P. B., Fierens, R. H. E., Vanderle. A., 1973. Non-isothermal laminar pipe flow - II. Experimental. Chemical Engineering Science, 28(6), 1317-1330.

Lyche, B. C., Bird, R. B., 1956. The Graetz-Nusselt problem for a power law non-Newtonian fluid. Chemical Engineering Science, 6(1), 35-41.

Mulley, E. A., Stumbo, C. R., Hunting, W. M., 1975. Kinetics of Thiamine degradation by heat - new method for studying reaction-rates in model systems and food products at

high-temperatures. Journal of Food Science, 40, 985-988.

Rahmani, R. K., Keith, T. G., Ayasoufi, A., 2006. Numerical study of the heat transfer rate in a helical static mixer. Journal of Heat Transfer, 128(8), 769-783.

Reed, G. F., Lynn, F., Meade, B. D., 2002. Use of coefficient of variation in assessing variability of quantitative assays. Clinical and Diagnostic Laboratory Immunology, 9(6), 1235-1239.

Saatdjian, E., Rodrigo, A. J. S., Mota, J. P. B., 2012. On Chaotic Advection in a Static Mixer. Chemical Engineering Journal, 187, 289-298.

Shrirao, P. N., Sambhe, R. U., Bodade, P. R., 2013. Convective Heat Transfer Analysis in a Circular Tube with Different Types of Internal Threads of Constant Pitch. International Journal of Engineering and Advanced Technology, 2(3), 335-340.

Sinnott, R. K., 2005. *Chemical Engineering Design: Chemical Engineering*. Elsevier Science, Oxford.

Steffe, J. F., 1996. *Rheological methods in food process engineering*. 2nd Edition. Freeman Press, East Lansing, Michigan.

Stumbo, C. R., Murphy, J. R., Cochran, J., 1950. Nature of thermal death time curves for P.A. 3679 and Clostridium Botulinium. Food Technology, 4, 321-326.

Tadepalli, S. C., Erdemir, A., Cavanagh, P. R., 2011. Comparison of hexahedral and tetrahedral elements in finite element analysis of the foot and footwear. Journal of Biomechanics, 44(12), 2337-2343.

CHAPTER 6.
DRAINAGE OF A FALLING NON-NEWTONIAN FILM UNDER SUPERIMPOSED OSCILLATIONS

Summary

The effects of superimposed sinusoidal oscillations on the drainage of a falling wall film are studied numerically by Computational Fluid Dynamics (CFD). Inelastic time-independent fluids of the Newtonian, power law and Bingham plastic types are investigated. Results show that the drainage of Newtonian films is unaffected by superimposed oscillations but the drainage of non-Newtonian films are greatly affected. The drainage of shear-thinning films and viscoplastic flilms is enhanced, whilst the flow of shear-thickening fluids is retarded. The effects of the various rheological as well as vibration parameters are studied in detail and show that the degree of enhancement is a function of vibration conditions and liquid rheology. Free drainage invariably results in a residual film draining extremely slowly on the wall in the case of viscous fluids, and an adhering static film in the case of yield-stress fluids. For high values of yield stress, residual films can have a significant thickness, thus, trapping considerable amounts of material. Mechanical oscillations are effective at reducing the thickness of this residual film potentially to a negligible value, if a sufficiently high oscillation acceleration is used.

6.1. INTRODUCTION

Fluid film drainage is defined as a progress of liquid, which was adhering to solid substrates, flowing downward by gravity (Tallmadge and Gutfinger, 1967). Film drainage problem is limited to the case in which no part of fluid is in contact with liquid bath. This problem is relevant to many industrial applications, including emptying of vessels and hoppers, lubrication, enameling, surface coating, chocolate enrobing, electroplating and surface cleaning.

This problem was first studied by Jeffreys (1930) who, ignoring the initial start-up conditions, derived a simple relationship for the local thickness δ of a Newtonian liquid film draining on a stationary semi-infinite vertical wall, thus:

$$\delta = \sqrt{\frac{\mu y}{\rho g t}} \tag{6.1}$$

where ρ and μ are, respectively, fluid density and viscosity, y is vertical position from the top of the film, g is the gravitational acceleration, and t is time. This theory is based on a number of assumptions: (i) the film is laminar and without ripples on the liquid surface; (ii) surface tension and inertia forces are neglected and flow is affected only by gravity and viscous forces; and (iii) the system is open, so pressure is uniform throughout.

Later Gutfinger and Tallmadge (1964) extended Jeffreys' work by including the acceleration term, and developed a more rigorous description which can be used for the earlier stage of drainage. The theory did not include the initial start-up phase of drainage, but included inertial effects which were found to become negligible after a very short period of time (a fraction of a second). More study with Newtonian fluid can also be seen in works by other researchers (Landau and Levich, 1942; Derjaguin, 1943; White

and Tallmadge, 1965). Solutions were then developed for the drainage of non-Newtonian fluids of power law type (Gutfinger and Tallmadge, 1965; Miladinova *et al*., 2004) or Bingham-plastic type (Gutfinger, 1964). Recently, Peralta *et al*. (2014), using generalized Newtonian fluid theory, developed relationships for the local film thickness, velocity and volumetric flowrate for a range of time-independent inelastic fluid models, including Casson, Bingham plastic and Herschel-Bulkley. None of these theories, however, included inertial or start-up effects.

In principle, fluids can be drained completely for those rheologies without a plastic character, for example, Newtonian and power law fluids. However, for viscous fluids, flow can be extremely slow and complete drainage is a challenge. Furthermore, viscoplatic fluids which exhibit an apparent yield stress are even more problematic, as the yield stress limits the extent of drainage that can be obtained under the sole effect of gravity, leading to an equilibrium unyielded solid film adhering to the wall wherein shear stresses are below the yield stress (Peralta *et al*., 2014). For significant values of yield stress, the thickness of the equilibrium film can be substantial. This is a particular challenge in industry, for example, in the emptying of vessels/hoppers filled with toothpaste (Metty, 2011), or in controlling coat thickness in dip coating or chocolate enrobing (Beckett, 2000).

Mechanical oscillations have been shown in our previous works to substantially enhance non-Newtonian fluid flow and heat transfer in pipes (Deshpande and Barigou, 2001; Eesa and Barigou, 2008; 2010; Tian and Barigou, 2015). In this chapter, a validated CFD model was used to numerically investigate the effects of mechanical oscillations on the drainage of a liquid film on a wall of arbitrary inclination. The fluids considered are time-independent inelastic fluids of Newtonian as well as non-Newtonian power law and Bingham plastic rheology. A detailed study is presented on the effects of rheological parameters (fluid consistency index, flow behaviour index, yield stress), oscillation parameters (amplitude, frequency) as well as wall inclination.

6.2. CFD MODEL

6.2.1. Rheological models

The fluids used in this study are assumed to be rheologically time-independent. Two non-Newtonian rheological models are considered, power law and Bingham plastic. The mathematical descriptions for these two models have been given in Chapter 2, by Eq. (2.1) for power law type and Eq. (2.2) for Bingham plastic type. All rheological parameters used in this chapter was summarised in Table 6.1.

Table 6.1: Rheological parameters used in simulations.

	ρ (kg m^{-3})	k (Pa s^n)	n (-)	μ_B (Pa s)	τ_0 (Pa)
power law	1000	0.5 - 50	0.5 - 1.6	-	-
Bingham plastic	1000	-	-	1	1 - 30

The Bingham model suffers from discontinuity and its implementation poses difficulties in numerical modelling. And some strategies are employed to circumvent the problem caused by the yield stress (see Section 2.1). One of the popular methods which was found to be better suited for the film drainage problem studied here, is to represent the Bingham fluid by the so-called bi-viscosity model using two finite viscosities (see Section 2.1.2). As depicted in Figure 2.3, the zero-shear region corresponding to $\tau < \tau_0$ is represented by a Newtonian fluid with a very high viscosity, μ_1; on the other hand, the flow region corresponding to $\tau \geq \tau_0$ is represented by another Newtonian fluid which has a viscosity equal to the plastic viscosity of the Bingham fluid, except for a very small region of overlap ($\tau_y - \tau_0$) which is represented by μ_1. The viscosities μ_1 and μ_2 used in this study is in a ratio of 1000 (Tanner and Milthorpe, 1983).

6.2.2. Harmonic oscillations

The effects of mechanical oscillations on the drainage of a falling liquid film inclined at an angle α to the horizontal are considered in this chapter, as illustrated in Figure 6.1. Oscillations are applied to the substrate in the direction parallel to the flow, and the wall displacement y is described by the harmonic function:

$$y = A\sin(\omega t) \tag{6.2}$$

where A is the amplitude of vibration, t is the time and ω is the angular frequency such that $\omega = 2\pi f$. The resulting linear velocity of the substrate is then:

$$u_y = \frac{\mathrm{d}y}{\mathrm{d}t} = A\omega\cos(\omega t) \tag{6.3}$$

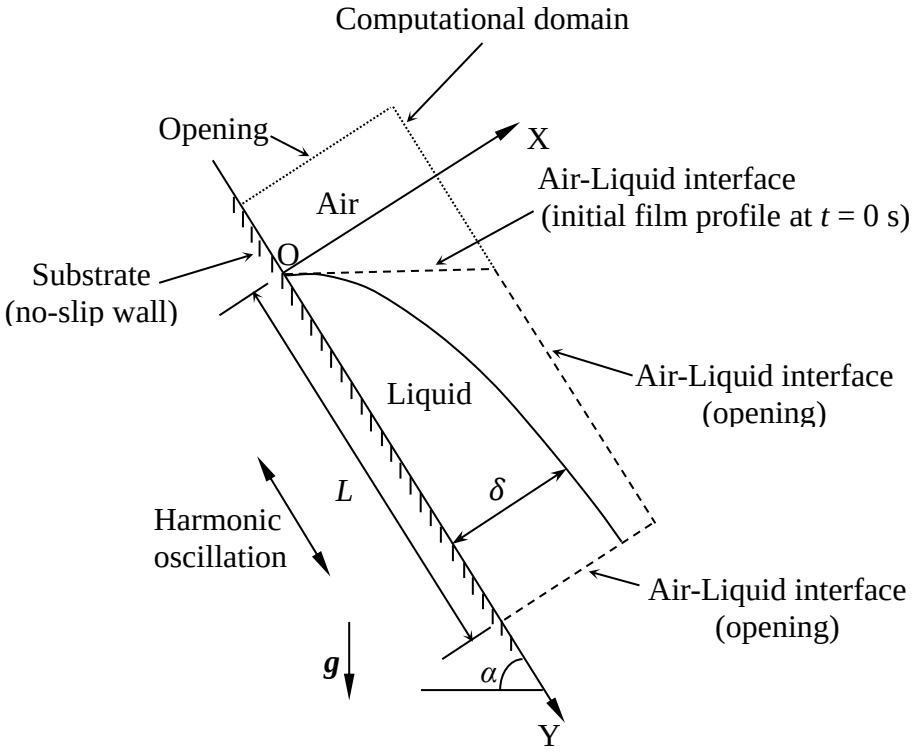

Figure 6.1. Schematic of a falling film subjected to harmonic oscillations.

6.2.3. Governing equations

For an isothermal non-evaporative process, the transport equations governing the drainage of a falling liquid film are those representing mass (Eq. (2.12)) and momentum (Eq. (2.13)). For an incompressible generalized Newtonian fluid and an open system, such equations reduce to the following form:

Continuity: $$\nabla \cdot \boldsymbol{U} = 0 \tag{6.4}$$

Moment: $$\rho \frac{\mathrm{D}\boldsymbol{U}}{\mathrm{D}t} = \nabla \eta\dot{\gamma} + \rho \boldsymbol{g} \tag{6.5}$$

where $\boldsymbol{U}$ is velocity vector and η is apparent viscosity function.

6.2.4. Theory of free drainage

The two-dimensional profile of a wall film draining under the effect of gravity is a function of liquid density, rheological parameters, drainage time and wall inclination. For a generalized power law (or Herschel-Bulkley) fluid described by the constitutive equation:

$$\tau = \tau_0 + k\dot{\gamma}^n \tag{6.6}$$

the relationship giving the local thickness at position *y* of a liquid film draining freely on a vertical plate has been derived by Peralta *et al*. (2014). Their result can be readily extended to a film inclined at an angle α with respect to the horizontal, thus:

$$\frac{\rho g \delta \sin\alpha}{k} - \frac{\tau_0}{k} - \left(\frac{y}{t\delta}\right)^n = 0 \tag{6.7}$$

when $\tau_0 = 0$, i.e. for a power law fluid, the above relationship reduces to:

$$\frac{\rho g \delta \sin\alpha}{k} - \left(\frac{y}{t\delta}\right)^n = 0$$

and the local liquid film thickness expression for power law fluid is given by:

$$\delta = \left[\left(\frac{k}{\rho g \sin\alpha}\right)^{1/n} \frac{y}{t}\right]^{\frac{n}{1+n}} \tag{6.8}$$

which was previously derived by Bird *et al*. (2007).

On the other hand, putting $n = 1$ and $k = \mu_B$ in Eq. (6.7), thus

$$\frac{\rho g \delta \sin\alpha}{\mu_B} - \frac{\tau_0}{\mu_B} - \frac{y}{t\delta} = 0$$

The film drainage relationship for a Bingham plastic fluid is obtained, as:

$$\delta = \frac{\tau_0 + \sqrt{\tau_0^{\,2} + 4\rho g y \mu_B \sin\alpha / t}}{2\rho g \sin\alpha} \tag{6.9}$$

At a given instant *t*, the mean thickness of the film is defined as:

$$\bar{\delta} = \frac{1}{L}\int_0^L \delta \mathrm{d}y \tag{6.10}$$

where L is the length of the film along the substrate, as shown in Figure 6.1.

6.3. CFD SIMULATIONS

6.3.1. Geometry and mesh

Referring to Figure 6.1, the film profile is assumed uniform in the *z* direction and, thus, the model reduces to a two-dimensional problem. The model was set up and run using the commercial software package ANSYS Workbench 14.5. The theory for free drainage described above in Section 6.2.4 assumes an infinite initial film thickness at t = 0 s. The CFD model, however, used a film of rectangular cross-section, as shown in Figure 6.1, of initial length 40 mm along *y* and initial thickness 30 mm along *x*.

The geometry was meshed with non-uniform hexahedral cells which are known to achieve a higher solution accuracy than tetrahedral meshes for the same number of cells, and provide the best resolution of a wall boundary layer with significantly fewer cells. Hexahedral elements also reduce numerical diffusion, aid convergence, and have important computing cost and stability advantages over tetrahedral elements (see for example, Tadepalli *et al*., 2011).

The computational grid was optimised through a mesh-independence study. This study started from a coarse mesh and continuously refine it until the numerical results was independent on the mesh size. The optimised mesh consisted of around 140,000 hexahedral cells. The mesh was refined near the wall using 30 inflation layers with a uniform cell size of approximately 0.05 mm increasing thereafter to 0.1 mm across the thickness of the film. In principle, one would also initially use a refined mesh near the air-liquid interface. However, because film drainage is initially very fast, the film profile shrinks very quickly within a fraction of a second and, thus, such a requirement is not necessary whilst being computationally very expensive. The overall quality of the mesh measured by its orthogonality and warpage was over 0.9, well above the generally accepted minimum value of 0.4 for a good mesh.

6.3.2. Boundary and initial conditions

Referring to Figure 6.1, apart from the solid substrate supporting the draining film where a no-slip condition was assigned, all other boundaries were treated as openings with a gauge pressure of 0 Pa. When mechanical oscillations were superimposed and additional harmonic velocity boundary conditions was assigned at the wall, as defined by Eq. (6.3). The origin of the coordinates was set at the point of intersection between the film free surface and substrate, 10 mm below the upper boundary of the computational domain to avoid liquid flowing out of the domain during oscillation. The top interface of the film was set as horizontal at t = 0 s, as shown in Figure 6.1.

6.3.3. Numerical scheme

The CFD code uses a finite-volume-based method to discretise the governing transport Eqs. (6.4) — (6.5). 'High Resolution' Advection Scheme and 'Second Order Backward Euler' transient scheme are implemented here. All simulations were executed in the transient mode. In general, a small time step of 10^{-3} s was used to enable the air-liquid interface to be treated as a narrow band with a liquid fraction varying from 0 to 1 across it, thus, ensuring a sharp well-defined film profile. For Bingham fluids, an even much smaller time step of 10^{-5} s was required to handle the large viscosity (μ_1) of the bi-viscosity model.

For drainage under vibration, free drainage is first allowed to proceed for a short period of time before oscillatory motion is superimposed, to avoid the boundary effects caused at start-up by the initial (assumed rectangular) profile of the film. This initial delay period depends on the initial thickness of the film as well as liquid properties and rheology. For the range of conditions investigated in this work, tests showed that such a period should be at least 1.6 s. Vibration is then started at time t_v = 0 s corresponding to t = 1.6 s, and allowed to proceed for a simulation period of 5 s.

Convergence of the numerical solution was assumed to be satisfactory when the root

mean square (RMS) of mass, momentum and energy residuals all reached 10^{-4} at each time step which is a good level of accuracy given the complexity of the problem. Achieving this level of convergence typically required 7 — 30 iterations per time step for vibrational flow and less than 5 iterations for free drainage without vibration. In practice, however, most of the equations generally reached RMS residual values well below the specified target ~ 2×10^{-5}.

6.4. VALIDATION OF CFD MODEL

CFX is a widely used code and has been proven to be generally stable and reliable. Nevertheless, in the absence of experimental or theoretical data on film drainage under the effects of vibration, free drainage simulations was validated against the analytical expressions introduced in the theory Section 6.2.4, Eq. (6.8) for Newtonian and power law fluids, and Eq. (6.9) for Bingham fluids. Results in Figures 6.2 — 6.4 show free drainage profiles predicted by theory and by CFD simulation for: (*a*) Newtonian fluid (Figure 6.2); (*b*) power law fluid (Figure 6.3); and (*c*) Bingham plastic fluid (Figure 6.4). For the Newtonian and power law cases, the agreement is excellent throughout. For the Bingham plastic fluid, however, there is excellent agreement over most of the film profile except at the top where there is a significant departure of the theoretical curve from the CFD prediction. This is probably attributed mainly to inertial effects which are not included in the analytical solution and, hence, the film interface near the top remains flat during drainage. Such effects, however, are taken into consideration by CFD which predicts a realistic parabolic profile throughout.

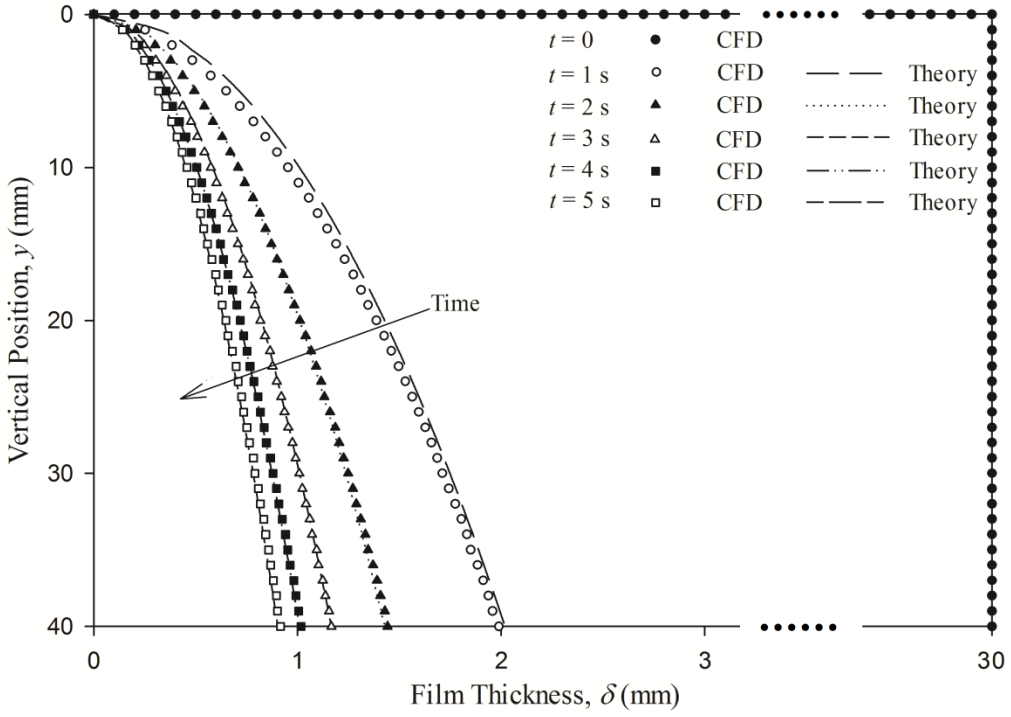

Figure 6.2. Free-drainage profile history of a Newtonian film:
μ = 1 Pa s; α = 90 deg.

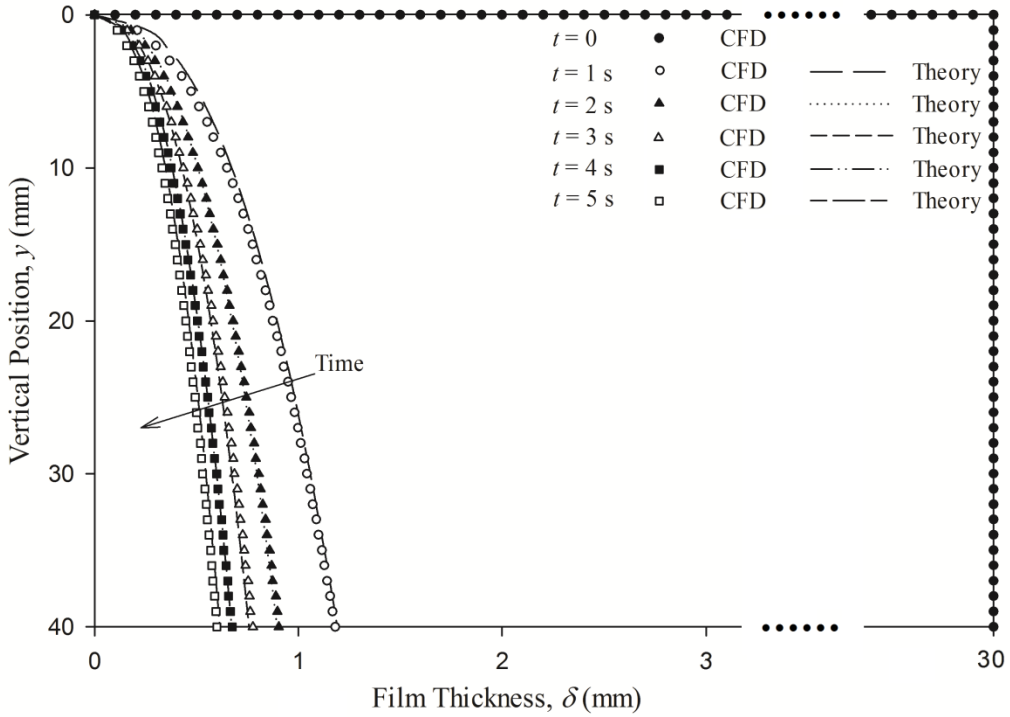

Figure 6.3. Free-drainage profile history of a power law film: k = 1 Pa s$^{0.7}$; n = 0.7; α = 90 deg.

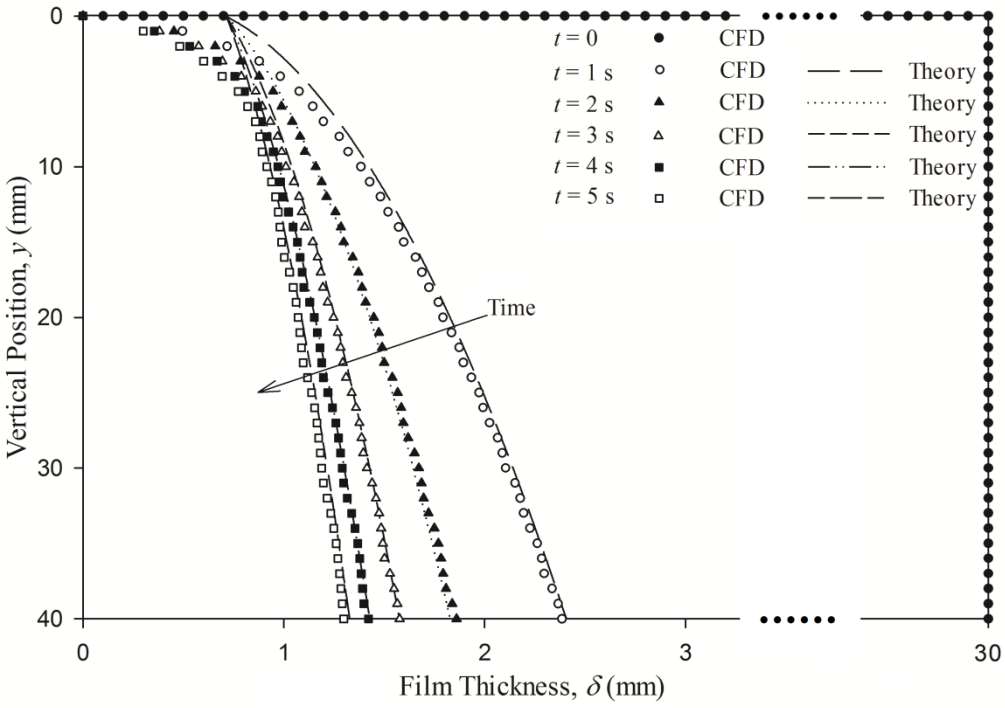

Figure 6.4. Free-drainage profile history of a Bingham plastic film: μ_B = 1 Pa s; τ_0 = 7 Pa; α = 90 deg.

6.5. RESULTS AND DISCUSSION

6.5.1. Power law fluids

6.5.1.1. Effects of vibration amplitude and frequency

The instantaneous film profile corresponding to t_v = 5 s is plotted as a function of vibration amplitude and frequency, respectively, in Figures 6.5 and 6.6. Increasing vibration amplitude or frequency leads to much thinner film profiles compared to free film drainage, but the effects are clearly non-linear.

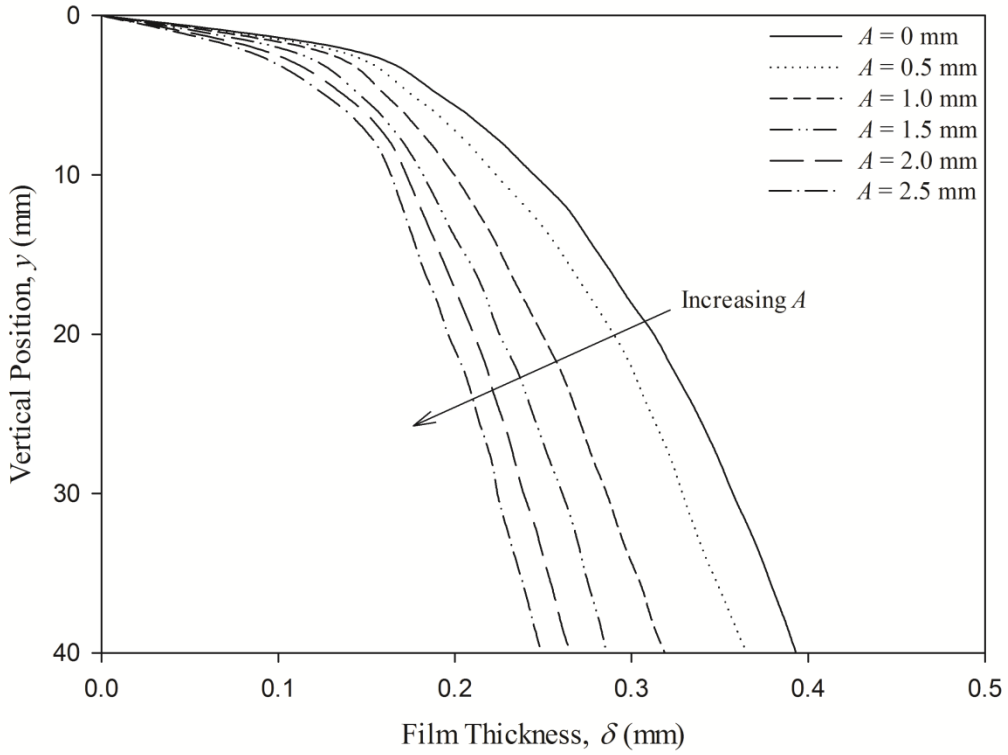

Figure 6.5. Effects of oscillation amplitude A on profile of a power law film: t_v = 5 s; k = 1 Pa s$^{0.5}$; n = 0.5; f = 20 Hz; α = 90 deg.

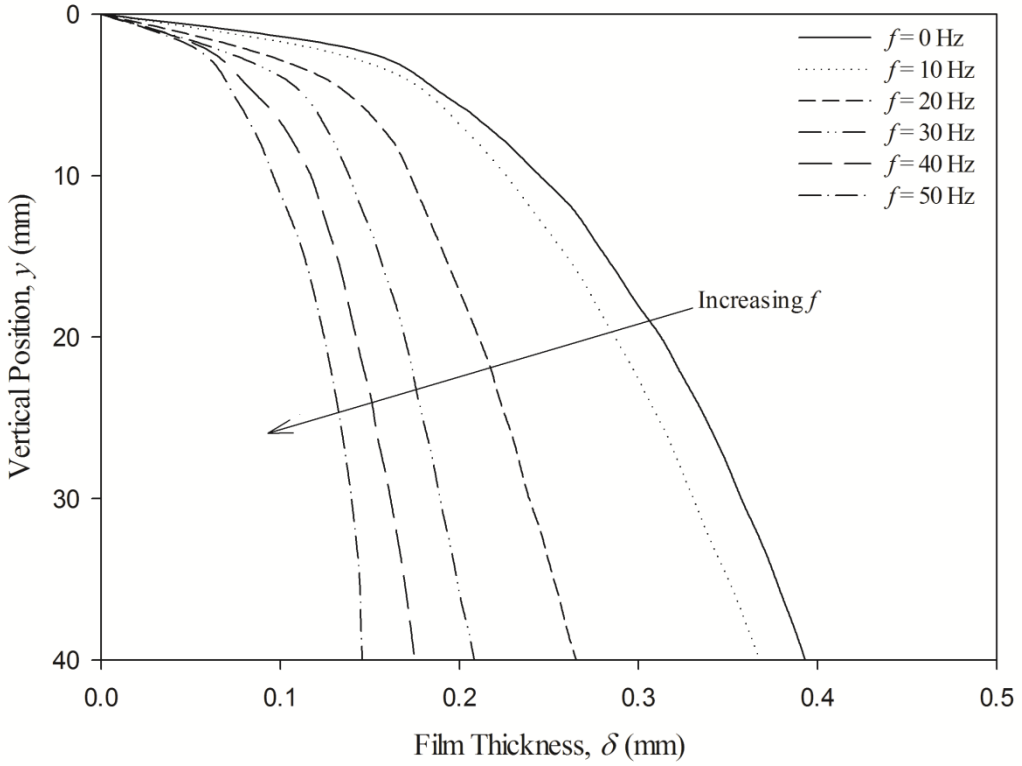

Figure 6.6. Effects of oscullation frequency f on profile of a power law flim: t_v = 5 s; k = 1 Pa s$^{0.5}$; n = 0.5; A = 2 mm; α = 90 deg.

Temporal variations of the mean film thickness are plotted in Figures 6.7 and 6.8, showing a much faster initial drainage rate as A and f increase, but in each case the effect reduces substantially as drainage proceeds, i.e. vibration becomes less effective as the film gets thinner. As what can be observed in Figures 6.5 and 6.6, as oscillation frequency or amplitude increases, mechanical vibration is more effective in enhancing the drainage comparing to free drainage of shear-thinning liquid through the vibration period (5 s).

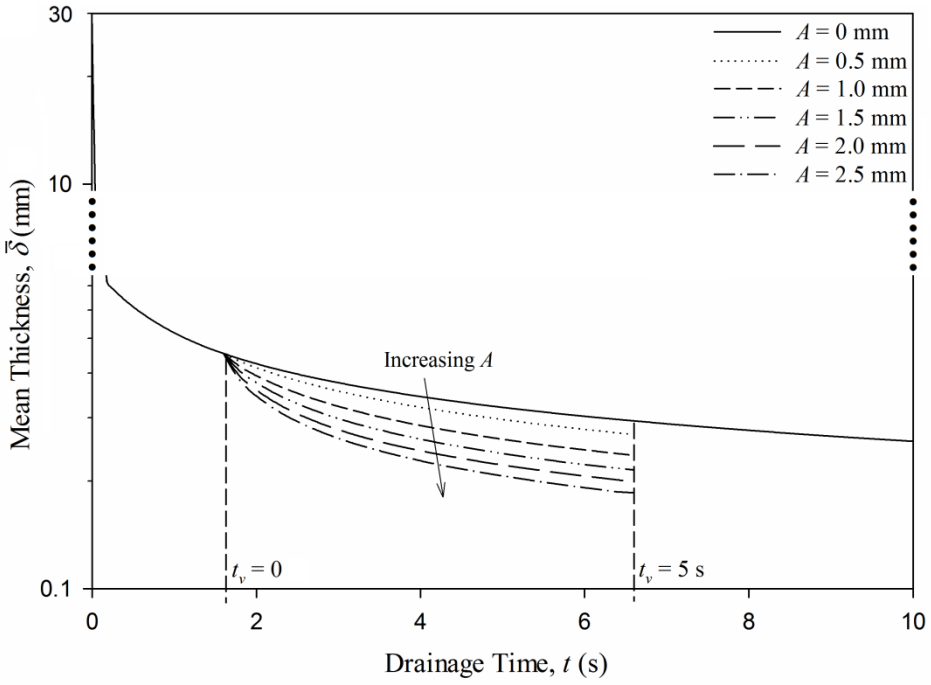

Figure 6.7. Effects of oscillation amplitude A on drainage transient of a power law film: k = 1 Pa s$^{0.5}$; n = 0.5; f = 20 Hz; α = 90 deg.

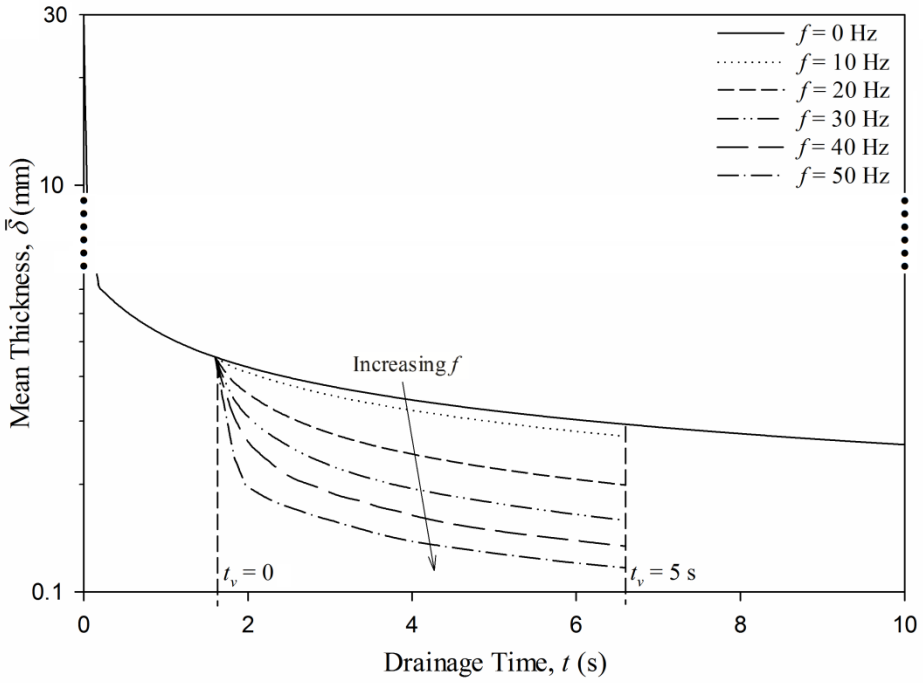

Figure 6.8. Effects of oscillation frequency f on drainage transient of a power law film: k = 1 Pa s$^{0.5}$; n = 0.5; A = 2 mm; α = 90 deg.

The drainage enhancement ratio, E, is defined as the ratio of flowrate in the vibrated film, Q_{Vib}, to the flowrate in the static (non-vibrated) film, Q_{Free}, both averaged over the vibration period (5 s), thus:

$$E = Q_{Vib} / Q_{Free} \tag{6.11}$$

The effects of vibration amplitude and frequency on drainage enhancement are represented in Figure 6.9. An increase in A or f generates higher enhancement ratios tending, for a given power law rheology, to a limiting value as maximum fluid structural breakdown is reached and no further significant reductions in viscosity can be achieved by the extra oscillatory shearing.

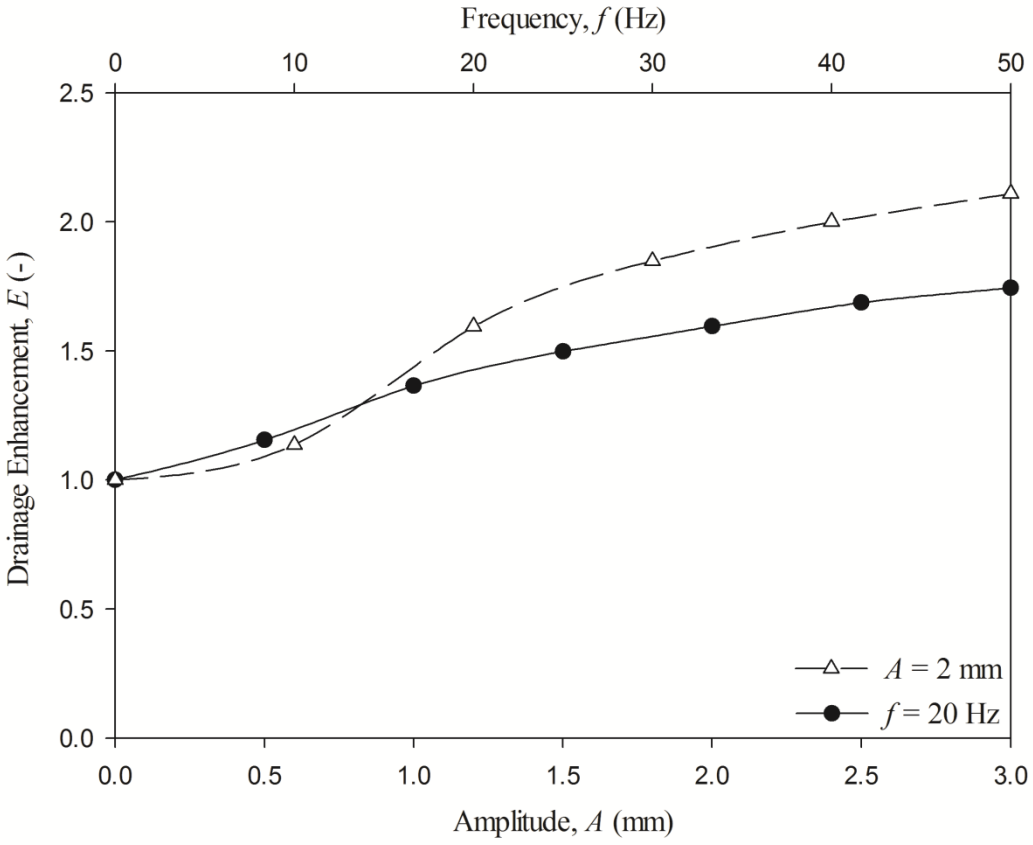

Figure 6.9. Effects of oscillation amplitude A and frequency f on drainage enhancement ratio for a power law film:
k = 1 Pa s$^{0.5}$; n = 0.5; t_v = 5 s; α = 90 deg.

Results presented in Table 6.2 summarise simulations of the drainage of a power law film under widely different conditions of vibration amplitudes and frequencies that give the same value of the peak acceleration $A\omega^2$. For a given fluid, the same enhancement ratio is obtained under all these conditions indicating that vibration forced drainage is a dynamic process governed by the acceleration of the harmonic oscillations.

Table 6.2. Drainage enhancement corresponding to a constant harmonic peak acceleration for a power law fluid.

A (mm)	f (Hz)	ω ($2\pi f$) (rad s^{-1})	$A\omega^2$ (mm s^{-2})	Drainage Enhancement, E (-) power law fluid: k = 1 Pa $s^{0.5}$; n = 0.5
2	10	62.83	7896	1.154
0.888	15	94.25	7888	1.149
0.5	20	125.66	7896	1.154
0.32	25	157.08	7896	1.150
0.222	30	188.50	7888	1.146

6.5.1.2. Effects of fluid consistency index

The index k is a measure of the consistency of the fluid, i.e. the higher the k the more viscous the fluid. For a static film, the history of the mean film thickness is depicted in Figure 6.10 for various values of k. As expected, drainage rates are faster at lower k values. In the initial stage, drainage is very fast as film thickness reduces sharply in a fraction of a second; this is followed by slow drainage where $\bar{\delta}$ tends to zero over a much longer, theoretically infinite, time (Eq. (6.8)). Superimposed oscillatory motion of

the film promotes its drainage and thinning of shear-thinning types, as shown in Figure 6.10, where for a given k value, the vibrated drainage curve lies much below its static counterpart implying a considerable enhancement in film drainage.

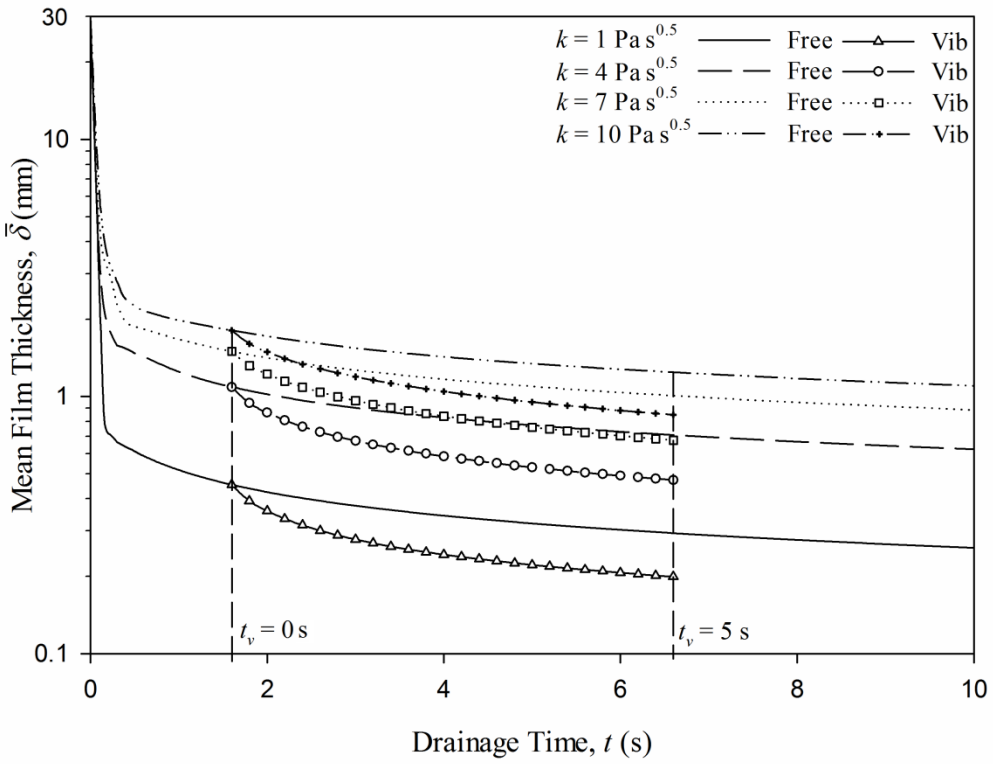

Figure 6.10. Effects of fluid consistency index k on drainage transient of a power law film:

n = 0.5; A = 2 mm; f = 20 Hz; α = 90 deg.

Increasing the value of k leads to higher flow enhancement ratios reaching values close to 2.0 over the range considered (Figure 6.11), indicating that mechanical oscillation is relatively somewhat more effective with more viscous fluids. For a given (A, f) pair of values, however, the trend levels off at high values of k which are typical of many thick fluids such as polymer solutions, paints, slurries, molten chocolate and purées (Holdsworth, 1993).

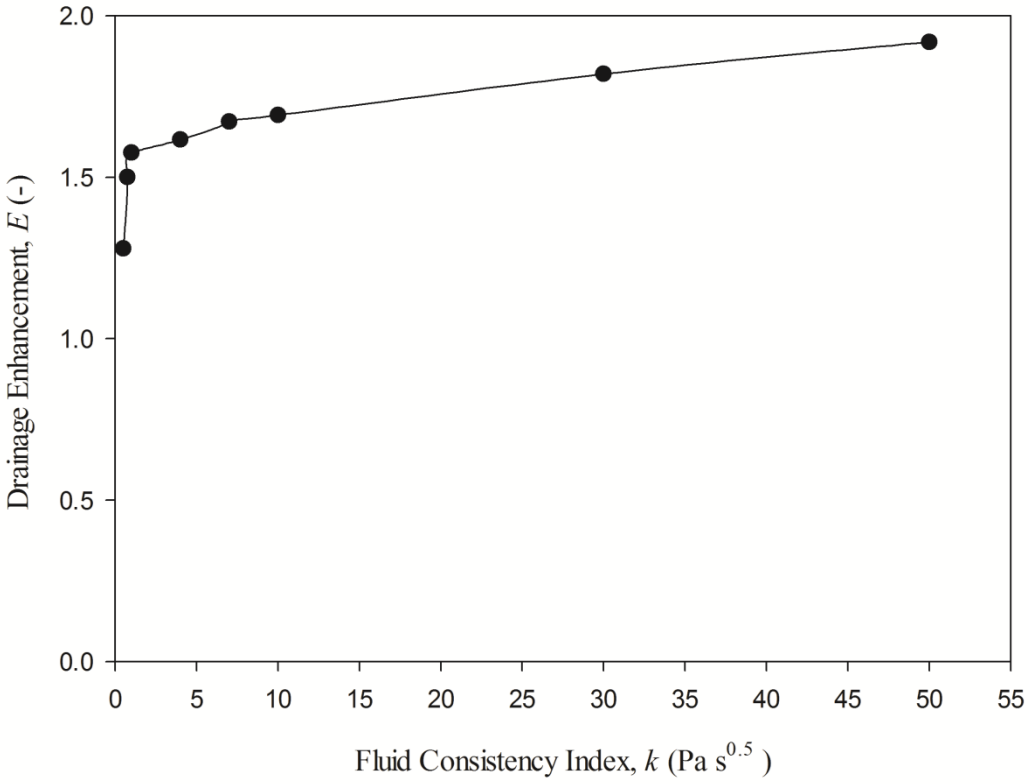

Figure 6.11. Effects of fluid consistency index k on drainage enhancement ratio for a power law film:
n = 0.5; A = 2 mm; f = 20 Hz; t_v = 5 s; α = 90 deg.

6.5.1.3. Effects of flow behaviour index

The flow behaviour index n is a measure of the degree of non-Newtonian behaviour; the greater the departure from unity the more pronounced are the non-Newtonian properties of the fluid. The history of the mean film thickness is depicted in Figure 6.12 for various values of n. In the initial stage, drainage is very fast as film thickness reduces sharply in a fraction of a second; this is followed by slow drainage. The drainage is promoted for shear-thinning fluids, retarded for shear-thickening fluids, and unaffected for Newtonian by superimposed oscillatory motion of the film, as shown in Figure 6.12.

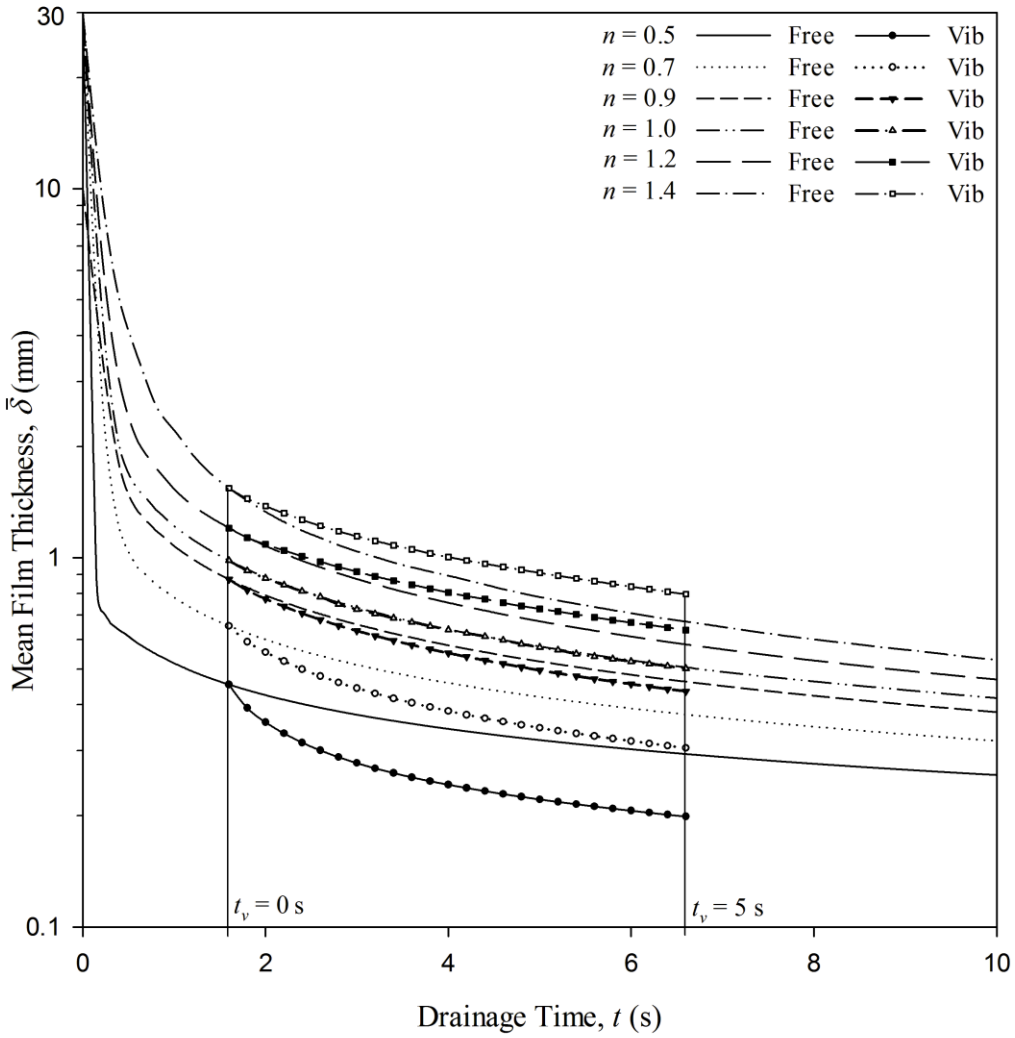

Figure 6.12. Effects of flow behaviour index n on drainage transient of a power law film: k = 1 Pa s^n; A = 2 mm; f = 20 Hz; α = 90 deg.

The drainage enhancement ratio varies with n as shown in Figure 6.13. Here, it can be seen that E is very sensitive to changes in n. In fact, the flow behaviour index has much more influence on drainage enhancement than the fluid consistency index, k. For shear-thinning or pseudoplastic fluids (n < 1), a reduction in n causes an almost exponential increase in drainage. For shear-thickening or dilatant fluids (n > 1), Figure 6.13 reveals that the superimposed oscillations lead to a negative drainage enhancement, i.e. drainage retardation whereby $Q_{Vib} < Q_{Free}$. This confirms the hypothesis that for fluids with a shear-rate dependent viscosity, it is the extra shear-thinning (or thickening)

induced by the oscillations which is responsible for the changes in the mean drainage rate, as previously reported for flow in pipes (Eesa and Barigou, 2008). For $n = 1$ the fluid is Newtonian and there is no drainage enhancement ($E = 1$).

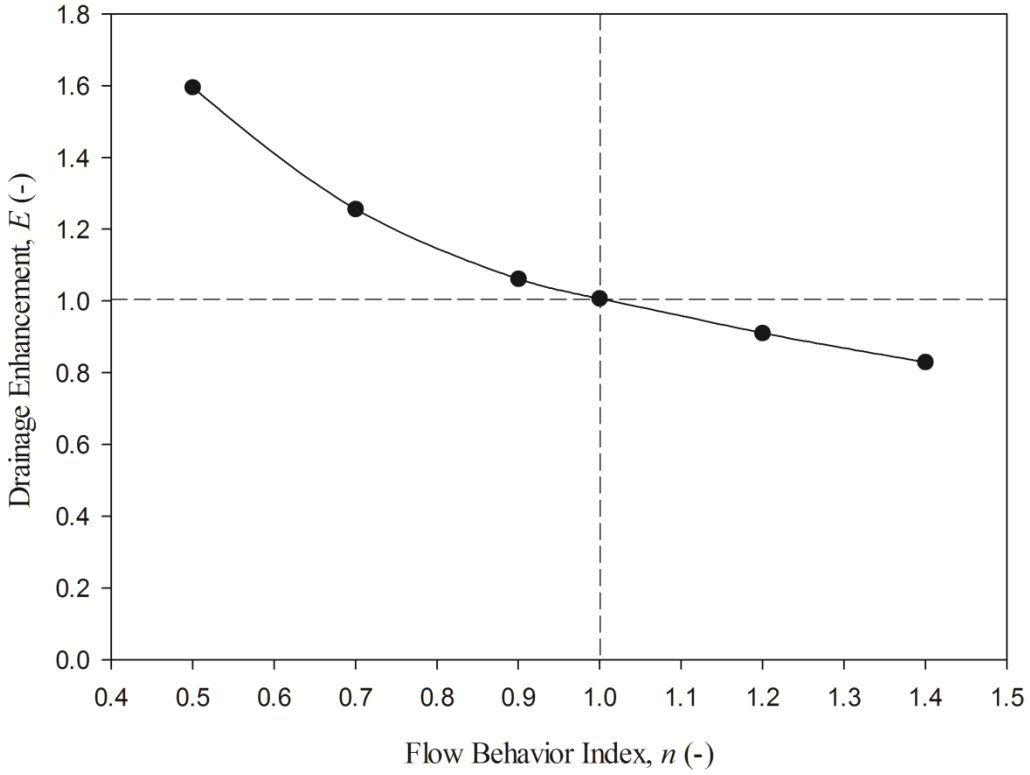

Figure 6.13. Effect of flow behavior index n on drainage enhancement ratio for a power law film:
$k = 1$ Pa s^n; $A = 2$ mm; $f = 20$ Hz; $t_v = 5$ s; $\alpha = 90$ deg.

6.5.1.4. Effects of wall inclination

The effects of changing the inclination of the falling film are depicted in Figure 6.14. Reducing the film inclination angle α with respect to the horizontal (see Figure 6.1) from 90 degrees down leads to a slow gradual increase in drainage enhancement relative to free drainage. Counterintuitively perhaps, however, at some critical angle (around 10 degrees for the particular fluid considered here), E starts to increase rapidly tending to infinity as $\alpha \to 0$. This does not imply that vibrating at low angles is better, but rather as

the substrate inclination approaches a horizontal position, the forced oscillatory drainage becomes small and at the same time free drainage tends to zero and, hence, $E \to \infty$. Therefore, it is more efficient to use vibration at the smallest inclination possible (i.e. highest α) where both free drainage as well as forced drainage would be fastest and the amount of fluid removal from the substrate is largest.

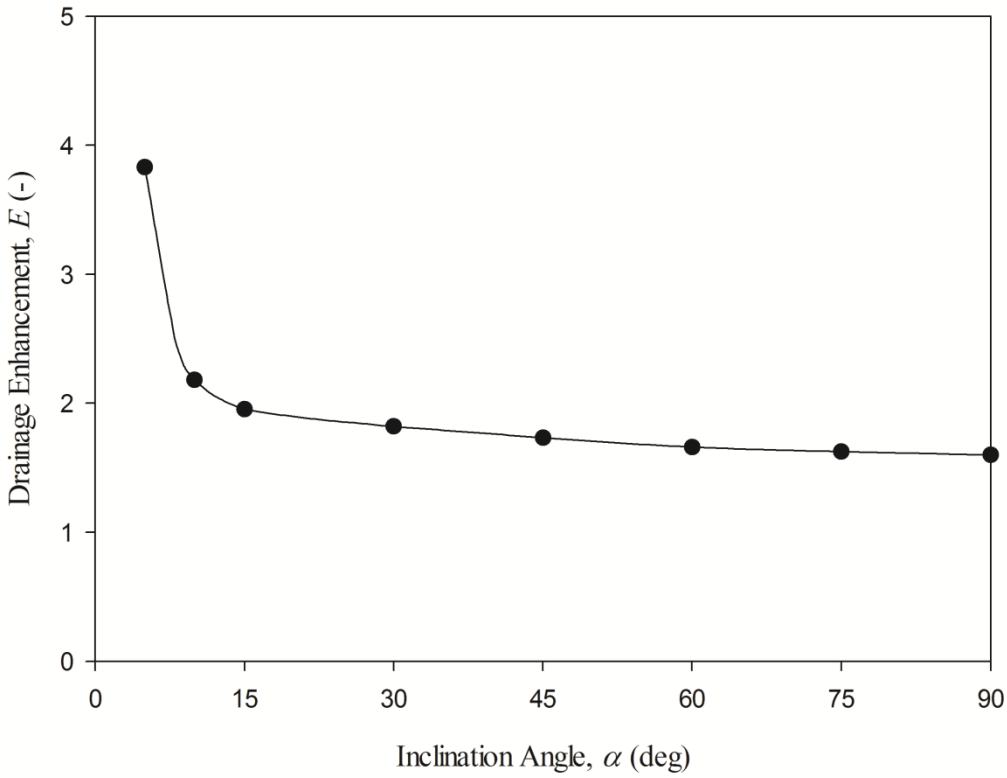

Figure 6.14. Effect of inclination angle α on drainage enhancement ratio for a power law film:
k = 1 Pa s$^{0.5}$; n = 0.5; A = 2 mm; f = 20 Hz; t_v = 5 s.

6.5.2. Bingham plastic fluids

6.5.2.1. Effects of vibration amplitude and frequency

The temporal profile of a free draining Bingham plastic film predicted by CFD is depicted in Figure 6.15 for a fairly high yield stress of 30 Pa.

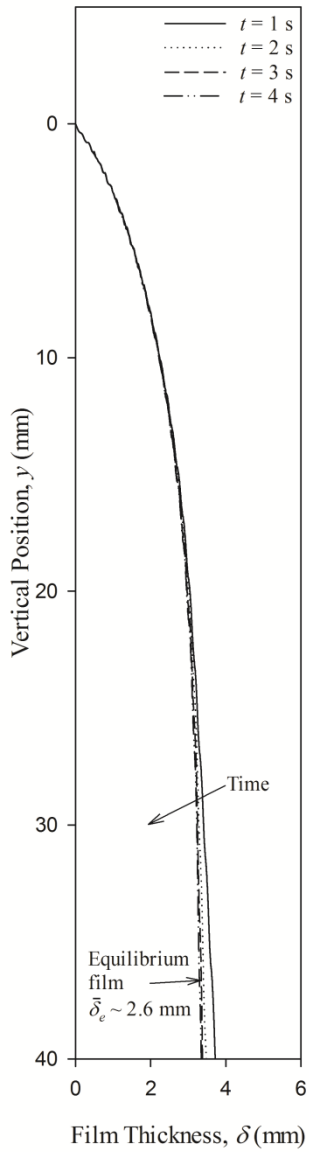

Figure 6.15. Free-drainage profile history of a Bingham plastic film:
μ_B = 1 Pa s; τ_0 = 30 Pa.

After a short period of time, drainage stops leading to an equilibrium film with a mean thickness $\bar{\delta}_e$ ~ 2.6 mm after approximately 1.3 s of free drainage (corresponding to a 0.01 point slope on the drainage transient). Results plotted in Figure 6.16 show that a Bingham fluid is affected by vibration amplitude and frequency in a similar way to a power law fluid, i.e. an increase in *A* or *f* leads to significantly enhanced drainage.

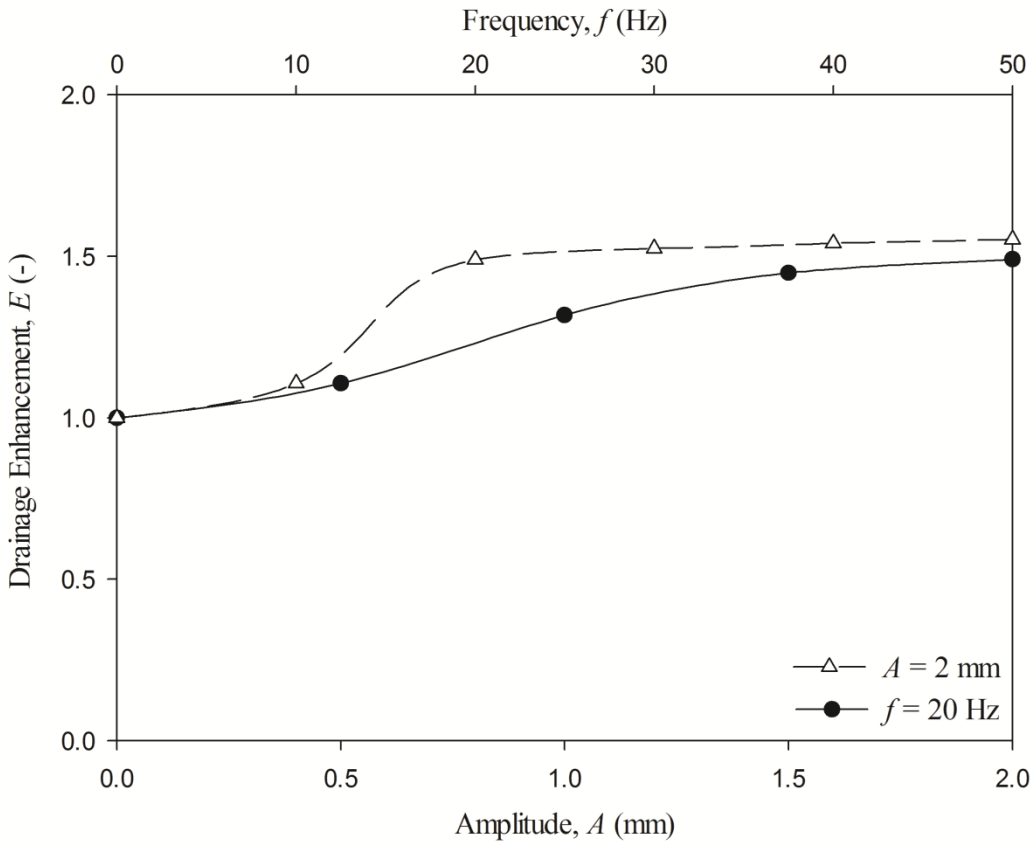

Figure 6.16. Effects of oscillation amplitude A and frequency f on drainage enhancement ratio for a Bingham plastic film:
μ_B = 1 Pa s; τ_0 = 5 Pa; t_v = 5 s; α = 90 deg.

Results presented in Table 6.3 summarise simulations of the drainage of a Bingham plastic film under widely different conditions of vibration amplitudes and frequencies that give the same value of the peak acceleration $A\omega^2$. For a given fluid, the same enhancement ratio is obtained under all these conditions indicating that vibration forced drainage is a dynamic process governed by the acceleration of the harmonic oscillations.

Table 6.3. Drainage enhancement corresponding to a constant harmonic peak acceleration for a Bingham plastic fluid.

A (mm)	f (Hz)	ω ($2\pi f$) (rad s^{-1})	$A\omega^2$ (mm s^{-2})	Drainage Enhancement, E (-)
				Bingham plastic fluid: μ_B = 1 Pa s; τ_0 = 5 Pa
2	10	62.83	7896	1.137
0.888	15	94.25	7888	1.146
0.5	20	125.66	7896	1.145
0.32	25	157.08	7896	1.149
0.222	30	188.50	7888	1.144

6.5.2.2. Effects of yield stress

The variations of E as a function of yield stress are plotted in Figure 6.17, showing an almost exponential rise in drainage enhancement as a function of τ_0. The effects are similar to those caused by reducing the index n of a power law fluid, as shown in Figure 6.13. It should be pointed out that, similar to a pseudoplastic fluid, a Bingham plastic fluid exhibits an apparent viscosity that decreases hyperbolically with increasing shear rate, thus:

$$\begin{cases} \eta = \mu_B + \tau_0/\dot{\gamma}, & \text{for} \quad \tau > \tau_0 \\ \eta \to \infty, & \text{for} \quad \tau \le \tau_0 \end{cases} \tag{6.12}$$

At very low shear rates, the apparent viscosity is effectively infinite just before yielding occurs and flow commences. It is thus possible to regard these materials as possessing a particular type of shear thinning, hence, the similarity in behaviour with power law fluids

under the influence of vibration.

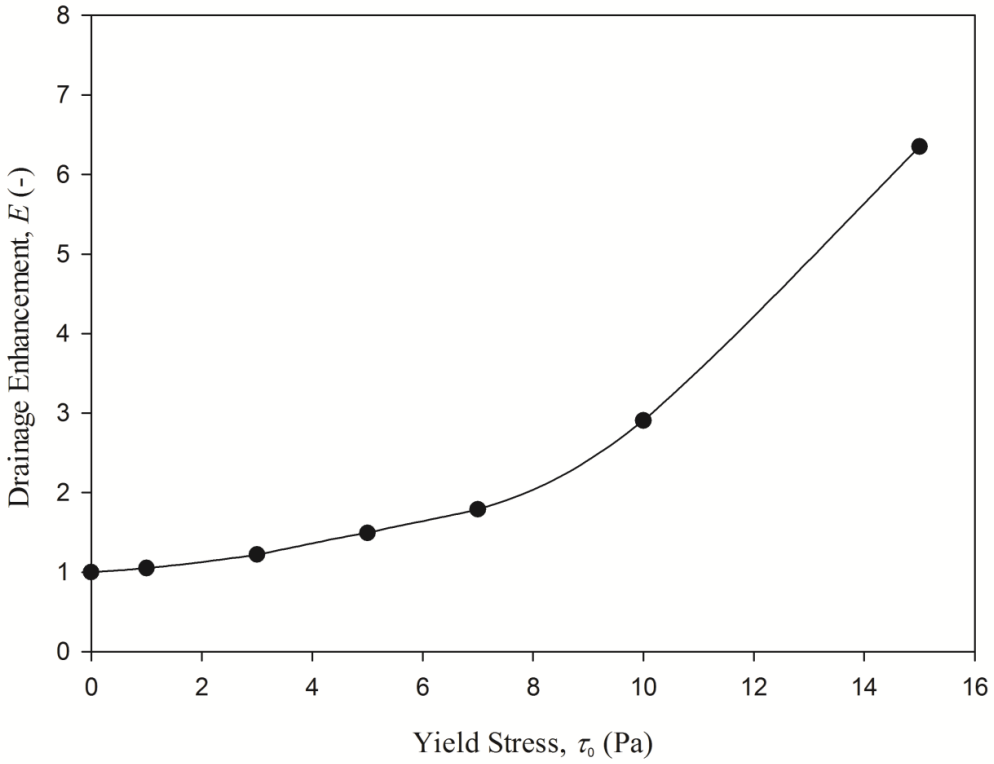

Figure 6.17. Effects of yield stress τ_0 on drainage enhancement ratio for a Bingham plastic film:
μ_B = 1 Pa s; A = 2 mm; f = 20 Hz; t_v = 5 s, α = 90 deg.

The mean thickness of a Bingham free-falling film decreases as drainage proceeds according to the history curves depicted in Figure 6.18, and more slowly so for larger values of τ_0. Drainage is initially extremely fast but slows down dramatically after a very short lapse of time, leading to a plateau where the film reaches an equilibrium thickness beyond which there is no further free drainage. At this point the weight of the residual film is supported by the wall shear stress. Such an equilibrium thickness is larger for larger values of yield stress. Superimposing oscillatory motion enables drainage to proceed further, however, leading to considerable thinning of the residual film, depending on the value of yield stress and the vibration parameters used. A

vibrated-film drainage history curve is shown in Figure 6.18. And it is worth to note that for τ_0 = 30 Pa, the mean equilibrium film thickness, which is reached after 1.3 s of the free drainage process, is reduced from 2.6 mm to 1.0 mm after 5 s of vibration using A = 2mm and f = 20 Hz. In fact, drainage stops completely after approximate 13.5 s of oscillation when $\bar{\delta}_e$ ~ 0.8 mm.

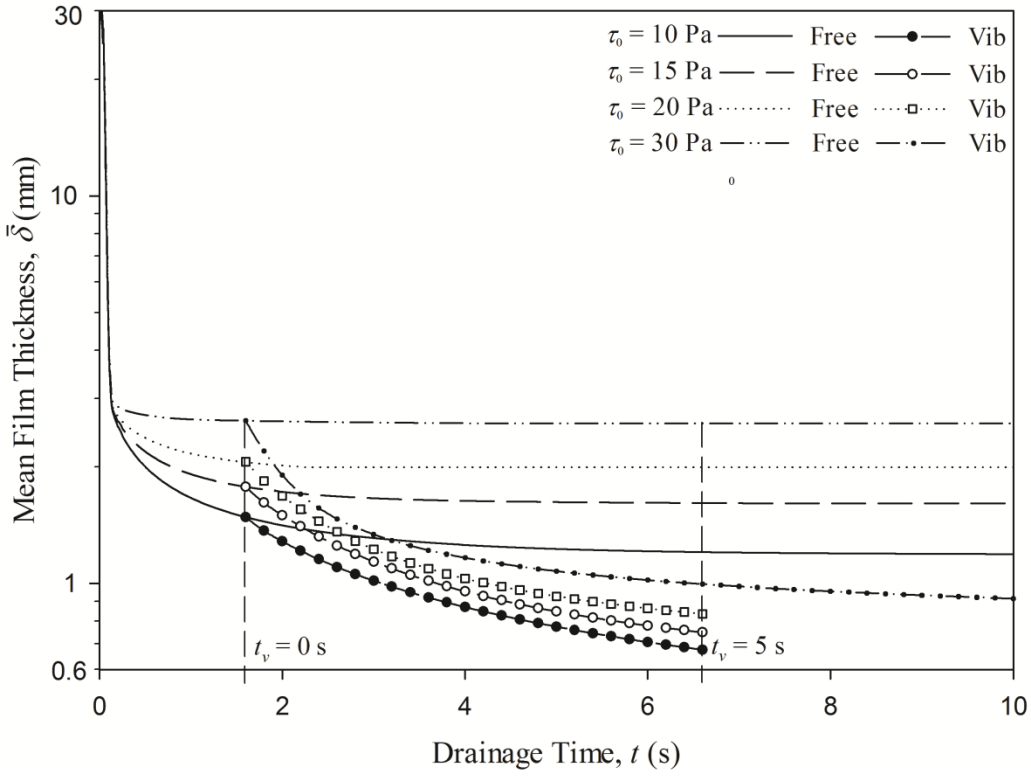

Figure 6.18. Effects of yield stress τ_0 on drainage transient of a Bingham plastic film: μ_B = 1 Pa s; A = 2 mm; f = 20 Hz; α = 90 deg.

6.5.3. Emptying of hoppers filled with viscous fluids

Based on the discussion in Sections 6.5.1 and 6.5.2, it can be concluded that mechanical oscillation is potential of affecting the drainage of non-Newtonian liquid films on both vertical and inclined substrates. Although the investigations have been sufficient to predict the effectiveness of vibration in emptying the vessel or hopper, a geometry, which are obtained by extruding one degree in azimuthal direction from a joint planar

geometry consisting of one vertical and one inclined boundary (shown in Figure 6.19), is still employed to study the performance of mechanical oscillation in increasing the flowrate of liquid film in vessel.

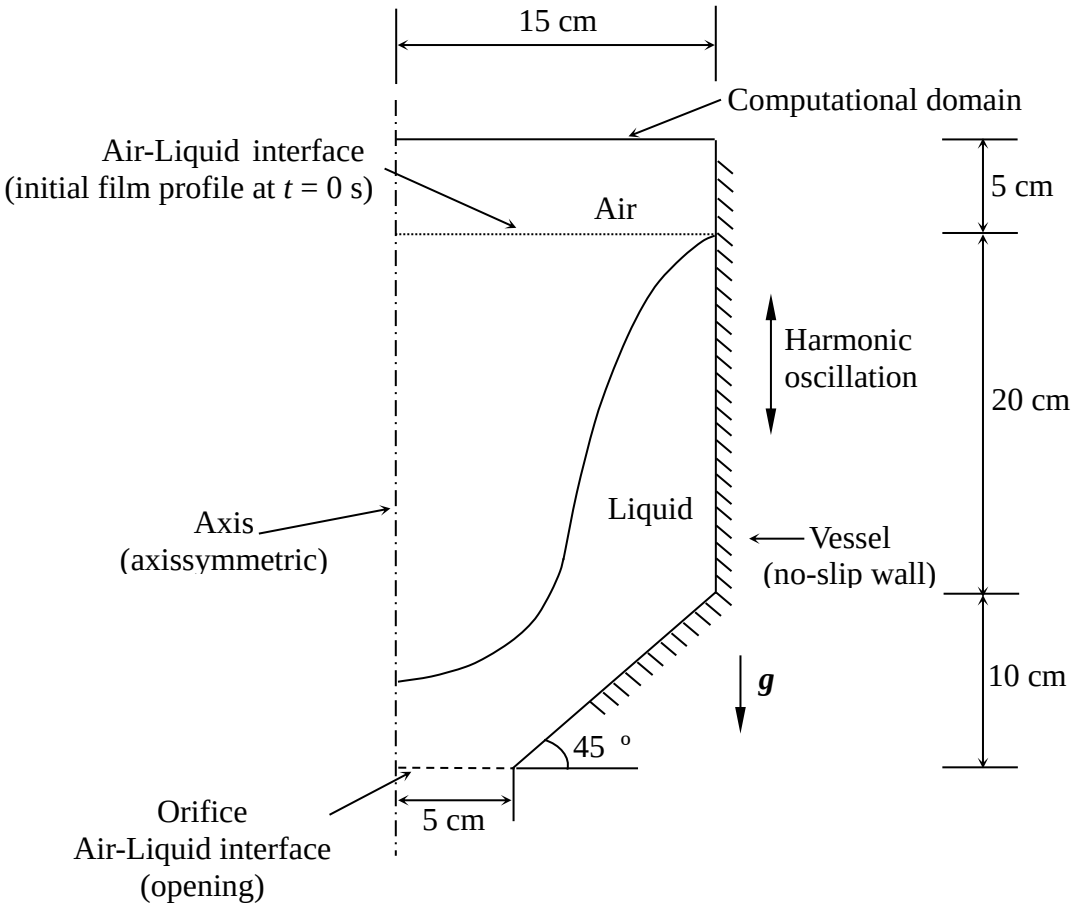

Figure 6.19. Schematic of drainage in a vessel subjected to harmonic oscillations.

As that detailed investigations have been presented above, only one pair of simulations (i.e. free drainage case and its corresponding drainage under mechanical oscillation with one pair of oscillation frequency, 20 Hz and amplitude, 2 mm) were executed to demonstrate the effect of oscillation on enhancing the drainage of power law fluid (k = 10 Pa $s^{0.5}$, n = 0.5).

As depicted in Figure 6.19, vessel is a closed geometry and does not suffer the boundary effect. However, for consistency, oscillation is still imposed on the vessel after free drainage of 1.6 s. Figure 6.20 depicted the history of the mean film thickness, and it can be clearly concluded that oscillation is effective in emptying the vessel for a shear-thinning fluid.

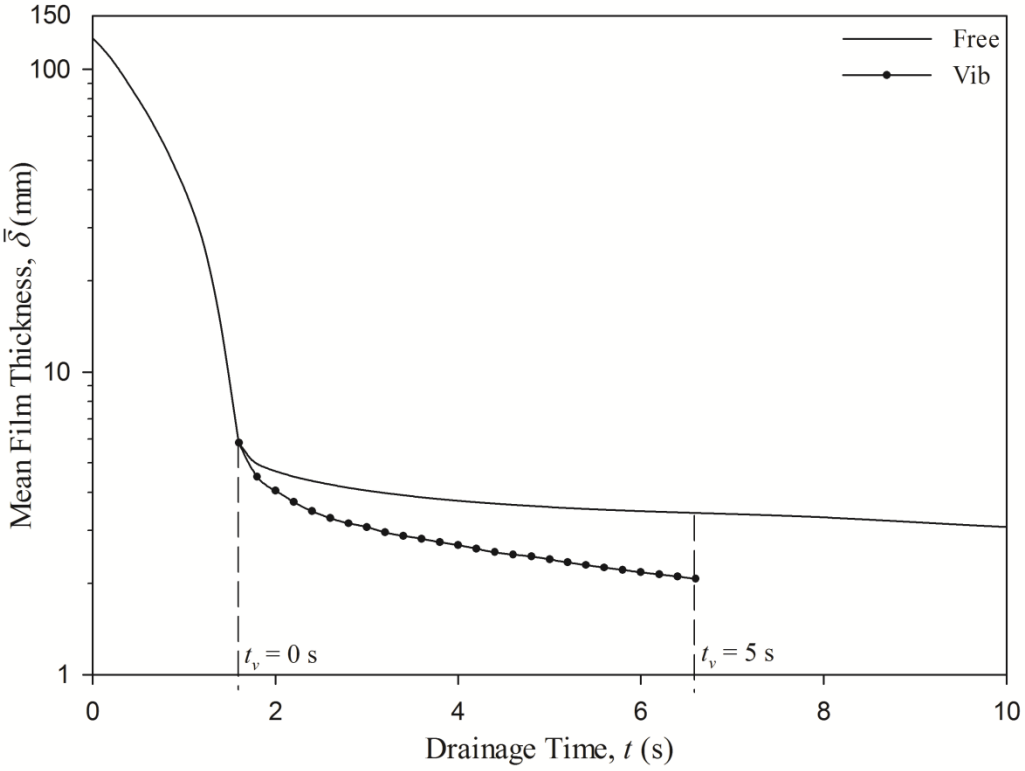

Figure 6.20. Drainage transient of a power law film in a vessel:
k = 10 Pa s$^{0.5}$; n = 0.5; A = 2 mm; f = 20 Hz.

6.6. CONCLUSIONS

A CFD model was used to simulate the drainage of a wall liquid film. Validation of free drainage simulations against analytical theory showed that the model was accurate and reliable. Whilst Newtonian fluids are not affected, the superimposition of harmonic oscillations increases the rate of drainage in non-Newtonian pseudoplastic (shear-thinning) films by a substantial factor, depending on the rheology of the fluid and vibration intensity. Shear-thickening fluids, however, undergo retardation in drainage when subjected to vibration. Viscoplatic fluids, by virtue of their apparent yield stress, display shear-thinning characteristics similar to pseudoplastic fluids, and their drainage is affected by mechanical oscillation in a similar way. In particular, for a given fluid rheology, power law or Bingham plastic, the same enhancement ratio achieved is obtained under conditions of identical peak acceleration.

The emptying of highly viscous non-Newtonian fluids including yield-stress fluids from vessel and hoppers is a challenging industrial problem as free drainage invariably results in a residual film draining extremely slowly on the wall in the case of viscous fluids, and a static film in the case of yield-stress fluids. For high values of yield stress, equilibrium films can have a significant thickness, thus, trapping considerable amounts of material as well as making cleaning more difficult. Harmonic oscillations are effective at reducing the thickness of this equilibrium film potentially to a negligible value, if a sufficiently high vibration acceleration is used. In addition to its potential for assisting the emptying of vessels filled with complex fluids, vibration could also be employed as a tool for controlling the thickness of films in surface coating applications.

NOTATION

A Vibration amplitude, m

$A\omega^2$ Peak acceleration, m s^{-2}

f Vibration frequency, Hz

k Fluid consistency index, Pa s^n

L Film length, m

n Flow behaviour index, -

Q_{Free} Time-averaged flowrate over the non-vibrated period, m^2 s^{-1}

Q_{Vib} Time-averaged flowrate over the vibration period, m^2 s^{-1}

t Time, s

t_v Vibration time, s; $t_v = t + 1.6$ s

u_y Velocity in radial direction, m s^{-1}

x Position perpendicular to the substrate, m

y Position along the substrate, m

Greek symbols

α Inclination angle, deg

δ Local film thickness, m

$\bar{\delta}$ Mean film thickness, m

$\bar{\delta}_e$ Mean equilibrium film thickness, m

μ Viscosity for Newtonian fluid, Pa s

μ_B Plastic viscosity for Bingham plastic fluid, Pa s

$\dot{\gamma}$ Shear rate, s^{-1}

ρ Density, kg m^{-3}

η Apparent viscosity, Pa s

τ Shear stress, Pa

τ_0 Yield stress, Pa

ω Angular function of frequency of vibration, rad s^{-1}

REFERENCES

Barth, T. J., Jespersen, D. C., 1989. The design and application of upwind schemes on unstructured meshes, 27th aerospace sciences meeting. AIAA, Paper 89-0366, Reno, Nevada.

Beckett, S. T., 2000. Private communication, Nestec, York, UK.

Bird, R. B., Armstrong, R. C., Hassager, O., 1987. *Dynamics of polymeric liquids: Fluid mechanics*. Wiley, New York.

Bird, R. B., Stewart, W. E., Lightfoot, E. N., 2007. *Transport phenomen*a. Wiley, New York.

Deshpande, N. S., Barigou, M., 2001. Vibrational flow of non-Newtonian fluids. Chemical Engineering Science, 56, 3845-3853.

Eesa, M., Barigou, M., 2008. CFD analysis of viscous non-Newtonian flow under the influence of a superimposed rotational vibration. Computers & Fluids, 37, 24-34.

Eesa, M., Barigou, M., 2010. Enhancing radial temperature uniformity and boundary layer development in viscous Newtonian and non-Newtonian flow by transverse oscillations: A CFD study. Chemical Engineering Science, 65, 2199-2212.

Gutfinger, C., 1964. Films of non-Newtonian fluids in laminar motion on vertical plates. Yale University.

Gutfinger, C., Tallmadge, J. A., 1964. Some remarks on the problem of drainage of fluids on vertical surfaces. AIChE Journal, 10, 774-780.

Gutfinger, C., Tallmadge, J. A., 1965. Films of non-Newtonian fluids adhering to flat plates. AIChE Journal, 11, 403-413.

Holdsworth, S. D., 1993. Rheological models used for the prediction of the flow properties of food products: A literature review. Transactions of the Institution of Chemical Engineers, 71, 139-179.

Jeffreys, H., 1930. The draining of a vertical plate. Mathematical Proceedings of The Cambridge Philosophical Society, 26, 204-205.

Metty, K. T., 2011. Private communication, GlaxoSmithKline(GSK) Hawthorn, USA.

Miladinova, S., Lebon, G., Toshev, E., 2004. Thin-film flow of a power-law liquid falling down an inclined plate. Journal of Non-Newtonian Fluid Mechanics, 122, 69-78.

Mitsoulis, E., 2007. Flows of viscoplastic materials: Models and computations. In: Binding DM, Hudson NE, Keunings R (eds) Rheology reviews 2007. Glasgow, Universities Design & Print, pp 135 - 178.

Peralta, J. M., Meza, B. E., Zorrilla, S. E., 2014. Mathematical modeling of a dip-coating process using a generalized Newtonian fluid. 1. Model development. Industrial & Engineering Chemistry Research, 53, 6521-6532.

Peralta, J. M., Meza, B. E., Zorrilla, S. E., 2014. Mathematical modeling of a dip-coating process using a generalized Newtonian fluid. 2. Model validation and sensitivity analysis. Industrial & Engineering Chemistry Research, 53, 6533-6543.

Tadepalli, S. C., Erdemir, A., Cavanagh, P. R., 2011. Comparison of hexahedral and tetrahedral elements in finite element analysis of the foot and footwear. Journal of Biomechanics, 44, 2337-2343.

Tanner, R. I., Milthorpe, J. F., 1983. Numerical simulation of the flow of fluids with yield stress, num. Meth. Lam. Turb. Flow, in: Taylor, C., Johnson, J.A., Smith, W.R. (Ed.), Processing 3rd International Conference Pineridge Press, Swansea, Seattle, pp. 680-690.

Tian, S., Barigou, M., 2015. An improved vibration technique for enhancing temperature uniformity and heat transfer in viscous fluid flow. Chemical Engineering Science, 123, 609-619.

CHAPTER 7.
SEDIMENTATION OF SPHERICAL PARTICLE IN NON-NEWTONIAN FLUIDS UNDER SUPERIMPOSED OSCILLATIONS

Summary

The effects of superimposed sinusoidal oscillations on the sedimentation of a single spherical particle in non-Newtonian fluids are studied numerically by Computational Fluid Dynamics (CFD). Inelastic time-independent non-Newtonian fluids of the power law, Bingham plastic, and Newtonian types are investigated. Results show that superimposed oscillations unaffected the time-averaged terminal velocity of particle in Newtonian fluid, but greatly affected that in non-Newtonian fluids. Settling of particles is accelerated in shear-thinning and Bingham plastic fluids, whilst retarded in shear-thickening fluids. The effects of the rheological properties as well as vibration parameters are studied in detail and show that the degree of enhancement of the settling velocity is a function of vibration parameters and rheological properties.

7.1. INTRODUCTION

The sedimentation motion of single particle in liquids is of great interest by theoretical and experimental study due to its high demand in a wide range of processing applications, such as, gravity-based solid-liquid separator, transportation of particles in slurry, falling ball viscometer and so on (Gavignet and Sobey, 1989; Li and Kuru, 2003). Investigations on this problem can be categorised into two classes by nature that the liquid is quiescent or not. On one hand, when a quiescent particle is released in a quiescent fluid without yield stress, it would be accelerated under gravity, until the drag force balanced its buoyant weight. Beyond which, particles settled at a constant speed, named as terminal settling velocity, noted as w_o (Chhabra, 1998). On the other hand, in a moving liquid, particle often settle at varying velocities due to the changing fluid velocity field. However, no matter the fluid is quiescent or not, settling velocity of particle was always of great importance and thus desired the most attention.

In a solid-liquid system, particle is influenced by gravity, inertial force and interaction force between the solid and fluid. Particle's settling velocity is controlled by various factors, for example: (i) particle's density, ρ_s, shape and dimension (e.g. diameter d in case that particle is spherical); (ii) the kinestate of its surrounding liquid (e.g. the liquid is quiescent or moving); (iii) liquid boundary, and (iv) physical properties of fluids, including the density, ρ and rheological parameters.

To quantitatively describe particle's terminal falling velocity in quiescent liquids has absorbed considerable investigation efforts, and most of which focused on the behaviour of spherical particles. A dimensionless quantity, named as drag coefficient C_D is introduced and defined as,

$$C_D = \frac{8F_D}{\pi d^2 \rho w_o^2} \tag{7.1}$$

where F_D is drag force exerting on the particle. The most widely known work on the spherical particle is done by Stokes (1851). His work was based on Newtonian fluids in creeping flow region where inertial effect can be neglected. Creeping flow is also named as Stokes' flow and determined by Reynolds number (i.e. Re << 1). Stokes' law can be described by

$$C_D = \frac{24\mu}{d\rho w_o} \tag{7.2}$$

where μ is viscosity for Newtonian fluid. Experimental work showed that Stokes' law contributed reliable results for Re up to about 0.1 (Chhabra, 2006). Stokes' solution was extended for a wider range of applicability by numerous researchers, for example, Oseen (1927), and Ockendon and Evans (1972). As the inertial effect is more significant while Re increases, numerical investigation were executed, for example, by Jenson (1959) for Re up to 40, LeClair *et al*. (1970) for Re up to 400 and Fornberg (1988) for Re up to 5000. Abundant works were also carried out for power law (Crochet *et al*., 1984; Gu and Tanner, 1985; Tripathi *et al.*, 1994; Graham and Jones, 1994) in creeping flow region.

In principle, particle is able to keep settling under the gravity in fluids without a plastic character, such as Newtonian and power law types. However, for very viscous fluids, the settling may be extremely slow because of the high viscous force. Furthermore, in cases of yield stress fluids, the gravity of particle may be supported by its yield stress, leading to a problem that particle may suspend in yield stress fluids (Chhabra, 2006).

Mechanical oscillations have been shown in the previous works to substantially enhance non-Newtonian fluid flow and heat transfer in pipes (Deshpande and Barigou, 2001; Eesa and Barigou, 2008; 2010; Tian and Barigou, 2015). In this chapter, a validated CFD model was used to numerically study the effects of mechanical oscillations on the settling of single solid spherical particle. The fluids considered are time-independent

inelastic fluids of Newtonian as well as non-Newtonian power law and Bingham plastic rheology. A detailed study is presented on the effects of rheological parameters (fluid consistency index, flow behaviour index, yield stress) and oscillation parameters (amplitude, frequency).

7.2. CFD MODEL

7.2.1. Rheological models and particle properties

7.2.1.1. Rheological models and physical properties of particle

The fluids used in this study are assumed to be rheologically time-independent. Two non-Newtonian rheological models are considered, power law and Bingham plastic. The mathematical descriptions for these two models have been given in Chapter 2, by Eq. (2.1) for power law type and Eq. (2.2) for Bingham plastic type.

The Bingham model suffers from discontinuity and its implementation poses difficulties in numerical modelling. And some strategies are employed to circumvent the problem caused by the yield stress (see Section 2.1). One of the popular methods which was found to be better suited for the particle settling problem studied here, is to represent the Bingham fluid by the so-called exponential model using a regularization parameter of m to approximate the Bingham plastic rheology (see Section 2.1.3). As Figure 2.4 shows, exponential model (Eq. (2.9)) leads to sufficiently accurate approximations of ideal Bingham plastic for $m \geq 100$ s (Blackery and Mitsoulis, 1997). However, values of m used in this study were 10000 s and 1000 s for free-settling and settling under vibration separately beyond which results no longer change with the growth of m.

Particle was assumed rigid sphere of glass with radius of 1 mm. The density of particle, noted as ρ_s, was specified as 2500 kg m^{-3}, satisfying that the gravity of particle is greater than the buoyance generated by fluid. The density was assumed as 1000 kg m^{-3} for all fluids studied in this work.

7.2.2. Harmonic oscillations

The effects of mechanical oscillations on the settling of a spherical particle are considered in this chapter. Oscillations are applied to pipe wall in direction parallel to the axis, as illustrated in Figure 7.1, and the wall displacement z is described by the

harmonic function:

$$z = A\sin(\omega t) \tag{7.3}$$

where A is the amplitude of vibration, t is the time and ω is the angular frequency such that $\omega = 2\pi f$. The resulting linear velocity of the wall is then,

$$u_z = \frac{\mathrm{d}z}{\mathrm{d}t} = A\omega\cos(\omega t) \tag{7.4}$$

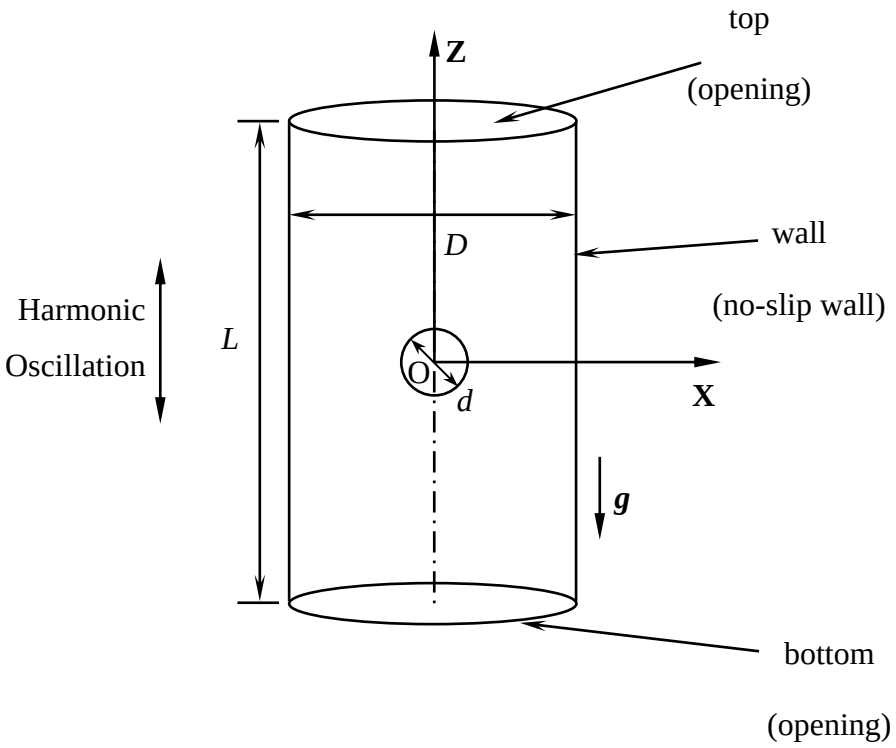

Figure 7.1. Schematic of a settling spherical particle in a fluid.

7.2.3. Governing equations

The laws governing the particle's motion under isothermal conditions are equations of mass and momentum (Eqs. (2.12) and (2.13)). For an incompressible fluid, Eqs. (2.12) and (2.13) can be rewritten as

Continuity: $$\nabla \cdot \boldsymbol{U} = 0 \tag{7.5}$$

Momentum: $$\rho \frac{\mathrm{D}\boldsymbol{U}}{\mathrm{D}t} = -\nabla p + \nabla \eta\dot{\gamma} + \rho \boldsymbol{g} \tag{7.6}$$

where $\boldsymbol{U}$ is velocity vector, ρ is density of fluid, η is apparent viscosity function, p is pressure, $\dot{\gamma}$ is shear rate, $\boldsymbol{g}$ is gravitational acceleration.

7.2.4. Terminal settling velocity.

Creeping flow region is characterized by Re << 1, and Reynolds number for different types of rheologies is defined as

Newtonian: $$\mathrm{Re} = \frac{\rho w_o d}{\mu} \tag{7.7}$$

power law: $$\mathrm{Re} = \frac{\rho {w_o}^{2-n} d^n}{k} \tag{7.8}$$

Bingham plastic: $$\mathrm{Re} = \frac{\rho w_o d}{\mu_B} \tag{7.9}$$

where k is fluid consistency index, n is flow behaviour index and μ_B is plastic viscosity. Thus, Stokes' law, i.e. Eq. (7.2) can be rewritten to its well-known form, in the form of Reynolds number as,

$$C_D = \frac{24}{\mathrm{Re}} \tag{7.10}$$

7.2.4.1. Terminal velocity in unbounded power law fluids

In creeping flow region, the terminal velocity, w_o can be achieved after a very short transition period, e.g. only a few diameters distance of travelling (Chhabra *et al*., 1998; Chhabra and Richardson, 1999).

The drag coefficient in power law fluids is dependent on the fluid behavior index *n*, and can be developed from the Stokes' law by introducing a deviation factor, $X(n)$. Therefore, the drag coefficient is expressed by

$$C_D = \frac{24}{\mathrm{Re}} X(n) \tag{7.11}$$

For different values of fluid behaviour index, values of $X(n)$ have reported in literatures (Crochet *et al*., 1984; Gu and Tanner, 1985; Tripathi *et al*., 1994; Tripathi and Chhabra,1995). The values of $X(n)$ used in this work are listed in Table 7.1.

Table 7.1. Values of $X(n)$ for a sphere in creeping flow for power law fluids (Gu and Tanner, 1985; Tripathi and Chhabra,1995).

n	0.1	0.2	0.3	0.4	0.5	0.6	0.7	0.8	0.9	1.0	1.2	1.4	1.6
$X(n)$	1.354	1.413	1.458	1.442	1.42	1.382	1.32	1.24	1.14	1.002	0.827	0.569	0.390

The drag, comparing to its Newtonian value, reduces in shear-thinning fluids ($X(n) > 1$), whilst increases in shear-thickening fluids ($X(n) < 1$). Thus, the terminal settling velocity in unbounded quiescent power law fluids can be calculated as follow:

$$w_o = \frac{gd^{n+1}(\rho_S - \rho)^{1/n}}{18kX(n)} \tag{7.12}$$

where ρ_S is the density of particle. While $n = 1$, Eq. (7.12) reduce to its form for Newtonian fluids (i.e. Stokes' law), in other words, $X(1) = 1$ and $k = \mu$. It is worth to note that, as stated in Chapter 3 and Chapter 6, the flow behaviour index is a measure of the degree of non-Newtonian behaviour. As n decreases from unity, the non-Newtonian properties are more pronounced. However, counterintuitively, although some divergence in various work, all investigations seem to conclude that, with shear-thinning fluids, the maximum drag force above the corresponding Newtonian value is obtained at $n \sim 0.35$ (Chhabra, 2006).

7.2.4.2. Terminal velocity in unbounded Bingham plastic fluids

As stated in Section 7.1, viscoplastic behaviours may cause particle to suspend in the fluids under gravity even the particle's density is greater than the density of fluids. However, confusion is still showing in the critical value of Y_G corresponding to the initiation of sphere motion. While Y_G is so-called yield-gravity parameter and defined as,

$$Y_G = \frac{\tau_0}{gd(\rho_S - \rho)} \tag{7.13}$$

Conclusions have been reported on the values of Y_G with a wide range from ~ 0.04 to ~ 0.2. In case that sphere motion commence, the terminal velocity in Bingham plastic

materials can be given, similarly to that in power law fluids by introducing correcting factor, X into Eq. (7.11). However, in Bingham plastic fluids, X is a function of Bingham number Bi (Beris *et al*., 1985; Blackery and Mitsoulis, 1997), as:

$$X = 1 + a\,(\mathrm{Bi})^{b} \tag{7.14}$$

where, a and b are factors measured numerically (Blackery and Mitsoulis, 1997) or experimentally (Chhabra and Uhlherr, 1988), Bi is defined as,

$$\mathrm{Bi} = \frac{\tau_0 d}{\mu_B w_o} \tag{7.15}$$

7.2.5. Wall effect

Wall effect is another reason which may affect particle's behaviour if it settles in a confined liquid. This effect, f_{wall} is defined as

$$f_{wall} = \frac{w_c}{w_o} \tag{7.16}$$

where w_c is settling velocity in a confined liquid. The wall effect has been investigated in power law fluids (Missirlis *et al*., 2001; Song *et al*., 2009; Despeyroux *et al*., 2011; Rajasekhar and Kishore, 2012) and viscoplastic fluids (Blackery and Mitsoulis, 1997)

7.3. CFD SIMULATIONS

7.3.1. Geometry and mesh

As shown in Figure 7.1, particle was assumed as a solid glass sphere with radius of 1 mm and in the centre of the tube at $t = 0$, and to settle along the centre of the tube (i.e. only motion in z direction is considered). Thus, the model reduces to a two-dimensional problem. The model was set up and run using the commercial software package ANSYS Workbench 14.5. The CFD model consists of a sector, which is extruded for one degree from a planar geometry, which is of 15 mm in radius (D = 30 mm), 200 mm in axial direction and with a half circle of 1 mm in radius cut out in the middle of axis.

The geometry was meshed with non-uniform hexahedral cells. Hexahedral meshes are known to achieve a higher solution accuracy than tetrahedral meshes for the same cell amount, and provide the best resolution of the boundary layer close to walls with significantly fewer cells. Hexahedral elements also reduce numerical diffusion, aid convergence, and have important computing cost and stability advantages over tetrahedral elements (see for example, Biswas and Strawn, 1998; Tadepalli *et al*., 2011).

The mesh was optimised through mesh-independence study. This study started from a coarse mesh and continuously refine it until the numerical results was independent on the mesh size. The final mesh consisted of 2960 hexahedral cells. The mesh was refined using inflation layers, which progressively reduces to 0.1 mm near the tube wall and 0.05 mm near sphere wall. The spherical surface was uniformly meshed by 69 nodes along the circle, contributing a high quality mesh measured by orthogonality and warpage of over 0.6, which is well above the generally accepted minimum value of 0.4 for a good mesh, as shown in Figure 7.2.

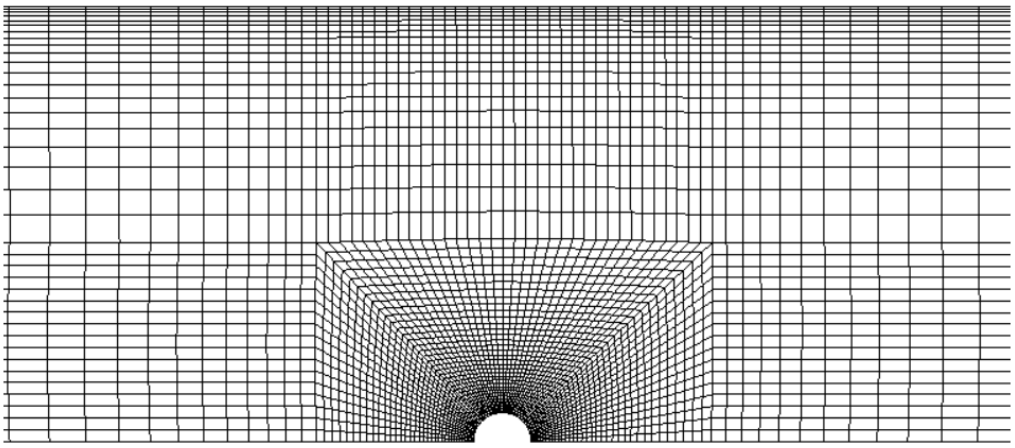

Figure 7.2. Schematic of the mesh near spherical surface.

7.3.2. Boundary and initial conditions

The geometry consists of four surfaces: top, bottom, wall, and the spherical surface. Top and bottom were specified as opening condition with a gauge pressure of 0 Pa, and the other boundaries were treated as wall. When mechanical oscillations were superimposed and additional harmonic velocity boundary conditions was assigned at the wall, as defined by Eq. (7.4). At t = 0 s, the sphere was stationary and assumed at the centre. The origin of the coordinates was set at the centre of the sphere. Gravity act along the negative y axis (Figure 7.1), in other words, the particles settles along the positive y axis.

7.3.3. Numerical scheme

The CFD code uses a finite-volume-based method to discretise the governing transport Eqs. (7.5) — (7.6). 'High Resolution' Advection Scheme and 'Second Order Backward Euler' transient scheme are implemented here. All simulations were executed in the transient mode. In general, a small time step of 10^{-6} s was used to avoid the error of negative or folding mesh. Simulations were required to execute until further execution of modelling would not affect the terminal velocities for free settling or time-averaged terminal velocities for forced settling under vibration.

Convergence of the numerical solution was assumed to be satisfactory when the root mean square (RMS) of mass and momentum residuals both reached 10^{-4} at each time step which is a good level of accuracy given the complexity of the problem. Achieving this level of convergence typically required 1 — 4 coupling iterations per time step and 40 — 60 coefficient loop iterations for free settling, and 10 — 50 coupling iterations per time step and 20 — 80 coefficient loop iterations for settling drainage with vibration. In practice, however, most of the equations generally reached RMS residual values well below the specified target.

7.4. CFD VALIDATION

CFX is a widely used code and has been proven to be generally stable and reliable. The model used in this study was validated with the free settling simulations against the previous published results introduced in the theory Section 7.2.4, Eq. (7.12) for power law fluids.

In Table 7.2, the terminal velocities predicted by our model were compared against those from previous publications for series of shear-thinning power law fluids with ranges of k from 1 Pa s^n to 10 Pa s^n, n from 0.5 to 0.9 and Newtonian fluid of μ = 1 Pa s. Wall effect factor f_{wall} for varying n were collected from previous work (Missirlis *et al*., 2001) and used to calculated the terminal settling velocity corresponding to the diameter ratio d/D = 1/15, which is used in this study. The excellent agreement can be confirmed by the maximum difference of ~ 2 % for all the rheologies investigated.

Table 7.2. Validation of CFD model with power law fluids.

Fluid consistency index k (Pa s^n)	Flow behaviour index n (-)	Unconfined terminal velocity w_o (mm s^{-1}) Eq. (7.12)	Confined terminal velocity w_c (mm s^{-1}) (Missirlis *et al.*, 2001)	Confined terminal velocity w_c (mm s^{-1}) CFD predicted	Difference (%)
1	0.4	2.337	2.337	2.336	-0.04
1	0.5	2.445	2.420	2.368	-2.14
4	0.5	0.150	0.148	0.148	0.00
7	0.5	0.0487	0.0480	0.0482	0.42
10	0.5	0.0239	0.0237	0.0236	-0.42
1	0.6	2.494	2.449	2.428	-0.85
1	0.7	2.614	2.504	2.516	0.48
1	0.8	2.781	2.584	2.616	1.24
1	0.9	2.994	2.680	2.739	2.20
1	1	3.252	2.790	2.821	1.11

7.5. RESULTS AND DISCUSSION

Figure 7.3 depicted the history of settling velocity for a particle in a quiescent power law fluid. Particle greatly accelerated under the action of gravity after it commenced to settle at t = 0 s, and reached the maximum speed of 0.148 mm s^{-1} at ~ 0.001 s. Beyond which settling velocity kept unchanged. In other words, particle settles at a constant velocity (i.e. its terminal settling velocity).

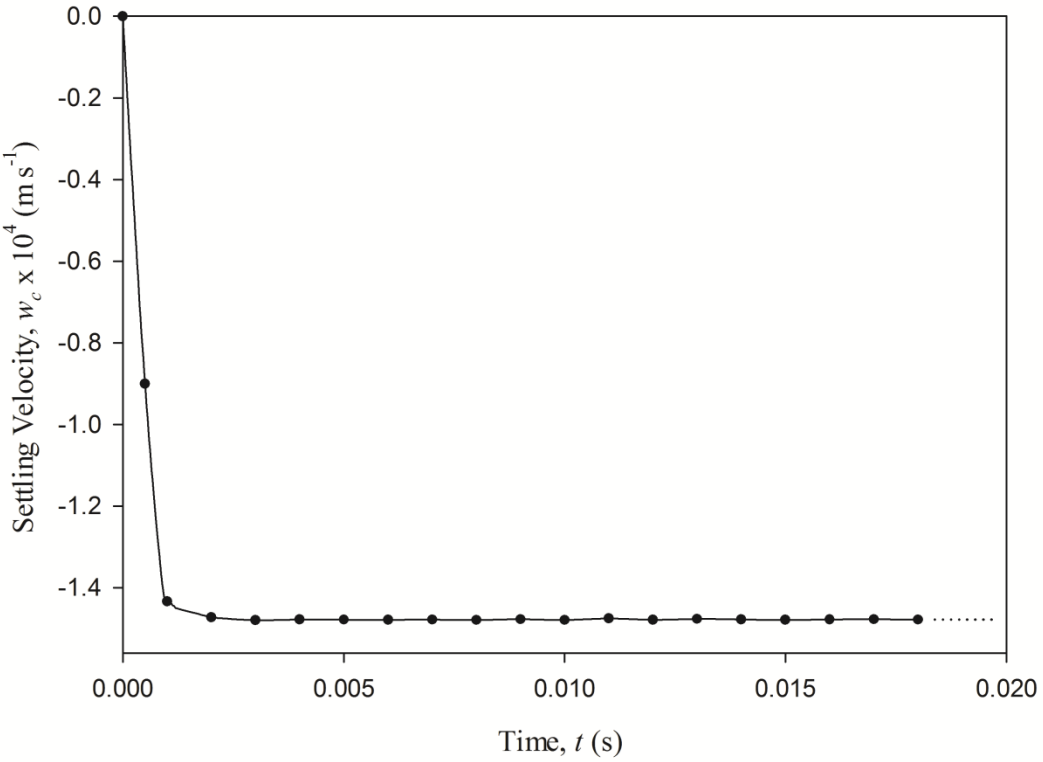

Figure 7.3. The history of settling terminal velocity in a quiescent power law fluid: k = 4 Pa $s^{0.5}$; n = 0.5.

Figure 7.4 showed the trajectory of a particle in a vibrated power law fluid. Under vibration, particle behaved a motion upward and downward, the settling velocity of particle, w_v is varying. Therefore, the motion of particle was investigated by time-averaged terminal velocity, which is calculated over one oscillation cycle as,

$$\overline{w}_v = \frac{\int_t^{t+\frac{1}{f}} w_v \mathrm{d}t}{\frac{1}{f}} = f\int_t^{t+\frac{1}{f}} w_v \mathrm{d}t \tag{7.17}$$

CFD results show that, after several oscillation periods, the time-averaged settling velocity reached constant, which can be calculated by the trajectory of particle, as shown in Figure 7.4.

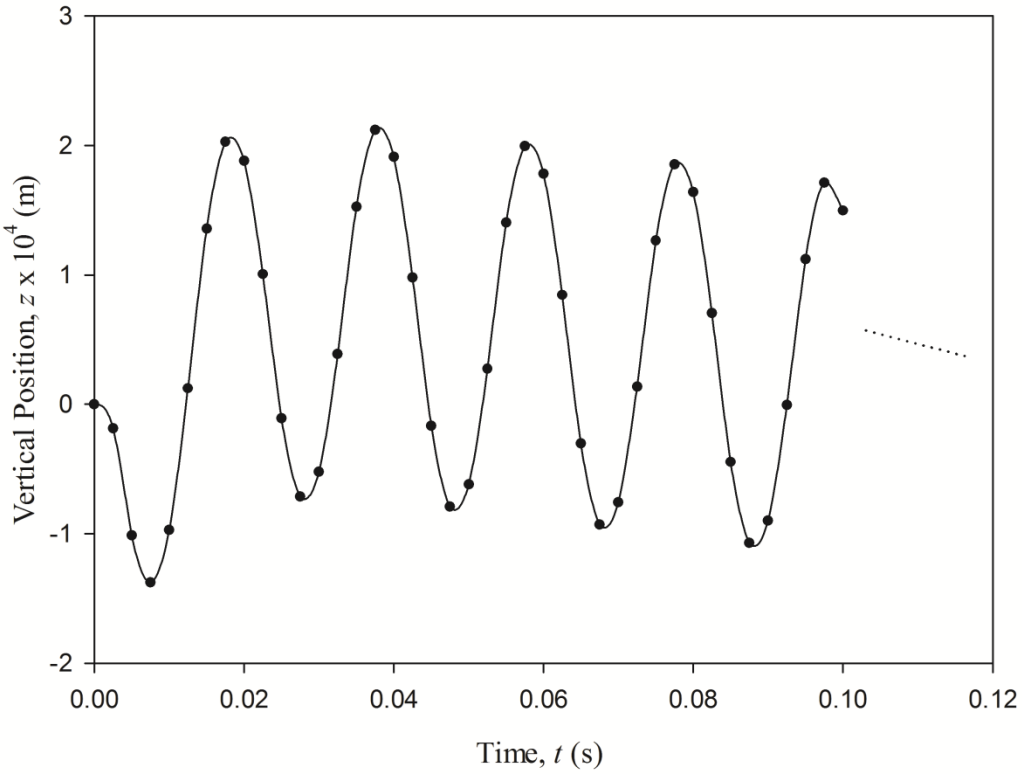

Figure 7.4. The trajectory of a particle under the vibration in an oscillatory power law fluid:
k = 4 Pa s$^{0.5}$; n = 0.5; f = 50 Hz; A = 2 mm.

The terminal velocity enhancement ratio, E is defined as the ratio of time-averaged settling velocity particle in an oscillatory fluid to its free settling terminal velocity in the same fluid, as:

$$E = \frac{\overline{w}_v}{w_c} \tag{7.18}$$

7.5.1. Effects of vibration amplitude and frequency

The effect of vibration amplitude A and frequency f on terminal velocity enhancement ratio is presented in Figures 7.5 and 7.6. Increasing vibration amplitude and frequency leads to higher terminal velocity enhancement ratios tending, however a limiting value for a given fluid rheology.

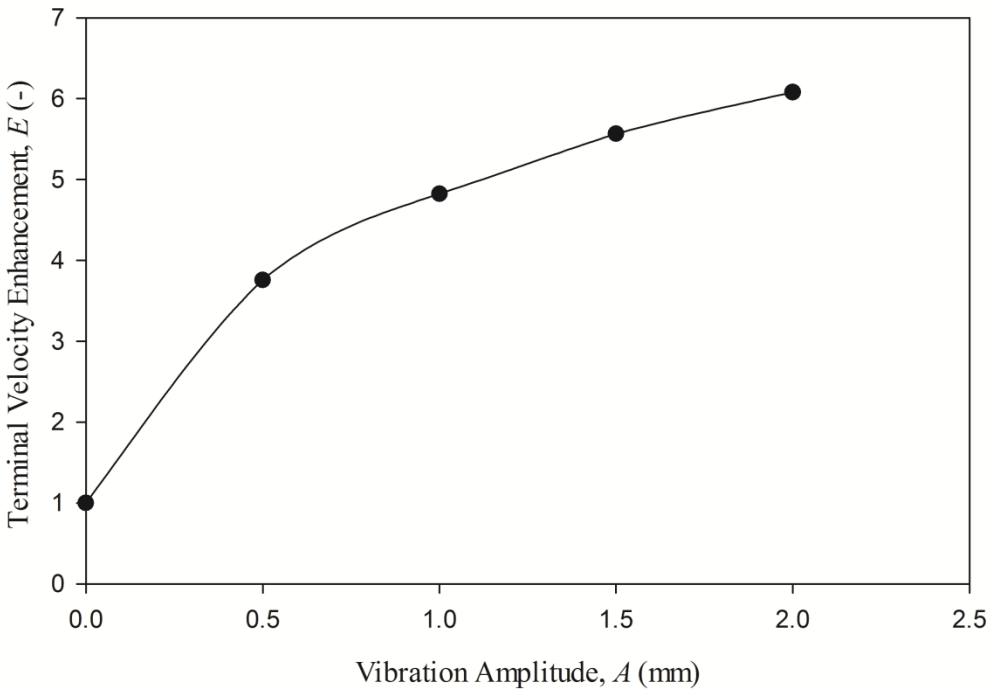

Figure 7.5. The effect of vibration amplitude on the terminal velocity enhancement in an oscillatory power law fluid:
k = 4 Pa s$^{0.5}$; n = 0.5; f = 50 Hz.

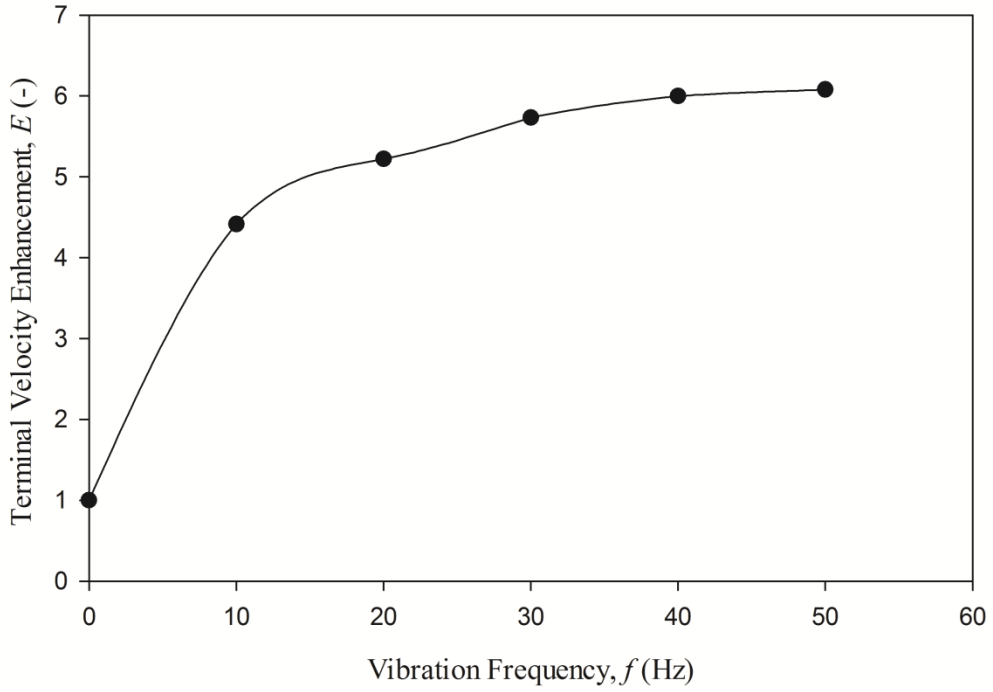

Figure 7.6. The effect of vibration frequency on the terminal velocity enhancement in an oscillatory power law fluid:
k = 4 Pa s$^{0.5}$; n = 0.5; A = 2 mm.

7.5.2. Effects of fluid consistency index

The index k is a measure of the consistency of the fluid, the higher k the more viscous the fluid. For settling in quiescent liquids, the terminal velocity is depicted in Figure 7.7 for various values of k with shear-thinning power law fluids. The terminal settling velocity decreases and tends to zero as k theoretically increases to infinite. Superimposed oscillatory motion of the liquid generates larger time-averaged terminal velocities of particle. Increasing the value of k leads to higher velocity enhancement ratios over a the range investigated in this study (Figure 7.8) indicating that mechanical oscillation is more effective with more viscous fluids.

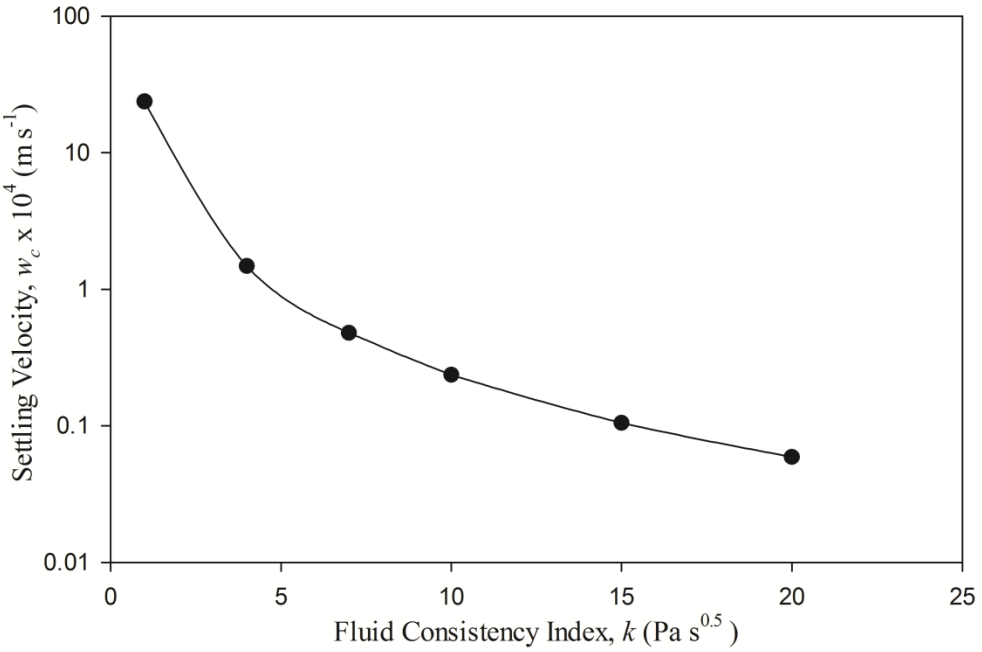

Figure 7.7. The effect fluid consistency index on settling terminal velocity in a quiescent power law fluid:

n = 0.5.

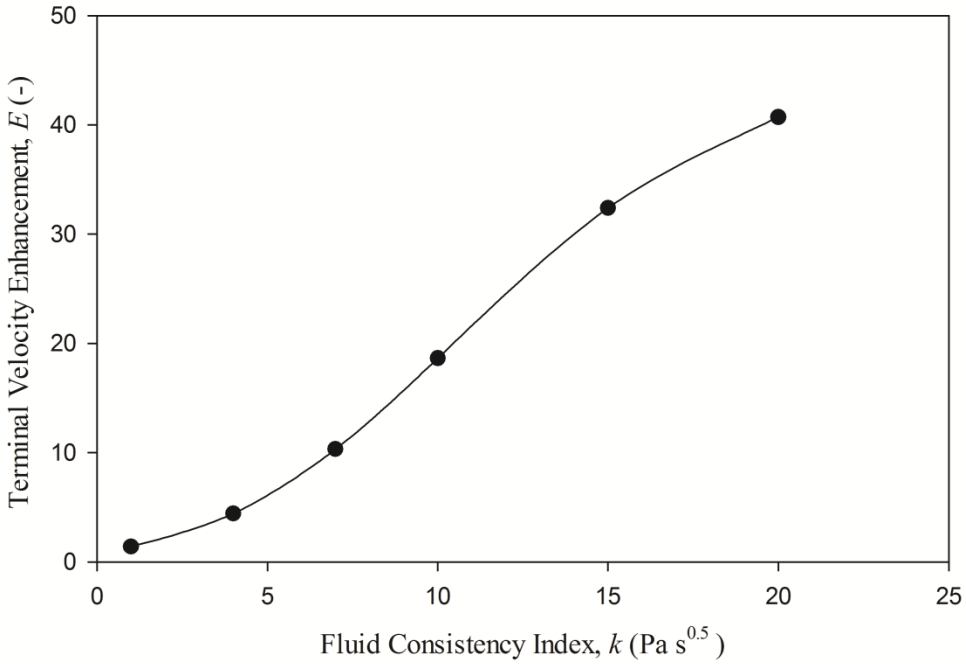

Figure 7.8. The effect of fluid consistency index on the terminal velocity enhancement in an oscillatory power law fluid:

n = 0.5; f = 50 Hz; A = 2 mm.

7.5.3. Effects of flow behaviour index

The flow behaviour index *n* is a measure of the degree of non-Newtonian behavior; the greater the departure from unity the more pronounced are the non-Newtonian properties of the fluid. The terminal settling velocity enhancement ratio varies with *n* as shown in Figure 7.9.

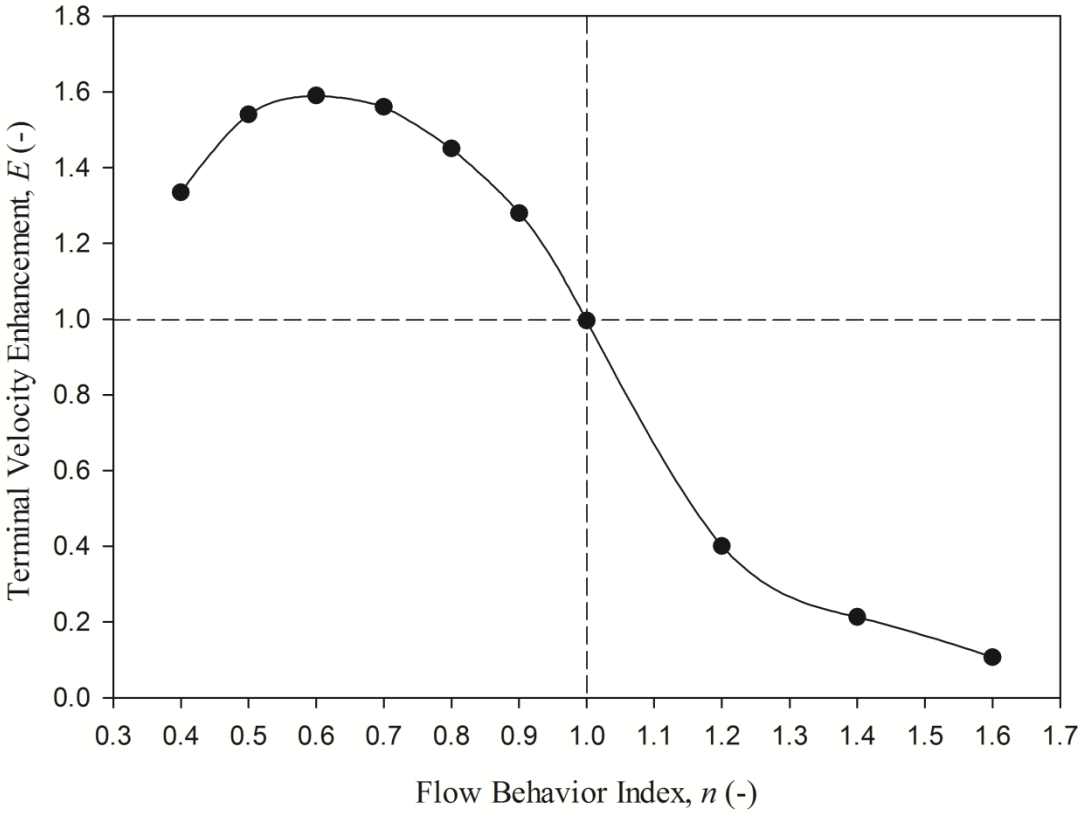

Figure 7.9. The effect of fluid behavior index on the terminal velocity enhancement with a power law fluid:
k = 1 Pa s^n; f = 50 Hz; A = 2 mm.

From Figure 7.9, it can be concluded that the enhancement ratio is very sensitive to changes in *n*. For shear-thickening or dilatant fluids ($n > 1$), an increase in *n* causes an almost exponential decrease in settling, i.e. settling retardation whereby $\overline{w}_v < w_c$. For

shear-thinning or pseudoplastic fluids ($n < 1$), Figure 7.9 reveals that the superimposed oscillations lead to positive settling acceleration. The terminal velocity enhancement increases as n reduces until ~ 0.6. However, a maximum velocity enhancement is achieved with $n \sim 0.6$. While n decreases from 0.6, the terminal velocity enhancement ratio started to decline. It seems can be supported by the conclusion that the maximum drag is obtained at $n \sim 0.35$ for a power law fluid above its Newtonian value (Chhabra, 2006). Superimposed oscillations contributes to an equivalently power law fluid with more significant pseudeopasty effect than that with quiescent liquid. Thus, maximum drag force is obtained with $n \sim 0.6$ under oscillation of A = 2 mm and f = 50 Hz, comparing to $n \sim 0.35$ in a quiescent fluid. However, more analysis is still required to explain the decay of E while $n < \sim 0.6$. The comparison on the effect of n, depicted in Figure 7.9 confirms that for fluids with a shear-rate dependent viscosity, it is the extra shear-thinning (or thickening) induced by the oscillations which is responsible for the changes in time-averaged settling velocity. For $n = 1$ the fluid is Newtonian and there is no settling velocity enhancement ($E = 1$).

7.5.4. Effect of yield stress

The variations of E as a function of yield stress are plotted in Figure 7.10, showing an almost exponential rise in drainage enhancement as a function of τ_0. The effects are similar to those caused by reducing the index n of a power law fluid while $n > \sim 0.6$, as shown in Figure 7.9. It should be pointed out that, similar to a pseudoplastic fluid, a Bingham plastic fluid exhibits an apparent viscosity that decreases hyperbolically with increasing shear rate, thus:

$$\begin{cases} \eta = \mu_B + \tau_0/\dot{\gamma}, & \text{for} \quad \tau > \tau_0 \\ \eta \to \infty, & \text{for} \quad \tau \le \tau_0 \end{cases} \tag{7.19}$$

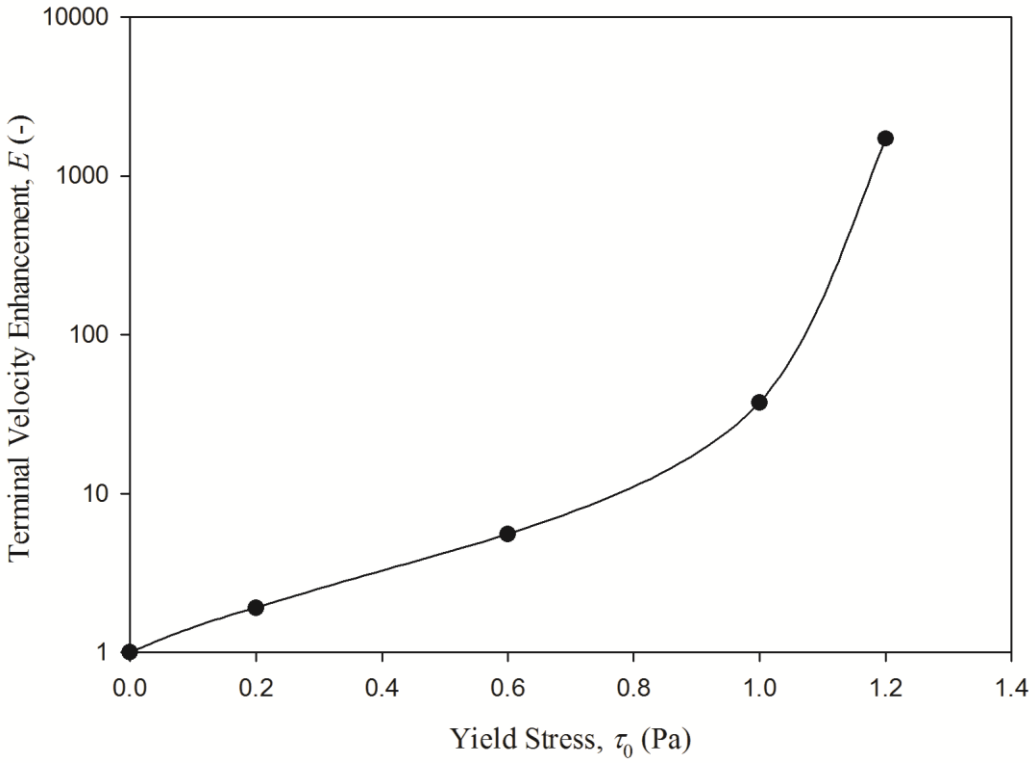

Figure 7.10. The effect of yield stress on the terminal velocity enhancement with a Bingham plastic fluid:

μ_B = 1 Pa s; f = 50 Hz; A = 2 mm.

7.6. CONCLUSIONS

A CFD model was used to simulate the settling of a spherical solid particle in various fluid rheologies, including Newtonian type and non-Newtonian of power law and Bingham plastic types. Validations with free settling simulations against analytical theory showed that the model was accurate and reliable. Whilst Newtonian fluids are not affected, the time-averaged settling velocity in oscillatory non-Newtonian pseudoplastic (shear-thinning) fluids is enhanced by a substantial factor, depending on fluid rheological parameters and vibration intensity. Settling in a viscoplatic fluids, which display the yield stress characteristic, is affected by mechanical oscillation in a similar way as shear-thinning rheologies. Shear-thickening fluids, however, undergo retardation in settling when subjected to vibration.

NOTATION

A Vibration amplitude, m

Bi Bingham number, -

C_D Drag coefficient, -

D Diameter of the tube, m

d Diameter of particle, m

E Settling velocity enhancement, -

F_D Drag force, N

f Vibration frequency, Hz

f_{wall} Wall factor, -

$\boldsymbol{g}$ Gravitational acceleration, m s^{-2}

k Fluid consistency index, Pa s^n

m The growth exponent in exponential model for Bingham plastic fluids, s

n Flow behaviour index, -

Re Reynolds number, -

t Time, s

t_v Vibration time, s; $t_v = t + 1.6$ s

w_c Settling velocity in a confined quiescent liquid, m s^{-1}

w_o Settling velocity in an unconfined quiescent fluid, m s^{-1}

w_v Settling velocity in an oscillatory liquid, m s^{-1}

$\overline{w}_v$ Mean settling velocity over one oscillation cycle in an oscillatory liquid, m s^{-1}

$X(n)$ Deviation factor, -

x Position perpendicular to the substrate, m

Y_G Yield-gravity parameter, -

z Axial position, m

Greek symbols

μ Viscosity for Newtonian fluid, Pa s

μ_B Plastic viscosity for Bingham plastic fluid, Pa s

$\dot{\gamma}$ Shear rate, s^{-1}

ρ Density of fluid, kg m^{-3}

ρ_s Density of particle, kg m^{-3}

η Apparent viscosity, Pa s

τ Shear stress, Pa

τ_0 Yield stress, Pa

ω Angular function of frequency of vibration, rad s^{-1}

REFERENCES

Beris, A. N., Tsamopoulos, J. A., Armstrong, R. C., Brown, R. A., 1985. Creeping motion of a sphere through a bingham plastic. Journal of Fluid Mechanics, 158, 219-244.

Biswas, R., Strawn, R. C., 1998. Tetrahedral and hexahedral mesh adaptation for CFD problems. Applied Numerical Mathematics, 26, 135-151.

Blackery, J., Mitsoulis, E., 1997. Creeping motion of a sphere in tubes filled with a Bingham plastic material. Journal of Non-Newtonian Fluid Mechanics, 70, 59-77.

Chhabra, R. P., 1998. Rising velocity of a swarm of spherical bubbles in power law fluids at high reynolds numbers. The Canadian Journal of Chemical Engineering, 76, 137-140.

Chhabra, R. P., 2006. *Bubbles, drops, and particles in non-Newtonian fluids*, second edition. CRC Press, Florida, US.

Chhabra, R. P., Richardson, J. F., 1999. *Non-Newtonian flow in the process industries: Fundamentals and engineering applications*. Butterworth-Heinemann, Oxford.

Crochet, M. J., Davies, A. R., Walters, K., 1984. *Numerical simulation of non-Newtonian flow*. Elsevier Science. Amsterdam.

Deshpande, N. S., Barigou, M., 2001. Vibrational flow of non-Newtonian fluids. Chemical Engineering Science, 56, 3845-3853.

Despeyroux, A., Ambari, A., Richou, A. B., 2011. Wall effects on the transportation of a cylindrical particle in power-law fluids. Journal of Non-Newtonian Fluid Mechanics, 166, 1173-1182.

Eesa, M., 2009. CFD studies of complex fluid flows in pipes, Department of Chemical Engineering. University of Birmingham, Birmingham, UK.

Eesa, M., Barigou, M., 2008. CFD analysis of viscous non-Newtonian flow under the

influence of a superimposed rotational vibration. Computers & Fluids, 37, 24-34.

Fornberg, B., 1988. Steady viscous flow past a sphere at high reynolds numbers. Journal of Fluid Mechanics, 190, 471-489.

Gavignet, A. A., Sobey, I. J., 1989. Model aids cuttings transport prediction. Journal of Petroleum Technology, 41, 916-921.

Graham, D. I., Jones, T. E. R., 1994. Settling and transport of spherical particles in power-law fluids at finite reynolds number. Journal of Non-Newtonian Fluid Mechanics, 54, 465-488.

Gu, D. H., Tanner, R. I., 1985. The drag on a sphere in a power-law fluid. Journal of Non-Newtonian Fluid Mechanics, 17, 1-12.

Jenson, V. G., 1959. Viscous flow round a sphere at low reynolds numbers. Proceedings of the Royal Society of London A: Mathematical, Physical and Engineering Sciences, 249, 346-366.

LeClair, B. P., Hamielec, A. E., 1970. Viscous flow through particle assemblages at intermediate reynolds numbers. Steady-state solutions for flow through assemblages of cylinders. Industrial & Engineering Chemistry Fundamentals, 9, 608-613.

Li, Y., Kuru, E., 2003. Numerical modelling of cuttings transport with foam in horizontal wells. Journal of Canadian Petroleum Technology, 42, 54-61.

Missirlis, K. A., Assimacopoulos, D., Mitsoulis, E., Chhabra, R. P., 2001. Wall effects for motion of spheres in power-law fluids. Journal of Non-Newtonian Fluid Mechanics, 96, 459-471.

Mitsoulis, E., 2007. Flows of viscoplastic materials: Models and computations. In: Binding DM, Hudson NE, Keunings R (eds) Rheology reviews 2007. Glasgow, Universities Design & Print, pp 135 - 178.

Ockendon, J. R., Evans, G. A., 1972. The drag on a sphere in low reynolds number flow. Journal of Aerosol Science, 3, 237-242.

Oseen, C. W., 1927. Neuere methoden und ergebnisse in der hydrodynamik. Akademische Verlagsgesellschaft, Leipzig.

Rajasekhar Reddy, C., Kishore, N., 2012. Wall retardation effects on flow and drag phenomena of confined spherical particles in shear-thickening fluids. Industrial & Engineering Chemistry Research, 51, 16755-16762.

Song, D. Y., Gupta, R. K., Chhabra, R. P., 2009. Wall effects on a sphere falling in quiescent power law fluids in cylindrical tubes. Industrial & Engineering Chemistry Research, 48, 5845-5856.

Stokes, G. G., 1851. *On the effect of the internal friction of fluids on the motion of pendulums*. University of Pittsburg Press, Pittsburg.

Tadepalli, S. C., Erdemir, A., Cavanagh, P. R., 2011. Comparison of hexahedral and tetrahedral elements in finite element analysis of the foot and footwear. Journal of Biomechanics, 44, 2337-2343.

Tripathi, A., Chhabra, R. P., 1994. Hydrodynamics of creeping motion of an ensemble of power law fluid drops in an immiscible power law medium. International Journal of Engineering Science, 32, 791-803.

CHAPTER 8.
CONCLUSION AND FUTURE WORK

8.1. CONCLUSIONS

The behaviours of Newtonian and non-Newtonian fluids under harmonic mechanical oscillations were investigated by using validated CFD models in five aspects: (i) efficacy comparison of three modes of oscillations in affecting pipe flow with and without heat transfer; (ii) effect of transverse vibration on heat transfer in a tube; (iii) application of transverse vibration in the continuous process of food sterilisation; (iv) application of mechanical oscillation in enhancing liquid film drainage; (v) application of vibration in affecting settling motion of spherical particle in liquid.

In the first study, results showed that the oscillation of pipes conveying viscous fluids has a good potential for the processing of these materials. Whilst the flow of Newtonian fluids is unaffected by any type of vibration, the flow of shear-thinning and shear-thickening fluids can be, respectively, substantially enhanced or retarded by the superimposition of longitudinal, transverse or rotational oscillations. Longitudinal oscillations are generally the most effective in this respect, producing flow enhancements which exceed those generated by transverse and rotational vibration by a considerable margin, while transverse and rotational oscillations also produce significant flow enhancements of comparable magnitudes, especially under large vibration intensity. However, transverse oscillations are always more sensitive to the change in fluid consistency index, flow behaviour index and yield stress than either longitudinal or rotational vibrations. For all these three types of vibration, the extent of the flow enhancement produced is a function of the amplitude and frequency of vibration and fluid rheology. Vibration results in a sharpened velocity profile in shear-thinning fluids and a blunted velocity profile in shear-thickening fluids comparing to steady state.

In the second study, results showed that, unlike longitudinal and rotational oscillations, forced transverse vibration superimposed on the steady laminar flow of a fluid in a tube with an isothermal wall generates a vigorous swirling fluid motion represented by a strong vorticity field and complex spiralling fluid streamlines and trajectories. The method has been shown to have substantial benefits for heat transfer including a large

(several folds) increase in wall heat transfer, a much more uniform radial temperature profile, a rapid development of the temperature profile along the tube, rapid heating of the core region of the flow, and relatively short processing tubes.

A new enhanced technique has been introduced in this work which combines transverse vibration with a step rotation of oscillation orientation. This technique produces much more improved effects compared to transverse vibration alone, resulting in much shorter processing tubes. It also excels in comparison with the well-known Kenics helical static mixer which has the disadvantages of being unsuitable for hygienic fluid processing and causes large pressure drops. On the other hand, the mechanical power input associated with the vibration process is modest.

In the third study, results showed that, the superimposition of transverse vibratory motion with step change in oscillation orientation on the steady laminar flow of a viscous single-phase fluid, introduces chaotic fluid motion which leads to vast improvements in wall heat transfer and radial temperature uniformity. When applied to a continuous heat-hold-cool sterilisation process, these effects translate into large improvements in thermal processing uniformity and efficiency compared with a conventional process with or without an inline static mixer fitted. Simple oscillations without a change in orientation also give good improvements but they are not nearly as effective.

The novel (**VF-SR**) technique leads to fast nearly-uniform heating and cooling of the product, thus, achieving much higher levels of sterility with low loss of product quality in much shorter processing tubes, thus, obviating the need for a holding stage and overall reducing the length of the conventional heat-hold-cool sterilisation process by one or two orders of magnitude, depending on processing conditions. Vibration, therefore, appears to create processing conditions that are much more in agreement with the high temperature for short time (HTST) assumption which is often contradicted in conventional steady flow processing. This shows that the **VF-SR** technique has considerable potential in optimising the continuous sterilisation process by creating

conditions for achieving HTST processing, a long-standing problem in food sterilisation.

Whilst this numerical analysis has been fairly well validated, a full experimental validation, as is usual practice, would be needed to fully confirm the benefits of oscillatory perturbations on the sterilisation process. It should also be noted that the above conclusions are only valid for single-phase flows as considered in this analysis. Heat transfer in two-phase solid-liquid flows where particle properties such as size and density are such that the mixture cannot be treated as a homogenous fluid, is much more complex and the applicability of the oscillatory perturbation technique to such flows warrants a more detailed study.

Furthermore, it can be argued that the chaotic flow would have added practical benefits: first, for the reduction of fouling because of the cleaning action that the fluid motion would create at the wall, and second in two-phase solid-liquid flow, assuming that the applicability of the oscillatory technique is proven, it would be expected to help keep solid particles in suspension and may also potentially enhance liquid-particle heat transfer. Whilst the use of vibration industrially may not always be feasible, in processes where this is possible, however, results indicate that benefits can be very significant.

In the fourth study, results showed that, whilst Newtonian fluids are not affected, the superimposition of harmonic oscillations increases the rate of drainage in non-Newtonian pseudoplastic (shear-thinning) films by a substantial factor, depending on the rheology of the fluid and vibration intensity. Shear-thickening fluids, however, undergo retardation in drainage when subjected to vibration. Viscoplatic fluids, by virtue of their apparent yield stress, display shear-thinning characteristics similar to pseudoplastic fluids, and their drainage is affected by mechanical oscillation in a similar way. In particular, for a given fluid rheology, power law or Bingham plastic, the same enhancement ratio achieved is obtained under conditions of identical peak acceleration.

The emptying of highly viscous non-Newtonian fluids including yield-stress fluids from vessel and hoppers is a challenging industrial problem as free drainage invariably results in a residual film draining extremely slowly on the wall in the case of viscous fluids, and a static film in the case of yield-stress fluids. For high values of yield stress, equilibrium films can have a significant thickness, thus, trapping considerable amounts of material as well as making cleaning more difficult. Harmonic oscillations are effective at reducing the thickness of this equilibrium film potentially to a negligible value, if a sufficiently high vibration acceleration is used. In addition to its potential for assisting the emptying of vessels filled with complex fluids, vibration could also be employed as a tool for controlling the thickness of films in surface coating applications.

In the fifth study, the results showed that, the time-averaged settling velocity is not affected in Newtonian fluids, but enhanced by a substantial factor in oscillatory non-Newtonian pseudoplastic (shear-thinning) fluids, depending on fluid rheological parameters and vibration intensity. Settling in a viscoplatic fluids, which display the yield stress characteristic, is affected by mechanical oscillation in a similar way as shear-thinning rheologies. In shear-thickening fluids, however, settling of particle was retarded when subjected to vibration.

8.2. FUTURE WORK

Based on the work reported in this thesis on the applications of mechanical oscillations, further work is recommended to be carried on in following aspects:

(i) Different forms of mechanical vibrations could be introduced in all the work reported in this thesis. This can help to assess the feasibility of vibration, with different forms, as a technique to enhance the flow and heat transfer in industry.

(ii) Transverse or rotational harmonic oscillations could be attempted to apply in the investigation of liquid film drainage and settling of solid particles.

(iii) Understanding on the work reported in Chapter 4 could be improved by a further parametrical study by investigating the effect of geometry for example. Moreover, the performance of vibration with non-Newtonian fluids, such as power law, viscoplastic and viscoelastic fluids could also be studied.

(iv) Transverse vibration could be used to enhance the heat transfer between solid particles and the surrounding liquid in a solid-liquid system.

(v) Single particle system studied in Chapter 7 could be extended to multi-particle system. Moreover, discharge of gas bubble from liquid can be affected by imposed oscillation, however the deformation of bubble should be considered.